Determination of Sea Ice Surface Elevation with Laser and Radar Altimetry and Comparison with Ice Thickness Data Sets in the Arctic and Antarctic

Bestimmung der Oberflächenhöhe von Meereis mit Laser- und Radaraltimetrie und Vergleich mit Eisdickendatensätzen in der Arktis und Antarktis

---

Sibylle Göbell

Ber. Polarforsch. Meeresforsch. 559 (2007)
ISSN 1618 - 3193

Universität Bremen
Fachbereich Geowissenschaften

1. Gutachter: Prof. Dr. H. Miller
2. Gutachter: Prof. Dr. H. Villinger

Determination of Sea Ice Surface Elevation with Laser and Radar Altimetry and Comparison with Ice Thickness Data Sets in the Arctic and Antarctic

Dissertation zur Erlangung des Grades
Doktor der Naturwissenschaften
– Dr. rer. nat. –

Sibylle Göbell

Bremerhaven, Februar 2007

Alfred-Wegener-Institut
für Polar- und Meeresforschung

Klimawissenschaften
Meereisphysik

Sibylle Göbell

Alfred-Wegener-Institut
für Polar- und Meeresforschung
Postfach 120161
D-27515 Bremerhaven

Die vorliegende Arbeit ist die inhaltlich unveränderte Fassung einer Dissertation, die 2007 dem Fachbereich Geowissenschaften der Universität Bremen vorgelegt wurde. Die Arbeit wurde zusätzlich als Printmedium veröffentlicht, wobei die Farbabbildungen in Graustufen umgewandelt wurden:
S. Göbell (2007): Determination of Sea Ice Surface Elevation with Laser and Radar Altimetry and Comparison with Ice Thickness Data Sets in the Arctic and Antarctic. Berichte zur Polar- und Meeresforschung, Band XXX.

Abstract

The knowledge of sea ice thickness plays a critical role in the discussion of global climate change related issues. Up to now, satellite missions have been used to map the extent of sea ice but it has been impossible to measure its thickness directly. Recent and upcoming satellite missions such as ICESat and CryoSat-2 measure the surface elevation, and freeboard respectively of sea ice which can be transformed to total thickness.

In this study, surface elevation is defined as the height of the snow surface and freeboard as the height of the ice surface above local sea level throughout the ice floe. Measurements of surface elevation have been performed by means of laser altimetry and differential GPS (DGPS) using a helicopter suspended sensor. Surface elevation is derived from the difference between the laser range measurement above the snow surface and the instrument's height above the geoid determined by DGPS (GPS height) yielding the geolocated elevation above the geoid (ground elevation). Ground elevation is different from surface elevation because the local sea level deviates from the geoid which is used as reference for the GPS height due to geoid errors and the unknown dynamic sea surface topography. Therefore, after the first processing, the ground elevation of open water sites between the ice floes is not zero. This bias can be removed by implementing a specific filtering operation. On average, the accuracy of the surface elevation is estimated as ±0.1 m. However, it can increase considerably depending on the roll angle of the sensor.

Results of surface elevation are compared with coincident profiles of a laser scanner, in-situ measurements, and sea ice thickness measured in the Lincoln Sea in the Arctic and in the Weddell Sea in the Antarctic. Besides, comparisons are conducted with coincident profiles generated by airborne radar altimetry. The coincident thickness profiles have been obtained using an electromagnetic thickness sounding instrument that was also included in the sensor suspended beneath the helicopter. Results show that thickness/surface elevation ratios are smaller over sea ice in the Weddell Sea than in the Lincoln Sea according to a thicker snow cover in the Antarctic. This has fundamental consequences for the ice thickness retrieval from spaceborne altimeter missions.

Furthermore, the high variability of R-values which result from the coincident measurements of surface elevation and ice thickness is addressed and approaches are introduced in the case if thickness measurements are not available. Transforming surface elevation to total thickness by solving the hydrostatic equilibrium equation and assuming specific densities for sea ice, sea water, and snow as well as snow depth, resulted in unacceptably large uncertainties. However, snow depth can be computed from the coincident surface elevation/thickness measurements which in turn is suitable in supporting airborne and spaceborne missions with respect to transforming surface elevation, and freeboard. In the future, snow depth derived from the different penetration depths between laser and radar beams could complement this data set, and thus improve sea ice thickness results from airborne and spaceborne platforms.

Zusammenfassung

Die Kenntnis der Meereisdicke spielt eine entscheidende Rolle bei der Diskussion von Fragestellungen hinsichtlich des globalen Klimawandels. Bis heute werden Satellitenmissionen genutzt, um die Ausdehnung von Meereis zu erfassen aber es ist nicht möglich, die Eisdicke direkt zu messen. Letzte und anstehende Satellitenmissionen wie ICESat und CryoSat-2 messen die Oberflächenhöhe, beziehungsweise das Freibord von Meereis, welche in Gesamtdicke transformiert werden können.

In dieser Arbeit wird Oberflächenhöhe als die Höhe der Schneeoberfläche und Freibord als die Höhe der Eisoberfläche an jedem Punkt der Eisscholle über dem lokalen Meeresspiegel definiert. Die Messungen der Oberflächenhöhe wurden mittels Laseraltimetrie und differentiellem GPS (DGPS) unter Verwendung eines vom Helikopter geschleppten Sensors durchgeführt. Die Oberflächenhöhe wird aus der Differenz zwischen der Laserentfernungsmessung und der Instrumentenhöhe über dem Geoid mit DGPS (GPS Höhe) abgeleitet, die zunächst die Höhe über dem Geoid (Bodenhöhe) ergibt. Die Bodenhöhe ist von der Oberflächenhöhe verschieden, weil der lokale Meeresspiegel aufgrund von Geoidfehlern und der unbekannten dynamischen Meerestopographie von dem Geoid abweicht, das als Referenz für die GPS Höhe benutzt wird. Deshalb ist die Bodenhöhe über offenem Wasser zwischen den Eisschollen zunächst nicht Null. Diese Abweichung wird im Folgenden durch eine spezielle Filterungsmethode korrigiert. Die Genauigkeit der Oberflächenhöhe wird mit $\pm 0.1\,\mathrm{m}$ abgeschätzt. Allerdings kann sie, in Abhängigkeit vom Rollwinkel des Sensors, erheblich zunehmen.

Die Ergebnisse der Oberflächenhöhe werden mit übereinstimmenden Profilen eines Laserscanners, in-situ Messungen und der Meereisdicke verglichen, die in der Lincolnsee in der Arktis und im Weddellmeer in der Antarktis gemessen wurden. Außerdem werden Vergleiche mit übereinstimmenden Profilen durchgeführt, die mit einem Flugzeug-Radaraltimeter erzeugt wurden. Die übereinstimmenden Dickenprofile werden mittels eines Instrumentes für elektromagnetische Dickensondierung gewonnen, das sich ebenfalls in dem vom Helikopter geschleppten Sensor befand. Aufgrund der dickeren Schneeauflage in der Antarktis ergibt sich ein kleineres Verhältnis von Gesamtdicke zur Oberflächenhöhe. Dies hat elementare Auswirkungen bei der Bestimmung der Eisdicke mit Satelliten.

Desweiteren wird die hohe Variabilität der R-Werte angesprochen, die aus den übereinstimmenden Messungen von Oberflächenhöhe und Eisdicke resultieren. Verschiedene Ansätze werden vorgestellt für den Fall, daß keine Dickenmessungen verfügbar sind. Die Transformation von Oberflächenhöhe in Gesamtdicke erwies sich als inakzeptabel wenn die hydrostatische Gleichgewichtsbedingung, unter Annahme spezifischer Dichten für Meereis, Meerwasser und Schnee sowie der Schneehöhe gelöst wurde. Die Schneehöhe kann jedoch aus den übereinstimmenden Oberflächenhöhen- und Dickenmessungen berechnet werden, die wiederum hinsichtlich der Transformation von Oberflächenhöhe und Freibord verwendbar ist und damit flugzeug- und satellitengetragene Missionen unterstützt. Künftig könnte dieser Datensatz durch Schneehöhen ergänzt werden, die aus der unterschiedlichen Eindringtiefe von Laser- und Radarstrahlen resultieren und somit die Ergebnisse der Meereisdicke von flugzeug- und satellitengetragenen Plattformen verbessern.

Contents

List of Figures

List of Tables

1 Introduction

1.1 Motivation

Natural events trigger an increased sensitivity and awareness among people regarding the global climate change. Storm events in winter and summer, floods caused by heavy rain or sudden snowmelt, landslides, avalanches, unusually dry summer months, and forest fires are the most prominent natural events we are facing today and which are associated with the effects of a changing climate. In recent years, the ice-free North Pole, the iceshelf break-off in the Antarctic, and the thinning of Greenland's ice sheet have all made the headlines. Television, newspaper and several magazines report glacier retreat, global sea level rise in the past years, and melting of the polar ice caps. Regarding the latter, special scenarios pose the question as to what would happen to the northern part of Germany near the coast if the sea level rose to a certain level or what would happen to the Inuit in Greenland without the polar bears and seals which serve as a basis for living and sustenance? Many other scenarios are conceivable but the most obvious fact is the rise of global temperatures. The response of nature can be seen directly in the retreat of glaciers in the Alps. Everyone can see the difference in images between the extension of a glacier tongue today and a couple of years ago, but how can a change in polar ice be examined?

The surrounding sea waters of the Antarctic continent and the Arctic Ocean respectively, freeze up during winter time: sea ice has formed. Since sea ice forms due to low air and sea water temperatures and is relatively thin compared to the ice sheets that blanket Greenland and Antarctica, changes in its state are observed more easily and can be related directly to changes within the atmosphere and ocean, and hence the global climate. Therefore, the extent and thickness of sea ice are considered as two key indicators for the global climate change.

Sea ice extent is measured using special instruments (e. g., SSM/I since 1987) carried onboard satellites and thus it is possible to detect seasonal and interannual variability. Long-scale measurements of several years allow even a general trend to be recognized. However, due to the unknown ice thickness, sea ice volume cannot be calculated based only on its extent seen in satellite imagery. The ice thickness varies, because of strong ocean currents and wind patterns which may have pushed the ice in a certain direction. Thus, the same volume of sea ice can be present, although the apparent extent has decreased. In order to investigate changes in ice volume the knowledge of sea ice thickness plays a decisive role. In other words, knowledge of sea ice thickness is essential in order to understand the dynamics and thermodynamics of the ice cover, the heat budget of the polar oceans, and the interactions between the atmosphere and ocean which directly influence the global climate.

With a general decrease of sea ice thickness, the northernmost sea routes through the Arctic Ocean become more attractive to shipping companies. At the end of the 19th century the famous north-east passage from Scandinavia through the Siberian Sea and the north-west passage connecting the northern Atlantic Ocean with the Pacific Ocean through the Bering Strait were already well known to be the shortest routes to Asia. Especially, the north-east passage was thought to be the ideal route, under economical aspects, to open up natural resources in Siberia. But, up to now this passage has not become a common sea route, instead, it has been used only by individual adventurers. If future ice conditions may allow these shortcuts to be taken through the Arctic Ocean, the knowledge of sea ice thickness will become even more essential, for the purpose of understanding climate change as well as navigation.

Sea ice thickness, however, is not simple to measure on a global and spatially dense scale. Currently, there is no satellite that can achieve this directly. One possibility is to measure the height of the snow surface or ice surface above sea level, the so-called snow-freeboard or surface elevation and ice-freeboard, or freeboard, respectively, and then to transform it to ice thickness. The transformation is based on the assumption of hydrostatic equilibrium. Besides assuming specific densities for snow, sea ice, and sea water, the depth of the covering snow (snow depth) has to be known. Surface elevation, with the snow depth being included, is measured by laser altimetry since the laser beam is always reflected by the uppermost surface layer. Such a snow cover is typical on sea ice. Because radar beams penetrate through the snow cover and are reflected at the snow/ice interface, freeboard is measured commonly by radar altimetry. The former technique has been applied to the measurements of NASA's ICESat satellite, which is the first satellite to make it possible to determine the sea ice thickness indirectly by laser altimetry. In contrast, CryoSat-2 will measure the freeboard of sea ice by radar altimetry and, hence, sea ice thickness will be derived after its expected launch in Spring 2009. However, validation of the derived ice thickness will not be simple because of missing comparable measurements.

The best method for validation would be a technique that enables measurements of surface elevation and total thickness (surface elevation plus ice depth below sea level) of sea ice simultaneously. The measured surface elevation could be transformed to total thickness and in this way directly compared to the measured total thickness. Thus, the error characteristics of transforming surface elevation to total thickness could be estimated. These findings, could be utilized in the next satellite mission, in which it would be sufficient to continue measuring the surface elevation and freeboard, respectively, of sea ice.

1.2 Sea Ice in the Polar Regions

Fig. 1.1 shows general maps of the two polar regions with sea ice concentration in both hemispheres on May 18, 2006. The Antarctic itself is a continent embedded in the circumpolar Southern Ocean, whereas the Arctic comprises the Arctic Ocean, which is similar to an enclosed water basin surrounded by adjacent land masses. This has direct effects on the sea water exchange, and thus, the growth and decay of sea ice. The sea water exchange in the Arctic occurs mainly through the Fram Strait, between Svalbard and Greenland, the only deep passage connecting the Arctic Ocean with the Atlantic (WADHAMS, 2000). Besides the narrower and shallower passage of Nares Strait between Greenland and Ellesmere Island, which allows some connection with Baffin Bay, there are many other shal-

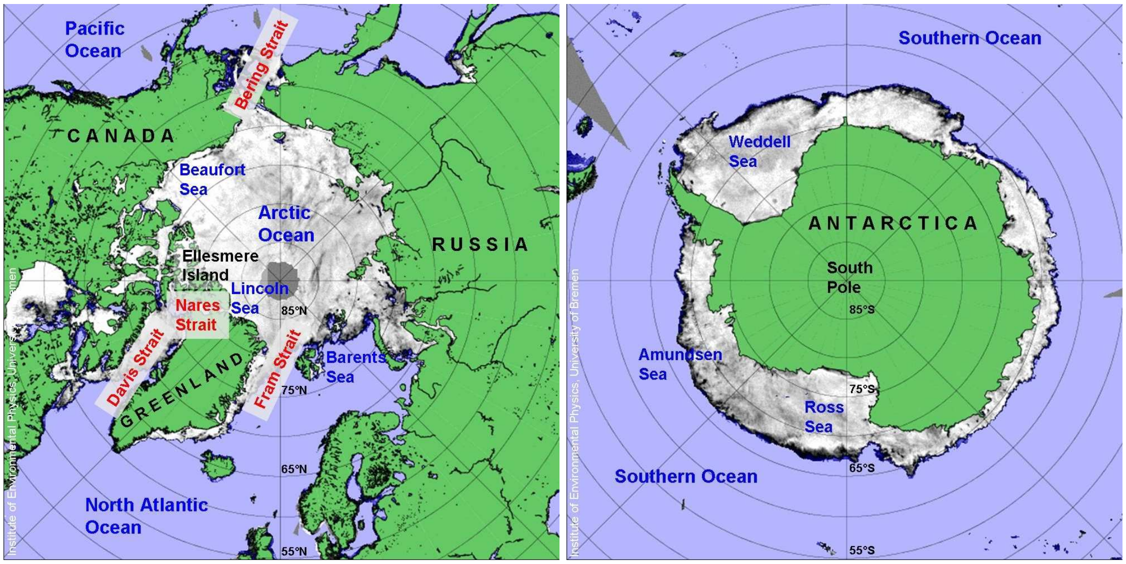

Figure 1.1: The Arctic basin surrounded by continents (left) and the continent of Antarctica (right) with sea ice concentration on May 18, 2006.

low links with the Atlantic and Pacific, e. g., through the Barents Sea, and the Bering Strait. Significant also, are the continental shelves of up to 100 m depth bordering the Arctic Ocean. With a mean depth of 1800 m (Wadhams, 2000) the Arctic Ocean is clearly shallower than the Southern Ocean with its depths between 4000 m and 6500 m, comprising the southern ends of the Pacific, Atlantic, and Indian Oceans. Even if sea ice can take on special forms, as described in Section 2.1.3, the conditions required for its production are the same for the Arctic and Antarctic. Whereas fresh water freezes at 0 °C water surface temperature, salty sea water freezes at around $-1.8°$ C, forming sea ice. This temperature is primarily found in shallower seas above continental shelves (Wadhams, 2000).

In the Antarctic, the Weddell Sea, the Amundsen Sea, and the Ross Sea are the prime locations for sea ice formation. In the Antarctic winter, the maximum sea ice extent is reached in September covering an area of 18.8×10^6 km^2 and ranging in latitude from 55° S to 75° S. A mean ice thickness of 0.5 to 0.6 m was found by Wadhams (2000). Ice thickness comprises the visible height of the ice floe above sea level and the part below sea level. The minimum extent is reached in February when only 1/6 of the maximum sea ice cover is left (Comiso, 2003). This small fraction survives one period of the Antarctic summer before it melts or drifts northward. Sea ice, which is formed new each year and disappears in the same season, is called *first-year ice*. *Multi-year ice*, however, survives at least one summer and becomes thicker. The direct connection of the Antarctic shelf seas with the open ocean causes the sea water to freeze in a special way: the *pancake ice* is formed. Pancake ice forms if sea water is in continuous motion during freeze-up. The continuous motion is largely due to the wind-driven surface circulation of the Antarctic Circumpolar Current (westward) and the Antarctic Coastal Current (eastward).

In the Arctic, the Barents Sea, Kara Sea, Laptev Sea, East Siberian Sea, Beaufort Sea, and Greenland Sea are the most famous shelf seas for sea ice production. The motion of the sea ice and surface waters is also mainly wind-driven and consists of the anticyclonic (clockwise) *Beaufort Gyre* in the Canada Basin, and the *Trans-*

polar Drift Stream in the Eurasian Basin as shown in Fig. 1.2. However, the Arctic Ocean is not as rough as the exposed Antarctic sea waters which leads to almost calm water conditions during freeze-up. For a complete circuit in the Beaufort Gyre the sea ice takes about seven to ten years (WADHAMS, 2000). The Transpolar Drift Stream, which transports ice and water from the Eurasian shelves across the Pole and down towards the Fram Strait requires about three years. After leaving the Arctic Ocean through the Fram Strait, the Transpolar Drift Stream is renamed the *East Greenland Current*. The maximum sea ice extent in the Arctic is reached in March covering an area of 15.7×10^6 km^2 and ranges from the North Pole to 44° N, the northern end of the Sea of Japan. More than half of the maximum sea ice cover persists five to seven years as multi-year ice and the remaining smaller fraction is first-year ice. Hence, a mean ice thickness of 5 m was found by WADHAMS (2000) in 1976.

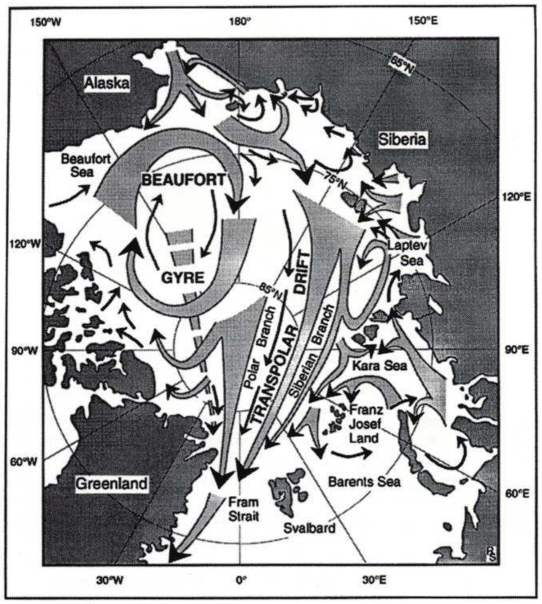

Figure 1.2: Long-term average surface circulation of ice and water in the Arctic Ocean (after WADHAMS (2000)).

The depth of snow covering the sea ice is also different for both hemispheres. Antarctic sea ice has a deeper snow cover than Arctic sea ice (WADHAMS, 2000). In the former, snow depths of up to 0.8 m have been found by in-situ measurements during campaigns considered in this investigation, whereas in the latter, snow depths of up to 0.5 m have been measured.

Importance for the global Climate

Sea ice extent and thickness are governed by growth and decay as well as by drift triggered by ocean currents and wind patterns. As sea ice interacts with the ocean and the atmosphere, it is controlled by these influences but the sea ice itself also affects the atmosphere and the ocean, and therefore, the global climate. Sea ice acts as an insulating layer for the exchange of thermal energy between ocean and atmosphere while the sea ice snow cover controls the albedo of the surface. The albedo is the fraction of the incident short-wave radiation reflected from a surface, which is higher for sea ice than for open water. Therefore, the sea ice snow cover controls the radiation surface energy balance (EICKEN, 2003). Table 1.1 shows the different albedo for sea ice of different thicknesses and snow. The values are taken from HALL & MARTINEC (1985) and PEROVICH (1985).

Table 1.1: Observed values for albedo of sea ice and snow (HALL & MARTINEC, 1985; PEROVICH, 1985). Ice thicknesses for grey ice and white ice are given in parentheses.

Characteristics	**Albedo (%)**
Weathered snow	< 40
Grey ice (10 – 15 cm)	50
White ice (15 – 30 cm)	70
Fresh snow	90

Whereas the albedo reaches values up to 90 % for freshly fallen snow it drops below 40 %, if the snow surface is weathered or dirty (HALL & MARTINEC, 1985). The albedo for sea ice ranges between 50 % for bare first-year ice and 70 % for thicker white ice (PEROVICH, 1985). If the surface energy balance is upset by global warming causing the sea ice to decrease, the reduced ice cover in turn increases the amount of solar energy absorbed by the system (ice-albedo feedback) (CURRY et al., 1995). Special studies by MAYKUT & UNTERSTEINER (1971) reveal that the summer Arctic ice cover would completely disappear with an increase in air temperature of 3 to 5° C.

The ocean is affected by sea ice in a way that it contributes to the *thermohaline circulation* by salinity changes induced by freezing and melting. Unlike the wind-driven surface circulation, it is a vertical circulation, driven by heat and salt differences within the ocean (WADHAMS, 2000). With the absence of sea ice, the transfer of e. g., nutrients from the deep ocean to the surface would be hampered. Furthermore, the Gulf Stream, which carries warm surface waters northwards from the Gulf of Mexico to the sub-polar waters east of Greenland, significantly moderating the climate in Europe, would be affected. The warm surface waters cool and sink as they reach the Arctic. Arriving in the Arctic, the salinity increase triggered during sea ice formation amplifies the density increase, and thus the sinking of the surface waters. This process is comparable to an acting pump, driving deep ocean water from the polar regions to the equator, while warmer water masses flow on the surface northwards. If this circulation pattern were disturbed by reduced Arctic sea ice there would be a strong effect on the strength and direction of the Gulf Stream, because at the same time there would be an additional freshwater input from melting of the continental Greenland ice sheet. Both scenarios lead to a reduced ocean circulation due to the decrease of salinity and, hence, density changes.

Because of the sensitivity of the polar regions to small perturbations in the ocean or atmosphere and thus in the global climate, the study of the polar regions, and especially the study of sea ice, has become a prominent research field in the past years.

1.3 Sea Ice Thickness Measurement Techniques

Drilling

Several attempts have been made to estimate sea ice thickness. The oldest and most accurate method of measuring sea ice thickness is by drilling. WADHAMS (2000) mentions Nansen who did the first systematic measurements of ice thickness in the Arctic. During his expedition in 1893 – 1896 he drilled through undeformed ice. Since then, several techniques have been applied. Manual drilling is still the most exhausting method, but supported by a battery-powered head, the semi-manual drilling is the safest approach. Gasoline-powered head drills and hot water drills are faster but sometimes tricky and difficult to handle. Before the hole refreezes, a tape measure with a weight in the form of a pair of scissors at the end, is sent down the hole to read off ice and snow depth. Drilling is indeed a good technique of estimating mean ice thickness at a small scale and essential for validating any other method. However, used as a stand-alone technique, in-situ measurements are time consuming, spatially limited and thus lack the necessary investigations of regional variability.

Radar Sounding and EM Induction Sounding

In the mid-1970s, impulse radar sounding of sea ice was studied e. g., by CAMPBELL & ORANGE (1974); ROSSITER et al. (1977); KOVACS (1978). This technique, today known as ground-penetrating radar (GPR), is very suitable for freshwater ice. For sea ice its use is rather limited (OTTO, 2004) due to the brine content of the ice, which decreases the permittivity of the ice and thus limits the propagation distance of radio-frequency energy (ROSSITER, 1980). Since the early 1980s, the technique of electromagnetic (EM) induction sounding from airborne platforms has been tested (ROSSITER & LALUMIERE, 1988; KOVACS & HOLLADAY, 1990; PRINSENBERG et al., 1992; HOLLADAY, 1993). HAAS et al. (1997) applied the EM technique by pulling a kayak over sea ice with an EM sensor placed inside. The first obtained ground-based thickness profiles with the Geonics EM 31 looked very promising, especially, after the comparisons with drill-hole measurements. A combination of the EM 31 and a laser altimeter allows EM sounding from onboard ice-breakers during voyages through the Arctic and Antarctic oceans to yield regional ice thickness distributions (HAAS, 1998; HAAS et al., 1999). Thus, the characteristics of different ice regimes can be clearly distinguished and studied. The ship-based measurements, however, suffer from the fact that always the easiest route through the ice is chosen, which means that thicker, older ice is statistically underrepresented. Therefore, the idea of a fully digital airborne sensor platform was adopted again and the so-called *EM bird* was built on behalf of the Alfred-Wegener-Institute for Polar and Marine Research (AWI), Bremerhaven in 2000. Another one followed in 2004. The helicopter EM (HEM) bird, hereafter termed EM bird, was used for the first time in the Arctic in 2001. It was suspended by a 20 m long cable beneath a helicopter. Since then, the EM bird has been used routinely during several cruises with the RV Polarstern as well as during several land-based scientific campaigns. For details on the general EM technique see Section 2.3.6.

Submarine and moored upward looking Sonars

Another possibility is the profiling of the ice underside by upward looking sonars (ULS) from submarines or moorings, from which the ice thickness distribution can be inferred. U.S. and British military submarines have been collecting sonar data in the Arctic since the middle of the 20th century. The problem with these data is that they were obtained during military operations, and thus the exact tracks are not published. Also, no systematic repeat measurements took place. The use of sonar on autonomous underwater vehicles (AUV) (BRANDON et al., 2003; WADHAMS et al., 2006) is an adequate alternative to military submarines (WILLIAMS et al., 1975; WADHAMS & HORNE, 1980; WADHAMS, 1988; ROTHROCK et al., 1999). With moored ULS, time series of regional variability at a fixed location are generated. Experiments were conducted in shallow water in the Beaufort Sea (HUDSON, 1990; PILKINGTON & WRIGHT, 1991; MELLING & RIEDEL, 1995; MELLING et al., 2005), and in deeper water in Fram Strait (VINJE et al., 1997). In the Weddell Sea moored ULSs have been used by HARMS et al. (2001) and in East Antarctica by WORBY et al. (2001).

Nagurny buoys

Sea ice thickness can also be derived measuring the wave dispersion at long wavelengths propagating through the ice. It was shown by NAGURNY et al. (1994) that the spectrum of flexural-gravity waves passing through sea ice has a peak at a frequency that is a function of area-averaged sea ice thickness. This peak period is a product of a resonance mechanism. It offers the possibility of measuring the spectrum of surface oscillations using a two-axis tiltmeter array, transmitting the data back by the Iridium low-orbit satellite system, and thus mapping mean ice thickness from a buoy array.

Airborne Laser Altimetry

The equivalent to sonar profiling, but from the air, is laser profiling of the visible sea ice height above sea level. KETCHUM (1971); WADHAMS (1976); TUCKER et al. (1979); WEEKS et al. (1980); KRABILL et al. (1990) sought a relationship between the frequency and height distributions of pressure ridge sails and the spatial distribution of the surface state, represented by the surface roughness. In 1987, during the joint experiment of a U.S. aircraft with an airborne laser and a British submarine it was possible to match a laser profile of ice surface against a coincident sonar profile of ice draft. A direct comparison of the two measured parameters followed by WADHAMS (1990); COMISO et al. (1991); WADHAMS (1991); WADHAMS et al. (1992). A major issue in laser profiling has been the removal of the aircraft motion from the obtained laser range. HIBLER (1972) presented a three-step process in which first a conventional high-pass-filtering operation is carried out before minimum points are estimated in the raw laser profile, which can be used to estimate an ice roughness base line. Ice roughness is described as elevation above the mean height of undeformed ice. This ice roughness base line is then low-pass filtered, and the resulting curve is taken to be the aircraft altitude variation which can then be subtracted from the initial profile. COMISO et al. (1991) followed the same technique, except that they manually constructed a smooth line through the minima points. These points were selected to be either from very thin ice or open water areas that were identified from aerial photographs. Thus, by estimating the sea level, they derived the true height of ice floes as opposed to HIBLER (1972) who could only determine a mean surface roughness. For thin ice with thicknesses around 0.2 to 0.3 m, ISHIZU et al. (1999) developed a slightly different approach for estimating the sea level. Since WADHAMS et al. (1992) mentioned a positioning accuracy of only 30 to 50 m with an onboard GPS receiver and ISHIZU et al. (1999) reported malfunctioning differential GPS receivers during their study, the GPS had not been routinely used in laser profiling. With the GPS becoming more popular due to increasing accuracies, a new approach considering the removal of aircraft motion was used by taking the difference between the height derived with GPS and the laser range. HVIDEGAARD & FORSBERG (2002) developed a new method for estimating sea ice thickness by airborne laser altimetry combined with precise GPS and a geoid model derived from airborne gravity measurements (FORSBERG et al., 2000). Within the Arctic Gravity Project special geoid models for the Arctic have been generated (KENYON, 2000; FORSBERG & KENYON, 2003). Most recently, an improved Arctic geoid model has been derived, combining terrestrial gravity data with the GRACE geoid model (FORSBERG & SKOURUP, 2005). Today, the use of GPS together with a precise geoid model is a common method to derive surface elevation and this was also used in this investigation. Besides single-beam laser altimeters, laser scanning systems have also been used successfully (FORSBERG et al., 2001). With this technique, cross-track scans are possible, covering a wider path on the ground and thus allowing more measurements than with a single-beam laser. Generally, ice thickness is derived from sea ice surface elevation by multiplying it with a factor derived from a study in climatology (WADHAMS, 2000).

Spaceborne Laser Altimetry

With the launch of NASA's ICESat satellite in January 2003, laser altimetry was possible on a large-scale for the first time, covering most of the Arctic Ocean (ZWALLY et al., 2002; KWOK et al., 2004; SCHUTZ et al., 2005; KWOK et al., 2006). Its measurement principle is shown in Fig. 1.3 (left). The height of the snow surface above sea level is derived by comparing measurements over sea ice with measurements over water. The measurement is averaged over 60 m diameter laser footprints spaced at 172 m along-track (ZWALLY et al., 2002). To derive ice thickness, KWOK et al. (2004) estimate the local sea level by identifying open water or thin ice along the ICESat tracks with RADARSAT imagery. The established freeboard height at the leads is used as a reference to level the ICESat elevation profiles. The remaining uncertainty in converting the derived sea ice surface elevation to ice thickness is the snow depth. Therefore, KWOK et al. (2004) use the snow climatology given by WARREN et al. (1999).

Spaceborne Radar Altimetry

As opposed to satellite-borne laser altimetry, radar altimetry from satellites (KWOK & CUNNINGHAM, 2002; LAXON & PEACOCK, 2003) has been conducted since the launch of SEASAT in 1976, followed by GEOSAT in 1986, ERS-1 in 1991, TOPEX/POSEIDON in 1992, ERS-2 in 1995, and ENVISAT in 2002. However, CryoSat-2 will be the first satellite equipped with a radar altimeter that enables sea ice freeboard measurements covering the polar regions due to its near-polar

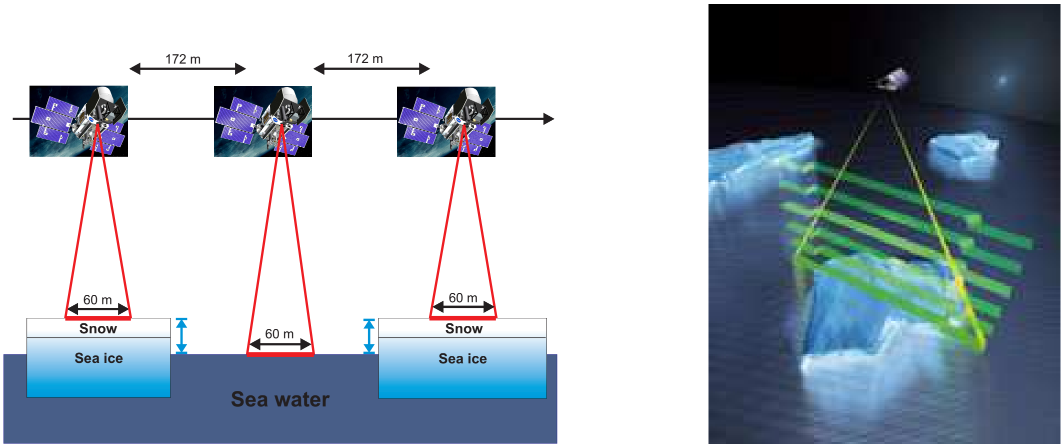

Figure 1.3: Measurement principle of ICESat (left) and CryoSat-2 (right).

orbit. The purpose of the CryoSat-2 (Wingham, 2003; Drinkwater et al., 2004; Wingham et al., 2006) mission is to determine trends in the ice masses of the Earth. The primary mission goals can thus be summarized as the determination of regional and basin-scale trends in Arctic sea ice thickness and mass, and the determination of regional and total contributions to global sea level of the Antarctic and Greenland Ice Sheets. The advantage over ICESat is that transforming freeboard to sea ice thickness is less sensitive and hence, less dependent on snow depth as shown in Section 2.2.2. The radar altimeter will be used in the *Synthetic Aperture Radar* (SAR) mode which will allow more efficient operation. Here, the entire (beam-limited) along-track signal history contributes to height measurement, rather than only the much smaller pulse-limited area. Thus, very narrow across-track strips are formed, which reduce the footprint size to 250 m. The *SAR-Interferometric* mode provides improved elevation estimates over ice sheets with variable topography. Generally, the surface is not planar over ice sheets, and a method for determining the echo location is required. A second radar antenna is added and used to form an interferometer across the satellite track. The angle of the echo at each range may be determined, and this, together with the range, determines the elevation and across-track location of the surface (Wingham, 1999). The height of the bare ice above sea level (without the overlying snow), is derived by comparing measurements over ice with measurements over water. The measurement principle is shown in Fig. 1.3 (right).

Airborne Radar Altimetry

In anticipation of the ICESat and CryoSat mission, experiments with a special delay-doppler phase-monopulse (D2P) radar (Raney, 1998) took place to demonstrate the use of two enhancements to satellite radar altimetry. In 2002, a joint campaign of laser and radar (LaRa) altimetry was conducted in northern Greenland. The aircraft carried two D2P radar altimeters and a laser scanner. The aim was to assemble critical measurements of land and sea ice in order to help scientists understand and quantify the best methods for retrieving ice thickness by using a combination of laser and radar altimeter measurements.

To validate the radar measurements of CryoSat-2, an airborne version was developed by the European Space Agency (ESA). The Airborne Synthetic Aperture and Interferometric Radar Altimeter System (ASIRAS) instrument came into use for the first time during a campaign over the Greenland Ice Sheet in 2004 (HAWLEY et al., 2006). In Spring 2005, ASIRAS was used for the first time over sea ice during a joint campaign between AWI Bremerhaven and the Finnish Institute of Marine Research (FIMR) Helsinki in the Bay of Bothnia (HELM et al., 2006). In addition to the radar, a single-beam laser altimeter and a laser scanner were used for measurements of the surface elevation. Results are presented within this investigation. In May 2006, ASIRAS was flown together with a laser scanner by colleagues from the Danish National Space Center (DNSC). Data of the first test flight have been processed and the first results are shown.

1.4 Overview

The data processing and determination of surface elevation, the transformation to total thickness and the comparison to the measured total thickness constitute the majority of the work in this study. For this reason, measurement techniques are briefly described which enable simultaneous measurements of surface elevation and total thickness. The simultaneity of the measurements allows a direct comparison between both data sets and thus, the study of error influences. Further, it enables the calculation of snow depth which is the principle uncertainty in transforming surface elevation. For this reason, this investigation contributes to indirect sea ice thickness measurement techniques which are currently the only methods to measure sea ice thickness from air at higher altitudes, or from space.

After a brief introduction to ice formation, growth, and ice thickness distribution, measurement techniques applied within the present study are described and facts about the transformation between the measured quantities are given (Chapter 2).

Since the measurements include different error sources, the first step is to derive surface elevation above the local sea level. In the following, this is discussed in detail for the polar regions after the data collection is described. Problems occurring in quantity transformations and various error influences, e. g., the initial unknown snow depth on top of the ice floe, will be investigated and analyzed (Chapter 3).

Results of surface elevation and the comparison with simultaneously measured total thickness of sea ice by the EM bird are shown in Chapter 4. Additionally, results are presented from one coincident flight between the EM bird and the aircraft, equipped with a laser scanner from DNSC. Further, the method of deriving surface elevation is also applied to the area north of the Fram Strait where no coincident total thickness was measured. In this case, scatterometer data are used for comparison. Moreover, results of snow depth calculation are compared with in-situ measurements (Chapter 4).

Regarding the upcoming CryoSat-2 mission, a similar radar altimeter, ASIRAS, has been used aboard an airplane as a pre-validation instrument. To make use of the different penetration depths of laser and radar beams, coincident flights with laser and radar altimetry have been performed over pre-defined validation lines. The difference between both measurements yields the snow depth, of which the results are shown (Chapter 5).

A general discussion and the conclusions with an outlook conclude this study (Chapter 6 and Chapter 7).

2 Fundamentals

This chapter briefly summarizes the physical properties of sea ice and snow in the polar regions and explains the meaning of probability distributions of ice thickness and its interpretation. It also introduces terms and definitions used in this work. Further, the transformation of surface elevation to total thickness of sea ice is explained and the relationship between these two quantities, which is linked to snow depth, is discussed. Finally, the applied measuring methods are introduced and briefly described.

2.1 Sea Ice and Snow

2.1.1 Physical Properties of Sea Water and Sea Ice

Three physical properties of sea water that are closely related are salinity, temperature, and density. The relationship is shown in Fig. 2.1. Salinity is measured in practical salinity units (psu). When the salinity exceeds 24.7 psu, the temperature of maximum density disappears, and cooling of an ocean by a cold atmosphere will always make the surface water more dense and will continue to cause thermohaline convection until the upper water layer (mixed layer) is at the freezing point. In the Arctic, this mixed layer can reach a thickness of approximately 50 m (LEWIS et al., 1994).

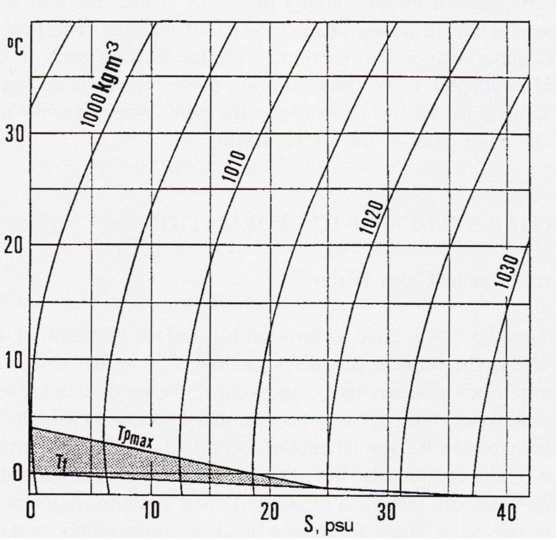

Figure 2.1: Temperature of density maximum (Tρ_{max}) and freezing point of sea water (T_f), showing how these lines meet at 24.7 psu. The shaded triangle is the range over which cooling at the sea surface can take place without convection. Contours of sea water density are also shown (after WADHAMS (2000)).

Salinity is directly related to sea ice growth, ice and atmospheric temperature, and age. A typical salinity value for the open ocean is 35 psu (LEWIS et al., 1994). The freezing point for sea water with 34 psu salinity is at −1.8° C (WADHAMS, 2000). In the Antarctic, surface salinities are 35 psu in most places. Even in the Arctic Basin, where river run-off is a diluting factor, surface salinities usually exceed 30 psu. When ice cores are melted, the resulting water from young sea ice may have a salinity of about 10 psu, from first-year ice 4 – 6 psu, and from multi-year ice 1 – 3 psu (WADHAMS, 2000). As the ice ages, the brine is expelled into the underlying water and the ice becomes less saline (similar to ice formation). However, some of the brine is still trapped within the growing ice in the form of liquid and solid inclusions, creating *brine pockets* (LEWIS et al., 1994).

The density of sea ice decreases with age as the brine pockets are replaced by ice (WEEKS & LEE, 1958). LEWIS et al. (1994) find densities of newly formed ice at Hopedale, Labrador, as high as $945\,\mathrm{kg/m^3}$. SCHWARTZ & WEEKS (1977) and EVANS (1965) report densities of first-year ice in the range of $910\,\mathrm{kg/m^3}$ to $920\,\mathrm{kg/m^3}$, while values for multi-year ice are quoted as $910\,\mathrm{kg/m^3}$ to $915\,\mathrm{kg/m^3}$. EICKEN et al. (1995) studied 66 locations in the Eurasian sector of the Arctic Ocean and found a mean density of the ice cover ranging from $720\,\mathrm{kg/m^3}$ at the top, increasing to greater than $880\,\mathrm{kg/m^3}$ below 0.4 m depth. Air bubbles can further decrease the sea ice density. COX et al. (1984) report average densities of $875\,\mathrm{kg/m^3}$ for deformed ice, i. e. after the ice floes have collided and formed pressure ridges (see Section 2.1.4).

The temperature in ice increases linearly from the atmospheric temperature at the ice/air interface to about $-1.8°\,\mathrm{C}$ at the ice/water interface (LEWIS et al., 1994).

2.1.2 Physical Properties of Snow

The density of snow depends primarily on its compaction (LEWIS et al., 1994). Following the definition of BADER (1962), snow is a porous, permeable aggregate of ice grains, which is deposited on the ground. After deposition, compaction and metamorphosis sets in, yielding different stages of the snow cover. The main physical properties of snow are expressed by density, porosity, air permeability, and grain size. The difference between all types of snow and ice is that snow has a connected system of air pores, whereas ice has closed air pores and a higher density. Significant changes in the physical properties of snow-covered sea ice occur during the onset of melt (LEWIS et al., 1994). The density of snow depends primarily on its compaction. Observations based on snow pit measurements from 1987 to 1991 by GARRITY (1991) report the average spring snow density in the Greenland and Barents Sea as $360\,\mathrm{kg/m^3}$ over first-year and multi-year ice. During summer, the average density decreases to $300\,\mathrm{kg/m^3}$. WARREN et al. (1999) find $300\,\mathrm{kg/m^3}$ as the average snow density, with little geographical variation. In the Weddell Sea, Antarctic, the average snow density is found to be $280\,\mathrm{kg/m^3}$ over first-year ice and $370\,\mathrm{kg/m^3}$ over multi-year ice due to a thicker snow cover. A comprehensive study about snow on Antarctic sea ice was done by MASSOM et al. (2001).

2.1.3 Sea Ice Formation and Growth

Ice formation begins at the sea surface with the formation of a suspension of small ice crystals known as *frazil*. These crystals are pure water ice and take the form of small needles as described by KUMAI & ITAGAKI (1988). The formation of frazil takes place within the upper few meters of the ocean. In calm conditions with little or no wind, the frazil crystals float to the sea surface, where they form an unconsolidated layer known as *grease ice*. MARTIN (2004) compares the smooth appearance of grease ice to an oil slick where propagating waves are slowed down. Grease ice has a low albedo, giving the surface a matt appearance. Continued freezing results in a thin, elastic, weakly consolidated layer of *young ice*. When it is still transparent, it is called *nilas*. There is a discrimination between *dark nilas*, when the layer is only as much as 5 cm thick and fully transparent, and *light nilas*, when the ice grows up to 10 cm in thickness and takes on a grey and later a white appearance. When nilas forms under pressure, a pattern of interlocking fingers, *finger rafting* builds up, where the fingers are thrusted alternately on top and underneath an opposite. Consolidation progresses by water crystallizing in the brine within the ice sheet and results in a salinity increase in the remaining liquid. Some of the brine is released into the sea beneath the growing ice and to the surface. The rest stays within the ice. Further ice growth occurs on the bottom of the young ice layer as congelation ice (LEWIS et al., 1994). According to the sea ice nomenclature (WMO, 1989), *grey ice* (10 – 15 cm) is less elastic than nilas and breaks on swell, but still rafts under pressure, whereas *grey-white ice* (15 – 30 cm) is more likely to ridge than to raft under pressure. This process yields first-year ice, which reaches a thickness of 1.5 – 2 m in a single season in the Arctic (WADHAMS, 2000). Because this ice is grown thermodynamically, without the influence of dynamic pressure, it is called *level ice*. When grease ice is formed under rough conditions, i. e. strong winds and a turbulent sea, it is blown into streamers, rather than forming a homogeneous surface. Continued wind and wave stress cause the windrows to break into circular pieces of ice with diameters of 0.3 – 3 m. Due to collisions of single pieces with one another, raised rims are formed, which give the so-called *pancake ice* its typical appearance. Further freezing aggregates the single pancakes into collections of large floes until the ice cover has consolidated into a continuous solid sheet of large ice floes. Around the Antarctic, this is the most common mechanism for ice formation. First-year ice reaches a thickness of 0.5 – 1 m (WADHAMS, 2000), while multi-year ice can grow up to the range of 2.2 – 2.8 m. In the Arctic it reaches thicknesses of up to 4 m.

Depending on the arrangement of the formed ice, the sea ice nomenclature distinguishes between *fast ice*, which forms and remains fixed along the coast and *pack ice*, which is mobile. Pack ice can easily become grounded in shallow water, forming *grounded ice*. The boundary between the fast ice and pack ice is the so-called *fast ice boundary*. For specific terms, used for expressing the ratio of ice concentration and for describing the size of ice floes, refer to the sea ice nomenclature (WMO, 1989).

2.1.4 Deformation Processes

Sea ice is under the continuous influence of wind and ocean currents which leads to convergence and divergence of the ice cover. Diverging ice floes lead to openings in the ice. According to the sea ice nomenclature, several types of openings are described: *fractures* and *cracks* comprise any break through compact pack or very close pack ice. While *leads* are mostly linear-shaped fractures or passage ways through sea ice, used by ships for navigating, *polynyas* are non-linear shaped openings enclosed in the ice. Furthermore, different locations of the polynya can be distinguished, depending on the position closer to shore or within the pack ice. Convergence leads to collisions of single ice floes. Continuous pressure causes a composition of loosely stacked angular ice blocks, forming walls. These walls are known as *pressure ridges*. As a pressure ridge ages, the base freezes together and becomes consolidated. The dynamically grown ridges can reach several meters in thickness, especially if they are formed between multi-year ice floes. Pressure ridges consist of *ridge sails* above and *ridge keels* below sea level. The part below sea level is also described as *draft*.

Another kind of deformation process due to damage is the melting of sea ice. As a result of surface warming the snow cover starts to melt, forming pools of melt water, known as *melt ponds*. In the Arctic this is the most common appearance during melt season. Because most of the first-year ice survives the melt season, the melt ponds freeze-up during the following freezing period. The closed form of the Arctic Basin plays a prominent role in keeping the ice floes. In the Antarctic, however, most of the ice moves directly northward where the majority of the ice melts completely, resulting in very little melt ponding.

2.1.5 Sea Ice Thickness Distribution

Fig. 2.2 (left) shows a typical sea ice thickness profile of first-year ice derived from a measurement flight with the EM bird (see Section 2.3.6) in the southern Lincoln Sea. The profile is arbitrarily chosen. It is 4 km long and stretches along undeformed level ice without any cracks or leads, but includes some prominent pressure ridges. The graph shows surface elevation above and draft below sea level. With respect to one pressure ridge, its sail and keel is marked. Obviously, changes in ice thickness of 1 m appear within short distances. Regarding thickness profiles of multi-year ice, thickness changes of more than 5 m are possible after the formation of pressure ridges. Due to the dynamic mixing of thermodynamically grown level ice and deformed dynamically grown ice, the ice surface is quite rough, causing a small-scale variability which requires long survey profiles with a short measurement point spacing. The probability distribution, or histogram, for sea ice thickness (right) is dominated by the thickness of first-year

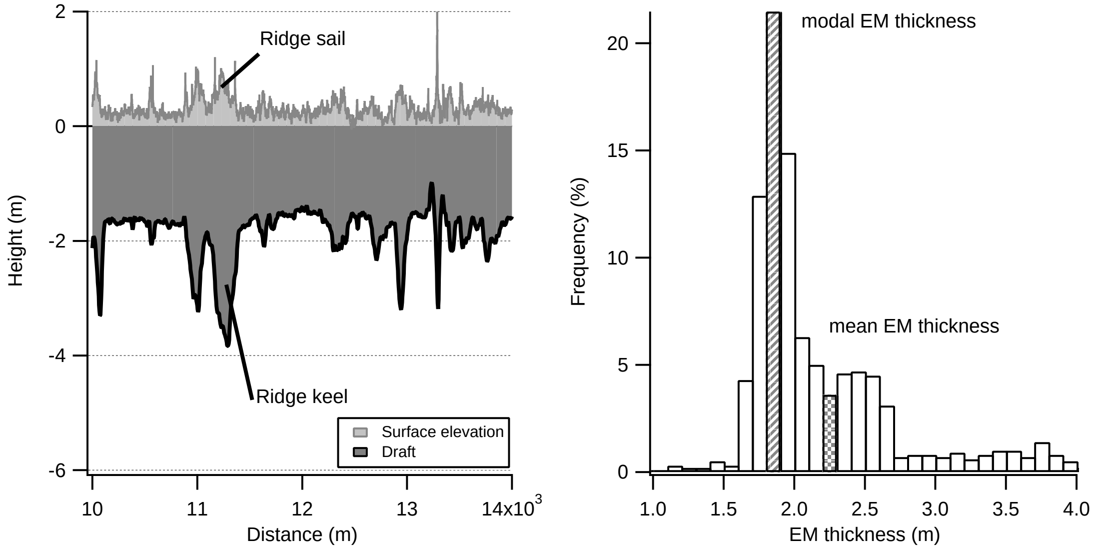

Figure 2.2: Sample EM thickness profile (left) of first-year ice and frequency distribution (right). The frequency distribution shows one clear mode at 1.9 m ice thickness.

ice, the so-called *modal ice thickness* or short *mode*, at 1.9 m. It means, that this is the ice thickness that is most frequent in the sample profile. The modal ice thickness gives a better representation of the thickness of thermodynamically grown ice (level ice) than the mean ice thickness, which would reach a value of 2.3 m. The difference is that the ice thickness is not gaussian-shaped, as seen in the arbitrarily formed composition of level ice and pressure ridges (left) and in the probability distribution (right). It is rather log-normal distributed (THORNDIKE et al., 2005). A decrease in level ice thickness can be inferred as an increase in air or water temperature and thus to a change in climate, if this fact is observed over several years to decades (KARCHER et al., 2003). However, due to changing wind patterns and/or ocean currents, level ice may be underrepresented at the cost of more deformed ice which makes an interpretation regarding the climate change more complicated. For example, the mean ice thickness can still be the same, even after a severe decrease of level ice and an increase of deformed ice and is thus not representative for such interpretations. Therefore, it is necessary to consider long profiles covering different ice thicknesses of thermodynamically and dynamically grown sea ice. More about this discussion and the ice thickness variability is found in HAAS (2003). The pressure ridges are found to the right in the histogram tail (Fig. 2.2, right). Depending on the thickness, the modes represent first-year ice (1 – 2 m) or multi-year ice (3 – 4 m) depending on the region. A mode at 0 m represents open water or very thin ice (see Section 3.5.3).

2.2 Measurement Quantities

2.2.1 Definitions

Instead of distinguishing between height of the sea ice floe surface with and without the snow cover, the term *freeboard* (f) is introduced in this study as the height of the snow/ice interface above sea level (see Section 1). Additionally, *surface elevation* (*selev*) is the total height of sea ice above sea level, including the *snow depth* (h_s) on top of the sea ice. As mentioned in Section 1, radar altimeters are sensitive to freeboard, while laser altimeters recover the surface elevation. The quantity *total thickness* (t) comprises the visible surface elevation above and the *draft* (d) below sea level (or, *ice thickness* (h_i) plus snow depth). The term *EM thickness* is used for t measured by electromagnetic (EM) ice thickness sounding, while *total thickness* is used for t derived from laser altimetry. Fig. 2.3 illustrates these defined terms. Based on the hydrostatic equilibrium, the equations for surface

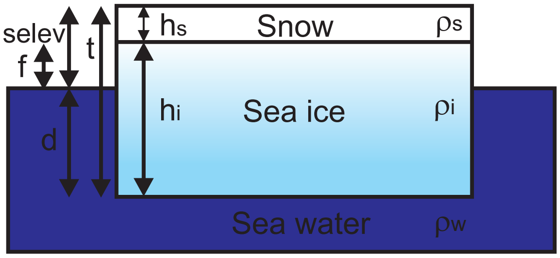

Figure 2.3: Definitions of surface elevation (*selev*), freeboard (f), snow depth (h_s), ice thickness (h_i), draft (d), and total thickness (t).

elevation

$$h_s\rho_s + (t - h_s)\rho_i = (t - selev)\rho_w, \tag{2.2.1}$$

and freeboard

$$h_s\rho_s + (t - h_s)\rho_i = (t - h_s - f)\rho_w \tag{2.2.2}$$

respectively, can be formulated. The assumptions for the densities ρ_w, ρ_i, ρ_s of sea water, sea ice, and snow, that were used in this study, are summarized in Table 2.1.

Table 2.1: Density assumptions for sea water, sea ice, and snow.

	Density (kg/m^3)
Sea water	1024
Sea ice	915
Snow	300

2.2.2 Relationship between Surface Elevation, Freeboard, and Total Thickness

2.2.2.1 Influence of Snow Depth

To derive total thickness from surface elevation or freeboard, derived with Eq. (2.2.1), and Eq. (2.2.2) respectively, have to be solved for t. Because of the unknown snow depth, the equations cannot be solved directly. The left graph in Fig. 2.4 shows the relationship between surface elevation and total thickness for variable snow depths. It illustrates the sensitivity of the relation between surface elevation and total thickness for a varying snow cover. Considering that a variation in snow depth of only 15 cm results in a 0.9 m difference in total thickness, it is clear that even slightly incorrect estimations of snow depths have large effects on the calculated total thickness. In the case of freeboard measurements, the

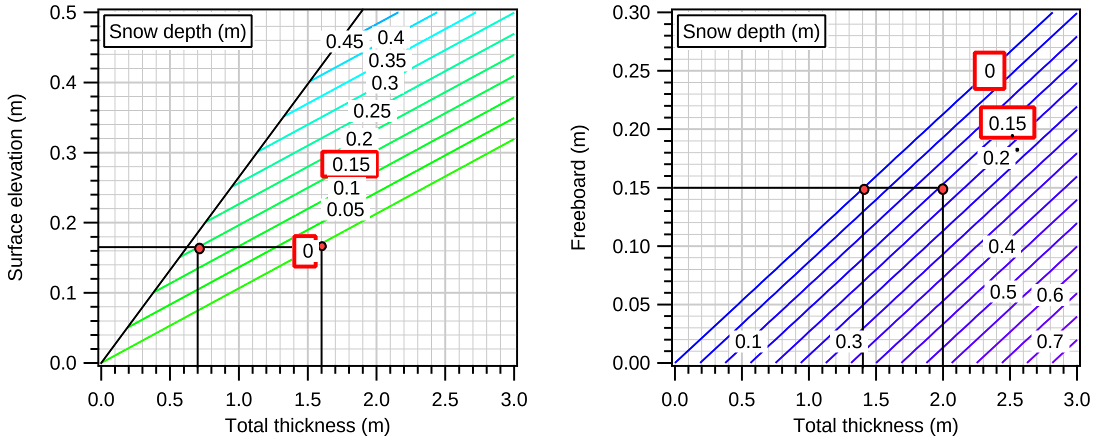

Figure 2.4: Surface elevation versus total thickness (left) and freeboard versus total thickness (right) for possible snow depths resulting from Eq. (2.2.1) and Eq. (2.2.2). The black diagonal line (left) shows the limit of maximum surface elevation for which the hydrostatic equilibrium is fulfilled.

possible snow depths are shown in the right graph of Fig. 2.4. Comparing it to the left graph it is obvious that transforming surface elevation is more sensitive to snow depth than freeboard. Here, a variation in snow depth of 15 cm results in a 0.6 m difference in total thickness. Because of the unknown snow depth, an empirical *R*-value (WADHAMS et al., 1992) is used to transform surface elevation to total thickness yielding:

$$t = selev \cdot R. \tag{2.2.3}$$

Generally speaking, the *R*-value is a function of the snow properties and the density variations of sea ice, leading to a high variability of *R*. The left graph in Fig. 2.5 shows the sensitivity of surface elevation to possible *R*-values regarding total thickness. *R* is undefined at 0 m surface elevation. The right graph shows the same for possible sea ice densities with an assumed constant snow depth of 0.2 m. The assumed densities for snow and sea water were taken from Table 2.1. The left graph clearly shows the ambiguity in the surface elevation to total thickness transformation. Regarding the right graph, an incorrect estimation of density is more critical for thicker ice as a variation of 20 kg/m^3 results in a 1.6 m difference in total thickness in contrast to a 0.4 m difference for thinner ice. The sensitivity of *R* to snow depth over a range of ice density is shown in Fig. 2.6.

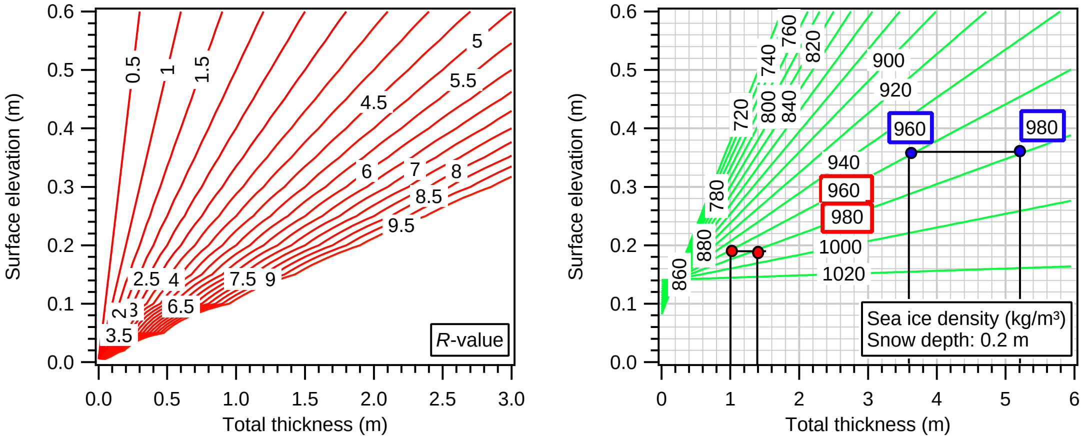

Figure 2.5: Surface elevation versus total thickness, and *R*-values resulting from Eq. (2.2.4), on the left. Densities for assumed snow depth of 0.2 m resulting from Eq. (2.2.3), on the right.

With the known surface elevation and total thickness, *R* is obtained by:

$$R = \frac{EM\ thickness}{selev}. \tag{2.2.4}$$

Replacing *t* in Eq. (2.2.1) with Eq. (2.2.3) yields:

$$R = \frac{h_s(\rho_s - \rho_i) + selev\,\rho_w}{selev(\rho_w - \rho_i)}. \tag{2.2.5}$$

If instead Eq. (2.2.4) the relation

$$R_{Wadhams} = \frac{\overline{d}}{\overline{selev}} \tag{2.2.6}$$

with *mean draft* $\overline{d}$ and *mean surface elevation* $\overline{selev}$ is used (WADHAMS et al., 1992), which is equivalent to

$$R_{Wadhams} = \frac{t - h_s - f}{f + h_s}, \tag{2.2.7}$$

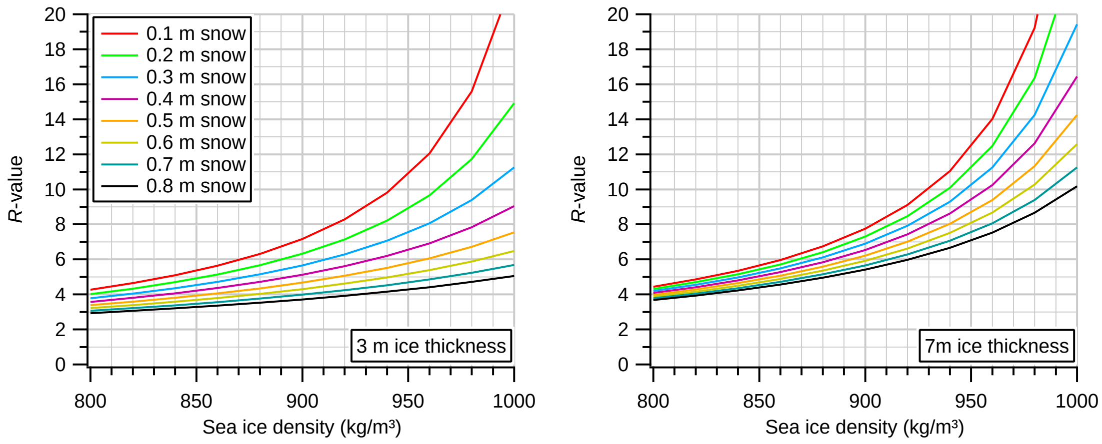

Figure 2.6: Sensitivity of R, expressed by the total thickness to surface elevation ratio, for eight snow depths and two total thicknesses of 3 m (left), and 7 m (right) over a range of ice densities. The legend of the right graph is the same as for the left graph.

it follows, that

$$R = R_{Wadhams} + 1. \tag{2.2.8}$$

See also HVIDEGAARD & FORSBERG (2002). From Fig. 2.6 can be seen that an R-value of 5.889[1] could be generated by the assumed ice density of 915 kg/m^3, with associated snow depths ranging from 0.33 m (over 3 m ice) to 0.79 m (over 7 m ice). This supports once more the conclusion that it is very uncertain to derive total ice thicknesses with constant estimates for the snow cover, even if they are based on local field experiments as done by MAYKUT & UNTERSTEINER (1971). That sea ice with a standard mean density of 915 kg/m^3 takes on values of R in the range from 8 (for 0.1 m snow depth) to 4 (for 0.8 m snow depth) over 3 m ice, and from 9 to 6 over 7 m ice respectively, underlines the high sensitivity of R to different snow loads.

2.2.2.2 Snow Depth and Influence of Sea Ice Density

Coincident ice thickness and surface elevation data allow calculation of snow depth on the basis of hydrostatic equilibrium. Snow depth is, as well as sea ice thickness, an important parameter to be considered within the context of global climate change; knowledge of which also allows conclusions to be made regarding a change in ice growth (EICKEN, 2003). With the known R, snow depth can be calculated in turn from Eq. (2.2.5), yielding:

$$h_s = \frac{R(\rho_w - \rho_i) selev - selev\, \rho_w}{(\rho_s - \rho_i)}. \tag{2.2.9}$$

Using Eq. (2.2.1), snow depth is obtained with:

$$h_s = \frac{(t - selev)\rho_w - t\, \rho_i}{(\rho_s - \rho_i)}. \tag{2.2.10}$$

Presently, the snow cover is estimated from climatological models. As already noticed by WADHAMS (1990), the predictions from climatological models do not

---

[1] Following WADHAMS et al. (1992), a value of 4.889 is derived as mean value from April 30 and May 31 to June 8. With Eq. (2.2.8) a value of $R = 5.889$ is obtained.

necessarily match the results from calculated snow depths. Since snow depth is a function of R it is dependent on the specific densities for snow, sea water, and sea ice (see Eq. (2.2.9)). Snow depth is also dependent on surface elevation. Regarding the right graph in Fig. 2.5, it is seen that the sea ice density varies considerably for different thicknesses. Because only constant mean density values are assumed, the results for calculated snow depths may differ from models. Obviously, an incorrectly estimated sea ice density is more critical for thicker ice.

2.3 Applied Measuring Methods for Surface Elevation and Total Thickness

2.3.1 The Global Positioning System (GPS)

The Global Positioning System (GPS), initiated by the U.S. Department of Defense in 1973 (HOFMANN-WELLENHOF & LICHTENEGGER, 1992), is a well known and widely used satellite navigation system. It is designed to provide continuous, accurate coverage all over the world. This is accomplished by the space segment consisting of 24 satellites deployed in six orbital planes with an inclination of 55°. With the satellite altitude of 20200 km and a period of approximately 12 hours four to eight satellites are simultaneously observable above 15° elevation at any time. If the elevation mask is reduced to 5° as many as 12 satellites may be visible. The control segment consists of a master control station and worldwide monitor and ground stations. The main tasks of this segment are the tracking of the satellites for orbit and clock determination, time synchronization, and upload of the data message including the ephemerides and clock information to the satellites. Finally, the user with their receivers comprise the user segment.

GPS applications include navigation at sea, in the air, low Earth orbit and on the ground. The primary goals were military ones but its civil use was soon promoted. Since then the GPS has become a common tool in many scientific and engineering fields, in the car industry and many others, e. g., in mountaineering.

The principle of the position finding is based on ranging. With a known location of a satellite and the user's distance to it, the position of the user on a theoretical sphere with its center at the location of the satellite is indefinite. To obtain a three-dimensional (3D) position at least three satellites with known orbits are required. Taking into account the clock error of the receiver and satellite, four satellites are necessary to solve the observation equation for the 3D position and the clock error. Thus, the term *pseudorange* is used in literature. The pseudorange is derived either by measuring the time of the signal using its code and multiplying it by its velocity which is the speed of light or by measuring the phase of the signal. Two different frequencies are essential for eliminating the ionospheric refraction, the major source of error. The atmospheric refraction can be eliminated by forming differences as described later. The carrier signal $L1$ is modulated with the Coarse/Acquisition (C/A)-code and the more difficult accessible P-code, whereas the carrier $L2$ is modulated only with the P-code. The frequencies for $L1$ and $L2$ are summarized in Table 2.2.

Additionally, a navigation message containing information about the satellite's clock, its orbit and its health status is modulated onto the carriers. To measure the travel time the received signal from the satellite is matched with a generated code replica in the receiver. The phase measurement of the received

Table 2.2: GPS signal frequencies.

$L1 = 1575.42\,\text{MHz}$	primary carrier frequency
$L2 = 1227.60\,\text{MHz}$	secondary carrier frequency

signal is performed after the code is removed from the carrier. The phase observable is ambiguous by an integer number of signal wavelengths which means that the model for phase pseudoranges is augmented by an initial bias, called integer ambiguity. For further details see HOFMANN-WELLENHOF & LICHTENEGGER (1992).

Data Combinations

The code and phase pseudoranges are affected by systematic errors or biases and random noise. Systematic errors can be eliminated by forming differences. Single-differences between two receivers and one satellite eliminate the satellite clock bias. Double-differences resulting from the difference of two single-differences between two different satellites eliminate the receiver clock bias. If more than one observation epoch is considered, the time independent ambiguities are eliminated by differencing double-differences between two epochs. Thus, triple-differences are immune to changes in integer ambiguities, also called cycle-slips. Cycle-slips occur because of signal losses mainly caused by an obstructed line of sight. The differencing technique requires two receivers measuring simultaneously to the same satellites.

The technique of relative positioning is more accurate than a single point measurement with only one receiver. Some authors (STRANGE, 1985; OSWALD et al., 1986) use the term *relative* if the carrier phase observations are used and *differential* if code ranges are formed. However, in this investigation, the term *differential* will be used in reference to either code or carrier phase ranges. Generally speaking, the accuracy in differential positioning by code ranges is at meter level, whereas by carrier phases centimeter accuracy is achievable (CANNON et al., 1986). The latter technique requires the use of dual frequency receivers (LACHAPELLE et al., 1992) with both frequencies $L1$ and $L2$. Another advantage of using carrier phases is that they are less affected by multipath than code ranges. Multipath is caused by multiple reflections of the signal against obstacles near the ground while traveling from the satellite to the receiver.

When applying the differential GPS (DGPS) technique, one receiver, the *base station*, is located at a permanent fixed site with known coordinates and the position of the other receiver is to be determined. The base station is used in a static mode whereas the second receiver can be used in a static or kinematic mode. In the kinematic mode the moving receiver, which is usually flown aboard an aircraft, is often termed a *rover*. The principle is based on determining the vector or the *baseline* between the two receivers. The positional accuracy of the second receiver depends on the baseline length. After CANNON et al. (1986) it is 1 ppm (parts per million).

The baseline can either be determined in *real-time*, i. e. the positional results for the rover must be available immediately or by *post-processing* at any time after the data set is collected. In real-time mode, corrections calculated from the difference between the known position of the fixed site and the base station are transferred to the rover via a radio communication link. Since in most scientific applications the collected data is processed after the campaign, the GPS data is also processed later in a post-processing mode (see Section 3.2). In order to derive surface elevation, the post-processed GPS data need to be reduced to the geoid that is described in the next section.

2.3.2 The Geoid

Gravity, the total force acting on a unit mass is the resultant of gravitational and centrifugal force (HEISKANEN & MORITZ, 1993). More precisely, the magnitude of the gradient vector, or gravity vector, is called gravity. The magnitude g is measured in gals (1 gal= 1cm sec^{-2}), the unit being named in honor of Galileo Galilei. The numerical value of g is about 978 gals at the equator, and 983 gals at the poles. Density inhomogeneities in the Earth's internal structure and surface features cause an undulated level, or equipotential surface, of the gravity field. The direction of the gravity vector is the direction of the plumb line which is slightly curved since it intersects all level surfaces normally (Fig. 2.7). On a level or equipotential surface the gravity potential W is constant.

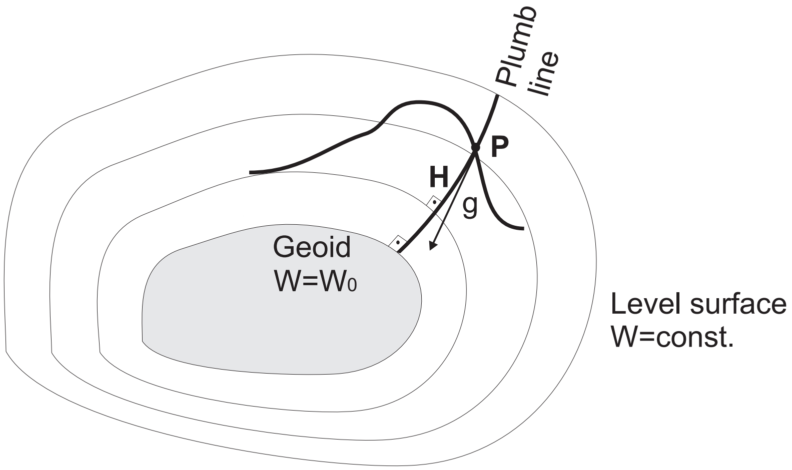

Figure 2.7: Orthometric height H of Point P measured along the slightly curved plumb line, intersecting level surfaces normally. Gravity vector g being tangent to the plumb line.

The gravity potential W is the sum of the potentials of gravitational and centrifugal force. After combining Poisson's equation for the gravitational potential V at a point $P(x, y, z)$

$$\Delta V = -4\pi\kappa\rho, \tag{2.3.1}$$

where κ is Newton's gravitational constant, ρ is the density of a unit mass, Δ is the Laplace operator, and

$$\Delta V = \frac{\partial^2 V}{\partial x^2} + \frac{\partial^2 V}{\partial y^2} + \frac{\partial^2 V}{\partial z^2} \tag{2.3.2}$$

with the differentiated centrifugal potential

$$\Delta\Phi = \frac{\partial^2 \Phi}{\partial x^2} + \frac{\partial^2 \Phi}{\partial y^2} + \frac{\partial^2 \Phi}{\partial z^2} = 2\omega^2, \tag{2.3.3}$$

the gravity potential W can be written as the generalized Poisson equation with ω being the angular velocity of the Earth's rotation:

$$\Delta W = -4\pi\kappa\rho + 2\omega^2. \tag{2.3.4}$$

The gradient vector of W, $g = \text{grad}\, W$ with components

$$g_x = \frac{\partial W}{\partial x},\ g_y = \frac{\partial W}{\partial y},\ g_z = \frac{\partial W}{\partial z}, \tag{2.3.5}$$

is the previously mentioned gravity vector. The surface of the oceans as a particular equipotential surface ($W = W_0 = \text{const.}$) was proposed as "the mathematical figure of the earth" by C. F. Gauss and was later termed the *geoid* (HEISKANEN & MORITZ, 1993). The height H of a point above the geoid, that is related to the potential W by

$$dW = -g\, dH \tag{2.3.6}$$

with

$$dW = \frac{\partial W}{\partial x}dx + \frac{\partial W}{\partial y}dy + \frac{\partial W}{\partial z}dz \tag{2.3.7}$$

and the length of the vector dx along the plumb line

$$dH = |dx|, \tag{2.3.8}$$

is called *orthometric height* and is measured along the curved plumb line. To determine the geoid and establish a model, respectively, the application of gravimetric methods are essential. Absolute gravity measurements by means of pendulums are very demanding. Therefore, relative gravity measurements are preferred which can be made by gravimeters. These relative measurements are tied to a uniform world gravimetric system. The present reference datum is the so-called *Potsdam system*, which is based on absolute gravity measurements performed around 1900 at the Geodetic Institute in Potsdam, Germany (HEISKANEN & MORITZ, 1993). Seaborne, airborne, and for the past few years spaceborne gravity measurements are used to determine the geoid.

The NASA Goddard Space Flight Center (GSFC), the National Imagery and Mapping Agency (NIMA), and the Ohio State University (OSU) have collaborated to develop an improved geoid model of the Earth's gravitational potential. The new model, Earth Gravitational Model 1996 (EGM96) incorporates improved surface gravity data, altimeter-derived anomalies from ERS-1 and the GEOSAT Geodetic Mission (GM), extensive satellite tracking data, including new data from Satellite Laser Ranging (SLR), the Global Positioning System (GPS), NASA's Tracking and Data Relay Satellite System (TDRSS), the French DORIS system, and the U.S. Navy TRANET Doppler tracking system, as well as direct altimeter ranges from TOPEX/POSEIDON (T/P), ERS-1, and GEOSAT (LEMOINE et al., 1998).

Starting in 1995, the first satellite (GFZ-1) of the GeoForschungsZentrum (GFZ) Potsdam was launched to improve the knowledge of the Earth's gravity field (KÖNIG et al., 1996). In 1997, GFZ Potsdam and Groupe de Recherche de Géodésie Spatiale (GRGS), Toulouse/Grasse jointly developed a new pair of global models of the Earth's gravity field. The new model exists in two parallel versions: the first one being derived exclusively from satellite tracking data acquired on 34 satellites (GRIM4-S4), the second one further incorporating satellite altimeter data over the oceans and terrestrial gravity data (GRIM4-C4) (SCHWINTZER et al., 1997). An evaluation of the first 30 months of GFZ-1 laser tracking data led to a new version of the global GRIM4-S4 satellite-only gravity field model: GRIM4-S4G (KÖNIG et al., 1999). In 2000 and 2002 the satellite missions CHAMP (REIGBER et al., 2005) and GRACE (TAPLEY et al., 2004) followed and are capable of determining the geoid with the highest accuracy to date. More about the generated geoid models is found in REIGBER et al. (2005) and TAPLEY et al. (2005).

For polar regions, however, the described geoid models are not sufficient due to weak coverage of the satellites which have been used to generate these models. Therefore, the Arctic Gravity Project (ArcGP) was established which is a new international effort dedicated to the compilation of a public-domain gravity grid of the Arctic gravity field north of 64° N. The 5′ x 5′ gravity grid is mainly based on all available surface, submarine, and airborne gravity data. The focus of the gravity grid is the Arctic Ocean, Greenland, and the continental margins of the Asian and North American continent (KENYON, 2000; KENYON & FORSBERG, 2001).

Recently, a new geoid model of the Arctic region has been generated by FORSBERG & SKOURUP (2005) as a combination of the current GRACE model and the most recently generated model from ArcGP. The accuracy is around 3 – 5 cm on long wavelengths and 20 – 30 cm on shorter wavelengths at a resolution of 10 – 20 km (personal communication with R. Forsberg). This model was used in this work for all data sets in the Arctic.

For the Antarctic, however, no special geoid exists. Acknowledging the success of the ArcGP, similar efforts are planned to be made to compile gravity data for the entire Antarctic (SCHEINERT, 2005). However, to date, no such geoid model is available, and the EGM96 geoid model (LEMOINE et al., 1998) from NASA/NIMA was therefore used as a data set in the Antarctic.

2.3.3 The Inertial Navigation System (INS)

The Inertial Navigation System (INS) was originally developed in the mid 1960s for missile guidance systems. Since then it has undergone an extensive development and has been introduced into civil aviation. Every object that is free to move in space has six degrees of freedom. Three degrees of freedom specify the velocity in the directions X, Y, Z, and the other three specify the rotations with regard to the attitude being pitch, roll, and yaw. The position determination is usually done with a GPS receiver. The attitude determination is solved by three accelerometers with their sensing axes orthogonal and three rate gyroscopes which measure the rotational velocity of the moving object. There are several implementation possibilities of assembling the accelerometers and the gyroscopes (KING, 1998). In the following, the technique of an INS and its error sources are not considered further. For details about the INS used during campaigns in the Arctic, see BOEBEL (2000). Importantly, with a combination of GPS and an INS it is possible to determine 3D coordinates of the ground location of a laser or radar beam. This is essential because if both a laser and radar altimeter are used inside an aircraft the vertical height difference of the ground location can be determined due to the difference of penetration depths. Regarding the surveying of sea ice, this vertical height difference of the ground location is comprised by the snow depth.

2.3.4 Laser Altimetry

Laser altimetry is an automated method of directly measuring ranges between an aircraft or satellite and the terrain. Typically, an infrared laser emits a short pulse towards the surface. Part of the reflected radiation returns to the laser altimeter where the travel time is recorded. The distance, or range, to the ground is obtained by multiplying the travel time by the speed of light. The other part of reflected radiation is scattered away or absorbed by the surface in such a way that it is too weak to be detected. In this case, no range measurement is possible. The accuracy at which range measurements are possible depends on the specific type of the laser altimeter. *RIEGL* Measurement Systems (http://www.riegl.com) mentions 0.05 m for the instrument used in this work. It is a so-called single-beam laser that can only do range measurements along-track. In order to obtain 3D-coordinates of the surface spots hit by the laser beam, the position of the aircraft or satellite and the direction in which the laser altimeter emitted its pulse must be known. Therefore, a GPS receiver and an INS are carried aboard the platform (see Section 3.4.2).

On the other hand, a laser scanner allows range measurements across the ground track of the aircraft (across-track) and thus provides a digital 3D-information sampling on the shape of the Earth's surface. In order to create an elevation map of the surface, thousands of range measurements per second are needed, each to a different spot on the surface (LINDENBERGER, 1993). To perform this, the laser beam is either scanned on a line across the direction in which the aircraft is flying, or it is scanned around the nadir. In each case this is achieved by a deflection unit, usually a rotating mirror. In the first case, the laser beam "jumps" from one line to the next, creating a virtual "strip", while the aircraft is moving forward. In the second case, a virtual "elliptical pattern" is created on the ground. The illuminated width of the virtual "strip" or the "elliptical pattern" on the ground, the swath width, is dependent on the flight altitude, the maximum angle of the radiated laser pulse, and the type of the laser altimeter.

The height of the sea ice floe surface above sea level is derived from the difference between measurements above ice and above water. The laser pulse is always reflected by the uppermost surface layer, which is mostly snow covering the sea ice. This is a major difference to radar altimeters which are described next.

2.3.5 Radar Altimetry

In contrast to laser beams, radar beams penetrate through the snow layer and are reflected at the snow/ice interface. The principal objective of a radar altimeter is to measure the time delay in receiving reflected signals from the ground scanned by passage of the instruments overhead. The distance to the ground is derived from the travel time of the signal multiplied by the speed of light. As opposed to laser altimetry, radar altimeters are unaffected by cloud cover. Radar height is defined as the minimum range between the radar and the ground. Height precision is primarily dependent on the radar pulse length. A conventional radar altimeter uses the echo delays from within the pulse-limited footprint to estimate minimum radar range. Outside the pulse-limited footprint, each scattered echo returns with relatively greater delay. The pulse length determines the diameter of the pulse-limited footprint associated with a corresponding area on the ground. The radar altimeter used in this work is the Airborne Synthetic Aperture and Interferometric Radar Altimeter System (ASIRAS) instrument which is similar to the radar altimeter that will be flown on CryoSat-2 (see Section 1.3). Due to the lower flight altitude of the airplane carrying ASIRAS, the footprint is of about 15 m x 25 m in across-track and along-track flight direction respectively. The measurement spacing is about 11 m at a flight speed of about 100 m/s.

2.3.6 EM Bird

During the late 1980s, the EM technique was first used for scientific large-scale sea ice thickness studies. The technique is based on the principle of electromagnetic induction in a conductive half-space. The EM bird consists of a set of transmitter and receiver coils operating at a frequency of 3.6 kHz with a coil spacing of 2.7 m (HAAS, 2003). The transmitted *primary* EM field induces eddy currents in a conductive layer, which in turn generates a *secondary* EM field. This secondary field is detected by the receiver coils. Thus, the apparent electrical conductivity of the subsurface is determined. Since sea ice is a very weak electrical conductor with conductivities between 0 and 50 mS/m (HAAS, 2003), the electrical conductor generating most of the secondary field strength is the sea water beneath the sea ice with conductivities of around 2500 – 3000 mS/m, depending on salinity. By measuring the amplitude and phase of the relative secondary field (in parts per million of the primary field), the distance from the transmitter to the sea water can be estimated. With an additionally mounted single-beam laser altimeter inside the EM bird, the distance from the bird to the top of the surface layer, which is mostly snow on ice floes, can be measured. The difference between these two distances gives the EM thickness, which is the ice thickness plus the depth of the overlying snow. Comparing the EM thickness with drill-hole measurements, an agreement within ±0.1 m has been obtained over level ice (HAAS et al., 1997).

For the geolocation of the EM thickness profile, there is also a GPS receiver inside the EM bird. The antenna on top is integrated in the bird's shell. The area, or *footprint*, depends on the EM parameters, where roughly 90 % of the induction process takes place. Here, the EM bird is operated at an altitude of about 14 m yielding a footprint of roughly 50 m (KOVACS et al., 1993; REID & VRBANCICH, 2004). Since ice thickness is averaged over this footprint, pressure ridges (more precisely the keel depths) are systematically underestimated. HAAS (2003) demonstrates this with the structure of ridge keels where the signal is also affected by the occurrence of eddy currents induced in the water next to those laterally confined deformed ice structures. The EM bird is 3.4 m long, weighs about 100 kg, and is suspended by a 20 m long cable beneath a helicopter (see Fig. 2.8). The flight speed is maintained at approximately 40 m/s. Due to warming of the electronics during operation, the measuring unit tends to drift. To correct this drift, the EM bird needs to be taken to very high altitudes (approximately 100 m) every 15 minutes. Between these ascending and descending trajectories of the helicopter, EM thickness data and laser data are not available.

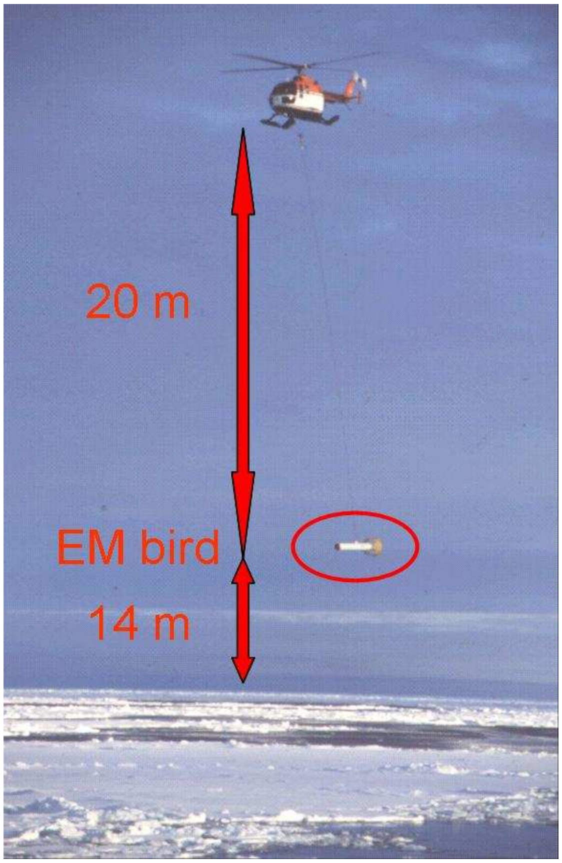

Figure 2.8: Operating EM bird suspended beneath a helicopter.

3 Data Acquisition and Processing

This chapter describes the collection of data used in the present work. To prepare the data for the derivation of surface elevation, the ground location of the reflected laser or radar signal must be determined. It will be distinguished between measurements with the EM bird (without INS) and measurements from an airplane (with INS). Subsequently, it is shown how surface elevation is derived. Further, possibilities of transforming surface elevation to total thickness are described as well as the calculation of snow depth. For the basics of the measuring methods see Section 2.3.

3.1 Data Collection

Fig. 3.1 shows the different areas in which data were collected in the Arctic (left) and in the Antarctic (right).

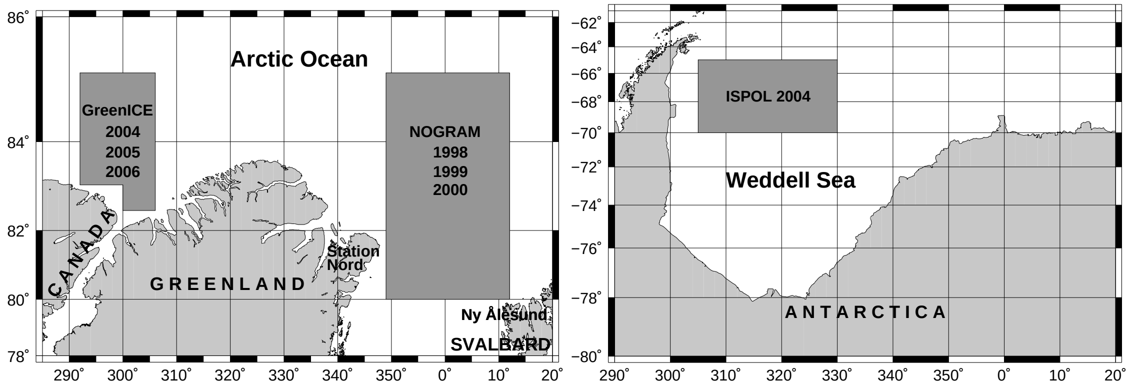

Figure 3.1: Survey areas in the Arctic (left) and Antarctic (right).

3.1.1 Arctic

In May 2004, data were collected north of Ellesmere Island, Canada (see Fig. 3.1, left). This campaign was planned within the EU-funded project (www.greenice.org) Greenlandic Arctic Shelf Ice and Climate Experiment (GreenICE) project during 2002 – 2006 (HAAS et al., 2006a). Two of the main aspects of this campaign were the scanning of the sea floor with hydrophones and the coring of sediment samples performed from the top of an ice floe while drifting along the shelf break of the Lomonosov Ridge in the Arctic Ocean (KRISTOFFERSON, 2004). The third aspect comprised ice thickness measurements. To fulfill the former, an ice camp was established about 200 km north of the coast of Ellesmere Island on a multi-year sea ice floe, approximately 2000 m wide and more than 4 m thick. In the beginning, the ice camp drifted at a speed of about 12 m/min, due to a heavy storm, before it slowed down to 6 m/min after the first week. The Canadian Forces Station (CFS) Alert served as base of operation for all service flights to and from the ice floe. The airfield of Alert was also the starting point for the helicopter flights with the EM bird and the survey flights with a laser scanner conducted by colleagues from the Danish National Space Center (DNSC) with a Twin-Otter aircraft from Air Greenland. The EM bird was equipped with a BD 950 card receiver from Trimble and a Hi-Speed L1/L2 antenna. A Trimble 5700 GPS receiver was used as a base station together with a Zephyr antenna. This base station was set up near the runway of Alert with good visibility of the sky. Both receivers logged data at 10 Hz. The first measurement flight on May 12, 2004 followed some waypoints of a submarine track, that operated in this area a couple of weeks earlier, and continued to the ice camp. In total, four flights, about 900 km long, were performed north, east and west of the sea ice camp. Additionally, ice thickness data taken with an EM 31 and snow depths measured with a meter stick along a 1400 m long profile as well as drill hole data were acquired. Further activities were canceled due to bad weather and postponed to the next field campaign.

In May 2005, two activities within the GreenICE project took place: the Danish laser scanner from the DNSC was flown aboard an Air Greenland Twin Otter and for the EM bird a Canadian helicopter was used again. The planned major objective was to repeat the northernmost helicopter flight from the previous year. However, bad weather and less than ideal sea ice conditions prevented the Twin Otter from landing on the sea ice to establish a refueling facility for the helicopter. Therefore, the farthest flight to the north was limited by the helicopter range of about 150 km one way reaching 84° N as opposed to 86° N in 2004. Another objective was a measurement flight in the Lincoln Sea due to prominent ice regimes of first-year and multi-year ice whose boundary is clearly distinguishable, and thus being highly important for sea ice studies, as well as at least one coincident flight with the Twin Otter. In total, two flights, each of 300 km, were performed in the Lincoln Sea, whereas one profile of about 100 km was surveyed coincidently with the laser scanning system of the Twin Otter. Another three (shorter) flights were conducted to the north of Ellesmere Island, with one flight leg being coincident with the Twin Otter track. To minimize the impact of ice drift on the coincident data, the helicopter took off earlier, so that the Twin Otter passed the helicopter approximately in the middle of the pre-defined profile. On the Lincoln Sea, flight the Twin Otter overtook the helicopter north of the middle, as planned, due to immobile ice in the south. The laser scanner data from DNSC was kindly provided to AWI. During each EM bird flight, photographs with a digital camera were taken in the flight direction approximately every 10 sec to 5 min for documentation of the sea ice characteristics. Additionally, five meteorological buoys were deployed on the ice and the snow depth was measured along a 100 m long profile with a meter stick at each deployment site.

The main difference in the sea ice situation compared to 2004 satellite imagery was the very large dynamic open polynya that stretched across the Lincoln Sea from the coast of Greenland to Ellesmere Island (see Fig. 3.2, right). Depending on the direction and strength of the wind the sea ice was pushed farther north or south resulting in a bigger or smaller polynya. A comparison of the sea ice thickness distribution between 2004 and 2005 is found in HAAS et al. (2006b).

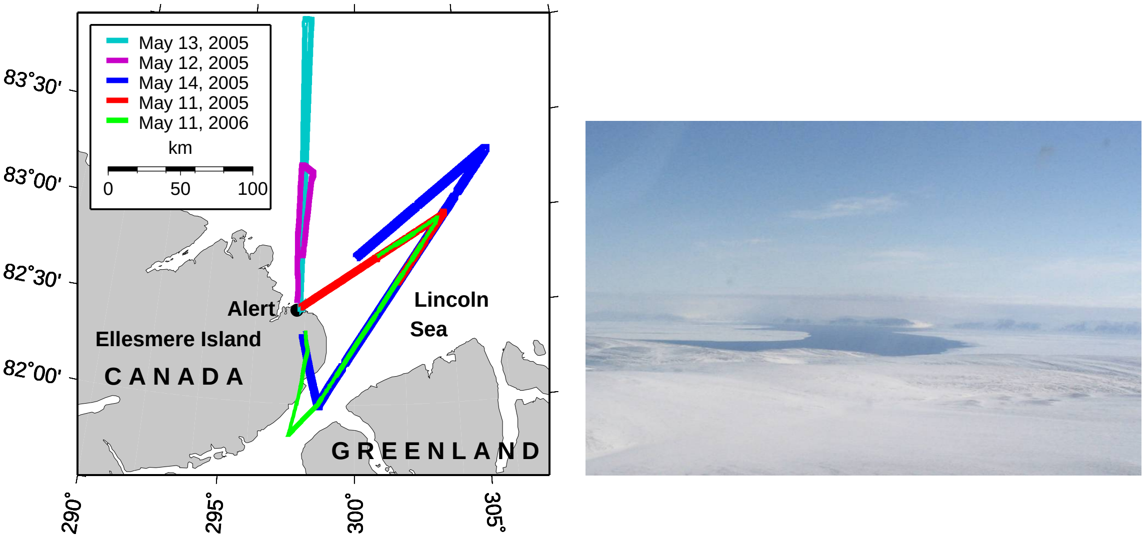

Figure 3.2: EM bird tracks in the Lincoln Sea and north of Ellesmere Island (left) and Polynya, roughly 4.4 km wide, in the Lincoln Sea (right) in May 2005.

In May 2006, the radar altimeter ASIRAS (see Section 2.3.5) was flown aboard an Air Greenland Twin Otter by colleagues from DNSC along two pre-defined validation lines north of Ellesmere Island, with corner reflectors at each end at a spacing of approximately 130 m. Additionally mounted was a laser scanner, GPS, and INS all of which were used the previous year. Further, EM bird flights along the validation lines as well as repeat measurements of the previous years were performed. The ASIRAS data of the first test flight was processed by AWI and the laser scanner data were kindly made available by DNSC in Summer 2006. First comparisons were done for the northernmost validation line. The southern validation line was established on multi-year level ice, the northern on first-year level ice. Both validation sites were on immobile fast ice.

Moreover, ground measurements including drilling of about 60 holes along a 300 m long profile by the Finnish Institute of Marine Research (FIMR) were conducted and also used for comparison with the ASIRAS, laser scanner, and EM bird data. Results are found in Section 4.6.2 and Section 5.2. Regarding the EM bird repeat measurements of the previous years, an overlapping section in the Lincoln Sea was used to compare the estimated dynamic sea surface topography (DSST) to the one from May 2005 which was estimated from two flights over the same section (see Section 3.5.4).

The second data set dealing with survey flights in the Arctic is the Northern Gravimetry and Magnetics (NOGRAM) project from 1998 to 2000 (see Fig. 3.1, left). During three campaigns, the area northeast of Greenland was mapped using airborne magnetics and gravimetry (see Section 4.5). The objective was the investigation of bathymetric-tectonic structures near the Fram Strait. The junction of the Gakkel Ridge and the Lena Trough were areas of major interest. Both tectonic structures are still active and therefore highly important for studying geodynamic processes such as seafloor spreading. For details of collecting and processing gravimetric data see Boebel (2000). In the present work the focus is on the GPS, INS and laser data. The GPS data were collected at 1 Hz, INS data at 20 Hz and laser data at 100 Hz. GPS base stations were set up in Longyearbyen (Svalbard), and at Station Nord (Greenland). For further details and results see Section 4.5.

3.1.2 Antarctic

In the Antarctic Spring from November 2004 until January 2005 the Ice Station POLarstern (ISPOL) campaign was conducted in the Weddell Sea (see Fig. 3.1, right). During that time, the RV Polarstern served as a drifting ice station for 50 days while it was anchored to a sea ice floe. Initially, the ice floe was about 10 km wide before it broke apart during a storm. Many scientific experiments from various disciplines were conducted (see www.ispol.de). Regarding the sea ice thickness studies, helicopter flights with the EM bird to the north, south, east and west were done, to cover different ice regimes. Additionally, ground measurements with the EM 31 as well as snow depth measurements and drilling holes were performed (HELLMER et al., 2006).

3.1.3 Bay of Bothnia

In March 2005, the first ASIRAS campaign over sea ice took place in the Bay of Bothnia (HELM et al., 2006) (see Fig. 5.1 in Section 5.1). The airplane, a Dornier 228, from the German Aerospace Center (DLR) was equipped with a Trimble 4700 GPS receiver, capable of logging 1 Hz data, Honeywell INS, ASIRAS, *RIEGL* laser scanner LMS-Q 280, *RIEGL* single-beam laser altimeter LD 90 producing output data at 25 Hz, hereafter termed LD 90, and a video camera. The objective was to validate ASIRAS by flying along two pre-defined validation lines marked with corner reflectors and given GPS waypoints at either end.

After the transfer flight to Stockholm, the instruments were switched on for the first measurement flight from Stockholm to Oulu as soon as sea ice was present. The two marked lines were overflown twice at four different altitudes for validating ASIRAS. The altitudes of 300 m, 500 m, 700 m and 1130 m were chosen according to the least and maximum possible range for ASIRAS and the laser, respectively. At the same time, the Finnish RV Aranda served as a base for intensive measurement activities on the sea ice along the northern validation line. Data of approximately one thousand drill holes and with the EM 31 were collected. Helicopter flights with the EM bird were performed several times, especially along the validation lines. Additionally, one coincident flight between the ASIRAS-airplane and the helicopter was performed. Unfortunately, no ASIRAS data file was recorded for this coincidently flown leg. Therefore, only surface elevation distribution of the LD 90 could be compared with total thickness of the EM bird. Since the EM bird operated without the DGPS facility during this campaign, no surface elevation could be derived that would have been comparable to the LD 90 surface elevation. However, several LD 90 and ASIRAS data files were recorded and allow a first comparison of the derived surface elevation, and freeboard respectively, and hence, a calculation of snow depth. For this comparison, a flight leg to the northwest of the overall airplane flight tracks was chosen. The helicopter flew along the same leg about 30 min earlier, and thus EM thicknesses are available as reference for interpreting features in the derived surface elevation and freeboard profiles. Additionally, photographs were taken along the helicopter flights for documentation of the sea ice characteristics. On the way to Stockholm, special flight maneuvers were conducted to calibrate the behavior of the INS. For this calibration, the maximum airplane pitch and roll angles were varied between ±5° and ±10°, respectively. After the transfer flight back to Bremerhaven, some assorted buildings at the airport Luneort were used for a cross-over flight to calibrate the laser scanner.

Within this work, the main aspects of the campaign in the Bay of Bothnia were neither a detailed study of the radar altimeter ASIRAS nor the laser scanner, but rather the analysis of the final processed ASIRAS data yielding freeboard. Results are found in Section 5.1.

3.2 GPS Post-Processing

Because of the remoteness of Arctic and Antarctic campaigns, permanent GPS stations with known coordinates in the International Terrestrial Reference Frame (ITRF) (ALTAMIMI et al., 1993, 2001; DICK & RICHTER, 2004) are not suitable as base stations. The baselines are too long for kinematic positioning. Also, these sites usually log GPS data at a 30 second interval and thus are inadequate for DGPS, since a GPS receiver at a higher frequency is used as the rover. Therefore, a base receiver is set up close to the starting point of the survey flights, usually the local airfield. The coordinates of this base receiver are determined in static mode, using the nearest permanent ITRF-GPS station. However, in the worst case the baselines between ITRF and base station are several hundred km in length. In the Antarctic, a slightly inclined, almost linearly increasing ground elevation is seen due to the drifting base station (see Section 3.5.3.3). The ice drifted with a speed of approximately 6 m/min. But still, a drifting base station was better for kinematic post-processing than using e. g., OHI2 (O'Higgins) at a distance of about 500 km. Besides, this station is not capable of logging 10 Hz data which is necessary for post-processing the 10 Hz GPS data of the EM bird. Regarding the GreenICE and NOGRAM data sets, the permanent GPS reference station at Ny Ålesund was used while during the campaign in the Bay of Bothnia the GPS reference stations at Kalajoki and Raahe, near Oulu were used. See Fig. 3.1 for the chosen reference stations in the Arctic, and Fig. 5.1 in Section 5.1 for the stations in the Bay of Bothnia.

Approximately two weeks after data collection, precise satellite orbits (ephemerides) are available and distributed by the International GNNS Service, formerly the International GPS Service (IGS) (BEUTLER et al., 1999). Since the precise ephemerides provide a position accuracy of about 2 cm for the satellite orbits, use of these is recommended instead of the immediately available broadcast ephemerides which have a significantly inferior accuracy. In the following kinematic post-processing, the baselines from the base station to the GPS receiver inside the EM bird are determined. As mentioned in Section 2.3.1 the positioning error amounts to 1 ppm of the baseline length. Regarding the survey flights with the EM bird, this error is approximated with 0.8 – 0.12 m depending on the distance[1] from the GPS base receiver. The post-processing was done with the software Trimble Geomatics Office (TGO), v1.62. Here, the tropospheric model from Niell (NIELL, 1996) was used. The antenna height measurements referred to the antenna phase center. The result are the 3D-coordinates X, Y, Z of the moving EM bird at a sampling rate of 0.01 s, which reference to the ellipsoid of the World

---

[1] The distance is shorter if the flight pattern is a triangle and longer if it consists of a straight line assuming the same flight length. Usually, triangle flights are performed with the EM bird.

Geodetic System introduced in 1984 (WGS 84) (LOHMAR, 1988).

With the software *geoip* which is part of the software package GRAVSOFT (TSCHERNING et al., 1992) it is possible to subtract geoidal heights of the most current and accurate geoid model (see Section 2.3.2) from the ellipsoidal WGS-height Z for given geographic coordinates. The relationship is expressed in the simplified form:

$$H = Z - N', \tag{3.2.1}$$

where H is the orthometric height of the GPS receiver above the geoid (hereafter termed *GPS height*), Z is the ellipsoidal height and N' is the geoidal height, or geoidal undulation, above the ellipsoid WGS 84 (see Fig. 3.7).

3.3 Processing of the EM Bird Laser Data

The EM bird laser altimeter is a *RIEGL* LD 90 producing output data at 100 Hz. It mainly supports the EM measurements (see Section 2.3.6), but in combination with DGPS it can also be used for the determination of surface elevation. The internal clock of the EM bird produces ticks at a separation of 0.1 s, which are used as a reference timestamp for all acquired data sets. The connection to UTC-time is estimated with the GPS timestamp. For each 0.1 s, hereafter termed *fid*, all data is written continuously to a file. The laser data is stored in the format: fid, range.

3.4 Ground Location

3.4.1 Synchronization of GPS and Laser in the case of the EM Bird

To match the laser ranges with the post-processed GPS height, the coarser NMEA GPS data at 1 s sampling rate are recorded together with the fid number. NMEA (www.nmea.org) is a standard protocol, used by GPS receivers to transmit data. Since the NMEA GPS data are sampled at 1 s, the fids are incremented by 10. However, sometimes the fids are incremented by a different number. Only, if two subsequent fids are exactly incremented by 10, these fids are taken for interpolating the intermediate fids (gpsfid), which match the 0.1 s from the GPS. Otherwise, the fid-assignment is too uncertain and data gaps occur. Finally, the post-processed GPS height versus gpsfid is interpolated to the grid of the equidistant 1/10 fids of the laser.

Since no INS is mounted inside the EM bird, it is not possible to derive the accurate 3D coordinates of the surface spot hit by the laser. Assuming that the laser is nadir-looking, the difference of the GPS height H from Eq. (3.2.1) (see Section 3.2) and laser range, i. e. *laser height*, yields the elevation of the ground location (*ground elevation* $gelev_{geoid}$) above the applied geoid model (see Fig. 3.7). Fig. 3.3 shows the elongation (left) and nadir offset (right) of the laser height versus the roll angle for the EM bird at 10 m, 14 m, and 18 m altitude while suspended by a 20 m long cable beneath a helicopter. At a roll angle of e. g., 4° an elongation of about 0.09 m is visible at 14 m altitude yielding an incorrect ground elevation, and hence incorrect surface elevation (see Section 3.5). The roll angle, that is affected by the pilot's aviation skills and wind, is changing during the survey. From visual observations roll angles of up to 10° were estimated.

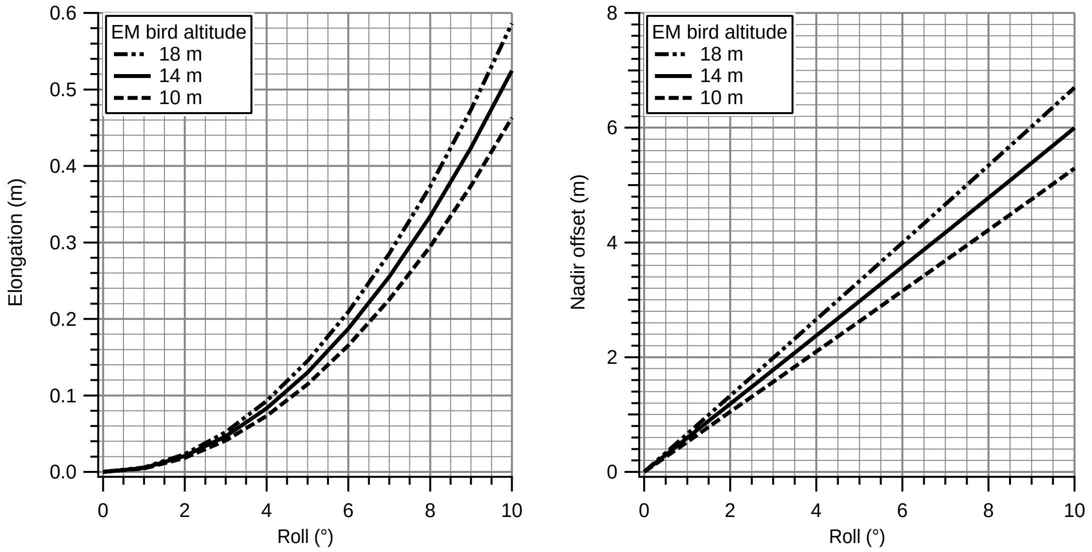

Figure 3.3: Elongation (left) and nadir offset (right) of laser range versus roll angle for the EM bird at 10 m, 14 m, and 18 m altitude while suspended by a 20 m long cable beneath a helicopter.

3.4.2 Synchronization of GPS, INS, and Laser in the case of Airplane Altimetry

As opposed to the problem of assigning the correct laser fid to the GPS height in the case of the EM bird, the following synchronization steps refer to timing problems between the systems. The timing problems are caused by combining the three data sets. Although time for each system is counted in parts of UTC-seconds, depending on the measurement frequency, each system has its own time axis. The time axes of the different systems are generally offset by up to $1-2$ seconds. In other words, there is a timeshift that prevents a correlation between the different data sets. A correlation, however, is required for processing. Usually, the GPS time is taken as the reference time.

The INS-timeshift was found with a cross-correlation. For the cross-correlation technique, the implemented function of the software package IGOR Pro (see www.wavemetrics.com) was used. For the laser-timeshift of the NOGRAM data as well as for the ASIRAS-timeshift of the ASIRAS data, a different technique had to be applied.

3.4.2.1 INS Timeshift

The timeshift of the INS relative to the GPS is determined by cross-correlating the first derivatives of the heading from the geographical GPS positions (λ, φ) of two GPS receivers aboard the aircraft (one in the front (f_r) and one in the rear (r)) with the yaw of the INS. In Fig. 3.4 the relationship of pitch and yaw is shown. First, the distance (D) in meters between the two receivers was calculated with

$$D = \arccos(\sin(\varphi_{f_r})\sin(\varphi_r) + \cos(\varphi_{f_r})\cos(\varphi_r)\cos(\lambda_{f_r} - \lambda_r))\frac{60}{\pi}1852. \qquad (3.4.1)$$

The heading (hd) resulted from

$$hd_1 = \arccos(\frac{(\sin(\varphi_{f_r}) - \sin(\varphi_r)\cos(D)}{\sin(D)\cos(\varphi_r)}); \qquad \sin(\lambda_{f_r} - \lambda_r) \geq 0, \qquad (3.4.2)$$

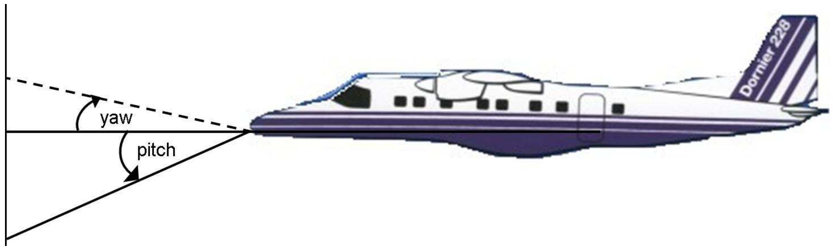

Figure 3.4: Pitch and yaw of an aircraft.

and respectively,

$$hd_2 = 2\pi - hd_1; \qquad \sin(\lambda_{f_r} - \lambda_r) \geq 0. \tag{3.4.3}$$

Next, the GPS-data were interpolated to match the frequency of the INS. The following cross-correlation was done stepwise to check the variability for the individual flights. Steps of 1 min, 10 min, and 15 min were chosen. For the NOGRAM-campaign in 2000 the INS-timeshift yielded 1.1 s for all steps and for all flights. To obtain a more precise number, the INS data were additionally oversampled with 50 Hz which resulted in 1.08 s for all flights. The INS-timeshift for the years 1999 and 1998 varied slightly between 1.02 s and 1.06 s for the individual flights. The INS-time was then corrected by adding the INS-timeshift. The equivalent cross-correlation between the first derivatives of height difference of the two GPS receivers with the pitch of the aircraft was neglected in the processing of the NOGRAM-data due to a sufficient result after correlating the rates of heading and yaw. The timeshifts of the ASIRAS campaign yielded -1.04 s for the pitch and -1.12 s for the yaw angle (personal communication with S. Hendricks).

3.4.2.2 Laser Timeshift

Determining the timeshift of the NOGRAM laser data relative to the GPS by applying the same cross-correlation technique as above, i. e. cross-correlating the entire GPS profile stepwise with the laser profile, yielded unsatisfactory results. Another means to determine the timeshift is to correlate the laser range with the range of the aircraft's own radar altimeter. Promising sections of data were the climb flight and the dive, since the altitude changes more rapidly than topography. Usually, this enables the success of the cross-correlation technique. However, applying this constant timeshift to the entire laser profile led to unacceptable results. Therefore, the technique from Hendricks (personal communication) was applied. The ASIRAS timeshift, which scattered similarly to the laser timeshift, required a new technique. The reason for this is that sea ice is too rough and hence the correlation is too variable at small-scales. Hendricks developed a method which is based on applying several timeshifts and observing its effects visually. Finally, the timeshift at which data correlate the best, is fixed.

This "visual" procedure of estimating the laser-timeshift was time-consuming but seemed to be the only adequate method. Fig.3.5 shows a laser profile before and after the applied timeshifts for INS and laser.

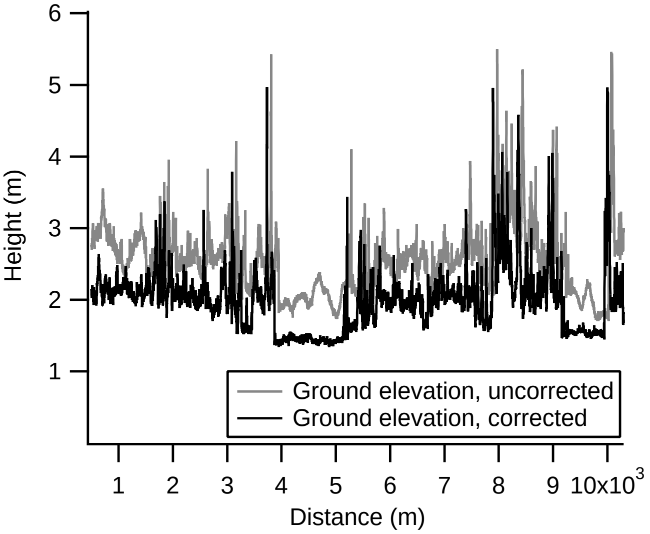

Figure 3.5: Ground elevation before (leads not horizontal) and after (leads horizontal) applied timeshifts for INS and laser.

3.4.2.3 Transformation of the Aperture Coordinate System to WGS 84

The mounted scientific systems aboard the aircraft define the aperture coordinate system. This differs from the aircraft body fixed coordinate system which is defined by the x-axis in the direction of the nose of the aircraft, the y-axis pointing to the right wing and the z-axis to complete a right-handed system. To determine the 3D-coordinates of the ground location relative to WGS 84, the aperture coordinate system needs to be rotated and translated to match the geocentric coordinate system of the WGS 84. A geoid model can then be applied to obtain ground location relative to the geoid. In this study, the software developed by HELM et al. (2006) within the ASIRAS-project, was used. Regarding the ASIRAS and LD 90 data from the Bay of Bothnia, the geolocated data were taken from the final processing by Hendricks. Although the geolocated ASIRAS data are always in reference to the nadir, due to this particular processing technique, the LD 90 geolocations may refer to an off-nadir position depending on the roll angle of the airplane. Both data sets were used to calculate the snow depth from the different penetration depths of radar and laser beams. Fig. 3.6 shows the elongation (left) and nadir offset (right) of the laser range versus the roll angle for an airplane at 500 m altitude. The roll angle varies considerably during the flight. On average, roll angles of ±0.3° were found for the ASIRAS airplane yielding a mean elongation in slant range of about 0.008 m. This was considered to be sufficient for a first comparison between the ASIRAS and LD 90 regarding the calculation of snow depth.

With the software geoip (see Section 3.2) the ground elevation above WGS 84 was reduced to the applied geoid (the same as was used in the case of the EM bird). The relationship can be expressed in simplified form (see Eq. (3.2.1)) as:

$$gelev_{geoid} = gelev_{WGS\,84} - N', \tag{3.4.4}$$

with $gelev_{geoid}$ being the ground elevation above the geoid, $gelev_{WGS\,84}$ the ground elevation above the ellipsoid WGS 84, and N' the previously introduced geoidal undulation see Fig. 3.7.

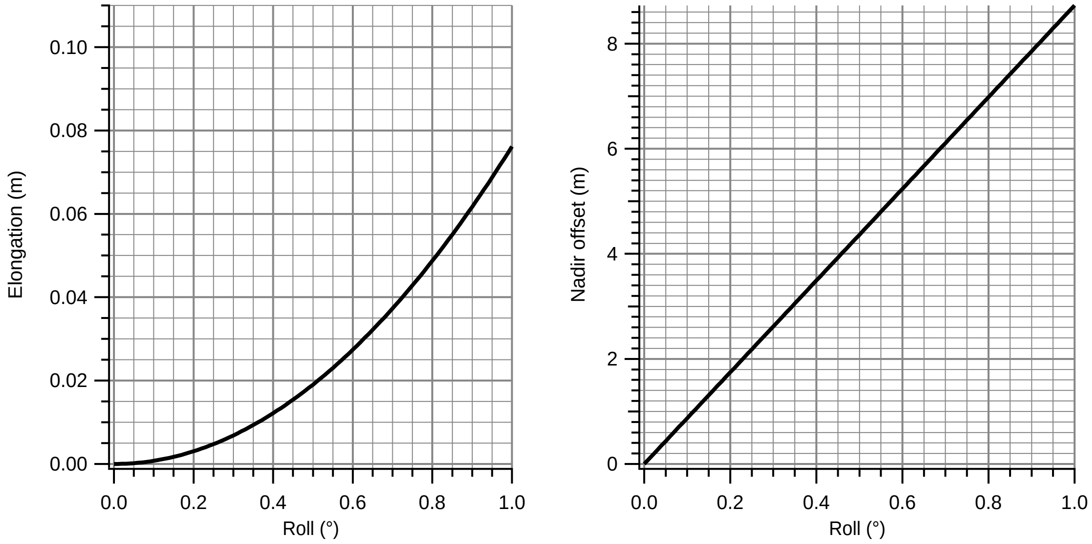

Figure 3.6: Elongation (left) and nadir offset (right) of laser range versus roll angle for an airplane at 500 m altitude.

3.5 Surface Elevation

The previously described ground elevation, which results from the difference between GPS height and laser height with respect to the EM bird, and from the ground location itself with respect to NOGRAM and ASIRAS, is based on the applied geoid model. Even the most accurate geoid model is still a model which approximates globally the *mean sea level* (CHAMBERS et al., 2002). In a state of rest or absence of external forces, the mean sea level would coincide with the geoid. However, due to ocean currents, air pressure variations, temperature and salinity variations, etc., this does not occur, not even as a long term average. The difference between mean sea level and the geoid is referred to as (stationary) mean sea surface topography (MDT). It varies globally in a range of ±2 m (WENZEL & SCHRÖTER, 2006). Dynamic sea surface topography (DSST) is the average difference between the (actual) *local sea level*, present at the time of the survey, and the geoid. It is caused by the steady state ocean current field, tides and local wind patterns. The tidal signals in the Arctic Ocean range between 3 and 4 cm (KOWALIK & PROSHUTINSKY, 1993).

Due to the deviation of the local sea level from the geoid (see Section 3.5.4), the ground elevation ($gelev_{geoid}$) needs to be corrected by the difference to derive surface elevation ($selev$). Fig. 3.7 shows the relationship of the addressed parameters. Methods of measuring DSST and deriving it from surface elevation are mentioned in Section 3.5.4. Besides DSST, the difference is caused by the geoid error (see 2.3.2).

Assuming, that each laser profile contains open water or thin ice of up to 10 cm, these data points are represented by the lowest values in the ground elevation. Thus, these values, which match open water or thin ice, have to be detected in order to estimate the difference (DSST in Fig. 3.7) between the geoid and local sea level. To account for the noise in the high resolution data, the surface elevation was smoothed with a moving average of 12 m. This smoothing factor reduces the noise considerably but still ensures that details of the surface topography like single ridges remain visible (see Section 3.5.3).

To detect the lowest values of open water, the standard deviation and mean was calculated for equally long sections (10 – 40 m) in the ground elevation. After assigning thresholds for standard deviation and mean, cracks and leads could be found by the different behavior of the two quantities. For instance, a lead was characterized by two major jumps in the standard deviation at the beginning and the end and a small mean value in between. The crucial part of this automated method was to choose the length of the section for which the standard deviation and mean should be determined. Sections, chosen too long resulted in a mean value no longer representative for open water or thin ice and those chosen too short caused thick but flat ice floes surrounded by ridges to be detected as leads. Since the automated experiments, used to detect the lowest values of open water, failed to give the desired results, a manual approach was implemented.

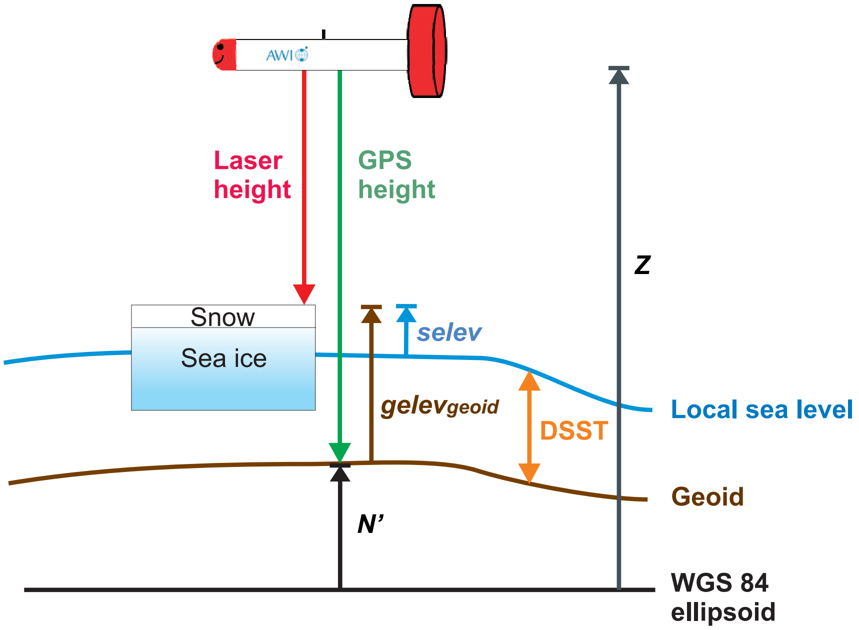

Figure 3.7: Ellipsoidal height Z, geoidal undulation N' and ground elevation $gelev_{geoid}$ resulting from the difference between GPS height and laser height. Surface elevation *selev* is derived from ground elevation by subtracting the lowest level of open water (corresponding to local sea level). Deviation of local sea level from geoid is defined as dynamic sea surface topography (DSST).

3.5.1 Detection of the Local Sea Level

In Fig. 3.8 an 10 km long section (a) of the entire GPS and laser data profile (c) is displayed. The bottom curve in (a) is the difference between the GPS height and laser height, the ground elevation. The lead at the mid-section of this curve is fairly obvious and easy to detect as open water, and hence was marked with a square in the zoomed-in mode (b). The same was done for the entire profile (c). Here, the lowest values were marked approximately every 10 – 20 km on average to match the resolution of the applied geoid model. Sometimes, however, the lowest values were picked at a shorter distance if prominent leads were present more often. With a linear interpolation technique a lowest level (corresponding to local sea level in Fig. 3.7) was fitted through the picked lowest values. The linear interpolation was found to be sufficient for distances at which the lowest values were detected for the most profiles. Results of a smoothing spline interpolation are shown in Section 3.6.1, Fig. 3.25 (a) and (c). Next, the lowest level was subtracted from the ground elevation, giving surface elevation (c). Additionally, the draft of the EM thickness is shown with the equivalent surface elevation (d). The clearly visible lead in the middle matches perfectly to the detected lowest value in (b). Thus, the good quality of detecting single lowest values manually is shown.

3.5.2 Surface Roughness and Advantage of GPS

In Section 1.3 (paragraph 'Airborne Laser Altimetry'), the removal of the aircraft motion from the obtained laser range was mentioned as a major issue in laser profiling. HIBLER (1972) removes the aircraft motion by applying a low pass filter, assuming that the aircraft motion is of long wavelength nature. However, this method does not allow to find open water in the measured profile which makes it impossible to reduce the derived surface roughness (elevation of the surface above the mean height of level ice) to surface elevation (elevation of the surface above sea level). The difference of surface roughness and surface elevation (derived with DGPS) is shown in Fig. 3.9. The graph on the left shows a profile section with a clearly identifiable lead[2] between 7900 m and 8200 m distance and a clear increase in the EM thickness at about 8300 m (from 0 m to about 5 m) and surface elevation (from 0 m to about 1 m). Considering the surface roughness, also a height of 0 m is visible for the lead section but a change in height for the adjacent 500 m, equivalent to the behavior of the EM thickness and surface elevation, is missing. Moreover, the surface roughness oscillates around 0.2 m reaching values up to 2 m (near 7700 m distance) and very often 0 m (at the distance between 7800 m and 8200 m). The graph on the right shows the equivalent histograms of surface elevation and surface roughness. The surface roughness distribution is dominated by one mode at 0 m whereas the surface elevation distribution shows one mode at 0 m and additionally one ice mode at about 0.7 m that corresponds to the increased surface elevation (at about 7700 m and between 8300 m and 8800 m) in the left graph.

The fact that no ice mode at all is visible in the surface roughness distribution makes clear that it is impossible to use the surface roughness for total thickness calculations. Thus, the advantage of GPS with respect to the removal of the aircraft motion, and moreover the feasibility to derive surface elevation, is obvious.

3.5.3 Accuracy and Problems

3.5.3.1 Smoothing Effects and Open Water or very thin Ice

As mentioned in Section 2.1.5, a histogram mode near 0 m represents open water or very thin ice. Fig. 3.10 (left) shows a profile section of very thin ice that is indicated by the surface elevation oscillating around 0 m and the EM thickness fluctuating within 0.1 m. This is confirmed by the photograph in Fig. 3.11 (left). Ideally, in the surface elevation histograms on the right, one clear peak should be visible with steep edges on each side. Instead, a gaussian-shaped distribution is visible, mainly caused by roll effects of the EM bird as mentioned in Section 3.4.1. Additionally, the surface elevation was smoothed with a moving average of 12 m.

---

[2] EM thickness and surface elevation at 0 m.

This value appeared to be the best smoothing factor as shown in Fig. 3.12. Here (Fig. 3.10, right), the histograms are shown for the unsmoothed and smoothed surface elevation. Obviously, the smoothing reduces the noise, causing a sharper peak at around 0 m but still a blurred mode up to ± 0.10 m at low probabilities. The standard deviations amount to 0.05 m for the unsmoothed, and 0.04 m for the smoothed surface elevation respectively.

Fig. 3.11 (right) displays a profile section of EM thickness and surface elevation which was smoothed over 12 m and 50 m. The resulting histograms are shown in Fig. 3.12. Smoothing the surface elevation over 12 m reduces the noise but allowing single ridges and the surface roughness to remain visible (Fig. 3.11, right) as mentioned in the previous section. This effect is also seen in the histogram (b) in which a sharper mode at around 0 m is visible than in (a). Further, the mode at 0.15 m is seen more clearly in (b) than in (a). The mode at 0.65 m (a), however, is slightly shifted to the right to 0.69 m (b). Smoothing the surface elevation over 50 m (Fig. 3.11, right) which corresponds to the footprint of the EM bird (see Section 2.3.6), is obviously too aggressive. Especially between 193.4 km and 193.7 km the aforementioned surface roughness is nearly smoothed out completely and the ridges are reduced to almost half of the original height. These effects are seen in the histogram in Fig. 3.12 (c) where the noise is reduced considerably, resulting in the very sharp modes for thin ice between 0 m and 0.2 m. On the other hand, the gap between 0.2 m and 0.6 m is an effect of the smoothed out surface roughness. Additionally, the mode for the thicker ice at 0.65 m (a) and 0.69 (b) is further shifted to the right to 0.71 m (c). Based on these findings, a smoothing over 12 m was chosen to be the optimum. For comparison, the EM thickness histogram is shown in Fig. 3.12 (d). One might conclude that surface elevation smoothed over 50 m (b) is the better result since this histogram looks very similar to the EM thickness histogram (d) in terms of the sharp distinct open water mode. Besides, the measurement accuracy of the EM thickness is known to be at ± 0.1 m. However, this is misleading since the ice underside, which is included in the EM thickness distribution, does not necessarily match the surface topography (see Fig. 2.2). Therefore, the results for surface elevation shown in Chapter 4 were smoothed over 12 m to ensure a noise reduction, but still preserving the surface roughness.

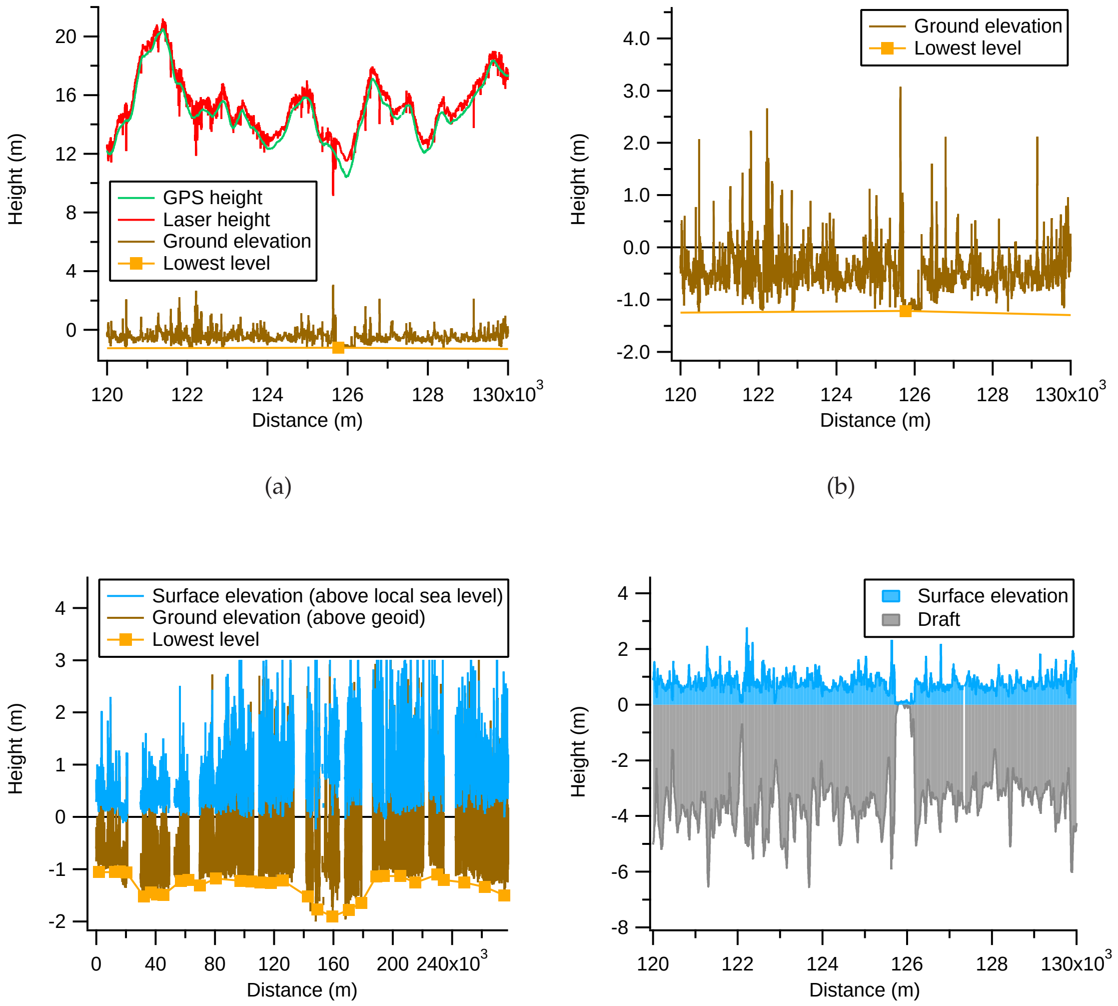

(a) (b)

(c) (d)

Figure 3.8: Difference of GPS and laser height, the ground elevation, and lowest level for an 10 km long section is shown in (a) and for the entire profile (c). Larger data gaps (roughly every 40 km) result from the instrument drift correction between the ascending and descending trajectories of the helicopter, smaller gaps are due to the fid-assignment issues mentioned in Section 3.4.1. Ground elevation and lowest level with the marked lead in the middle is displayed in (b). Subtracting the lowest level from the ground elevation, yields the surface elevation (c). Additionally, the draft of EM thickness is shown for the 10 km long section with the equivalent surface elevation (d). The clearly visible lead at the mid-section matches perfectly to the detected lowest value in (b).

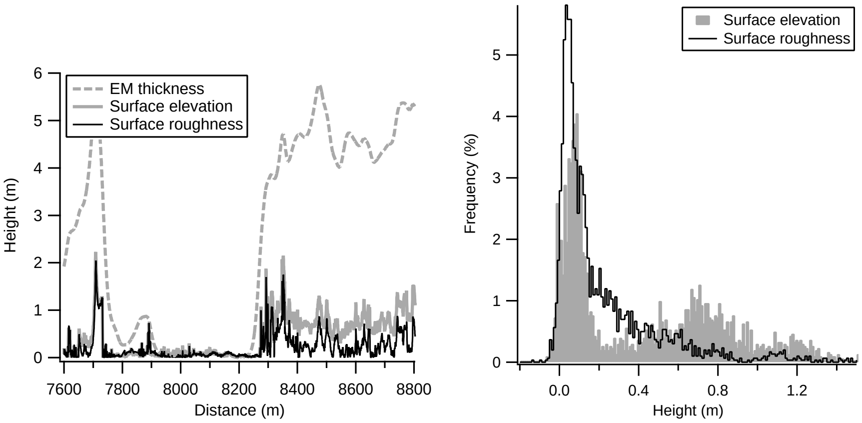

Figure 3.9: Profile of surface elevation, surface roughness and EM thickness (left), and histogram of surface elevation and surface roughness (right).

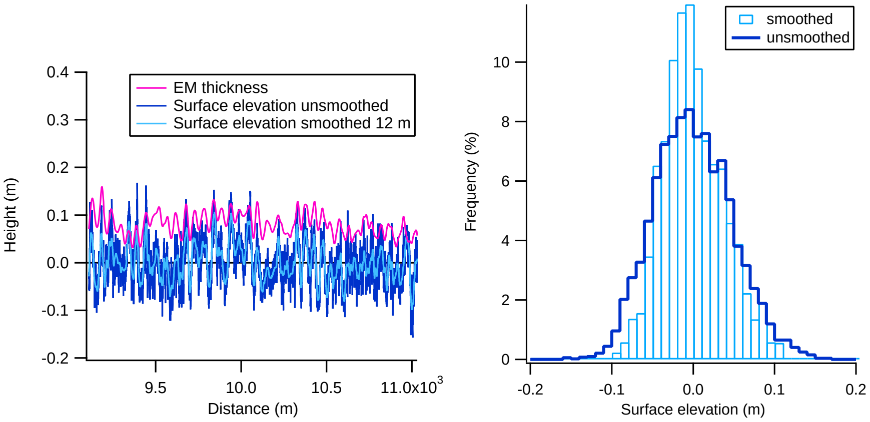

Figure 3.10: Surface elevation and EM thickness for a profile section of thin ice (left), and histograms of surface elevation (right). A moving average over 12 m was used for smoothing.

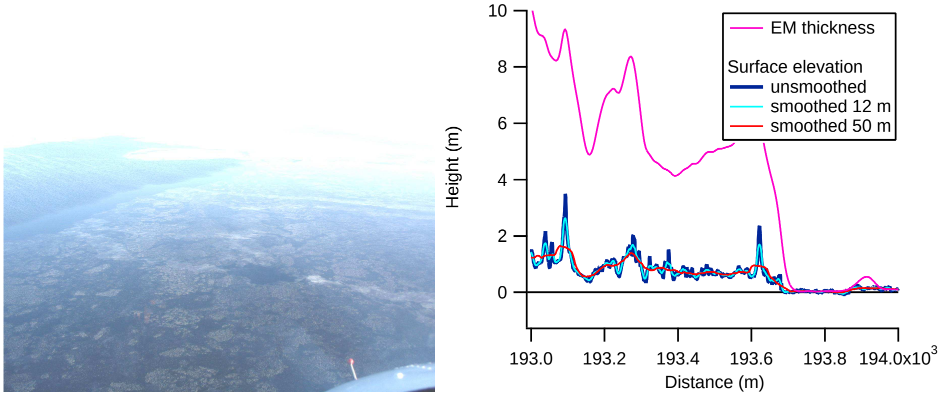

Figure 3.11: Very thin ice present on the profile section shown in Fig. 3.10 (left). Photograph was taken along-track.

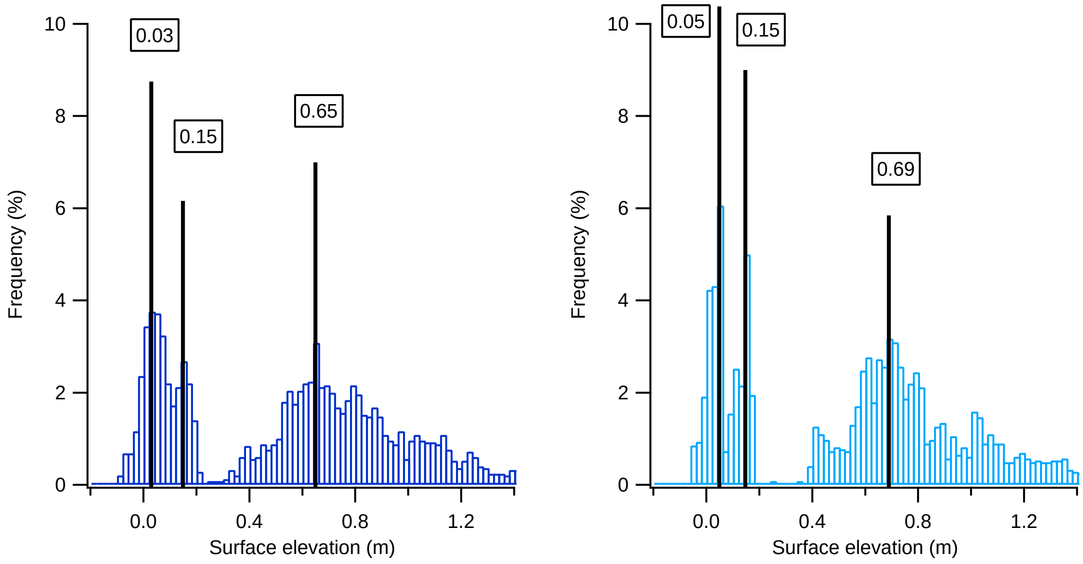

(a) unsmoothed

(b) smoothed over 12 m

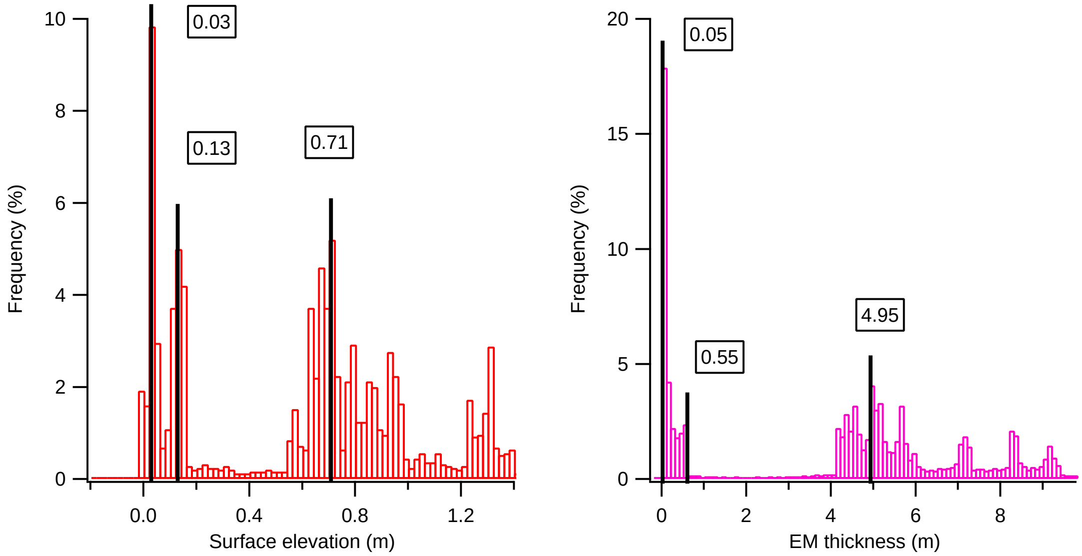

(c) smoothed over 50 m

(d)

Figure 3.12: Histograms of surface elevation raw (a) and smoothed (b, c) and histogram of total thickness.

3.5.3.2 Effect of Waves

The overall quality of the lowest level procedure, and hence the derived surface elevation is very much dependent on the presence of open water or very thin ice. The example in Fig. 3.8 (b) has shown that it is quite simple to detect small leads if they are present. However, if very large open water spots are present like the open polynya, roughly 4.4 km across (see Fig. 3.2, right), which is visible in Fig. 3.8 (c), and enlarged in Fig. 3.13 (a), then more than one "lowest value" needs to be marked. Marking lowest values at either end assures a "horizontal polynya" in the derived surface elevation. Besides, these were not the absolute minimum values that were marked but rather the mean values of this section. This was necessary to account for the increasing wave height from left to right. This is also seen in the wide, blurred mode in the histogram in Fig. 3.13 (b). Ideally, the peak of a sharp mode should be exactly at 0 m surface elevation and the histogram should have steep edges on either side representing very little noise (see Fig. 3.10, right). Here, the peak of the mode is close to 0 m surface elevation but the distribution gets quite wide at the bottom, reaching up to ±0.4 m. The reason for the increasing surface elevation, or more precisely wave height, was a strong southern wind with increasing fetch, while flying north. Even the smoothing over 12 m (c) led only to a slight reduction of this effect. The effects of the wavy polynya within the entire profile are seen in Fig. 3.14.

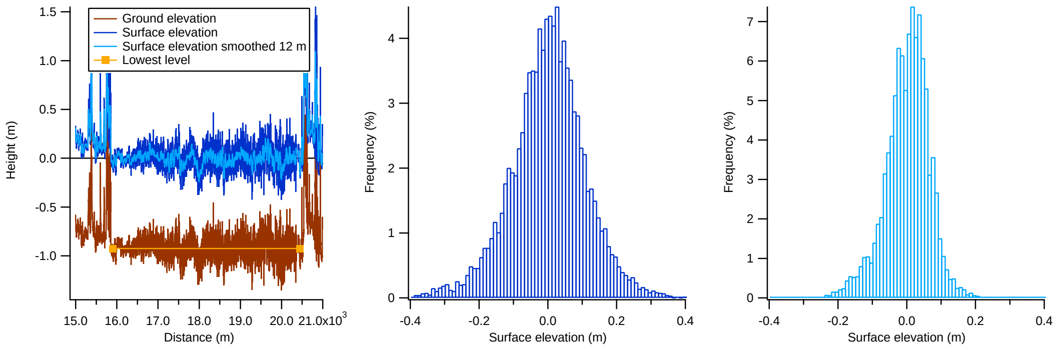

(a) (b) (c)

Figure 3.13: Ground elevation with the lowest level and the derived surface elevation for an open polynya strongly affected by wind (a). Additionally, the surface elevation smoothed over 12 m is displayed. Histograms of the unsmoothed (b) and smoothed surface elevation (c). Characteristic is the wide mode with its peak close to 0 m.

In the raw surface elevation histogram (a) a mode close to 0 m is scarcely visible. The histograms of the smoothed surface elevation (a and b), however, show a mode at 0.05 m that represents open water but is still influenced by the wavy surface of the very large polynya. Even, if the polynya is excluded (c), a clear mode is still not very sharp due to the lack of clear open water patches or very thin ice over the entire profile. The few adequate, thin refrozen leads are not distinct in a way that they could have been distinguished from the highly variable ground elevation. Ground elevation is especially variable if the profile contains a main fraction of first-year ice (see Section 4.1.1). A polynya of this size is a local event which was quite large in May 2005. Generally, it does not deleteriously influence the method of deriving surface elevation.

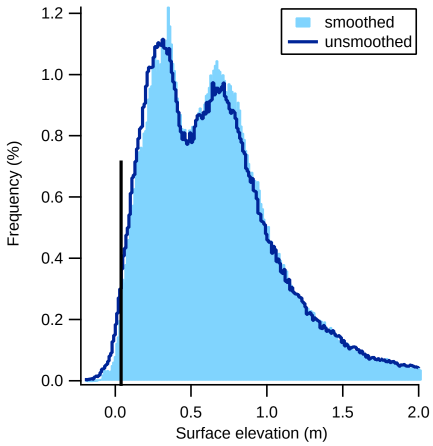

(a)

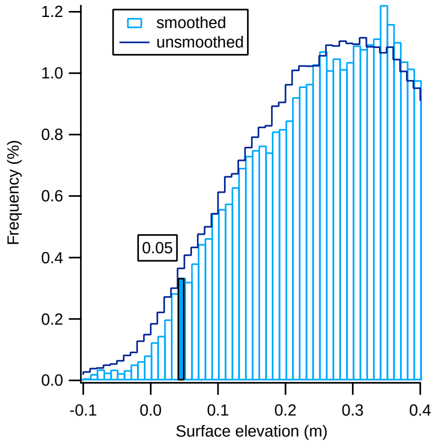

(b) graph (a) enlarged

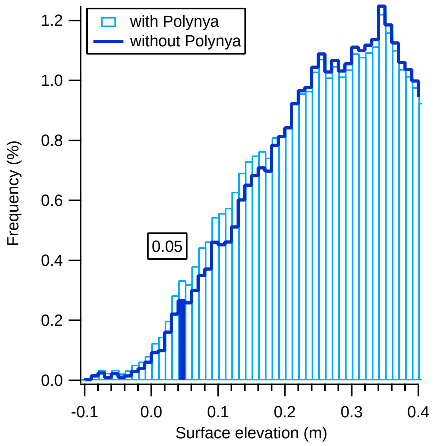

(c)

Figure 3.14: Histograms of the unsmoothed and smoothed (over 12 m) surface elevation for the entire profile (a), zoomed-in (b), and histogram of the smoothed surface elevation (over 12 m) together with the equivalent surface elevation without the polynya (c).

3.5.3.3 No Water or very thin Ice

Another critical factor for detecting the lowest level is the absence of open water spots or very thin ice. Fig. 3.15 shows an example for such a profile ('Dec. 15, leg3 west') in the Weddell Sea (see Section 4.2). In this case, the lowest values were estimated below ground elevation. More precisely, the lowest level curve was created in a way that the resulting surface elevation was approximately 1/4 of the EM thickness. The value of 1/4 was chosen to account for an average relationship between total thickness and surface elevation observed in that area. The markers for the lowest level curve were set approximately every 6 to 30 km to account for the slight inclined ground elevation mentioned in Section 3.2. This was only possible with the known EM thickness. The section in ground elevation between the distance of approximately 24000 m and 30000 m in Fig. 3.15 allowed to tie the hypothetical lowest level to the lowest values of ground elevation. Even if these lowest values did not clearly represent open water leads, they amounted at least to the same height from which the level of open water was inferred. The result of surface elevation is shown in Fig. 4.15 (e).

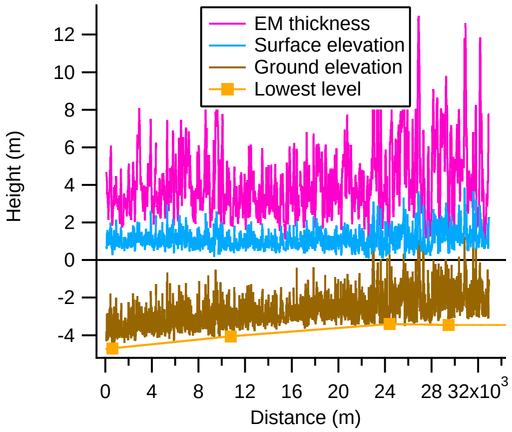

Figure 3.15: Ground elevation without open water sites for the profile 'Dec. 15, leg3 west' in the Weddell Sea.

3.5.3.4 Distribution of open Water or very thin Ice

Fig. 3.16 shows EM thickness, ground elevation, lowest level, and surface elevation for the flight on May 14, 2005 (left) and May 11, 2006 (right). In 2005, a few refrozen leads are present which are almost evenly spaced (recognizable at spots of about 0 m EM thickness). In 2006, hardly any open water spots or refrozen leads are visible, especially in the second half of the profile. For the first half, however, clear open water spots are present (between -59.7° W and -60.0° W). The distribution of open water spots or refrozen leads influences the designation of the lowest level. The surface elevation and EM thickness distributions for the profiles on May 14, 2005 and May 11, 2006 (see Fig. 3.16) are shown in Fig. 3.17. Although in 2005 only a few open water spots were present, the resulting surface elevation (a) for the profile matches the EM thickness (b) distribution quite well. In 2006, the surface elevation histogram looks different from the EM thickness histogram. Considering again the profile in Fig. 3.16 (right), one sees that the lowest level was designated in a strict fashion, meaning that each dip was selected in ground elevation which was shaped similarly to a thicker refrozen lead. Choosing the lowest level again, but this time "more generously", led to the profile and distribution of surface elevation in Fig. 3.18. More generously means that the lowest level was kept constant for the second half of the profile. Obviously, the histogram in Fig. 3.18 matches the EM thickness histogram in Fig. 3.17 (d) better in terms of three prominent modes. This underlines the need for consistently spaced open water patches or thin refrozen leads. In other words, at least one of those spots should be present for each section between the descending and ascending trajectories of the helicopter (see Section 2.3.6). If the sections contain none of those prominent spots at all, then it is better to keep the lowest level constant to the last chosen lowest value. The case in which the entire profile does not include any open water spots or very thin ice, was addressed in Section 3.5.3.3.

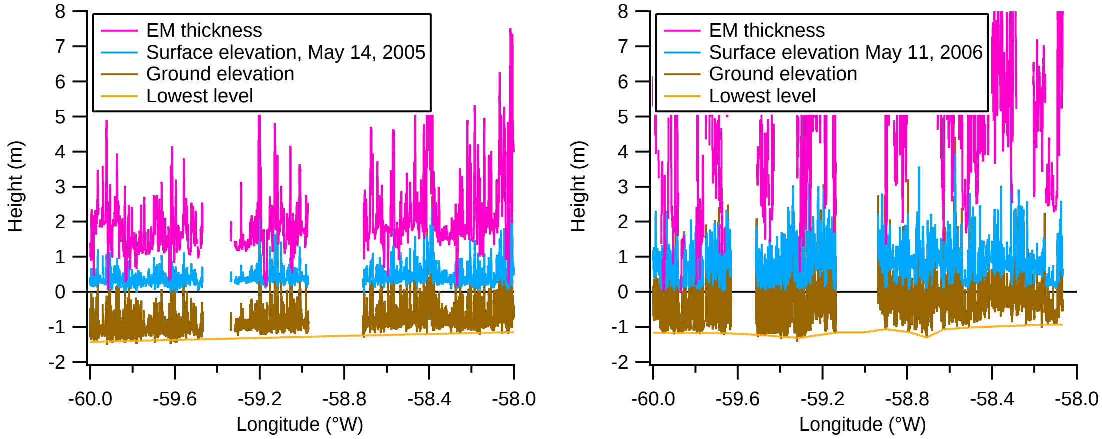

Figure 3.16: EM thickness and lowest level for profile on May 14, 2005 (left), and May 11, 2006 (right).

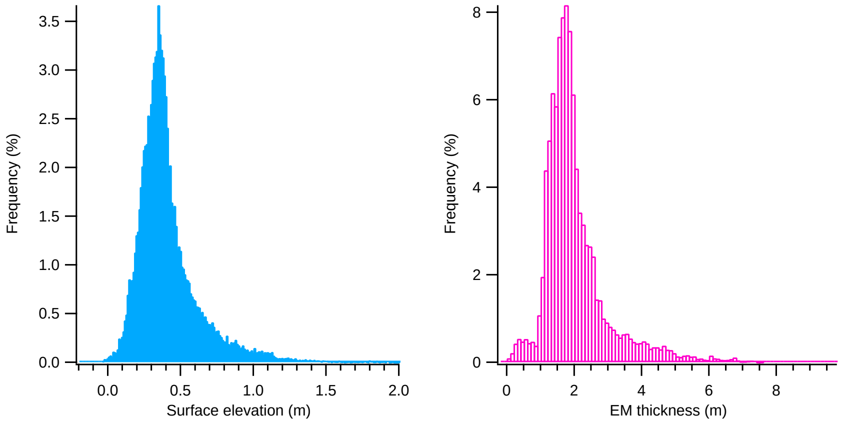

(a) May 14, 2005 (b) May 14, 2005

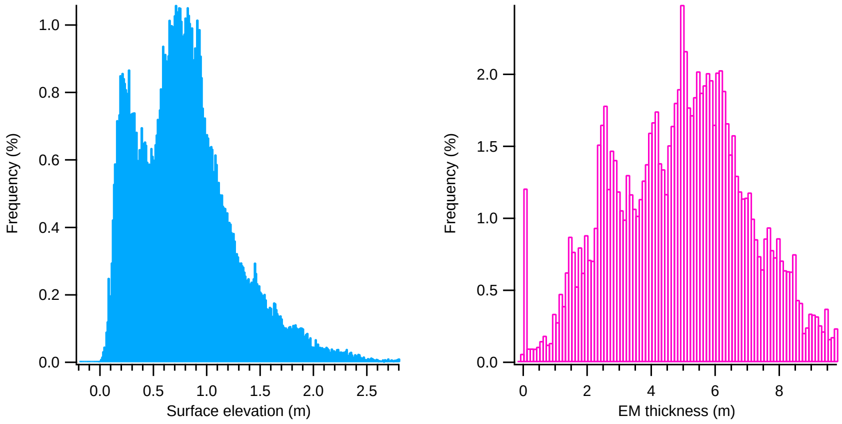

(c) May 11, 2006 (d) May 11, 2006

Figure 3.17: Histograms of surface elevation and EM thickness for profile on May 14, 2005 (a, b), and May 11, 2006 (c, d).

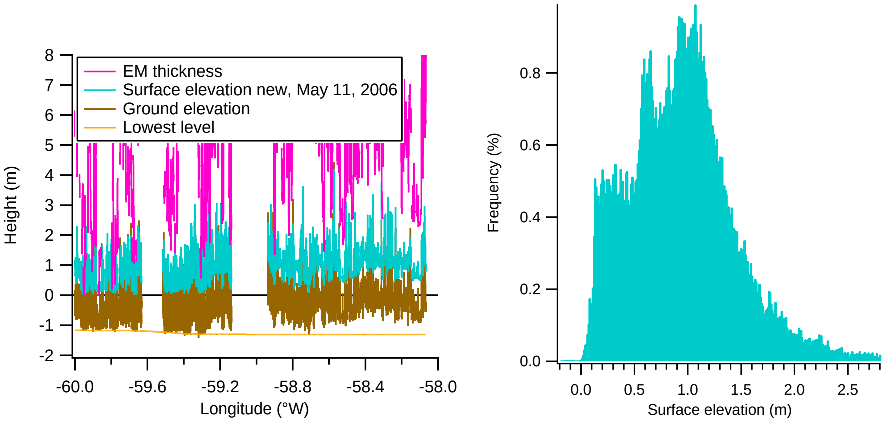

Figure 3.18: Surface elevation profile and histogram for profile on May 11 in 2006 with a more generous picked lowest level than in Fig. 3.16 (right).

3.5.4 Local Sea Level versus Geoid (DSST)

As mentioned in Section 3.5, the local sea level deviates from the geoid model by the dynamic sea surface topography (DSST) including tides. In general, continuous measurements of DSST increase the understanding of ocean circulation and seasonal changes and how the global ocean circulation changes through time. Monitoring the variation of global mean sea level and its relation to global climate change is another important aspect. Further, measurements of DSST improve the knowledge of ocean tides and hence contribute to an improved geoid model. Usually, DSST is derived from ship-going measurements of temperature and salinity at depth. In recent years, satellite altimetry systems have made it possible to measure sea surface topography directly (MARSH et al., 1990).

In the following, another approach of estimating DSST as a consequence of deriving surface elevation is introduced. With the software geoip (TSCHERNING et al., 1992) the GPS height above WGS 84 was reduced to the geoid to derive ground elevation as the difference between GPS height above the geoid and laser height (see Section 3.2). In this case the geoidal undulation N' (see Fig. 3.7) was subtracted from the ellipsoidal height above WGS 84 (Z). Here, the geoidal undulation, and the geoid respectively, is used as reference to show the deviation of the local sea level. With the knowledge of the local sea level ("lowest level" in Section 3.5.1), DSST can be estimated from the difference between the local sea level and the geoid. Since the lowest level is the height of the local sea level above the geoid, but the geoid is referenced to WGS 84 by the geoidal undulation (N'), the local sea level was derived by adding the geoidal undulation to the lowest level (see Fig. 3.7).

The two flight tracks on May 11, 2005 and May 14, 2005 partially overlapped, which is seen in the left graph of Fig. 3.19. The right graph in Fig. 3.19 shows the geoid (top curves) for the two flight tracks over the Lincoln Sea (May 11, 2005, left and May 14, 2005, right). For both flights, the northern turning point is clearly seen as a peak in the geoid indicating symmetry[3]. The local sea level is also shown for both flights (bottom curves). Again, the turning point is clearly seen as a peak confirming symmetry. The difference between the local sea level and the geoid (DSST) averages 0.40 m with a standard deviation of 0.07 m for the overlapping section marked by a rectangle. The zero point of the x-axis refers to the starting point of the flight May 14, 2005. Since the profile on May 11 was flown clockwise, whereas on May 14 it was flown counterclockwise, the data on May 11 are shown in reverse order (Fig. 3.19, right) to analyze the overlapping section of the two profiles in the same direction. Fig. 3.20 shows the same as the right graph in Fig. 3.19, except that the height above WGS 84 is plotted versus geographical longitude. The graph also includes the data from May 11, 2006. The geoid curves, of course, look similar for the three days apart from negligible differences in the flown tracks. The curves of the local sea level for all three days have nearly the same shape as the equivalent geoid models. Obviously, the local sea level from May 11, 2006 matches the local sea level on May 14, 2005 better than that on May 11, 2005. The storm event, however, was on May 14, 2005 while May 11, 2006 was calm, indicating that the discrepancy must be a result of different tides and air pressure.

---

[3] The symmetry is also seen in Fig. 3.8 (c). The absolute lowest marked value matches the peak of the geoid near the vertical bar in the right graph of Fig. 3.19.

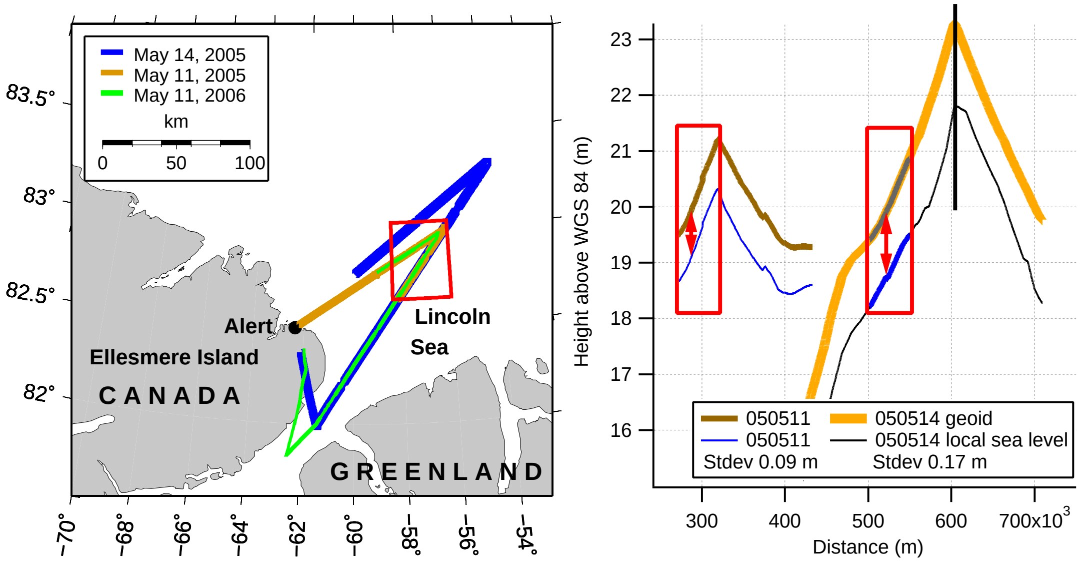

Figure 3.19: Deviation of local sea level from geoid by DSST marked with arrows (right) between equivalent flight tracks (left) and one partially overlapping profile section marked by a rectangle.

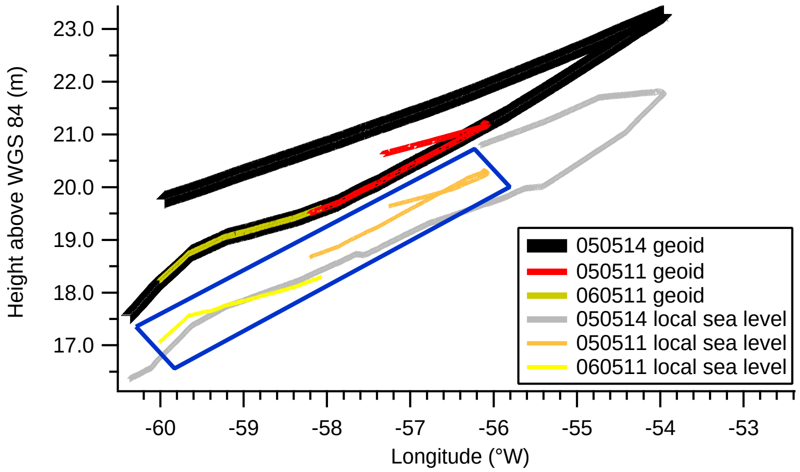

Figure 3.20: Difference of local sea level and geoid on May 11, May 14 in 2005, and May 11 in 2006. Data at the beginning of the profile on May 11, 2005 (left leg in Fig. 3.19, left) were deleted for better visibility of the overlapping section, marked by a rectangle (geoid curves coincide).

3.5.5 Dependency of lowest Level on the used Geoid

In the following, the dependency of the lowest level on the used geoid was tested. In Fig. 3.21, ground elevation derived with a different geoid is shown together with the derived surface elevation on May 11, in 2006 (left). Additionally, the histogram for surface elevation is displayed (right). A different geoid means that, inadvertently, 60° E was used to derive the GPS height above the geoid instead of −60° W. However, the surface elevation distribution looks very similar to the one in Fig. 3.17 (c), where the lowest level was chosen with a strict mindset. Here, the surface elevation was not selected in quite the same disciplined manner as was in Fig. 3.18 (right), causing slight differences in the histogram in Fig. 3.17 (c). Still, apart from slight differences, it is obvious that picking the lowest level, and thus deriving surface elevation is independent from the chosen geoid[4] as long as the resolution is similar. This was quite clear earlier, because picking the lowest level, and thus deriving surface elevation, is a relative and not an absolute method. The only major visible difference is the different offset of ground elevation. Comparing the ground elevation with Fig. 3.18 (left), small differences are visible, but these did not influence the selection of lowest values.

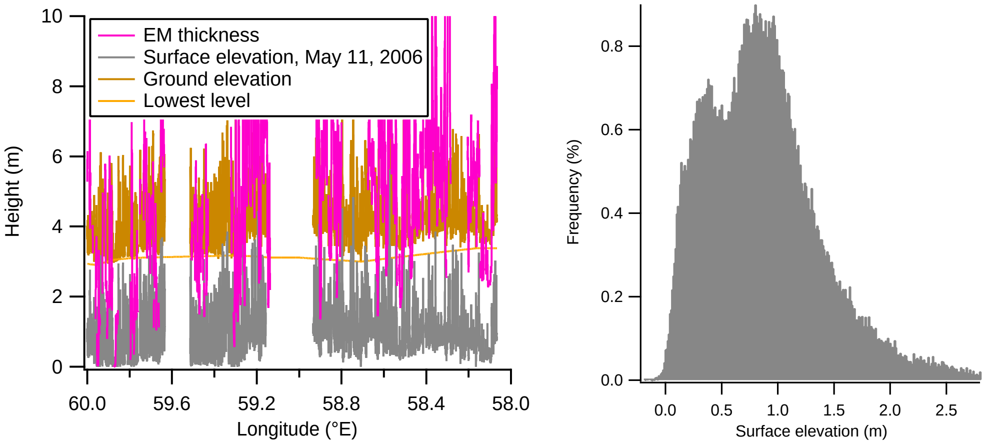

Figure 3.21: Surface elevation profile (left) and histogram for the profile on May 11, 2006 with the mistaken geoid.

---

[4] HVIDEGAARD & FORSBERG (2002) estimated the effect of using a geoid model in the Arctic Ocean as 0.04 m.

3.6 Transformation of Surface Elevation to Total Thickness

In Section 2.2.2, the relationship between surface elevation and total thickness was expressed by R. The R-value was introduced as a function of snow properties and density variations of sea ice and was derived from EM thickness and surface elevation (see Eq. 2.2.4). Thus, the equation of hydrostatic equilibrium in its typical form was neglected to circumvent the problem of the unknown snow depth. However, R is still dependent on the snow depth. Two approaches are possible for deriving R and are presented in the following.

3.6.1 Transformation with Histogram Modes

In the following, the modes of the probability distribution of the EM thickness and surface elevation were used to calculate R. For this purpose, the profile in the Lincoln Sea on May 14, 2006 (see Fig. 3.2, left) was considered. The numbers in Fig. 3.22 refer to the modes (in meters) of the EM thickness and surface elevation distribution, respectively. As mentioned in Section 2.1.5, the three modes represent open water, first-year, and multi-year ice. Table 4.1 and Table 4.3 summarize these values of the modes for the profiles in the Arctic and Antarctic (see

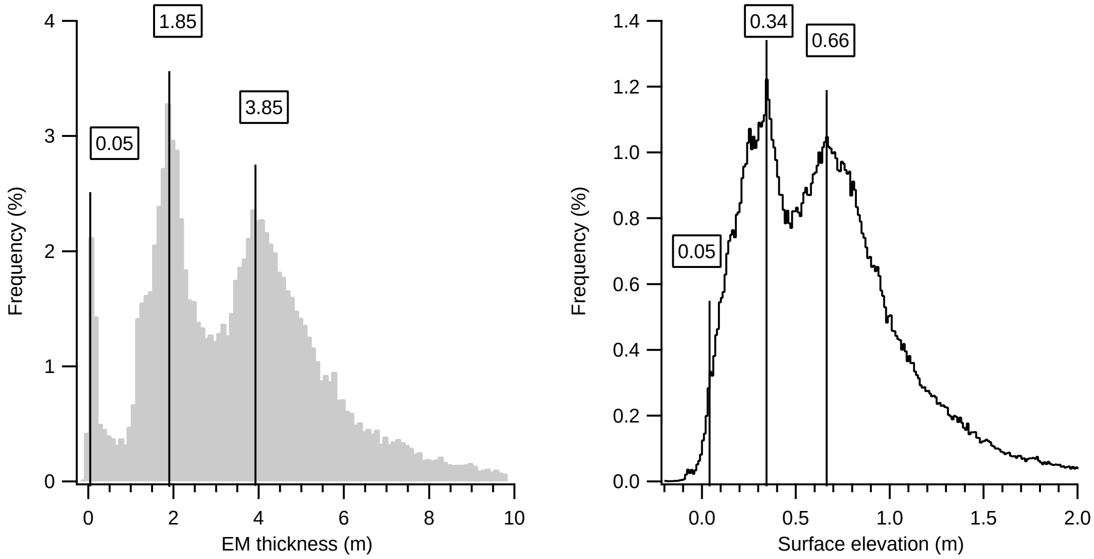

Figure 3.22: Histograms of EM thickness (left) and surface elevation (right) for the profile in the Lincoln Sea on May 14, 2005. Vertical lines with numbers mark the modes in meters.

Table 3.1: Modal values of EM thickness and surface elevation (selev) from histograms in Fig. 3.22.

Profile	**Surface elevation (m)**	**EM thickness (m)**	$R = \frac{EM\ thickness}{selev}$
Lincoln Sea	0.05	0.05	1.0
	0.34	1.85	5.44
	0.66	3.85	5.83

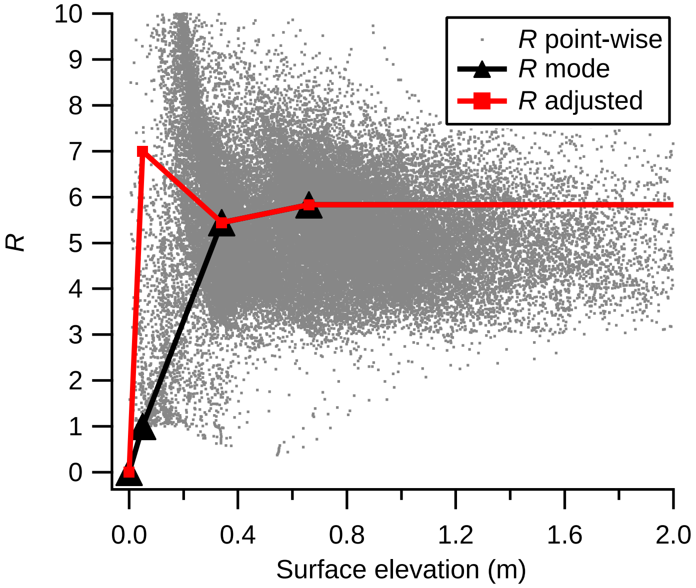

Figure 3.23: *R* versus surface elevation from the modes (triangles) and adjusted (squares). Dots show the result for the point-wise derived *R*-values for the entire profile.

Section 4.1.1 and Section 4.2.1). The equivalent *R*-values for the modes were calculated with Eq. (2.2.4). As an example, in Table 3.1 the values of the modes are displayed for the EM thickness and surface elevation from the histograms in Fig. 3.22. The derived *R*-values for the modes are also presented and used for interpolating the intermediate *R*-values. This is shown in Fig. 3.23. The triangles mark the *R*-values for the modes that are displayed in Table 3.1. The straight line connecting the triangles indicates linear interpolation. (In Fig. 3.25 the effect of a spline interpolation is shown for *R* and the resulting histogram.) With Eq. (2.2.3) and the equivalent interpolated *R*, total thickness was derived from each data point of the given surface elevation. Surface elevations of 0 m were transformed with an *R* of zero[5] and surface elevations greater than 5 m were transformed with the same *R* used for the multi-year ice mode, assuming a constant relationship between EM thickness and surface elevation for very large surface elevations. The value of 5 m was chosen under the assumption that the full range of possible surface elevations is covered. The histogram of the total thickness that resulted from transforming surface elevation (derived from the difference between the GPS height and laser height) is shown in Fig. 3.24 (a) and labeled 'GPS - laser'. Comparing the histogram for the derived total thickness with the EM thickness histogram, labeled 'EM bird', it is obvious that the modes coincide within one bin width of 0.1 m. Also, the shapes for the multi-year ice modes are similar. However, the shapes of the zero mode and first-year ice mode are different.

Another representation of *R* versus surface elevation is possible if Eq. (2.2.4) is used for each point of the entire profile of EM thickness and surface elevation, as it is shown by dots in Fig. 3.23, rather than only for the modes. This point-wise transformation is the basis for the second approach described in Section 3.6.2. In this case, the surface elevation was resampled to match the point spacing of the EM thickness. The dots in Fig. 3.23 show a pattern of three areas with a higher

---

[5] Strictly speaking, *R* is not defined at 0 m surface elevation. However, the value of 0.0 m surface elevation has never been detected in the data and thus this *R* was considered to be adequate.

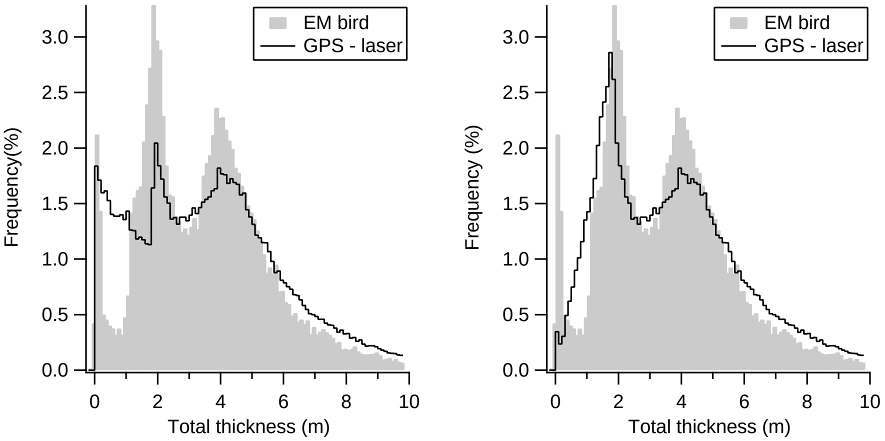

(a) *R* mode

(b) *R* mode adjusted

Figure 3.24: Histograms of total thickness ('GPS - laser') for the transformed surface elevation with the *R*-values being linearly interpolated (a) and additionally adjusted for the zero mode (b), and histograms of total thickness ('EM bird') for the measured EM thickness.

concentration and some single visible dots between. The three areas can be considered as the modes of a histogram, representing zero or very thin ice, first-year ice, and multi-year ice. Each of the triangles fall in one of these areas. However, the straight line of linearly interpolated *R*-values connecting the two triangles on the left leads to a histogram for total thickness (Fig. 3.24 a) which does not exactly match the EM thickness distribution. If *R* for open water or very thin ice was increased from 1.0 to 7.0, indicated by the squares in Fig. 3.23, and the given surface elevation was transformed again with newly interpolated *R*-values, the result is a histogram of the derived total thickness, seen in Fig. 3.24 (b). Obviously, this histogram for 'GPS - laser' matches the EM thickness histogram better than the histogram 'GPS - laser' in Fig. 3.24 (a). The reason for this is investigated in more detail in Section 3.6.2. The principle of adjusting *R* for the zero mode was applied to all profiles in the Arctic and Antarctic. Results for total thickness are shown in Section 4.1.2 and Section 4.2.2 respectively.

Instead of the linear interpolation, as mentioned above, it is possible to fit a smoothing spline through the given *R*-values for the modes. Fig. 3.25[6] (a) shows the result for *R* versus surface elevation for a smoothing spline with a weaker (0.5) and a stronger smoothing factor (1.0). The difference in the resulting total thickness is seen in the histogram (c). The differences in total thickness due to a different smoothing factor underlines the high sensitivity of *R* (and total thickness) and the difficulty of establishing the correct *R* for the individual surface elevation (see Section 2.2.2).

Fig. 3.25 (b) shows the effects of smoothing the surface elevation with different moving averages, introduced in Section 3.5.3.1. The result for total thickness is seen in the histogram (d). The similarity and its interpretation of the total thickness from the 'GPS - laser' (d) to the EM thickness (d) was mentioned in Section 3.5.3.1. Although for the chosen profile the histograms of total thickness

---

[6] Here, a different profile was used than for the histograms in Fig. 3.22 and Fig. 3.24, because adjusting the *R*-values for the modes improved already the total thickness distribution in Fig. 3.24 (b) sufficiently.

where R was derived with a smoothing spline, agree better to the EM thickness distribution (c) than the histograms of total thickness for which R was linearly interpolated (d) and smoothed, the latter was used for all profiles in Chapter 4 since total thickness could be derived adequately with linear interpolation for the majority of the profiles.

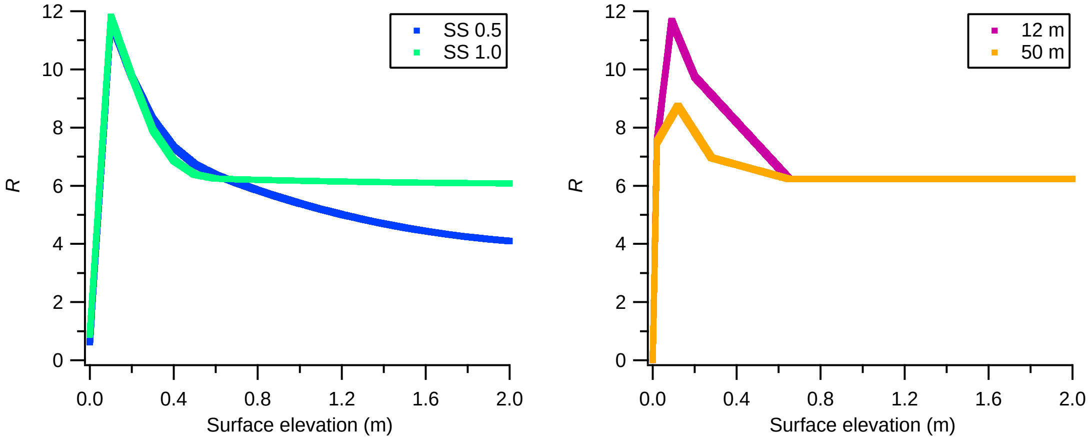

(a) smoothing spline

(b) linear

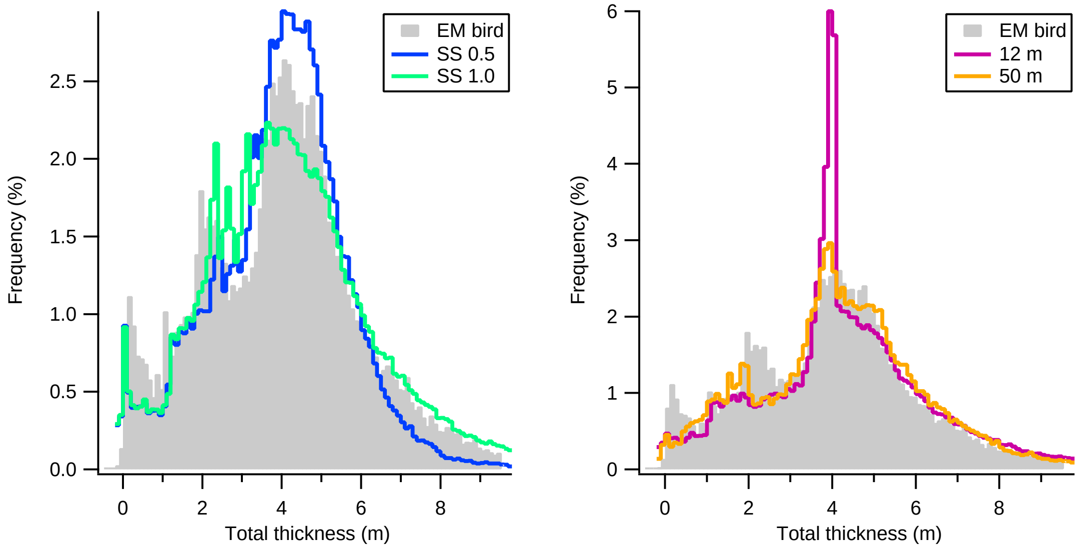

(c) smoothing spline

(d) linear

Figure 3.25: R-values interpolated with a smoothing spline versus smoothed surface elevation (a), R-values interpolated linearly versus surface elevation smoothed over 12 m, and 50 m (b), and histograms (c) and (d) for (a) and (b) for the profile in the Lincoln Sea on May 11, 2005.

3.6.2 Transformation with point-wise Fitting Functions

3.6.2.1 Arctic

Up to now, surface elevation can only be transformed to total thickness if the EM thickness is available[7]. If the EM thickness is not available, a different approach is necessary for deriving total thickness. An application for estimating sea ice thickness from surface elevation without coincident thickness measurements in the Arctic is shown for some flights of the NOGRAM campaign in Section 4.5.

This approach, here, allows to find transformation functions based on the given EM thickness for one profile in the Arctic, but which, in the following was applicable to all other profiles in that region, assuming that the EM thickness was not available. The profile for which the transformation functions were built, was the same as the one used in Fig. 3.22. Fig. 3.26 displays R-values resulting from Eq. (2.2.4) for each single measurement of EM thickness and surface elevation. The difference to the approach described in the previous section is that the complete profile was used point-wise and not only the modes. First, the surface elevation was resampled to match the measurement point spacing of the EM thickness. In Fig. 3.26 (left) the same dotted pattern is shown as in Fig. 3.23. Again, three areas of a higher concentration of dots are visible (more easily seen in Fig. 3.23). The three areas can be considered as the modes in a histogram of surface elevation and EM thickness, respectively. Considering the EM thickness histogram for this example (Fig. 3.22, left), three modes are visible, representing open water or very thin ice, first-year ice, and multi-year ice. Obviously, the number of the areas, or thickness classes, is dependent on the number of thickness modes. To classify the resampled surface elevation data and EM thickness data, i. e. to assign them to one of the three thickness classes, thresholds for the three thickness modes derived from the EM thickness histogram were used (see Table 3.2). The three thickness classes are shown in Fig. 3.26 (right) as differently marked areas. In a further step, three fitting functions were built in order to approximate the

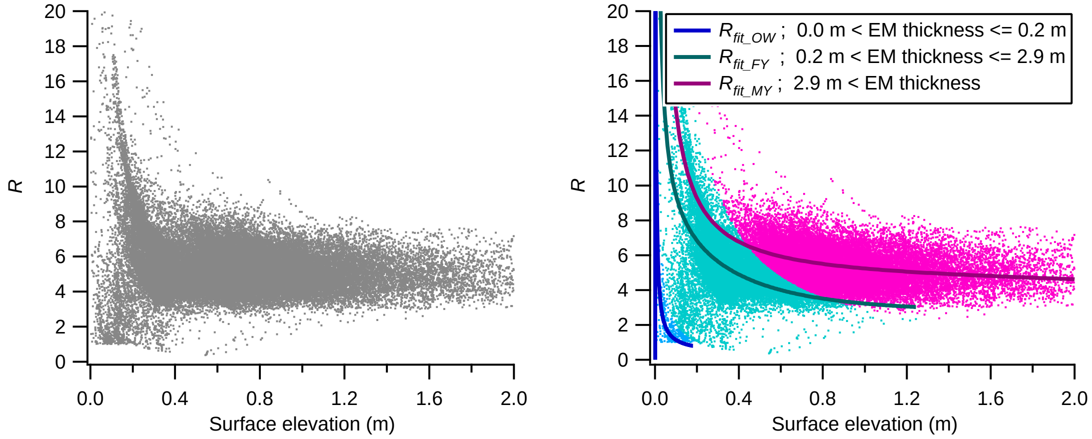

Figure 3.26: R versus resampled surface elevation. R-values result from the quotient of EM thickness and surface elevation, Eq. (2.2.4). The graph on the right shows additionally the fitting functions for three differently marked thickness classes of open water (OW), first-year ice (FY), and multi-year ice (MY).

---

[7] The possibility of using a certain R-value and assuming specific densities of snow, sea ice, and sea water and the snow depth was addressed in Section 2.2.2.

individual classes. From Eq. (2.2.5) it was concluded that it must be a function similar to $1/x$. Intensive testing, however, led to a function which is a linear combination of $1/x$ and an exponential function. The resulting three fitting functions are shown in Fig. 3.26 (right) as curves approximating the three marked thickness classes of open water (OW), first-year ice (FY), and multi-year ice (MY). The equations of the fitting functions for Fig. 3.26 (right) with the coefficients $a_0 - a_4$ and surface elevation ($selev$) are as follows:

$$R_{fit\_OW} = -a_0 + a_1 \frac{1}{a_2\, selev}, \tag{3.6.1}$$

$$R_{fit\_FY} = a_0 + \frac{1}{a_1\, selev} + a_2 \exp(-a_3\, selev + a_4), \tag{3.6.2}$$

$$R_{fit\_MY} = a_0 + \frac{1}{selev} + a_1 \exp(-a_2\, selev + a_3). \tag{3.6.3}$$

To transform surface elevation data and to assign them to the correct thickness class and thus the correct fitting function, the surface elevation was divided into sections of 40 m for which the standard deviation and mean value was calculated respectively. To indicate the individual sections, the fid number of the first surface elevation data entry of each 40 m section was used and assigned to the standard deviation (stdev) and mean of that section. The resulting standard deviations, mean values, and fid numbers of each 40 m section were written to a new file. To match the file length of the EM thickness data, the new file was interpolated yielding the intermediate standard deviations and mean values. The next step was to find thresholds of stdev and mean according to the chosen thresholds of EM thickness. Therefore, the interpolated stdev and mean were classified with the same procedure as the EM thickness and resampled surface elevation were classified before. From this classification thresholds of stdev and mean were derived. These thresholds are shown in Fig. 3.27 (left) as differently sized rectangles where one rectangle, labeled 'not classified' represents stdev and mean which did not match the characteristics of one of the three other rectangles. The thresholds refer to surface elevation. In Table 3.2 the thresholds for EM thickness and surface elevation, represented by standard deviation (stdev) and mean according to the thickness classes are summarized as numbers. To show how the surface elevation data represented by stdev and mean of 40 m long sections, split into the areas of the defined thresholds of stdev and mean (rectangles), these values are plotted in Fig. 3.27 (left) with differently marked dots according to the three thickness classes. A good agreement is visible between the areas of defined standard deviation and mean surface elevation (rectangles) and the three thickness

Table 3.2: Thresholds of EM thickness, standard deviation (stdev) and mean of surface elevation (rectangles in Fig. 3.27) for open water, first-year ice, and multi-year ice in the Arctic.

Ice class	**EM thickness (m)**	**Surface elevation Stdev (m)**	**Surface elevation Mean (m)**
Open water	$0.0 < \quad \leq 0.1$	≤ 0.08	< 0.1
First-year ice	$0.1 < \quad \leq 2.9$	≤ 0.4	$0.1 \geq \quad \leq 0.6$
Multi-year ice	> 2.9	≤ 0.6	> 0.6

classes (dots), meaning that the applied thresholds of standard deviation and mean for the surface elevation data are appropriate and that they generally can be used to transform surface elevation to total thickness with the correct fitting functions. The right graph in Fig. 3.27 shows the ENVISAT SAR image with the profile for which the fitting functions were created. If the thresholds of standard deviation and mean were applied to the entire profile of surface elevation, with the equivalent fitting functions, a good agreement is seen between the classified total thickness and the sea ice thickness that can be derived from the SAR image as dark grey shades represent open water and first-year ice and light grey shades represent multi-year ice. Notably, the transition from first-year to multi-year ice is clearly visible. The grey-white area between Ellesmere Island and Greenland visualizes the very large open polynya shown in Fig. 3.2 (right). Although this is open water, it is marked as 'not classified' in the derived total thickness due to its characteristics of stdev and mean which are different from open water, usually seen in the profile. Here, the polynya showed turbulent water. Gaps in the profile are due to the ascends and descends of the helicopter for the EM bird drift correction causing data loss.

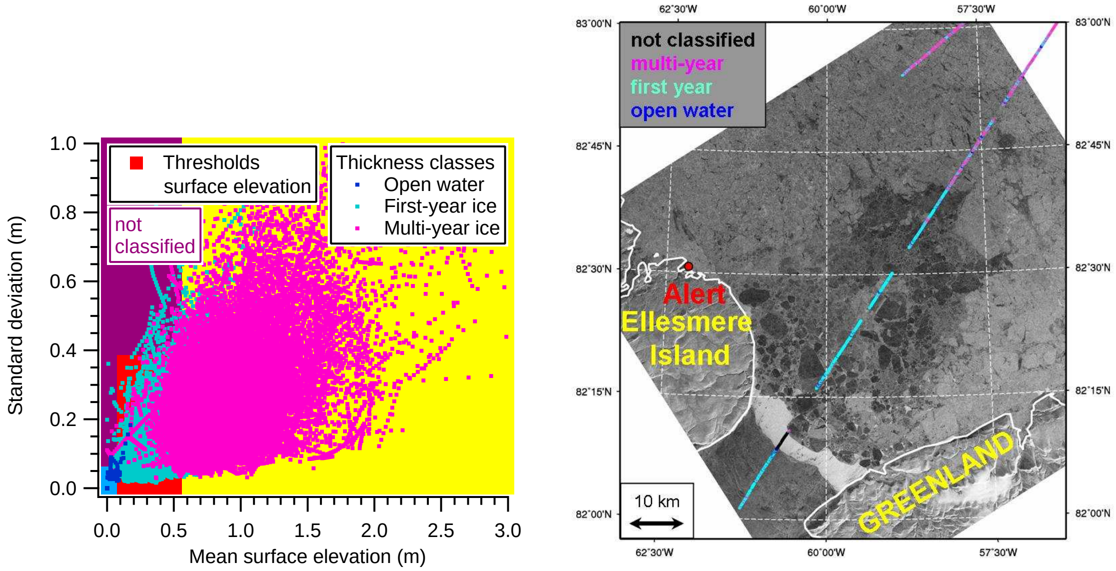

Figure 3.27: Thresholds of standard deviation and mean for surface elevation in the form of different sized rectangles, used to assign the surface elevation to the correct thickness class and thus the correct fitting function. Dots show standard deviation and mean of the three thickness classes, classified by thresholds of EM thickness (left). A good agreement is seen with the ENVISAT SAR image (right) if these thresholds were applied to the entire profile of surface elevation and the fitting functions were used to derive total thickness. The derived total thickness is shown color-coded for the entire profile plotted on the SAR image.

The fitting functions Eq. (3.6.1) – Eq. (3.6.3) were applied to all other flights in the Arctic, assuming that no EM thickness was available. The results are shown in Section 4.1.3. For the Antarctic, new fitting functions were necessary because of totally different ice thicknesses and snow depths. Fig. 3.28 shows the high variability of R (see Section 2.2.2) for a profile segment, that was arbitrarily chosen, in the Arctic (left) and Antarctic (right). No structure is visible except over leads, where the R-values decrease considerably. This underlines the difficulty of finding the correct R for surface elevation.

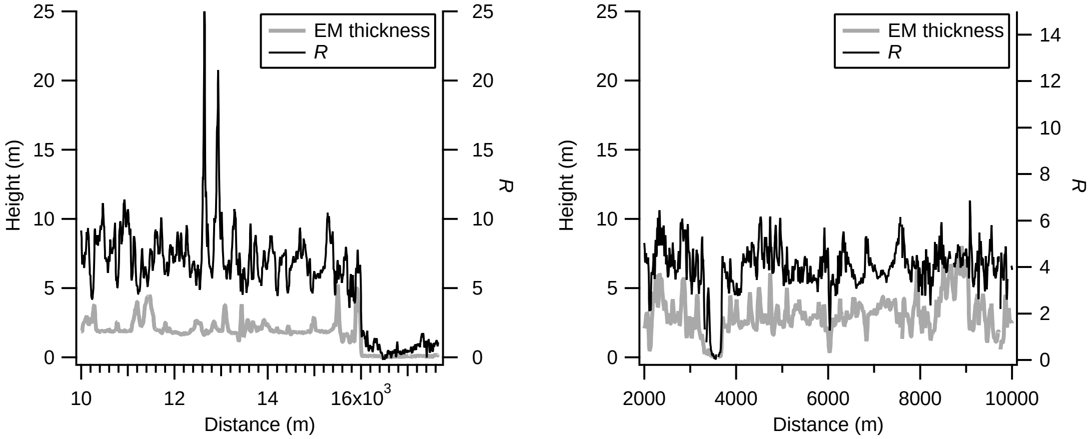

Figure 3.28: High variability of *R* for a profile section in the Arctic (left) and in the Antarctic (right). Only over leads the *R*-values decrease considerably.

3.6.2.2 Antarctic

As mentioned above, the fitting functions can be applied only in that region for which they were created. Furthermore, they work only for profiles similar to the one that was used to create the fitting functions. In the Weddell Sea with different snow and ice thicknesses, the fitting functions from the Arctic fail. However, it is possible to find another set of fitting functions for one profile of the Weddell Sea and then to apply these functions to other profiles with similar thickness distributions.

In the present study, three different sets of fitting functions were created for the Weddell Sea. This was necessary, because three different combinations of thickness modes were found in the histograms for surface elevation and EM thickness (see Fig. 4.14, Fig. 4.15, and Table 4.3 in Section 4.2.1). The three sets of the fitting functions with the coefficients $b_0 - b_5$ and surface elevation ($selev$) are the following:

Dec. 14, leg1 north:

$$\begin{aligned} R_{fit\_OW} &= -b_0 + b_1 \frac{1}{b_2\, selev}, \tag{3.6.4}\\ R_{fit\_MY} &= b_0 + \frac{1}{selev} + b_2 + b_3 \exp(-b_4\, selev - b_5), \tag{3.6.5}\\ & \tag{3.6.6} \end{aligned}$$

Dec. 14, leg4 north:

$$\begin{aligned} R_{fit\_FY} &= b_0 + \frac{b_1}{b_2\, selev} + b_3 \exp(-b_4\, selev + b_5), \tag{3.6.7}\\ R_{fit\_MY} &= b_0 + b_1 \frac{1}{selev} + b_2 \exp(-b_3\, selev + b_4), \tag{3.6.8}\\ & \tag{3.6.9} \end{aligned}$$

Dec. 14, leg1 south:

$$\begin{aligned} R_{fit\_OW} &= -b_0 + b_1 \frac{1}{b_2\, selev}, \tag{3.6.10}\\ R_{fit\_MY} &= b_0 + b_1 \frac{1}{selev} + b_2 \exp(-b_3\, selev + b_4). \tag{3.6.11} \end{aligned}$$

Even if Eq. (3.6.4) and Eq. (3.6.10) as well as Eq. (3.6.8) and Eq. (3.6.11) have the same appearance, the coefficients are different. The results of total thickness for the Antarctic are found in Section 4.2.3.

3.6.3 Error Approximation

Regarding the approach of deriving total thickness from the R-values of the histogram modes (see Section 3.6.1 and Section 4.1.2), the modes of the total thickness distribution coincided with the modes of the EM thickness distribution within ±0.1 m. Thus, the total thickness of level ice was accurately determined. The next step was to achieve a good agreement between the entire distributions, of total thickness and EM thickness, including deformed ice. Adjusting the R-value of the zero mode and the use of general fitting functions (see Section 3.6.2 and Section 4.1.3) were two adequate approaches. To estimate the quality of agreement between total thickness and EM thickness, the longest profile in the Lincoln Sea (May 14) was chosen as well as the longest one to the north of Ellesmere Island (May 13). In Table 3.3 mean values and standard deviations (stdev) of total thickness derived from R-values of the histogram modes labeled 'R modes' (see Table 3.1 and Table 4.1) and from the fitting functions labeled 'R fitting' (see Eq. (3.6.1) – Eq. (3.6.3)) are summarized. Additionally, the mean values and standard deviations of the EM thickness are shown and labeled 'EM bird'. Comparing the mean values, it can be seen that total thickness derived from the fitting functions matches the EM thickness slightly better. However, recalling the fact that pressure ridges are underestimated in the EM thickness, the correct mean total thickness should be larger than the given value for the EM thickness. Further, the footprint of the EM bird needs to be taken into account because this also affects the mean value and its standard deviation. Therefore, it is impossible to estimate the accuracy from comparing the mean values of total thickness. The comparison rather gives a rough estimate.

Table 3.3: Mean values and standard deviations (stdev) of total thickness derived from R-values of the histogram modes ('R modes') and from the fitting functions ('R fitting') and mean and stdev of EM thickness ('EM bird').

Profile	**Total thickness approach**	**Mean (m)**	**Stdev (m)**
Lincoln Sea (b)	R modes	3.93	2.62
(May 14)	R fitting	3.55	2.14
	EM bird	3.61	2.10
North (c)	R modes	4.97	2.62
(May 13)	R fitting	5.31	2.24
	EM bird	5.19	2.50

To approximate the error of total thickness for the profile in the Lincoln Sea on May 14, first, the error of R in dependence on surface elevation had to be determined. Here, the error of R was approximated for the histogram modes (EM_{mode} and $selev_{mode}$) for all profiles in the Arctic for open water (OW), first-year ice (FY), and multi-year ice (MY) with the Gaussian error propagation. Here, an error of 0.1 m was estimated for ΔEM_{mode} and 0.01 m for $\Delta selev_{mode}$:

$$\Delta R = \sqrt{\left(\frac{\partial R}{\partial EM_{mode}} \Delta EM_{mode}\right)^2 + \left(\frac{\partial R}{\partial selev_{mode}} \Delta selev_{mode}\right)^2}. \tag{3.6.12}$$

The resulting values are visualized in Fig. 3.29 (left). Subsequently, an exponential curve was fitted through the error approximations of R. The obtained exponential function, that is strictly monotonic decreasing, of the form

$$\Delta R_{selev} = y_0 + a\, exp^{-\frac{1}{\tau} selev}, \tag{3.6.13}$$

with the coefficients y_0, a, $-\frac{1}{\tau}$ was used to approximate the error of total thickness (t):

$$\Delta t = \Delta R_{selev}\, selev. \tag{3.6.14}$$

Fig. 3.29 (right) shows the derived total thickness error versus surface elevation from 0 m to 2 m for the profile in the Lincoln Sea (May 14). Clearly visible is a steep increase of the total thickness error Δt for very small surface elevations up to about 0.05 m before it decreases and finally increases linearly for surface elevations larger than about 0.2 m. The function of R in dependence on surface elevation is displayed in Fig. 3.30 (left) (see Fig. 3.23). It was obtained by interpolating the intermediate R-values between the given values at the modes which are marked by triangles and adjusting the R-value for the zero mode (squares) (see Fig. 3.23). Furthermore, the behavior of the plotted curve in Fig. 3.29 (right) is dependent on the chosen errors for the histogram modes of EM thickness and surface elevation. Generally, the graph confirms that the total thickness error is dependent on surface elevation and therefore it is impossible to specify only one error value that suits all surface elevations.

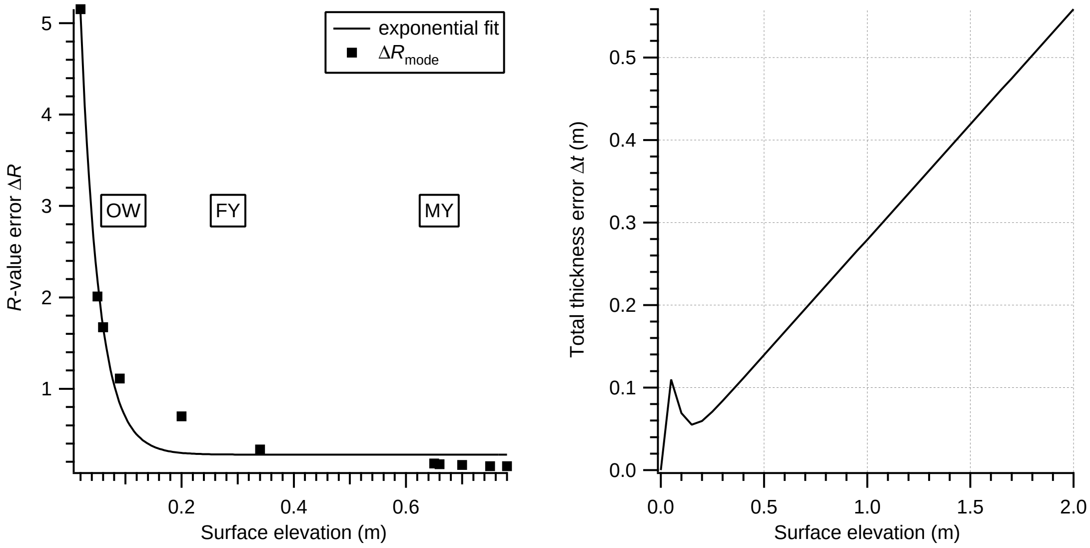

Figure 3.29: Error of R for the histogram modes in dependence on surface elevation (left) and error of total thickness in dependence on surface elevation (right).

In Fig. 3.30 (right) the relative thickness error $\Delta t_{rel} = \Delta t / t$ is shown in percent where t resulted from (2.2.3) with R being the function of the linearly interpolated R-values (see Fig. 3.30, left). Obviously, the percental error decreases rapidly for total thicknesses up to about 1 m. For total thicknesses larger than about 2 m the percental error slightly decreases before it stays constant. This behavior is an effect of the chosen relationship between R and surface elevation (see Fig. 3.30, left).

This error approximation confirmed a large uncertainty of R for small surface elevations as mentioned earlier yielding large uncertainties in the derived total thickness. The uncertainty increases and decreases before a linear increase is seen for surface elevations larger than 0.2 m.

A similar approximation of errors in R and total thickness is feasible with respect to the fitting functions. However, the main issue in terms of comparing total thickness with EM thickness was the agreement of the modal thicknesses as they represent the most frequent ice regimes to be found. Thus, this error investigation was considered to be sufficient and the focus was on the comparison of thickness distributions.

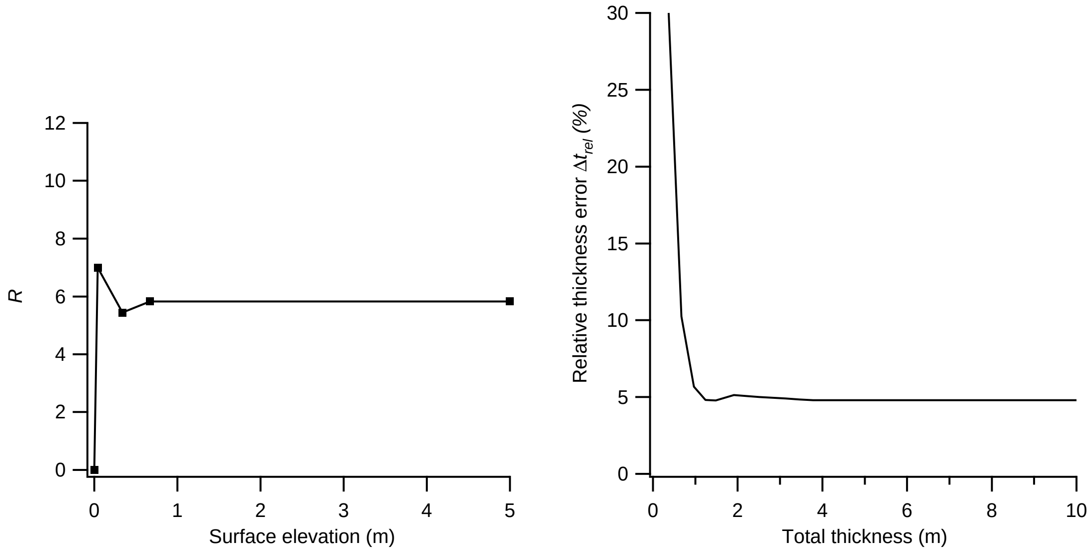

Figure 3.30: Function of *R* in dependence on surface elevation (left) and relative error of total thickness in dependence on surface elevation (right).

3.7 Calculation of Snow Depth

With the derived surface elevation and *R* from either the histogram modes of surface elevation and EM thickness or the point-wise fitting functions, snow depth can be directly calculated for each profile with Eq. (2.2.9). Here, the assumed densities for snow, sea water, and especially for sea ice play an important role as introduced in Section 2.2.2.2. Recalling, that snow depth is an important quantity in transforming surface elevation to total thickness, this section is an application for using the derived surface elevation in Section 3.5, as snow depth can also be derived from the difference between total thickness (or EM thickness) and surface elevation (see Eq. 2.2.10). The results for the calculated snow depth and a comparison with in-situ snow depth measurements are found in Section 4.6.

At the beginning of Section 2.2.2 it was stated that the hydrostatic relationship Eq. (2.2.1) needs to be solved for t to transform surface elevation to total thickness. But the snow depth was unknown and made it impossible to solve the equation directly. Possibilities of estimating snow depth as a constant, or even as a complete snow distribution, varying over the flown profile, have not been mentioned so far, since the results were not successful. However, with the introduced approach of the fitting functions to derive *R*, it is possible in a similar way, to fit the snow depth for the three classes of open water, first-year, and multi-year ice. The creation of the three classes is described in Section 3.6.2. In Fig. 3.31 snow depth was calculated for the same ice classes as shown in Fig. 3.26 (right). In contrast to Eq. (3.6.1) – Eq. (3.6.3), one fitting function with the coefficients $s_0 - s_3$ and surface elevation (selev) for the three ice classes of the form:

$$snow_{fit} = s_0 + s_1 \arctan(s_2\, selev + s_3) \tag{3.7.1}$$

was created to approximate the snow depth of the individual classes. According to Fig. 3.26 (right), the same thresholds for standard deviation and mean were used to assign the single surface elevation data to the correct class and thus to the correct fitting function for the individual snow cover. However, the fitting curve

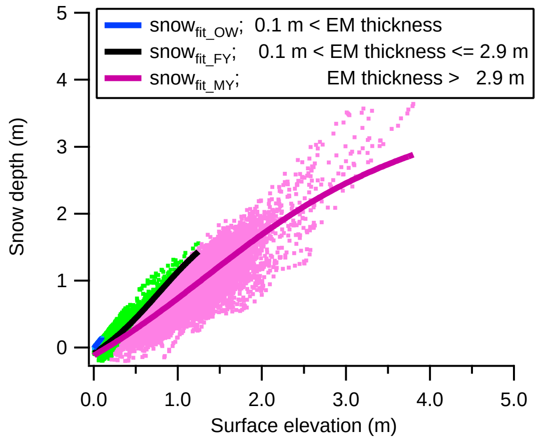

Figure 3.31: Snow depth versus surface elevation with fitting functions for snow depth.

of snow above multi-year ice in Fig. 3.31 does not perfectly fit snow depths for surface elevations greater than 2 m. On the other hand, only a few data points are affected by this section of a poor fit. Fig. 3.32 displays the calculated snow

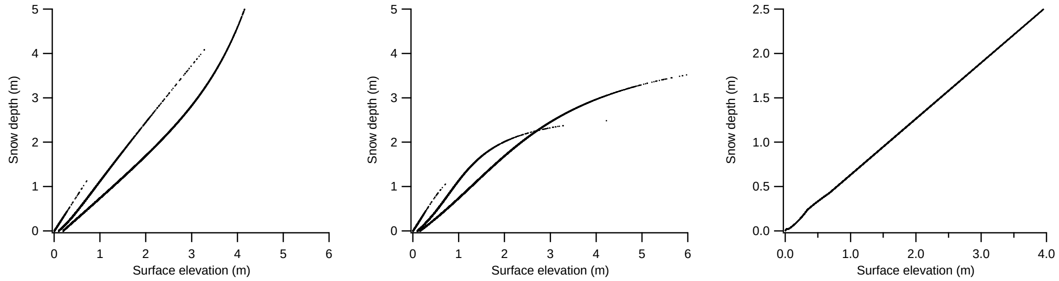

(a) (b) (c)

Figure 3.32: Snow depth derived with the snow fitting function (3.7.1) versus surface elevation (a), with R from the point-wise fitting function (Section 3.6.2) versus surface elevation (b), and with R from the histogram modes (Section 3.6.1) versus surface elevation (c).

depth versus surface elevation data of the entire profile. The graph in (a) shows snow depths derived using the snow-fitting function Eq. (3.7.1). The graph in (b) shows snow depths derived with Eq. (2.2.9) in which R results from the set of the point-wise fitting functions Eq. (3.6.1) – Eq. (3.6.3), and the graph in (c) shows snow depths derived with (2.2.9) with R taken from the histogram modes (see Section 3.6.1). Obviously, for surface elevations of less than one meter it makes very little difference if the snow depth is derived with the snow fitting function Eq. (3.7.1) (Fig. 3.32 a) or with Eq. (2.2.9) (Fig. 3.32 b). Regarding the graph in Fig. 3.32 (a), a stronger increase in snow depth is visible for surface elevations greater than 2 m which is due to the poor fit of snow depth in Fig. 3.31 as described above. The increase of snow depth in Fig. 3.32 (b) is due to the slightly decreasing, almost constant R for increasing surface elevations (see Fig. 3.26, right). Similarly, the straight line in Fig. 3.32 (c) is a result of the constant R for surface elevations greater than the highest modal value as seen in Fig. 3.30 (left). However, in Fig. 3.32 (c) an exponential increase in snow depth is seen for surface elevations below 0.5 m, before it increases linearly.

Generally, large snow depths of more than 2 m can be explained by the fact that pressure ridges are underestimated in the EM thickness measurement yielding lower R-values. As a consequence of the "lower measured" keel depth the difference to the actual "larger" keel depth must be compensated for to fulfill hydrostatic equilibrium as the surface elevation increases.

4 Results of Laser Altimetry

This chapter presents the results for surface elevation derived from helicopter-based laser altimeter measurements as well as the results of the transformed surface elevation, yielding total thickness. Additionally, the total thickness measured with the EM bird (EM thickness) is shown for comparison. The results are divided into sections for the Arctic and Antarctic.

The relevance for ICESat data is subsequently visualized. Besides, results are presented of the surface elevation measured coincidently with the laser scanner by the Danish National Space Center (DNSC) aboard the Twin Otter and the laser altimeter inside the EM bird. The laser scanner data were kindly made available by DNSC in Summer 2006.

Further, results of airplane laser altimetry are shown for which no simultaneously measured ice thickness was available. Instead, scatterometer data representing different ice regimes were used for comparison of different ice regimes. Moreover, the estimation of the dynamic sea surface topography (DSST) was covered and findings are presented.

The calculation of snow depth as a by-product of the results with the helicopter-borne measurements in the Arctic and Antarctic, was another topic within this study. The results are presented together with in-situ snow depth measurements.

4.1 Helicopter Measurements in the Arctic

Essentially, the results comprise the probability distributions of surface elevation and derived total thickness (see Section 3.5 and Section 3.6). The reason for negative values in these distributions was described in Section 3.5.3.1. Shown in this context, are the R-values which resulted from the comparison of the modes between the histograms of surface elevation and EM thickness. Mean R-values were derived for each profile resulting in a number that is within one standard deviation similar to the R derived from the model given in WADHAMS et al. (1992) (see Eq. (2.2.8) in Section 2.2.2).

Further, the surface elevation profiles were divided into three groups: open water, first-year ice, and multi-year ice. Accordingly, the previously derived R-values were assigned to these groups and a mean R was calculated for each group. The mean R-values were used subsequently to calculate the total thickness as an alternative approach. The results are illustrated in Section 4.1.2.1. For future surface elevation profiles without coincidently measured total thickness, these R-values can be applied to obtain total thickness. Additionally, the total thickness is shown for $R = 5.889$ that was derived from the model by WADHAMS et al. (1992) (see Section 2.2.2).

Another approach of transforming surface elevation is the transfer between the probability distributions of surface elevation and EM thickness. Here, the number of input values that fall within each of a number of value ranges (or "bins") is considered, rather than the single data points of the profile. First, the bins of surface elevation were multiplied with the R-values derived from the modes of surface elevation and EM thickness with the intermediate R being interpolated (see Section 4.1.2). Hereafter, the previously mentioned mean R was applied. The results are displayed in Section 4.1.2.2.

Fig. 4.1 shows the flights performed north of Ellesmere Island and in the Lincoln Sea in May 2005 and May, 2006 with the longest leg flown coincidently with the Twin Otter on May 13 and May 14, 2005.

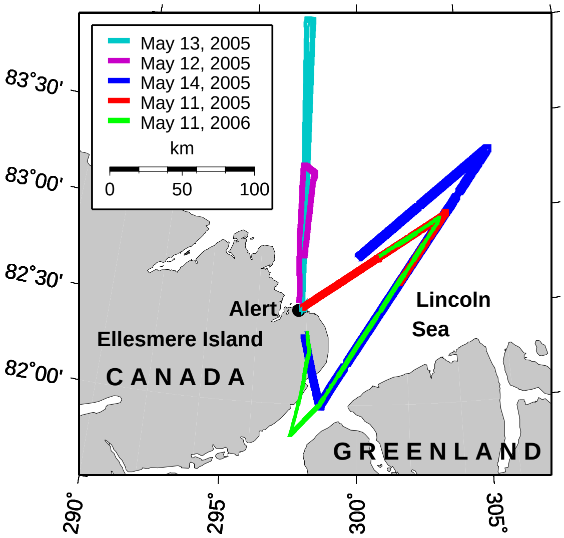

Figure 4.1: EM bird tracks north of Ellesmere Island and in the Lincoln Sea in May 2005 and May 2006.

4.1.1 Surface Elevation and EM Thickness

Fig. 4.2 and Fig. 4.3 show the surface elevation distributions (top row), and the equivalent EM thickness distributions (bottom row) derived for the profiles north of Ellesmere Island and in the Lincoln Sea in May 2005. The EM thickness histograms of the northern profiles in Fig. 4.2 (d) – (f) are dominated by two modes, the lower open water and the multi-year ice mode. Fig. 4.3 is characterized by histograms with three major modes in the EM thickness distribution (c and d) for open water, first-year ice, and multi-year ice. The surface elevation histograms of the profiles in the Lincoln Sea in Fig. 4.3 (a) and (b) show only a weak mode for open water. In (b), the surface elevation data of the very large polynya (see Section 3.5.3.2) were removed since this surface elevation was merely hypothetical because it was only turbulent water. Here, the presence of the first-year ice mode masks the zero mode within the accuracy. Generally, surface elevation was smoothed with a moving average over 12 m to minimize the small-scale surface roughness (see Section 3.5.3.1). Table 4.1 summarizes the values of the modes in Fig. 4.2 and Fig. 4.3, from which R was calculated with Eq. (2.2.4). Additionally, the mean R-values and standard deviations are displayed for comparison with the $R = 5.889$ that was derived from the model by WADHAMS et al. (1992) (see Section 2.2.2).

For the northern profiles (Fig. 4.2), the multi-year ice is thicker (modes between 0.7 – 0.78 m for surface elevation and 4.25 – 5.05 m for EM thickness) than in the Lincoln Sea (Fig. 4.3) (modes between 0.65 – 0.66 m for surface elevation and

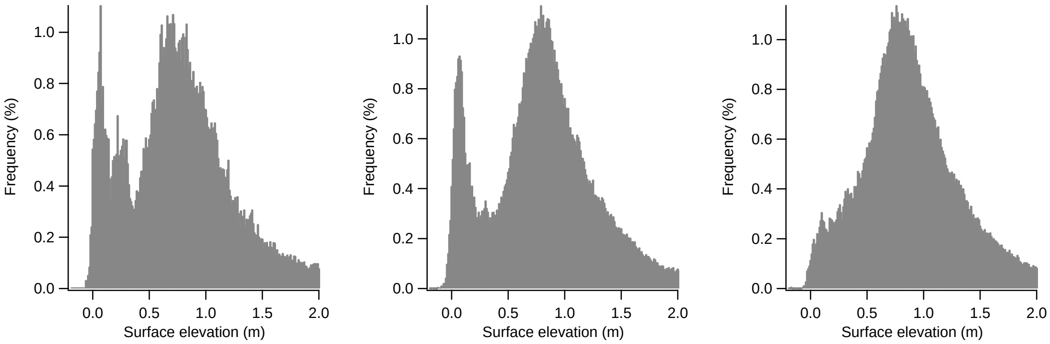

(a) May 6

(b) May 12

(c) May 13

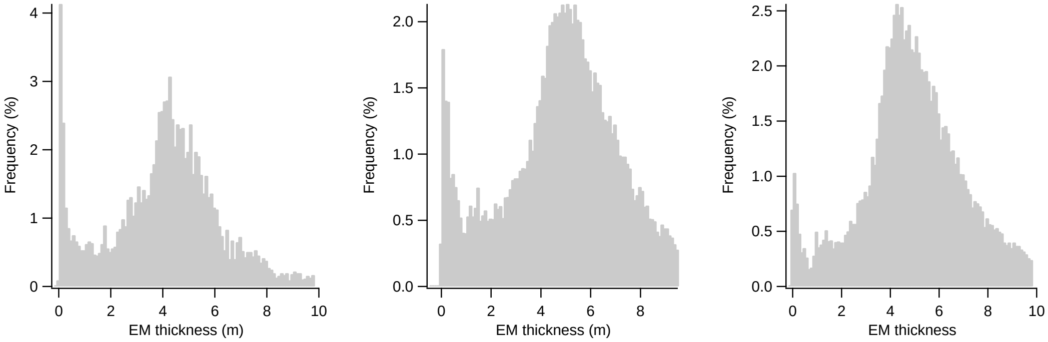

(d) May 6

(e) May 12

(f) May 13

Figure 4.2: Histograms of surface elevation (a – c) and EM thickness (d – f) for the profiles north of Ellesmere Island on May 6, May 12, and May 13, 2005.

3.85 – 4.05 m for EM thickness). The values for R range between 5.67 (*North (c)*) and 6.47 (*North (b)*), and between 5.83 (*Lincoln Sea (b)*) and 6.23 (*Lincoln Sea (a)*).

The modes for open water are only visible in the surface elevation and EM thickness histograms in Fig. 4.2 and in the EM thickness histograms in Fig. 4.3 (c) and (d). Regarding surface elevation, these modes are present but barely recognizable. Instead, modes representing first-year ice are clearly seen yielding R-values between 5.44 and 9.75 (*Lincoln Sea (b)* and *Lincoln Sea (a)*).

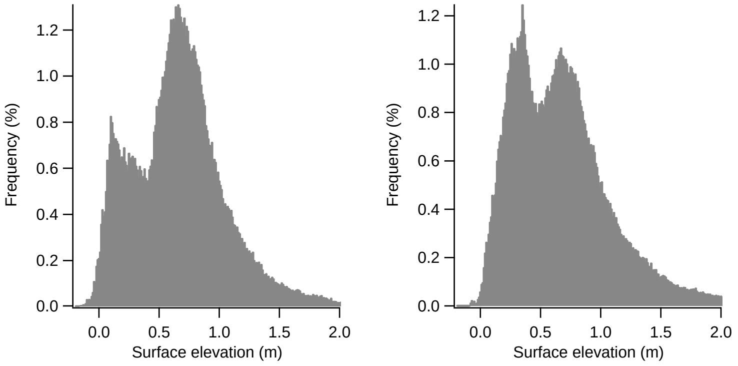

(a) May 11 (b) May 14

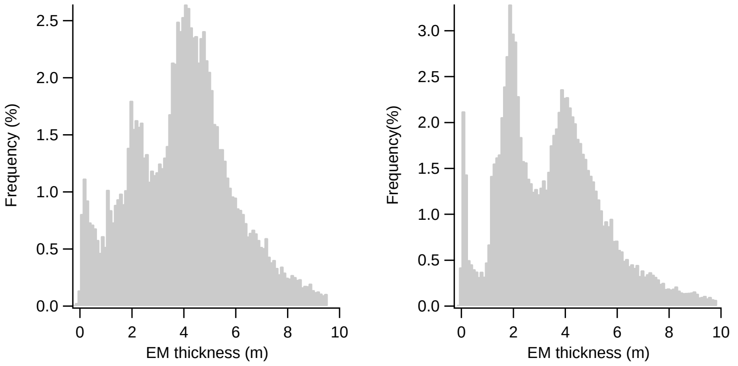

(c) May 11 (d) May 14

Figure 4.3: Histograms of surface elevation (a – c) and EM thickness (c – d) for the profiles in the Lincoln Sea on May 11, and May 14, 2005.

Table 4.1: Modal values of EM thickness and surface elevation (selev) from the histograms in Fig. 4.2 and Fig. 4.3.

Profile	**Surface elevation (m)**	**EM thickness (m)**	$R = \frac{EM\ thickness}{selev}$	**Mean *R*; ±Stdev**
North (a) (May 6)	0.06 0.70	0.05 4.25	0.83 6.07	4.86 ± 1.82
North (b) (May 12)	0.06 0.78	0.05 5.05	0.83 6.47	5.20 ± 1.94
North (c) (May 13)	0.02 0.75	0.05 4.25	2.50 5.67	5.23 ± 0.79
Lincoln Sea (a) (May 11)	0.09 0.20 0.65	1.05 1.95 4.05	11.67 9.75 6.23	7.26 ± 1.55
Lincoln Sea (b) (May 14)	0.05 0.34 0.66	0.05 1.85 3.85	1.00 5.44 5.83	5.35 ± 0.83

4.1.2 Total Thickness from Histogram Modes

Fig. 4.4 shows the relationship of R versus surface elevation (see Table 4.1) for the northern profiles (a – c) and in the Lincoln Sea (d and e) as achieved with the EM bird setup. Here, a linear interpolation was applied to derive the values for R between the modes (see Section 3.6.1). Although, in reality R is not defined for 0 m surface elevation (see Eq. (2.2.4)), here, $R = 0$ was assigned to a surface elevation of 0 m. Thus, the resulting R-values for surface elevations between 0 m and the zero mode were kept to small numbers yielding adequate total thicknesses (see Fig. 4.5). Otherwise, total thickness for these surface elevations would have been very large yielding a distorted total thickness distribution, because it would have been influenced by the large uncertainty of R for small surface elevations. For surface elevations greater than the multi-year ice mode, R was kept constant since it led to sufficient results for the total thickness. The variety of R is clearly seen.

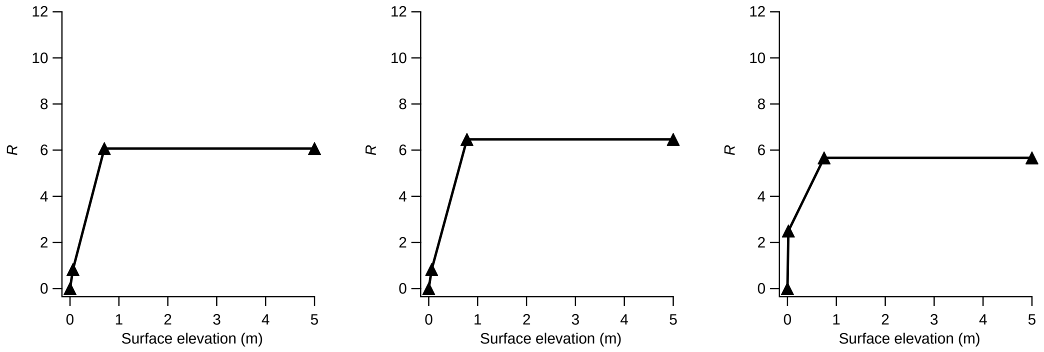

(a) May 6 (b) May 12 (c) May 13

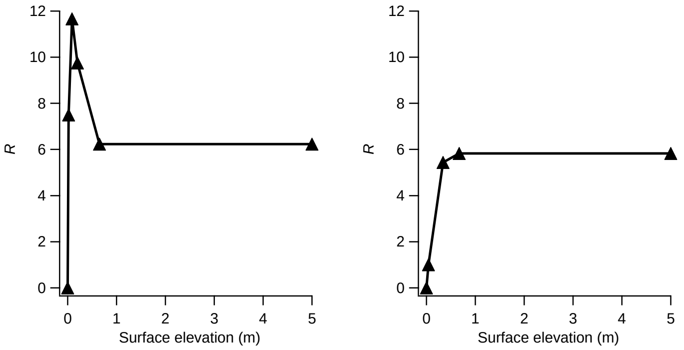

(d) May 11 (e) May 14

Figure 4.4: Relationship of R versus surface elevation for the northern profiles (a – c) and the Lincoln Sea (d and e).

Fig. 4.5 shows the histograms of total thickness calculated from surface elevation that was derived from the difference between the GPS height and laser height, indicated by 'GPS - laser' and histograms of total thickness for the measured EM thickness, labeled 'EM bird', for the profiles north of Ellesmere Island (a – c) and in the Lincoln Sea (d and e) for the R-values displayed in Fig. 4.4. In

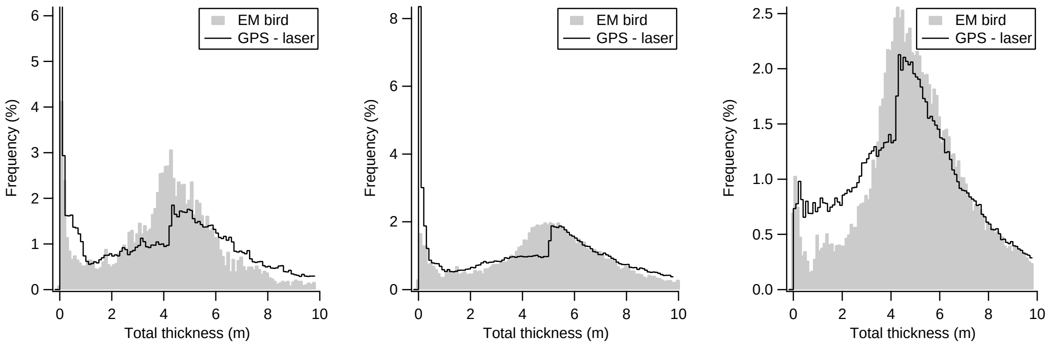

(a) May 6 (b) May 12 (c) May 13

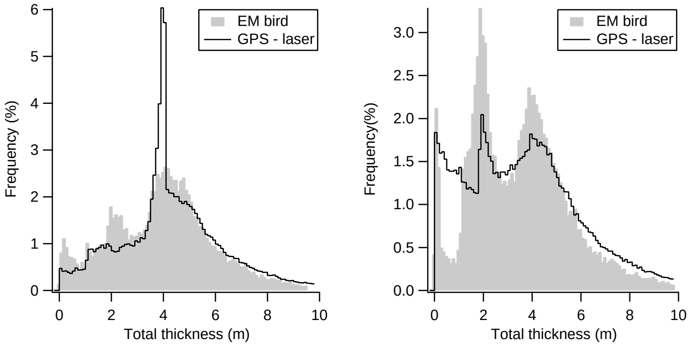

(d) May 11 (e) May 14

Figure 4.5: Histograms of total thickness ('GPS - laser') calculated from surface elevation with *R*-values from the histogram modes summarized in Table 4.1 and displayed in Fig. 4.4 and histograms of total thickness for the measured EM thickness ('EM bird') for the northern profiles (a – c) and the Lincoln Sea (d and e).

Fig. 4.5 the modes of 'GPS - laser' match the modes of the EM thickness within 0.1 m, but the overall fit of the histogram shape is rather poor:

- In (a), (b), (c), and (d), a sharp edge is present for the multi-year ice mode, and in (e) for the first-year ice mode of 'GPS - laser'. This is an effect of the linear interpolation described in Section 3.6.1. This underlines the high variability and sensitivity of *R*.
- In (d) and (e), a zero mode of 'GPS - laser' is now visible as opposed to the surface elevation histograms in Fig. 4.3 (a) and (b).

Following the approach of displaying *R* versus surface elevation in Section 3.6.1 and Section 3.6.2, in which *R* was derived point-wise from the entire profile of EM thickness and surface elevation, the dotted graphs in Fig. 4.6 were obtained. Additionally, the triangle-labeled curve from Fig. 4.4 is shown. In Section 3.6.1 it was shown that "adjusting" *R* for the zero mode does not significantly change the result of single total thickness values, since the zero mode is ideally close to zero. However, if the entire profile is considered, it does change the histogram for total thickness considerably (Fig. 4.7 a, b, and e). The square-labeled curve in Fig. 4.6 (a), (b), and (e) with the adjusted *R* for the zero mode fits the distribution of points better and leads to an improved result in Fig. 4.7 (a), (b), and (e) for the total thickness of 'GPS - laser' with respect to 'EM bird'. Here, R was adjusted only for the three profiles since the results for total thickness of 'GPS - laser' were extremely poor with respect to 'EM bird' in Fig. 4.5. The graphs in Fig. 4.7 (c) and (d) are the same as in Fig. 4.5 (c) and (d). They are shown again to allow a better comparison with the other histograms. The thickness distributions of 'GPS - laser' match the EM thickness distributions quite well in terms of the modes and better than in Fig. 4.5 (a), (b), and (e) in terms of the overall histogram shape. However, some misalignments remain:

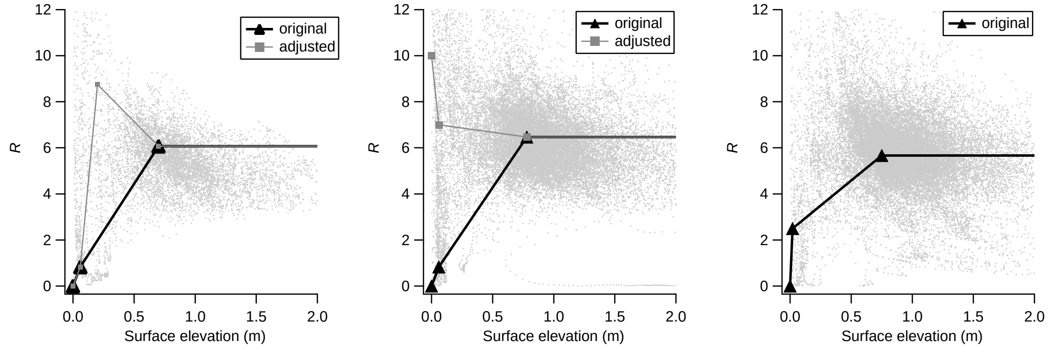

(a) May 6 (b) May 12 (c) May 13

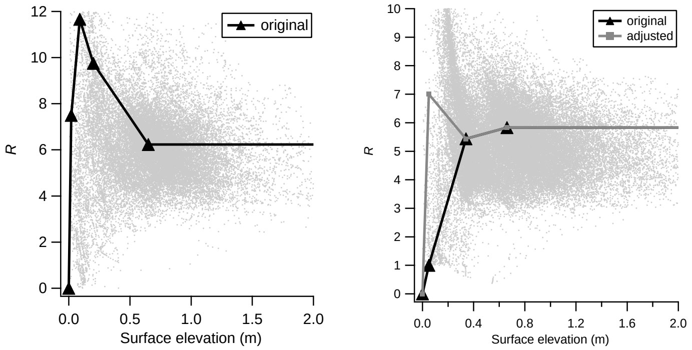

(d) May 11 (e) May 14

Figure 4.6: Relationship of R versus surface elevation for the northern profiles (a – c) and the Lincoln Sea (d and e) with the 'adjusted' R in (a), (b), and (e). The graphs (c) and (d) are the same as in Fig. 4.4 (c) and (d).

- In (a), the sharp edge of the multi-year ice mode is still present.
- In (b), an offset of about 0.2 m can be seen for the zero mode in the 'GPS - laser' distribution but the general fit between both thickness distributions is good.
- In (e), a zero mode in 'GPS - laser' is now visible as opposed to the surface elevation histogram in Fig. 4.3 (b) and the first-year ice mode matches better to the equivalent mode in the total thickness distribution than in in Fig. 4.5 (e). However, the probability of the zero mode is reduced considerably.

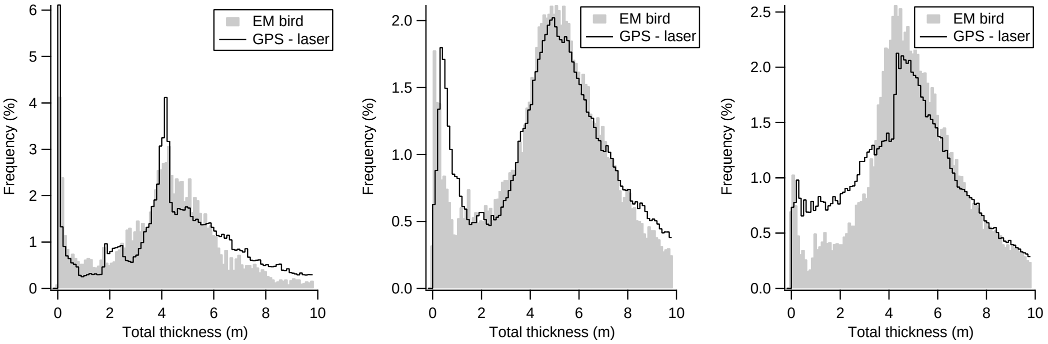

(a) May 6 (b) May 12 (c) May 13

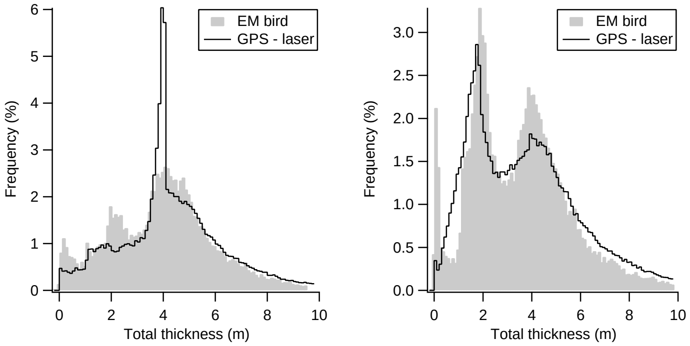

(d) May 11 (e) May 14

Figure 4.7: Same as Fig. 4.5 but (a), (b), and (e) with 'adjusted' R-values, displayed in Fig. 4.6. The graphs (c) and (d) are the same as in Fig. 4.5 (c) and (d).

4.1.2.1 Total Thickness from Histogram Modes – with mean R-Values

As mentioned in Section 4.1.1, the surface elevation profiles were divided into groups of open water (< 0.05 m), first-year ice (≥ 0.05 m, < 0.4 m), and multi-year ice (≥ 0.4 m). Accordingly, the previously derived R-values were assigned to these groups and a mean R was calculated for each group. This was done for all profiles, except the northern profile on May 6, yielding three mean R-values which were used subsequently to calculate the total thickness as an alternative approach. If the total thickness was not measured coincidently, these R-values can be applied to obtain total thickness. The data of the northern profile on May 6 were excluded from the calculation of a mean R to avoid an imbalance between the three northern profiles and the two profiles in the Lincoln Sea. Considering the individual profile lengths, the one on May 6 was the shortest and therefore it was chosen to be neglected. Table 4.2 displays the mean R-values for each group of the individual profiles and the mean R for each group if all profiles are considered ('Total').

Table 4.2: Mean R-values of open water (< 0.05 m), first-year ice (≥ 0.05 m, < 0.4 m), and multi-year ice (≥ 0.4 m) in the Arctic (see Table 4.1). Numbers in boxes indicate the thresholds of surface elevation for the three groups.

Profile	Open water	First-year ice	Multi-year ice
North (b)	0.37	1.82	6.18
North (c)	2.11	3.46	5.49
Lincoln Sea (a)	7.02	9.78	6.50
Lincoln Sea (b)	1.82	4.52	5.66
Total	2.83	4.90	5.96

The resulting total thickness for surface elevation, derived from the difference between the GPS height and laser height, is shown with the histograms 'GPS - laser with total R' in Fig. 4.9. Additionally, the total thickness derived from the model by WADHAMS et al. (1992) (see Section 2.2.2) is displayed by histograms labeled '$R = 5.889$' and the EM thickness by histograms labeled 'EM bird'. For comparison with the total thickness in which the R-values for the entire surface elevation were derived by smoothing spline interpolation, instead of linear interpolation, see also Fig. 3.25 (c). Regarding Fig. 4.9 (a), the same offset of 0.2 m between the zero modes is visible as in Fig. 4.7 (b) but in addition, a slight shift of about 0.3 m to the left is seen for the multi-year ice mode for '$R = 5.889$'. However, the same shift is seen in 'GPS - laser with total R' indicating that the multi-year ice in Fig. 4.9 (a) was thicker than the average. In contrast, in Fig. 4.9 (b), the multi-year ice modes of the three histograms agree well with a lower multi-year ice thickness. Regarding Fig. 4.9 (c) and (d), the multi-year ice mode of '$R = 5.889$' is similar to 'GPS - laser with total R'. The first-year ice mode in (c) is matched poorly by both approaches, because of the additional thinner first-year ice seen in the EM thickness. Here, a fourth group would have been necessary. In (d), the higher probability, the slim first-year ice mode, and the visible zero mode of 'GPS - laser with total R' agree better to the first-year ice mode of 'EM bird' than '$R = 5.889$'. In 'GPS - laser with total R' all modes are visible

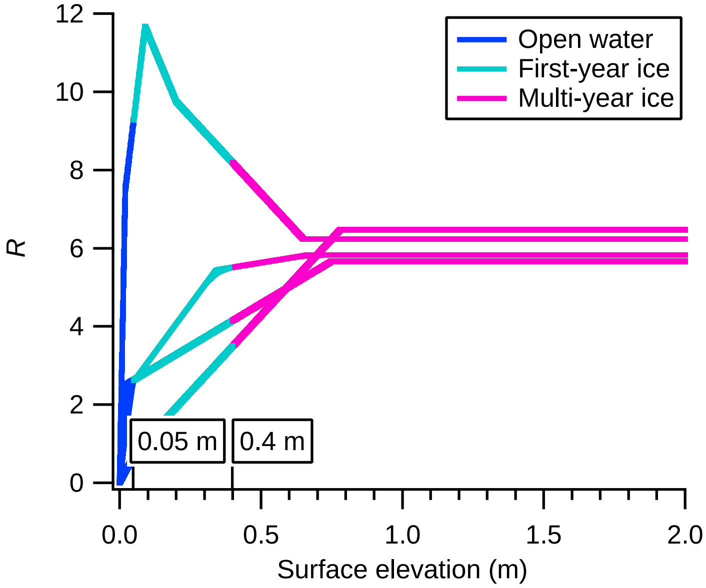

Figure 4.8: *R* versus surface elevation classified for open water, first-year ice, and multi-year ice for the northern flights and the Lincoln Sea in Table 4.2 (see Fig. 4.9). Numbers in boxes indicate the thresholds of surface elevation for the three groups.

that are not seen for '$R = 5.889$'. The gaps in the 'GPS - laser' distribution result from the multiple possibilities of assigning the correct *R*-value to the surface elevation. In other words, the missing total thicknesses cannot be represented by the classification of surface elevation. Surface elevation at the upper threshold of first-year ice (< 0.4 m) multiplied by the derived mean *R* yields a different total thickness than the lowest possible surface elevation of multi-year ice ($= 0.4$ m) multiplied by the equivalent mean *R* that is not consistently adjacent. In Fig. 4.8, the relationships between *R* versus surface elevation for open water, first-year ice, and multi-year ice, which led to the mean *R*-values in Table 4.2, are merged into one graph for the considered profiles (see Fig. 4.6 b – e). This underlines the high variability of *R* within one ice class even for the same survey area. Further, the *R*-values for open water should ideally be zero. However, a large variety of *R*-values is seen for 0 m surface elevation due to deficient EM thickness and surface elevation data.

The following main points of this section can be summarized:

- The transformation of surface elevation by the mean *R*-values can be seen as a first approach to derive total thickness if this was not measured coincidently by the EM bird. As opposed to the constant *R* derived from the model by WADHAMS et al. (1992), zero modes for open water are clearly visible, and thus better reflect reality.

- The shape of the first-year ice mode is represented better by a mean *R* as long as three classifications are sufficient.

- In the case of a thicker multi-year ice mode compared to the average, the obtained total thickness is too low for the mean and constant *R*.

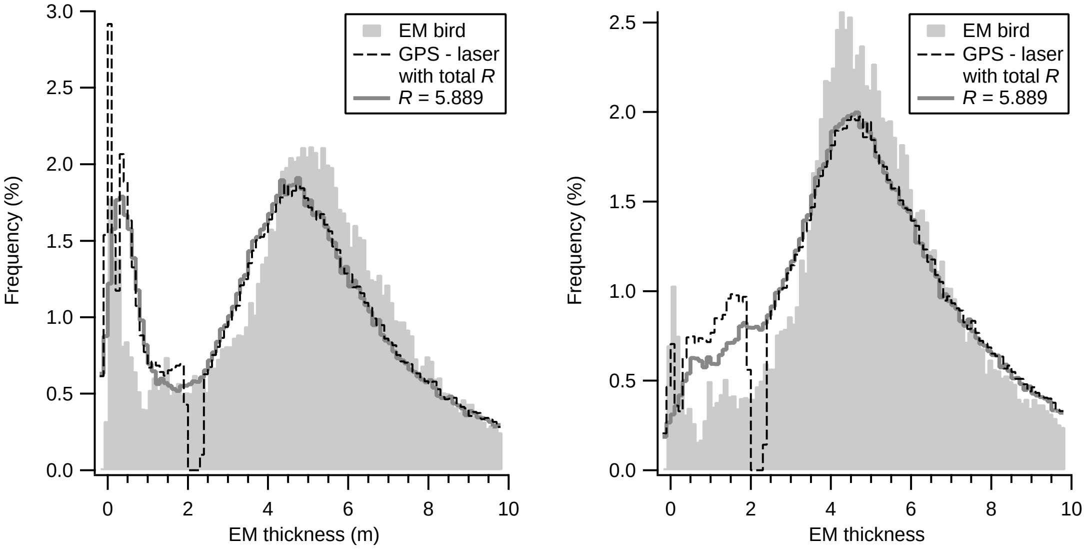

(a) May 12 (b) May 13

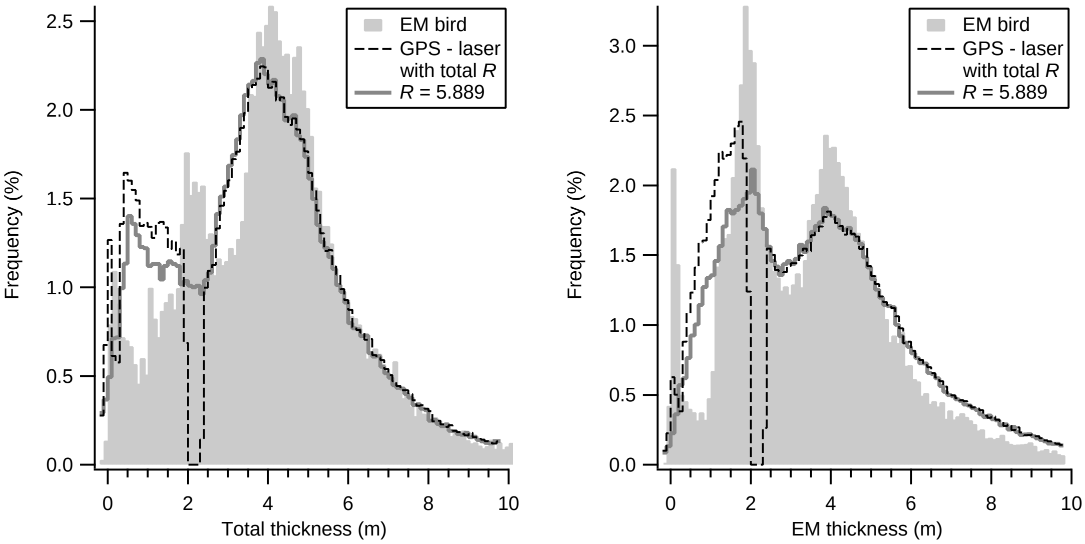

(c) May 11 (d) May 14

Figure 4.9: Histograms of total thickness calculated from surface elevation with mean R-values ('Total' in Table 4.2) for open water, first-year ice, and multi-year ice ('GPS - laser with total R') and histograms of total thickness for the measured EM thickness ('EM bird') for the northern profiles (a and b) and the Lincoln Sea (c and d). Additionally, total thickness distributions are shown for '$R = 5.889$'.

4.1.2.2 Total Thickness from Histogram Modes – bin-wise

Here, results are shown for the approach of transforming surface elevation by multiplying the single histogram bins rather than the single data points. R can either result from the modes of surface elevation and EM thickness for a certain profile (see Table 4.1) or from averaging the R-values over all profiles for open water, first-year ice, and multi-year ice (see Table 4.2, 'Total'). The resulting total thickness histograms for the surface elevation histograms in Fig. 4.2 (b), (c) and Fig. 4.3 (a), (b) are displayed in Fig. 4.10 (a) – (d) as 'R interpolated'. The total thickness distributions derived from averaging the R-values (see Table 4.2, 'Total') are termed 'R interpolated and averaged' in Fig. 4.10 (a) – (d). Additionally, the total thickness distributions are shown for the constant '$R = 5.889$' which are identical to the equivalent histograms in Fig.4.9, and furthermore, the EM thickness 'EM bird'. The histogram 'R interpolated and averaged' was scaled by 0.8 and '$R = 5.889$' was scaled by 0.6 for better visibility. Comparing the total thickness of 'R interpolated' in Fig. 4.10 with the EM thickness, an agreement of the first-year and multi-year ice mode is clearly seen, except in (c). However, the zero mode, especially in (d), is masked by the adjacent values. Regarding the total thickness of 'R interpolated and averaged', the two ice modes match the modes of the EM thickness within 0.1 m, whereas the modes of the histogram with the constant '$R = 5.889$' reflect the EM thickness modes within 0.2 m. In Fig. 4.10 (a), however, the EM thickness ice mode is matched by both approaches within 0.2 m.

The following points can be summarized:

- In comparison to the results of the previous Section 4.1.2.1, here, the overall shape of the histograms is more dependent on the shape of the surface elevation distributions. For this reason, the general fit between total thickness and EM thickness is better in Fig. 4.9 where the single data points were multiplied by R. Another difference is that the zero modes in (b) and (d) are not distinct (they are also invisible in the surface elevation histograms in Fig. 4.3 a, b) and that the gaps of the unknown total thickness disappeared (see Fig. 4.9).

- Comparing the histograms of 'R interpolated' to the equivalent histograms 'GPS - laser' in Fig. 4.7 (b) – (e), for which the R-values were partially adjusted, here, the peaks of the ice modes match exactly the peaks of the EM thickness modes, whereas e. g., in Fig. 4.7 (e) an offset of 0.1 m is present but not in Fig. 4.10 (d). However, the general fit of the histogram shape is better in Fig. 4.7, except in Fig. 4.7 (d), and the zero mode is visible for all profiles.

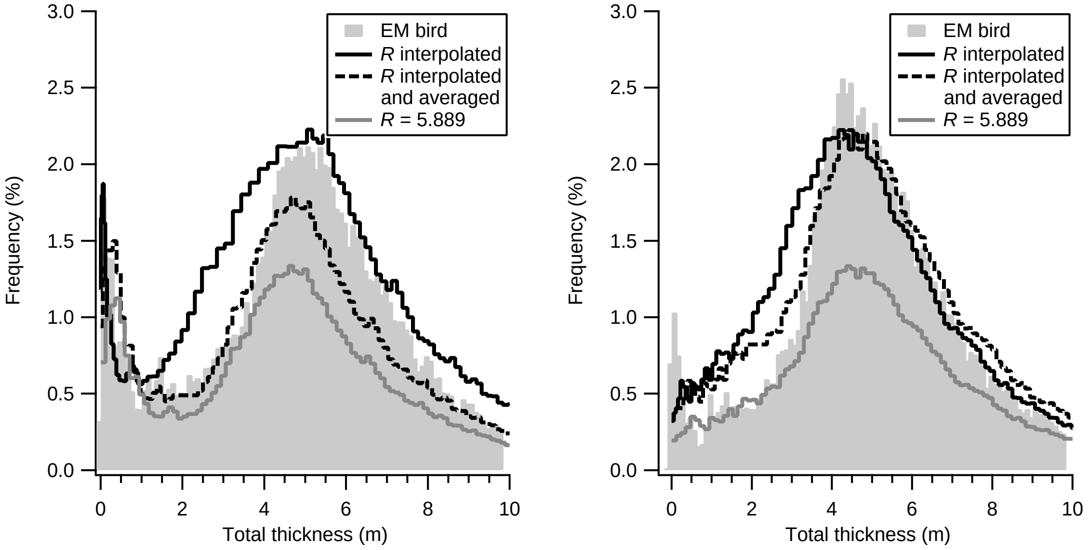

(a) May 12 (b) May 13

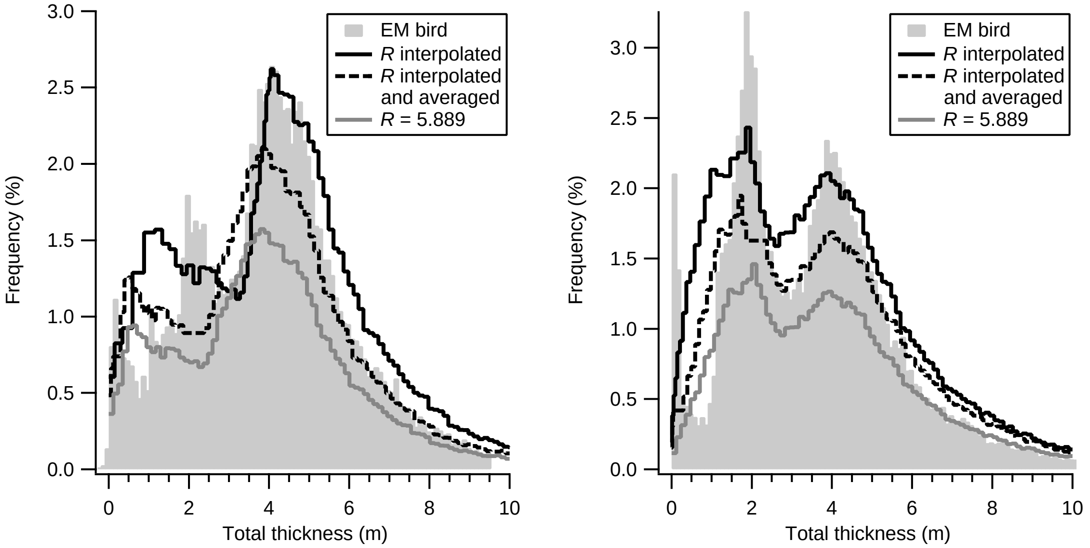

(c) May 11 (d) May 14

Figure 4.10: Histograms of total thickness for the northern profiles (a and b) and the Lincoln Sea (c and d) from applying *R*-values of the modes '*R* interpolated' (Table 4.1) and mean *R*-values '*R* interpolated and averaged' (Table 4.2) to the single bins of the surface elevation histograms in Fig. 4.2 (b), (c) and Fig. 4.3 (a), (b). Additionally, total thickness distributions are shown for '$R = 5.889$' and 'EM bird'. Total thickness for '*R* interpolated and averaged' and '$R = 5.889$' was scaled by 0.8, and 0.6 respectively, for better visibility.

4.1.3 Total Thickness from Fitting Functions

Another approach of transforming surface elevation to total thickness is the generation of point-wise fitting functions as described in Section 3.6.2. More precisely, the entire profile of surface elevation was divided into 40 m long sections for which the standard deviation and mean was calculated (see Section 3.6.2). The same thresholds of EM thickness, standard deviation and mean for classifying open water, first-year ice, and multi-year ice were used as described in Section 3.6.2 and summarized in Table 3.2. The total thickness for the different ice classes was calculated with Eq. (2.2.3) using the *R*-fitting equations generated for the profile in the Lincoln Sea on May 14 (see Fig. 4.11 e) summarized in Eq. (3.6.1) – Eq. (3.6.3). Fig. 4.11 shows the histograms of total thickness calculated from surface elevation that was derived from the difference between the GPS height and laser height, for the profiles north of Ellesmere Island (a – c) and in the Lincoln Sea (d – f) as 'GPS - laser, 3 modes fit'.

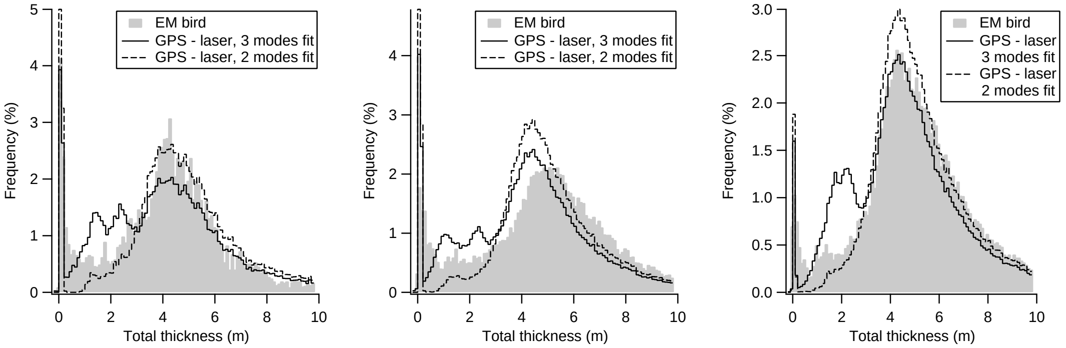

(a) May 6, 2005 (b) May 12, 2005 (c) May 13, 2005

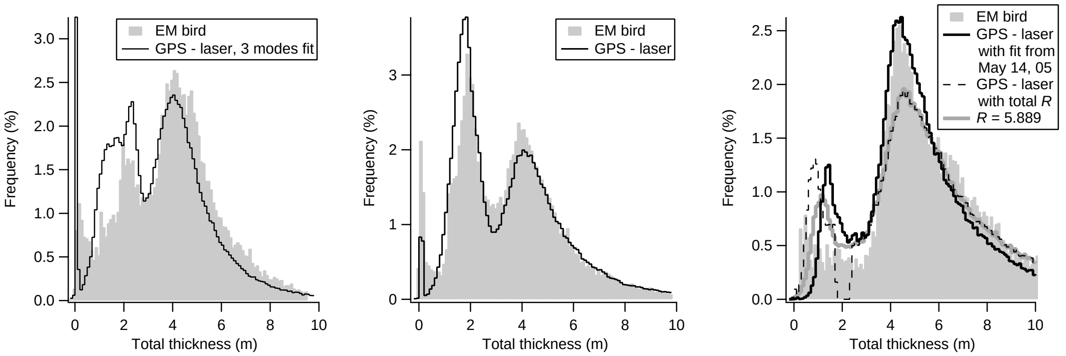

(d) May 11, 2005 (e) May 14, 2005 (f) May 14, 2006

Figure 4.11: Histograms of total thickness ('GPS - laser') calculated from surface elevation with point-wise fitting functions Eq. (3.6.1) – Eq. (3.6.3) for all three modes and two modes and histograms of total thickness for the measured EM thickness ('EM bird') for the northern profiles (a – c) and the Lincoln Sea (d – f) . The point-wise fitting functions were generated for the profile considered in (e). The graph in (f) shows total thickness ('GPS - laser') derived with the same fitting equations, which were generated for (e), but refers to the profile in May 2006. Additionally, the total thickness distribution is shown for the total *R*-values ('Total') in Table 4.2 and for the constant '$R = 5.889$'.

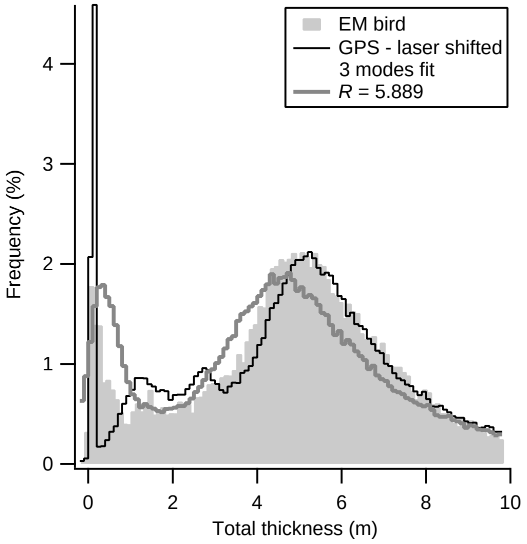

Figure 4.12: Histograms of shifted total thickness calculated from surface elevation ('GPS - laser') and EM thickness ('EM bird') for the northern profile in Fig. 4.11 (b). Additionally, the total thickness distribution is shown if the constant '$R = 5.889$' was used.

The total thickness distribution of 'GPS - laser, 3 modes fit' in Fig. 4.11 (a), (b), and (c) looks a bit unusual compared to the EM thickness distribution with respect to the modes for first-year ice. Regarding the number of modes for surface elevation in Fig. 4.2, only two modes for open water or very thin ice and multi-year ice are visible. Therefore, total thickness was calculated again without using the fitting function for first-year ice Eq. (3.6.2). The result is illustrated by the histograms for total thickness labeled 'GPS - laser, 2 modes fit'. Regarding the agreement of modes, the thickness distributions have improved considerably. Now, only two modes are visible which match the EM thickness modes quite well. Leaving out the fitting equation for first-year ice leads to the absence of first-year ice that is compensated in the thickness distribution ('GPS - laser, 2 modes fit') by a higher probability of the multi-year ice mode.

In Fig. 4.11 (b), a slight offset of the multi-year ice mode is seen compared to the EM thickness. Considering the value for this mode in the EM thickness, thicker multi-year ice of 5.05 m is found (see Fig. 4.2 b) than in (a) and (c). This indicates the remaining problem with creating and using generalized fitting functions which is summarized in Section 4.1.4.

Regarding the multi-year ice mode in Fig. 4.11 (c), a good agreement is visible for both ('EM bird' and 'GPS - laser, 2 modes fit) total thickness distributions. In contrast to (a), (b), and (c), all three fit functions from Eq. (3.6.1) – Eq. (3.6.3) were used in (d) and (e), since three modes are present, although difficult to see, in the equivalent surface elevation histograms (Fig. 4.3 a, b). The shape of the modes in (d) 'GPS - laser, 3 modes fit' does not coincide perfectly with total thickness obtained from the EM bird but the size of the mode values lie within measurement accuracy of the EM thickness. The graph in (e) shows the direct result for the total thickness with the fitting functions generated for this profile.

In Fig. 4.11 (f), the fitting functions from (e) were applied to one profile in the Lincoln Sea of the subsequent year. The result confirms the findings for the other profiles: as long as the modal EM thickness difference between the profile for which the fitting functions were created, and the profile on which they are applied is less than 1.20 m (difference for the profile shown in (b) that resulted in a poor fit), the fitting functions yield sufficient results. However, the first-year ice mode of the EM thickness is not nearly as distinct as in (e) for which reason it yielded a deficient total thickness.

Regarding the use of the mean R from Table 4.2, very small total thicknesses are represented slightly better in 'GPS - laser with total R' than in '$R = 5.889$', that resulted from the model by WADHAMS et al. (1992).

Fig. 4.12 shows the distributions for the same profile as Fig. 4.11 (b). Here, 'GPS - laser shifted, 3 modes fit' was additionally shifted according to the thicker multi-year ice mode of surface elevation with respect to the profile in Fig. 4.11 (e). The first-year ice mode of 'GPS - laser, 3 modes fit', however is an artifact caused by the fitting function for first-year ice. The total thickness was shifted by multiplying it with 1.18 (quotient of 0.78 m and 0.66 m of the multi-year ice modes for surface elevation of *North (b)* and *Lincoln Sea (b)* in Table 4.1). Thus, the total thickness can be adjusted manually if thicker modes for surface elevation are present than in the profile used for creating the fitting functions. This approach is to be seen as a possibility of treating different thicknesses in surface elevation with respect to the profile for which the fitting functions were generated. Thus, the fitting functions are generally applicable and independent from individual profiles with thicker surface elevation modes. Although the histogram 'GPS - laser shifted, 3 modes fit' still does not match the EM thickness histogram perfectly, the multi-year ice mode is represented better than for 'GPS - laser, 3 modes fit' that is not shifted (see Fig. 4.11 b). Unfortunately, this approach could only be tested for one profile since this is the only one where the multi-year ice modes of the 'EM bird' and 'GPS - laser, 3 modes fit' (see Fig. 4.11 b) disagree (due to thicker multi-year ice compared to Fig. 4.11 (e).

4.1.4 Summary

- The histograms of surface elevation showed a distinct zero mode only if a mode for first-year ice was absent. Otherwise it was hardly visible, because it was masked by noise of the first-year ice mode.
- According to the number of modes, groups for R could be derived. For the zero mode, values for R were found at around unity, for first-year ice between 5.67 and 9.75, and for multi-year ice between 5.67 and 6.47. The latter reflects a thicker snow cover and a lower density compared to first-year ice.
- The use of the coincidently measured EM thickness allowed adjustment of R for the zero mode to achieve a better overall match between the GPS/laser derived total thickness and EM thickness.
- The transformation of surface elevation by three mean R-values was a first approach to derive total thickness from GPS/laser data independent from coincidently measured EM thickness . The advantage over using one constant R was that the zero modes became visible in the total thickness distribution, and thus a better agreement with the EM thickness was possible. Here, the mean R was obtained from the average of four profiles. A larger number of profiles with varying modal thicknesses would not improve the mean R and hence total thickness as R depends on the snow depth.

- The bin-wise transformation of surface elevation guaranteed a perfect agreement of the distinct modes in surface elevation and EM thickness. However, the histogram shape is very much dependent on the shape of the surface elevation histogram.
- The use of the coincidently measured EM thickness also allows creation of a fitting function for each ice class of a chosen profile. The fitting functions can then be applied to surface elevation profiles in the same area for which no coincidently measured total thickness is available. According to the number of modes present in surface elevation, the equivalent fitting functions were used. In general, a better fit between total thickness derived by GPS/laser is generated, than with the transformation where R is used from the histogram modes. Problems remain, if different conditions in ice thickness are present compared to the profile that was used for generating the fitting functions. These different ice conditions are also visible in surface elevation from which necessary changes in the fitting functions could be concluded.

4.2 Helicopter Measurements in the Antarctic

Fig. 4.13 shows the flight tracks performed in the Weddell Sea during the ISPOL campaign in December 2004. The square indicates the position of the RV Polarstern that served as the base for the helicopter flights. As opposed to the Arctic where the entire flight profiles of surface elevation were considered, here, results of single profile segments are shown. The reason for this is due to the drifting GPS-base station during the survey flights (see Section 3.2). The profile segments were chosen according to obvious features in the EM thickness distributions[1] and are marked in Fig. 4.13. Three profiles which represent the main features of all profiles are marked in a different color and are described in Section 4.2.1.

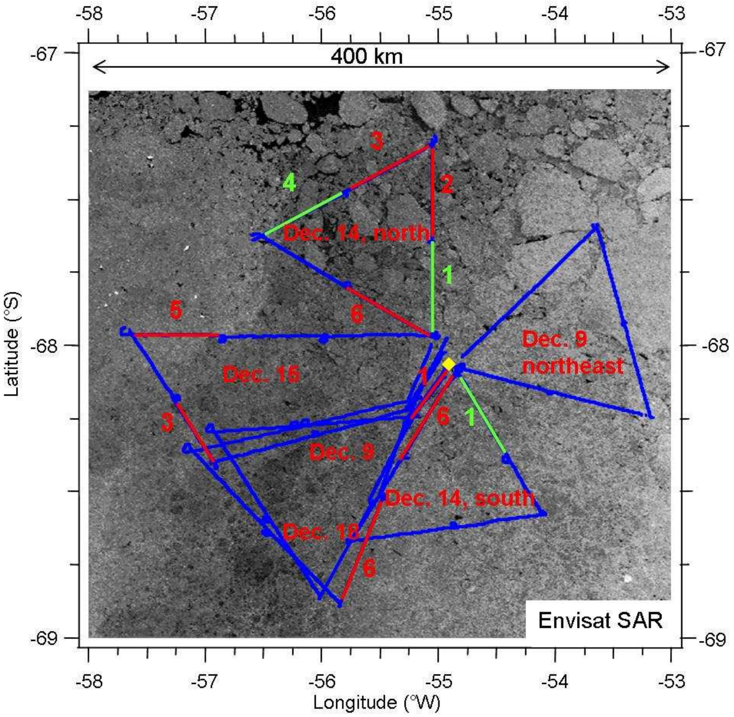

Figure 4.13: EM bird tracks in the Weddell Sea during the ISPOL campaign. Analyzed profile segments are marked of which three represent the main features visible in EM thickness. The position of the RV Polarstern is indicated by a square.

As mentioned in Section 4.1, the results of the helicopter measurements comprise the probability distributions of surface elevation and total thickness. Additionally, the R-values are shown which resulted from the comparison of the modes between the histograms of surface elevation and EM thickness.

4.2.1 Surface Elevation and EM Thickness

Fig. 4.14 shows the surface elevation distribution in (a) – (c) and (g) – (i), and the equivalent EM thickness distribution in (d) – (f) and (j) – (l), and Fig. 4.15

---

[1] Some EM thickness distributions show modes for extremely thick or thin ice, others show a clear zero mode or none open water at all.

shows surface elevation distributions in (a) – (c) and (g) – (h), and the equivalent EM thickness distributions in (d) – (f) and (i) – (j). Table 4.3 summarizes the numbers of the modes in Fig. 4.14 and Fig. 4.15 from which R was calculated with Eq. (2.2.4).

Table 4.3: Modal values of EM thickness and surface elevation (selev) from the histograms in Fig. 4.14 and Fig. 4.15.

Profile	**Surface elevation (m)**	**EM thickness (m)**	$R = \frac{EM\ thickness}{selev}$	**Fitting equation from**
Weddell Sea north (Dec. 14, leg1)	0.004 0.22 0.60	0.05 1.15 2.65	1.25 5.23 4.42	–
Weddell Sea (Dec. 9, leg1)	0.05 0.65	0.05 2.45	1.00 6.47	Dec. 14, leg1 north Dec. 14, leg1 north
Weddell Sea north (Dec. 14, leg4)	0.54 0.76	1.75 2.95	3.24 3.88	–
Weddell Sea west (Dec. 15, leg5)	– 0.75	– 2.95	– 3.39	– Dec. 14, leg4 north
Weddell Sea north (Dec. 14, leg2)	0.04 0.35	0.05 1.75	1.25 5.0	Dec. 14, leg1 north Dec. 14, leg4 north
Weddell Sea north (Dec. 14, leg3)	0.09 0.45	0.05 1.85	0.05 4.11	Dec. 14, leg1 north Dec. 14, leg4 north
Weddell Sea (Dec. 18, leg6)	0.16 0.57	1.25 1.85	7.81 3.25	– Dec. 14, leg4 north
Weddell Sea west (Dec. 15, leg3)	– 1.00	– 3.25	– 3.25	– Dec. 14, leg4 north
Weddell Sea south (Dec. 14, leg1)	0.03 0.61	0.05 2.15	1.67 3.25	–
Weddell Sea north (Dec. 14, leg6)	0.04 0.47	0.05 2.15	1.67 4.57	Dec. 14, leg1 north Dec. 14, leg1 south
Weddell Sea south (Dec. 14, leg6) (Dec. 14, leg6)	0.11 0.33 0.59	0.95 1.75 2.35	8.64 5.30 3.98	– Dec. 14, leg4 north Dec. 14, leg1 south

In Section 3.6.2.2, it was already mentioned that the flights in the Weddell Sea could be divided into three groups according to the presence of modes in the EM thickness:

- 'Dec. 14, leg1 north' (Fig. 4.14 d) shows three modes for open water, first-year, and multi-year ice.
- 'Dec. 14, leg4 north' (Fig. 4.14 f) shows only two modes for thicker first-year, and thicker multi-year ice than Dec. 14, leg1 north (Fig. 4.14 d).
- 'Dec. 14, leg1 south' (Fig. 4.15 f) shows two modes for open water, and intermediate multi-year ice.

Some of the remaining profiles fell exactly in one of the above groups, meaning that the equivalent modes were present and very similar to the modes of that group. Others matched only partly with the groups, e. g., ‘Dec. 15, leg5 west’ (Fig. 4.14 j) shows a similar multi-year ice mode as ‘Dec. 14, leg4 north’ in (f), meaning that it belongs to the group of ‘Dec. 14, leg4 north’ (Fig. 4.14 f). However, ‘Dec. 14, leg3 north’ in (l) shows one mode for open water, which corresponds to the zero mode of ‘Dec. 14, leg1 north’ (Fig. 4.14 d), and one mode for thicker first-year ice which is similar to the equivalent mode of ‘Dec. 14, leg4 north’ in Fig. 4.14 (f). This means that this profile belongs only half to the group of ‘Dec. 14, leg1 north’ and half to the group of ‘Dec. 14, leg4 north’ (see Table 4.3). So far, only the modes of the EM thickness histogram have been considered, because it is easier (compared to the surface elevation histogram) to distinguish between the different ice thickness modes. However, regarding the equivalent surface elevation histograms, the same grouping is possible as for the EM thickness.

With respect to R, the previous grouping does not work. For example, from Fig. 4.14 (a) and (b) values for R of the multi-year ice mode in the range between 4.42 and 6.47 were derived. But from Fig. 4.14 (h) and (i) and Fig. 4.15 (a), which belong to the group with a thicker first-year ice and and multi-year ice mode, values for R in the range between 3.25 and 5.0 were derived, indicating and confirming the high variability of R.

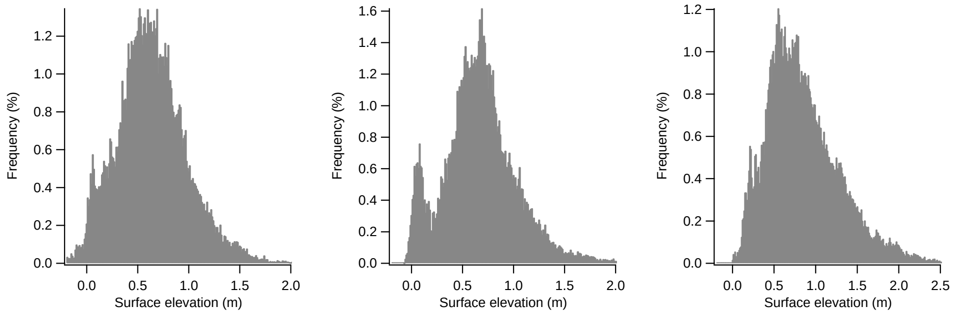

(a) Dec. 14, leg1 north (b) Dec. 9, leg1 (c) Dec. 14, leg4 north

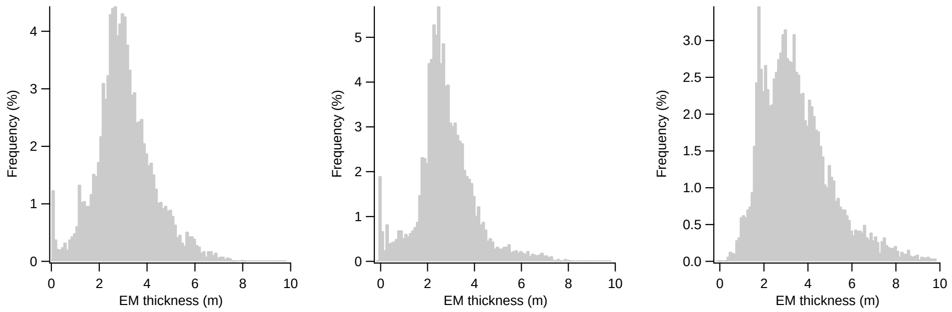

(d) Dec. 14, leg1 north (e) Dec. 9, leg1 (f) Dec. 14, leg4 north

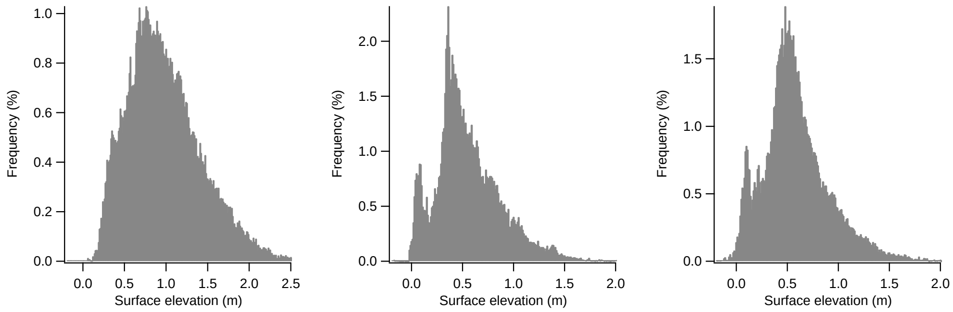

(g) Dec. 15, leg5 west (h) Dec. 14, leg2 north (i) Dec. 14, leg3 north

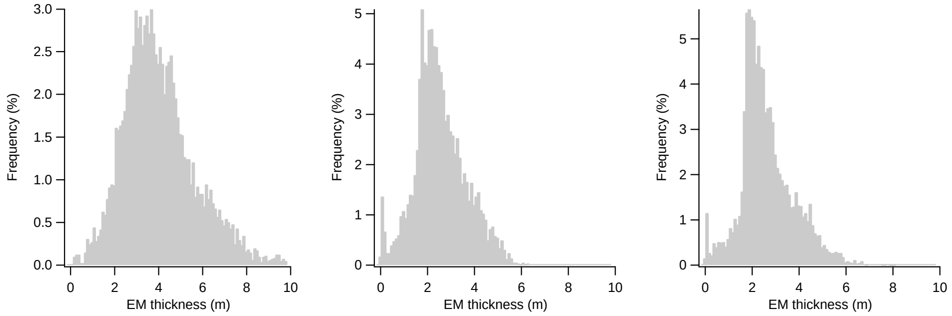

(j) Dec. 15, leg5 west (k) Dec. 14, leg2 north (l) Dec. 14, leg3 north

Figure 4.14: Histograms of surface elevation (a – c) and (g – i) and EM thickness (d – f) and (j – l) for the profiles in the Weddell Sea on Dec. 9, 14, and 15, 2004.

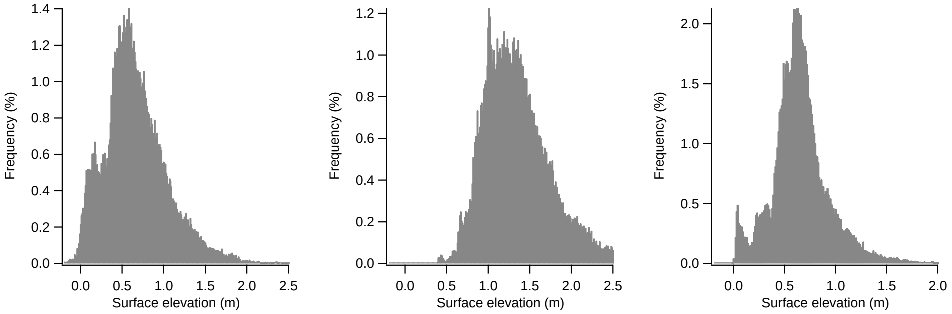

(a) Dec. 18, leg6 (b) Dec. 15, leg3 west (c) Dec. 14, leg1 south

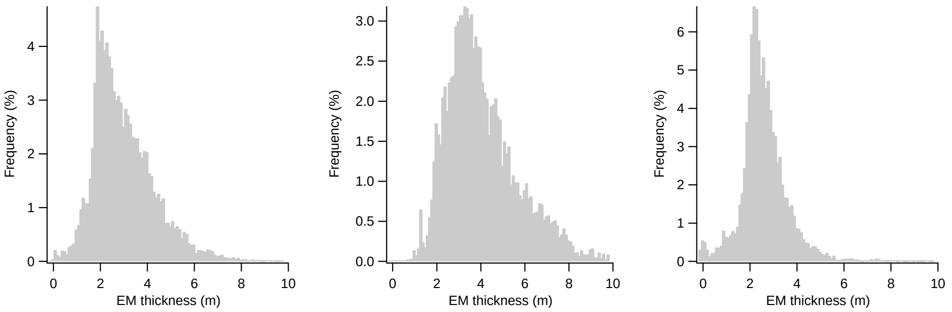

(d) Dec. 18, leg6 (e) Dec. 15, leg3 west (f) Dec. 14, leg1 south

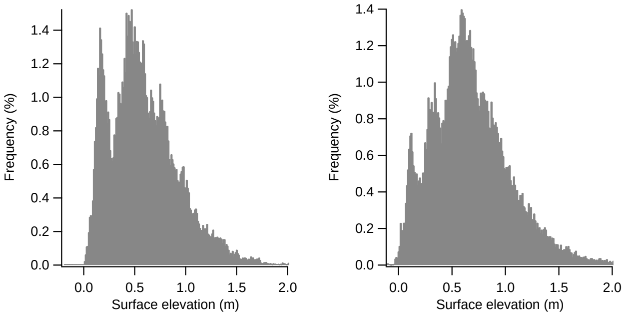

(g) Dec. 14, leg6 north (h) Dec. 14, leg6 south

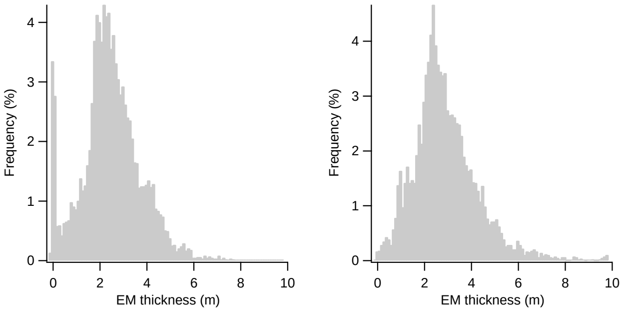

(i) Dec. 14, leg6 north (j) Dec. 14, leg6 south

Figure 4.15: Histograms of surface elevation (a – c) and (g – h) and EM thickness (d – f) and (i – j) for the profiles in the Weddell Sea on Dec. 14, 15, and 18, 2004.

4.2.2 Total Thickness from Histogram Modes

Fig. 4.16 shows the relationship of *R* versus surface elevation for the profiles in the Weddell Sea. *R* was taken from Table 4.3 whereas the *R*-values between the modes were linearly interpolated (displayed by the triangle-labeled curve in Fig. 4.16). Since the resulting total thickness distribution matched the EM thickness distribution poorly or not at all, *R* was adjusted for the zero mode of these profiles. The adjusted *R*-values are displayed by the square-labeled curve in Fig. 4.16 (a, b, c, g, h, j, and k). For the remaining profiles for which *R* was not adjusted, the resulting distribution of total thickness was already quite good compared to the one of EM thickness.

Fig. 4.17 shows the histograms of total thickness calculated from surface elevation that was derived from the difference between the GPS height and laser height, indicated by 'GPS - laser' with *R* being derived from adjusting the zero modes of the histograms for surface elevation and histograms of EM thickness, labeled 'EM bird', in the Antarctic. In (d), (e), (f), and (i) the zero modes were not adjusted as seen in Fig. 4.16. The total thickness distribution ('GPS - laser') matches the EM thickness distribution quite well in terms of the modes and the overall histogram shape. However, some peculiarities remain:

- In Fig. 4.17 (d), (f), (g), (h), and (k) the problems of the high variability and sensitivity of *R* are especially visible as mentioned in Section 3.6.1.

- In Fig. 4.17 (c), (d), and (h), for which open water spots or very thin ice are not present in the EM thickness distribution, the total thickness for 'GPS - laser' is still quite good. Only in (c) and (d) it does not perfectly match the EM thickness for ice thicknesses below the modal value of first-year ice.

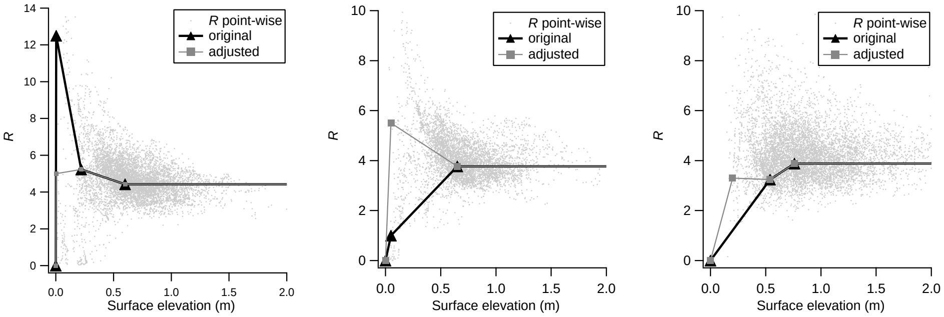

(a) Dec. 14, leg1 north (b) Dec. 9, leg1 (c) Dec. 14, leg4 north

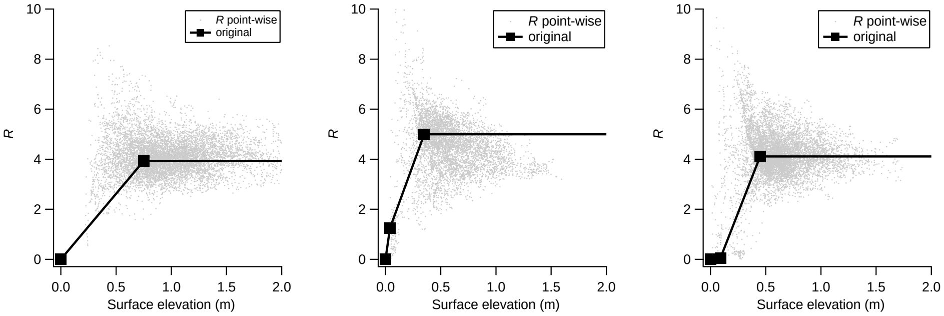

(d) Dec. 15, leg5 west (e) Dec. 14, leg2 north (f) Dec. 14, leg3 north

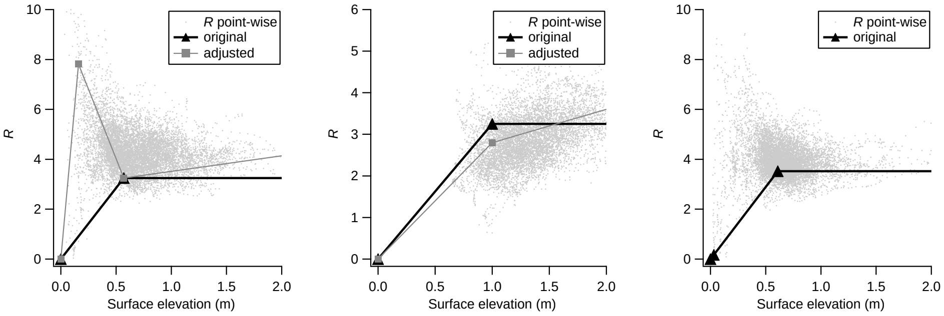

(g) Dec. 18, leg6 (h) Dec. 15, leg3, west (i) Dec. 14, leg1 south

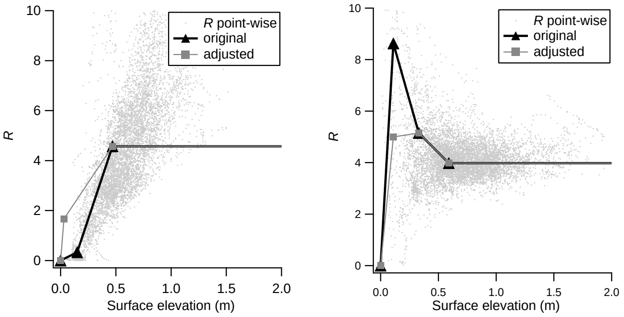

(j) Dec. 14, leg6 north (k) Dec. 14, leg6 south

Figure 4.16: Relationship of R versus surface elevation for the profiles in the Weddell Sea.

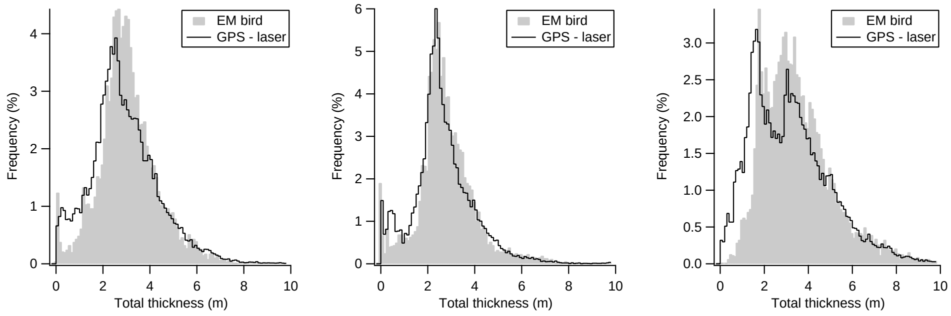

(a) Dec. 14, leg1 north

(b) Dec. 9, leg1

(c) Dec. 14, leg4 north

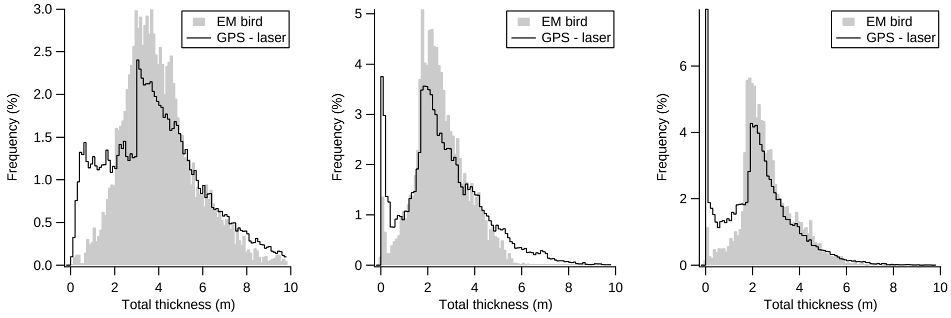

(d) Dec. 15, leg5 west

(e) Dec. 14, leg2 north

(f) Dec. 14, leg3 north

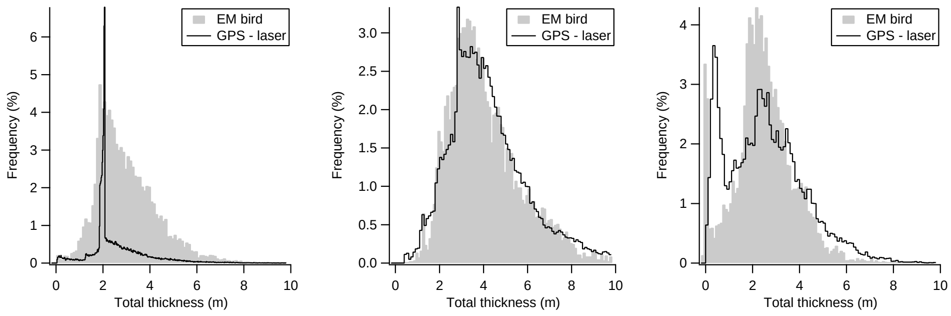

(g) Dec. 18, leg6

(h) Dec. 15, leg3, west

(i) Dec. 14, leg1 south

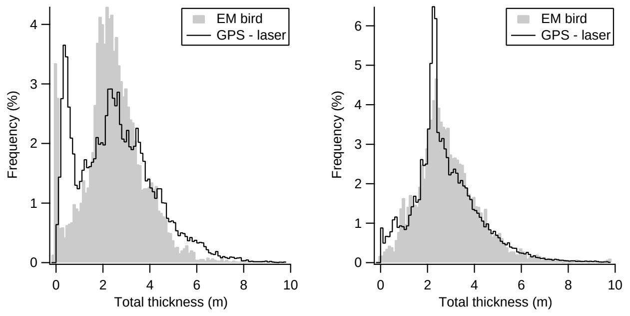

(j) Dec. 14, leg6 north

(k) Dec. 14, leg6 south

Figure 4.17: Histograms of total thickness ('GPS - laser') calculated from surface elevation with *R*-values from the histogram modes summarized in Table 4.3 and displayed in Fig. 4.16 and histograms of EM thickness ('EM bird') for the profiles in the Weddell Sea.

4.2.3 Total Thickness from Fitting Functions

The possibility of transforming surface elevation to total thickness using the point-wise fitting function was described in Section 3.6.2. As was done for the Arctic in Section 4.1.3, the entire profiles of surface elevation for which the histograms are shown in Fig. 4.14 and Fig. 4.15 were divided into 40 m long sections for which the standard deviation (stdev) and mean was calculated (see Section 3.6.2). The thresholds of the EM thickness, standard deviation and mean of surface elevation for creating the three thickness classes are summarized in Table 4.4. Depending on the presence of the modes, i. e. thinner or thicker first-year or multi-year ice, the EM thickness threshold for first-year ice was set to that for multi-year ice or changed equivalently.

Table 4.4: Thresholds of EM thickness, standard deviation (stdev), and mean of surface elevation for open water, first-year ice, and multi-year ice depending on the presence of thickness modes in the Antarctic.

Thickness class	EM thickness (m)	Stdev (m)	Mean (m)
Open water	< 0.1	≤ 0.08	< 0.1
First-year ice	$0.3 < \quad \leq 2.2$	≤ 0.4	$0.1 \leq \quad \leq 0.6$
Multi-year ice	> 2.2	≤ 0.6	$0.6 < \quad \leq 1.6$

According to the thresholds for standard deviation and mean, surface elevation data of the entire profile were assigned to one of the three thickness classes for which the equivalent fitting functions from Eq. (3.6.4) – Eq. (3.6.11) were used to calculate R. Subsequently, surface elevation was multiplied by the equivalent R yielding total thickness.

In Section 4.2.1 three combinations of ice thicknesses were described. Each combination or group consists of a set of fitting functions summarized in Eq. (3.6.4) – Eq. (3.6.11). According to the number and value of the modes present in the surface elevation histogram, the equivalent fitting function was taken from the three sets shown in Eq. (3.6.4) – Eq. (3.6.11). For some surface elevation profiles single fitting functions from different sets had to be applied, since the surface elevation showed another combination of modes not comprised by the three groups. The last column in Table 4.3 summarizes which fitting equations, dependent on the modes, were taken to transform surface elevation.

Fig. 4.18 shows the calculated total thickness for the profiles in the Weddell Sea as 'GPS - laser' with R being derived from the fitting functions with the equivalent combinations summarized in Table 4.3. Considering Fig. 4.18 (b) and comparing the result for 'GPS - laser' with the result for 'GPS - laser' in Fig. 4.17 (b), no improvement is visible, rather a worse agreement with the EM thickness is seen. The fitting equations from 'Dec. 14, leg1 north' was chosen, since the multi-year surface elevation mode of 0.6 m (see Table 4.3) is closer to the multi-year surface elevation mode in (b) (0.65 m) than the multi-year surface elevation mode in 'Dec. 14, leg4 north' (0.76 m), which would have been the other option.

Considering Fig. 4.18 (c) and comparing the result for 'GPS - laser' with the result for 'GPS - laser' in Fig. 4.17 (c), an improvement is visible regarding the EM thickness distribution. In Fig. 4.18 (c) the first-year ice mode of 'GPS - laser' matches the value and the shape of the equivalent EM thickness mode better than in Fig. 4.17 (c).

Further, Fig. 4.18 (d) shows also an improvement regarding the agreement of 'GPS - laser' with 'EM bird' compared to Fig. 4.17 (d). In this case, the multi-year ice mode of surface elevation (0.75 m) matches perfectly the equivalent mode of 'Dec. 14, leg4 north' (0.76 m).

Nearly the same is true for Fig. 4.18 (h), but the mode of surface elevation (1.0 m) is different from the mode in Dec. 14, leg4 north (0.76 m).

Total thickness shown in Fig. 4.18 (k) was derived by combining the fitting equations from two groups: the first-year ice mode of surface elevation (0.33 m) was taken from 'Dec. 14, leg4 north' (0.54 m), and for the multi-year ice mode (0.59 m) the fitting equation from 'Dec. 14, leg1 south' (0.61 m) was used. The thinner first-year ice mode (0.11 m) was neglected since none of the above fitting equations was adequate. The resulting total thickness in Fig. 4.18 (k) is considerably better than in Fig. 4.17 (k), although an offset of about 0.2 m is seen compared to the EM thickness distribution. However, the first-year ice mode agrees better with the equivalent mode of the EM thickness distribution.

With respect to Table 4.1 in Section 4.1.1, in Table 4.5 mean *R*-values are displayed for four profiles, arbitrarily chosen, in the Antarctic. Additionally, mean *R*-values are listed for the profiles in the Arctic. The mean *R*-values for the profiles in the Antarctic range from 3.58 to 4.6 whereas *R*-values between 5.20 and 7.26 are shown for the Arctic. This underlines the difficulty of finding one set of fitting functions that is valid for the Arctic AND the Antarctic.

Table 4.5: Mean *R*-values for the three profiles in the Antarctic marked in Table 4.3 and described in Section 4.2.1 and four profiles in the Arctic.

Profile	**Mean *R*-values**
Dec. 14, leg1 north	4.60
Dec. 14, leg4 north	3.62
Dec. 14, leg1 south	3.58
North (b)	5.20
North (c)	5.23
Lincoln Sea (a)	7.26
Lincoln Sea (b)	5.35

4.2.4 Differences in Total Thickness – Arctic and Antarctic

In Section 3.6.3 the error of total thickness was approximated for one profile in the Arctic. Here, the difference between one profile in the Arctic and one in the Antarctic is shown with respect to ice volume that was calculated over an area of 100 x 100 m from the thickness distributions of the GPS/laser derived total thickness and EM thickness. Thus, it was possible to calculate the deviation of the ice volumes whereas the volume derived from EM thickness was taken as reference. Furthermore, two approaches of deriving total thickness were considered: total thickness from the histogram modes and total thickness from the fitting functions. The ice volume was calculated for each bin of the thickness distribution using the percentage value of total thickness with respect to the area of

100 x 100 m. In Table 4.6 the ice volumes of total thickness ('Volume GPS/laser') and EM thickness ('Volume EM bird') as well as their deviations of the former to the latter are summarized. In addition to the volumes for total thickness derived from the histogram modes, the volumes are shown for total thickness from the fitting functions (for the '2 modes fit'). Regarding the two chosen profiles, the ice volume is considerably higher in the Arctic than in the Antarctic. Comparing the deviations between ice volumes of total thickness derived from the histogram modes and from the fitting functions for both polar regions, the deviation is negative for the first and positive for the second approach. Further, a smaller deviation is recognizable if the total thickness is derived from the fitting functions.

Table 4.6: Ice volumes over 100 x 100 m for total thickness and EM thickness and deviation with respect to EM thickness in the Arctic and Antarctic.

Profile	Volume GPS/laser (m^3)	Volume EM bird (m^3)	Deviation (%)
Arctic			
May 13, north (c), modes	**45434**	**48196**	**-5.7**
May 13, north (c), fitting	**49410**	**48196**	**+2.5**
Antarctic			
Dec. 15, leg5 west, modes	**37864**	**39555**	**-4.3**
Dec. 15, leg5 west, fitting	**39577**	**39555**	**+0.1**

However, general conclusions cannot be drawn from this investigation since only one profile in each polar region was considered.

4.2.5 Summary

- Surface elevation profiles for which open water spots or very thin ice are not present, the GPS/laser derived total thickness is still quite good compared to the EM thickness. But this good fit was only possible with the known EM thickness.

- The use of the coincidently measured EM thickness allowed slight adjustment of *R* from the modes to achieve a better match between the GPS/laser derived total thickness and EM thickness. Here, it was mainly the *R*-value of the zero mode that was adjusted for seven profiles.

- According to the different thickness modes in surface elevation, three groups with certain mode combinations were established: (1) three modes for open water, first-year, and multi-year ice, (2) two modes for thicker first-year, and thicker multi-year ice, and (3) two modes for open water, and intermediate multi-year ice. For each group, a set of fitting functions was created.

- Depending on the modes present in the histogram for surface elevation, only single fitting functions were taken from one of the group or a combination from two groups. Generally, a better match of the GPS/laser derived total thickness was achieved than with the approach of using the histogram modes.

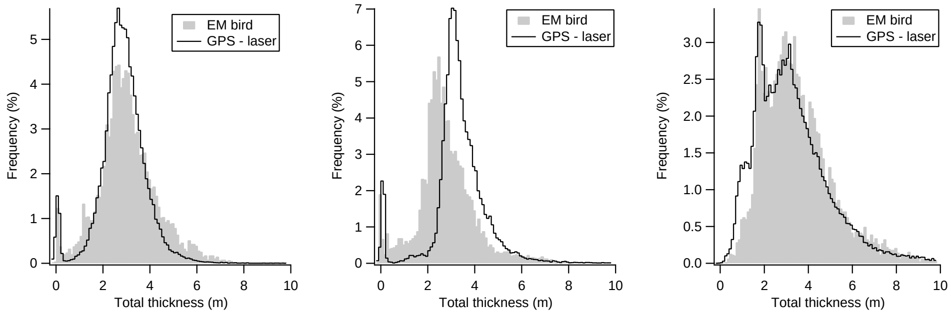

(a) Dec. 14, leg1 north

(b) Dec. 9, leg1

(c) Dec. 14, leg4 north

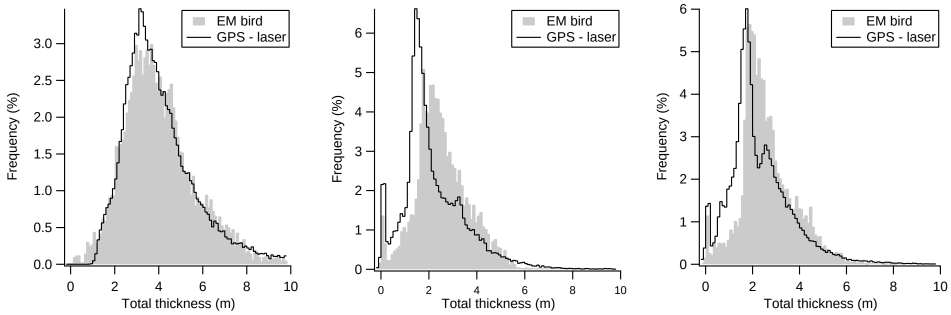

(d) Dec. 14, leg5 west

(e) Dec. 14, leg2 north

(f) Dec. 14, leg3 north

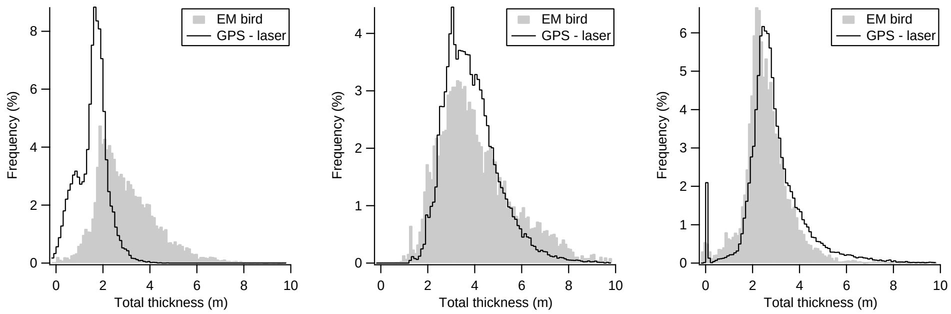

(g) Dec. 18, leg6

(h) Dec. 14, leg3 west

(i) Dec. 14, leg1 south

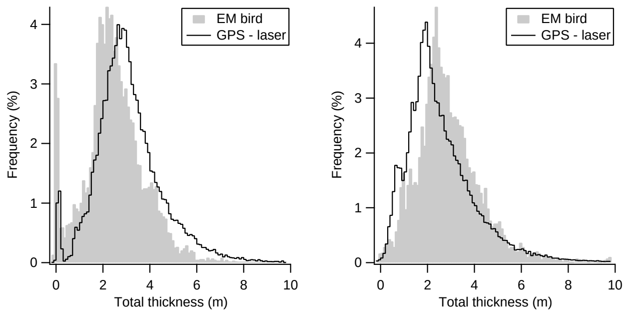

(j) Dec. 14, leg6 north

(k) Dec. 14, leg6 south

Figure 4.18: Histograms of total thickness ('GPS - laser') for the transformed surface elevation with the fitting functions summarized in Eq. (3.6.4) – Eq. (3.6.11) (see Table 4.3) and histograms of total thickness for the measured EM thickness ('EM bird') for the profiles in the Weddell Sea.

4.3 Relevance of Results for ICESat Data

To validate satellite missions, independent measurements are necessary along the same track on which the satellite is collecting data (FORSBERG & SKOURUP, 2005). Since no coincident measurements were conducted with ICESat (see Section 1.3) during this study, here, ICESat data were simulated and used subsequently to be validated with the GPS height and laser height measurements by the EM bird. The problem, however, is the large laser footprint of ICESat (60 m) compared to the laser footprint of the EM bird that is negligible due to the low operating altitude of the EM bird. As a consequence, narrow leads and sections of thin ice respectively which are detected by the EM bird laser are not "seen" by ICESat as it is shown below. In this case, the same profile was considered as that used to generate the fitting functions in the Lincoln Sea (see Section 4.1.3). Two approaches of simulating ICESat data are possible (see Fig. 4.19 a and b) while the first was used as reference to illustrate the differences of the second approach that simulates the derivation of real ICESat surface elevation more realistically:

(1) The surface elevation derived from the difference between the GPS height and laser height 'GPS - laser' with the EM bird setup is averaged and gridded to match the ICESat footprint of roughly 60 m with the spacing of about 172 m. In other words, a mean surface elevation along 60 m is calculated every 172 m. The resulting 'ICESat Surface elevation' is shown in Fig. 4.19 (a) and the equivalent histogram is displayed in Fig. 4.20 (left).

(2) The difference between GPS height and laser height (ground elevation, see Section 3.4.1) is averaged and gridded to match the footprint and spacing, labeled 'ICESat ground elevation'. In the latter, the method of finding the lowest level (see Section 3.5.1) had to be applied again to derive surface elevation. However, the establishment of the lowest level, and hence surface elevation, was only possible with the known EM thickness: If the EM thickness data showed thicknesses of about 0.1 m, this spot was marked in the ICESat ground elevation even if the ICESat ground elevation itself did not show a lead but was a local minimum as indicated at the distance of 1400 m by the "black square" in Fig. 4.19 (b). Problems occur due to the fact that leads are generally very narrow and "disappear" in 'ICESat ground elevation' through the averaging of ground elevation data. In Fig. 4.19 (b), a lead in 'GPS - laser ground elevation' is visible between roughly 1200 m and 1400 m, that is shown in the photograph in (c). (The photograph, taken across-track, shows the side of the lead that is narrower than the section being surveyed.) In 'ICESat ground elevation', however, this lead is no longer identifiable. As a consequence, the estimated sea level can be too high. In Fig. 4.19 (b), the lowest point in 'ICESat ground elevation' near 1400 m is marked as a lowest value in 'ICESat lowest level' and thus misrepresents the sea level as higher than the actual 'GPS - laser lowest level' detected in the 'GPS - laser ground elevation' (see legend from Fig. 4.19 a). Thus, an error of about 0.1 m is easily induced in ICESat surface elevation. The result for surface elevation, labeled 'ICESat surface elevation with lowest level' is also shown in (b). In the displayed section, an offset of about 0.1 m is visible between 'ICESat Surface elevation' and 'ICESat surface elevation with lowest level'.

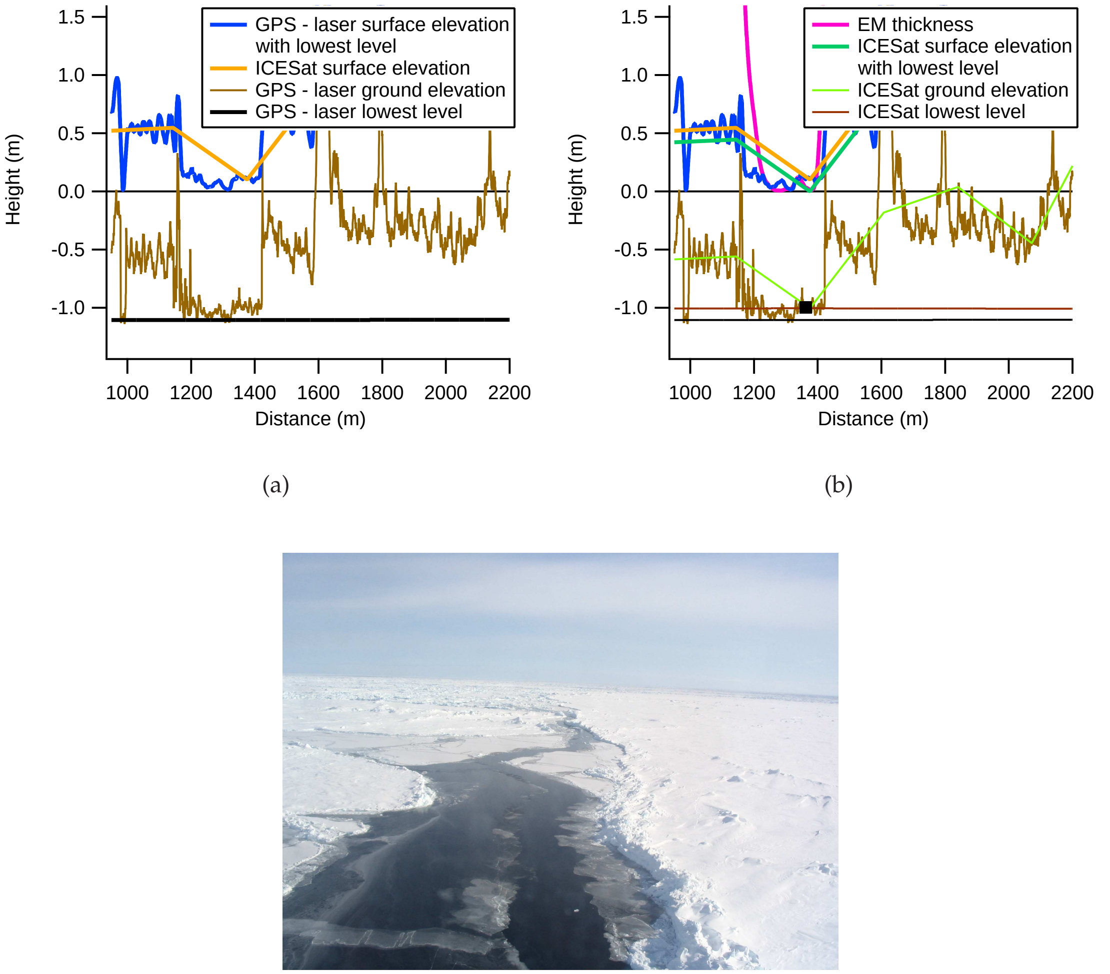

(a)

(b)

(c)

Figure 4.19: Profile of simulated ICESat data obtained with approach (1) and (2) (a and b). Legend of (a) refers also to (b). Photograph (c) shows lead between 1200 m and 1400 m in (a) and (b), taken across-track of flight direction.

Comparing the histograms of the ‘ICESat surface elevation’ (Fig. 4.19 a and b) derived with approach (1) and the surface elevation ‘GPS - laser’, the two modes for first-year ice and multi-year ice are clearly visible in Fig. 4.20 (left). However, the peak of the multi-year ice mode in the ICESat surface elevation is shifted to 0.1 m thicker surface elevations. The coarser resolution of the ICESat surface elevation required the use of a wider bin-width of 0.05 m than in Fig. 4.3 (b). To derive total thickness as described in Section 3.6.1, the modes of ICESat surface elevation at 0.05 m, 0.35 m and 0.75 m were used for creating R. The result of total thickness for approach (1) is shown in Fig. 4.20 (right). Regarding the EM thickness histogram in Fig. 4.20 (right), the zero mode in ‘ICESat’ is masked by thinner first-year ice (see Section 4.1.1). The two ice modes are visible but the multi-year ice mode is slightly shifted to higher numbers of about 0.1 m due to a similar shift in the ICESat surface elevation.

Regarding approach (2), the histogram derived from ‘ICESat surface elevation with lowest level’ (Fig. 4.19 b) is shown in Fig. 4.21 (a). As opposed to the ICESat

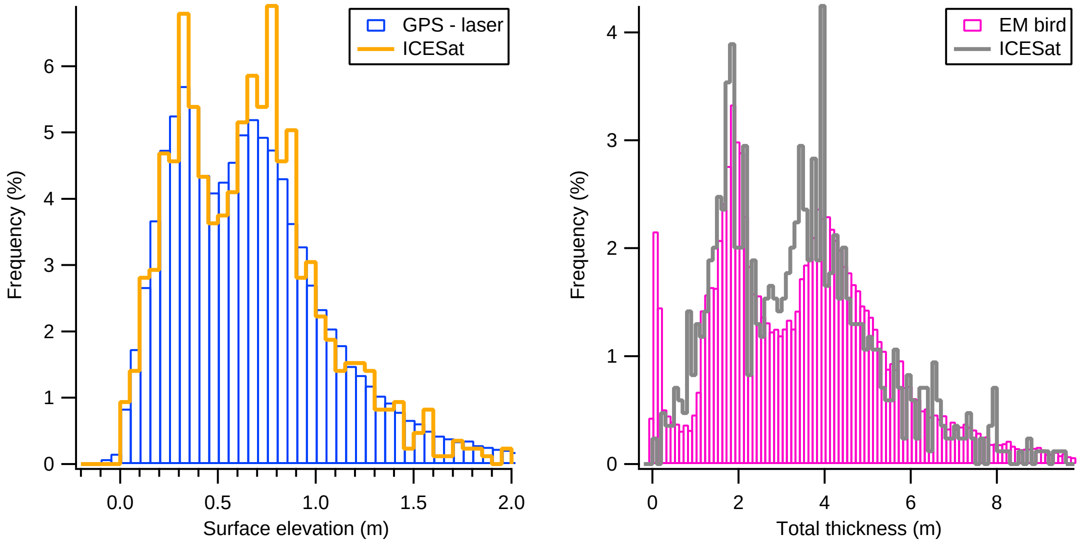

Figure 4.20: Histograms of ICESat surface elevation derived with approach (1) and surface elevation derived from GPS/laser (left) and total thickness from ICESat surface elevation and EM bird (right).

surface elevation distribution in Fig. 4.20 (left), the first-year ice mode is difficult to identify. Assuming, that no coincidently measured EM thickness is available, this surface elevation was transformed by applying the mean R-values for open water, first-year ice, and multi-year ice (see Section 4.1.2.1) and by applying the constant $R = 5.889$ (see Section 2.2.2). The results for total thickness are shown in Fig. 4.21 (b) and (c). In (b), a similar gap is visible as in Fig. 4.9 (d). The peak of the modes disagree with the equivalent modes present in the EM thickness (see Fig. 4.20, right). The same is true for the total thickness distribution in (c). Here, the multi-year ice mode is barely identifiable.

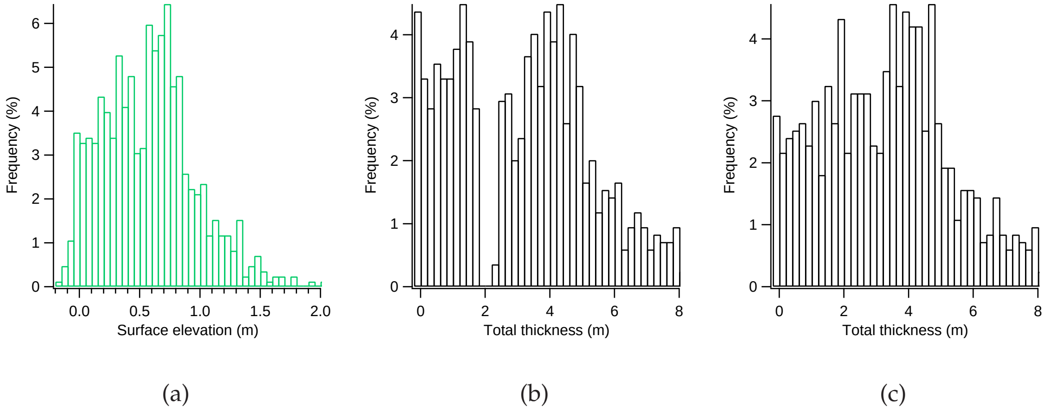

(a) (b) (c)

Figure 4.21: Histograms of surface elevation (a) derived with approach (1) and total thickness derived with three mean R-values (b) and $R = 5.889$ (c).

FORSBERG & SKOURUP (2005) found a steep decrease in the tail of the multi-year ice mode and concluded that ICESat underestimates pressure ridges. However, comparing the ICESat surface elevation and total thickness in Fig. 4.20 and Fig. 4.21 with the 'GPS - laser' surface elevation and EM thickness in Fig. 4.20, a similar steep decrease cannot be seen except for a slightly less uniform ending of the tail. Thus, the large footprint from ICESat that smoothes surface roughness and especially pressure ridges (as seen in Fig. 4.19) is compensated by the laser footprint of the EM bird setup that is considerably smaller and which does not smooth surface roughness to this extent.

In general, the applied steps of deriving total thickness work well for simulated ICESat surface elevation data obtained by approach (1) and give comparable results to the EM thickness. Regarding the more realistically derived ICESat surface elevation of approach (2), this method lacks the fact of non-detectable leads in ICESat ground elevation. Without coincident thickness measurements, it is hardly possible to detect open water or very thin ice. Therefore, the GPS/laser measurements with the EM bird setup are highly relevant for validating space-borne satellite data.

4.4 Coincident Flight of EM Bird and Twin Otter

The coincident flight of the EM bird with the internally mounted laser and the Twin Otter, that was equipped with a laser scanner from the DNSC, represents unique data sets obtained by two independent laser altimeter systems. Thus, a comparison between the two data sets allows differences and similarities to be seen in the derived surface elevation at large-scale (entire profile) and small-scale (e. g., single leads). Further, differences and similarities can be investigated in the lowest levels[2] (see Section 3.5.1) which were detected independently by two different operators. The use of different geoid models[3] had no effects on the results. In the following, results of the coincident flights in the Lincoln Sea are presented, whereas the profile of the EM bird is equal to that in Section 3.5.1 but shorter.

To assure that both laser altimeters "see" the same ice, the helicopter with the EM bird took off about 20 minutes earlier than the Twin Otter. Thus, the Twin Otter passed the helicopter near the middle of the pre-defined flight leg. In total, about a 135 km long section was surveyed coincidently. However, the profiles obtained from the EM bird and the laser scanner were shortened for analysis to 20 km before and 20 km after the Twin Otter passed the helicopter to minimize the influence of ice drift, and thus to achieve a good correlation between both data sets.

To allow a direct comparison between the surface elevation derived from the laser scanner and GPS/laser from the EM bird setup, the EM bird track was extracted from the laser scanner swath to find the corresponding surface elevations in the laser scanner data.

At the end of this section, results of a direct comparison of surface elevation exclusively over first-year ice are shown. Here, the beginning of the profile in the south was ideal since this ice was immobile, and hence, no shift is present between the derived surface elevations from the DNSC scanner and GPS/laser from the EM bird. Thus, another profile section was used for analysis.

4.4.1 Extraction and Correlation of Surface Elevation

At first, the laser data of the EM bird were reduced to match the grid of the laser scanner data (5 x 5 m). The corresponding laser scanner surface elevation was retrieved by a nearest neighbor search along the EM bird track. In Fig. 4.22, the laser scanner track, the EM bird track, and the extracted EM bird track are shown in color-coded surface elevations. The width of the stripe 'DNSC scanner' in (a) corresponds to the swath width of the laser scanner, which was approximately 120 m. The narrower stripe on the right edge represents the EM bird track with the derived surface elevations (squares) from 'GPS - laser' and the extracted EM bird track with the equivalent surface elevations from the laser scanner (crosses). In the enlarged graph in (b), the single data points are better visible. The white area in (b) represents open water in which the laser scanner sensor did not receive a signal. The laser altimeter inside the EM bird, however, did receive a signal indicated by squares representing surface elevation between 0 m and 0.2 m. Since no equivalent surface elevations were found in the laser scan-

---

[2] The detected lowest level in the laser scanner data was also kindly made available by DNSC.

[3] A geoid model from 2004 and 2006 was used for the DNSC data and the laser data from the EM bird, respectively.

ner data to match these data points in the EM track, the squares are not marked by crosses within the white area. North of 82.3346° N and south of 82.3338° N, "squares with crosses" are visible indicating the extracted surface elevation from the laser scanner data for the EM bird track.

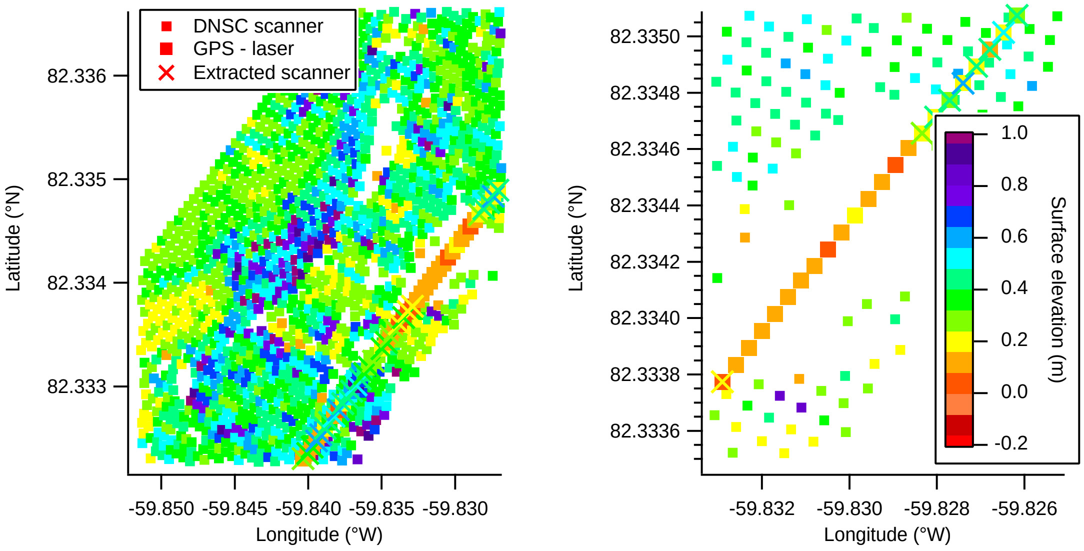

(a) (b)

Figure 4.22: Color-coded surface elevations from the DNSC laser scanner, GPS/laser, and the extracted laser scanner data for the EM bird track for the coincidently flown profile in the Lincoln Sea (a). A zoomed-in section of (a) is shown in (b). Legend and color scale refer to (a) and (b), respectively.

Fig. 4.23 shows profile sections about 20 km before (left) and about 20 km after the Twin Otter passed the helicopter (right). In the left graph, the vertical bar at 82.634° N indicates a change from uncorrelated to correlated surface elevations. In the right graph, the equivalent is shown for surface elevations which are no longer correlated. The changes in correlation are caused by the ice drift. Within a certain range, here approximately 40 km, the effects of ice drift are smaller than for the rest of the profile, whereas the length of this range is dependent on the ice drift speed. The shorter this range is centered around the location where the Twin Otter passed the helicopter, the smaller the ice drift effects are and the better the correlation is. In Fig. 4.25 (a), the surface elevation of 'GPS - laser' and 'extracted' from the laser scanner is shown along the 40 km of best correlation. The location where the Twin Otter passed the helicopter, is marked in Fig. 4.25 (a) and (b). The graph in (b) shows this section enlarged.

In Fig. 4.25 (c), the lowest levels[4] detected in the ground elevation of 'GPS - laser' and 'extracted scanner' are shown for the same section as in Fig. 4.25 (a). The mean amounts to -1.23 m with a standard deviation of 0.03 m for 'GPS - laser' and to -1.20 m with a standard deviation of 0.05 m for the DNSC laser scanner. Due to the good agreement of the mean lowest values, the detection of the lowest level by linear interpolation was considered to be sufficient.

---

[4] The 'DNSC lowest level' data were extracted from the scanner swath data similarly to the 'extracted scanner' surface elevation data.

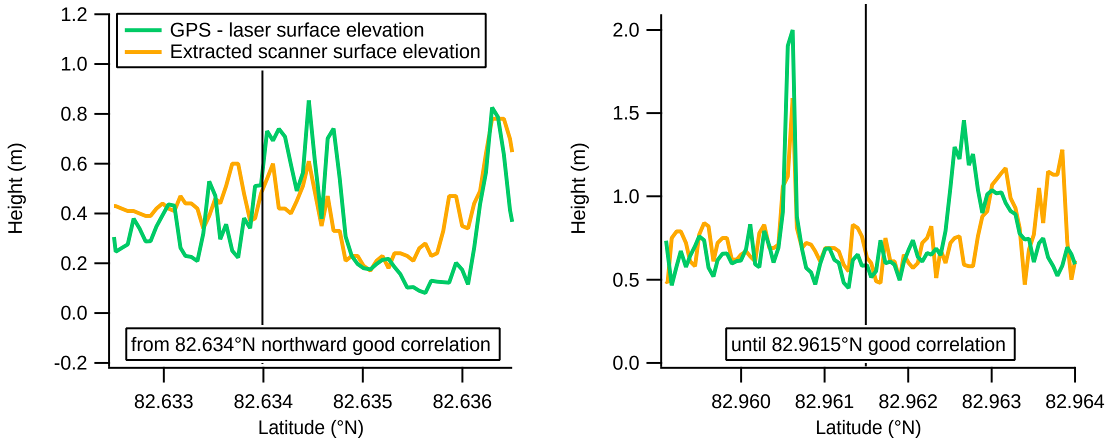

Figure 4.23: Surface elevation from GPS/laser and DNSC laser scanner for a section 20 km before (left) and 20 km after the Twin Otter passed the helicopter (right). Legend for the right graph is the same as for the left graph.

The corresponding histograms for the section displayed in Fig. 4.25 (a) are shown in Fig. 4.25 (d). In the histogram of the 'extracted scanner' two spikes are visible near 0.7 m and 1.0 m meaning that these surface elevations do not exist in the equivalent profile in Fig. 4.25 (a). The mean value of multi-year ice for the extracted laser scanner surface elevation amounts to 0.81 m, whereas it reaches 0.70 m for 'GPS - laser' surface elevation at an equal standard deviation of 0.39 m.

Further, hardly any surface elevations near 0 m are visible in the surface elevation histogram of the extracted laser scanner. However, in the 'GPS - laser' histogram one mode at around 0.05 m and one at around 0.15 m are visible and are confirmed by the equivalent modes in the EM thickness histogram in Fig. 4.24 (left). The difference between both surface elevation histograms in Fig. 4.25 (d) is displayed in the right graph of Fig. 4.24. The histogram confirms the shift of roughly 0.1 m that is equal to the shift between the modes seen in Fig. 4.25 (d) and to the difference in the mean values mentioned before.

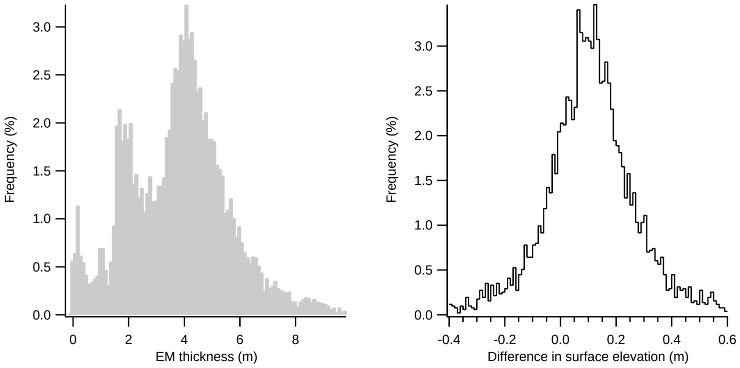

Figure 4.24: Histograms of EM thickness (left) and difference in surface elevation of Fig. 4.25 for the 40 km long section before and after the Twin Otter passed the helicopter (right).

4.4.2 Comparisons at Lead Crossings

Fig. 4.26 shows a profile section in the vicinity in which the Twin Otter overtakes the helicopter. In (a), a white area within the color-coded surface elevations is visible indicating a lead. This lead is shown in the photograph (c) with the shadow of the helicopter, front right, while flying to the north. The squares of the DNSC scanner within the white area indicate the nadir-looking beam of the laser scanner. As opposed to signals near the edge of the laser swath (Fig. 4.22), the center beam returns signals to the sensor with less data loss even above open water or very thin ice. However, even within the center beam some smaller white areas are visible. Regarding the extracted surface elevation, still some "squares without crosses" are visible meaning that no surface elevation was available in the laser scanner data although the EM bird track is close to the nadir-looking beam. In Section 4.4.1 it was mentioned that "white areas" in the laser scanner swath indicate open water from which the sensor did not receive a signal. However, in the photograph (c) very thin ice is visible on the lead, especially to the left side that corresponds to the white area left of the EM bird track in (a). Although this white area is outside the nadir-looking beam of the laser scanner, its sensor should still receive signals if it was affected only by open water patches. On the other hand, the laser of the EM bird did receive signals throughout the lead crossing.

In Fig. 4.26 (b), a gap in surface elevation of the 'extracted scanner' is visible representing the "missing crosses" in (a). The EM thickness of around 0 m also indicates open water and very thin ice, respectively. However, to the left and to the right side of the gap, surface elevations of about 0.1 m are recognized in the 'extracted scanner' data. Considering the 'GPS - laser surface elevation', values of about 0.1 m are also visible which is confirmed by the very thin ice seen in the photograph (c). Thus, the good agreement between both surface elevation data sets is shown. The vertical bar in (b) indicates where the photograph (c) was taken. The photograph in (d) shows the Twin Otter above the helicopter with the helicopter antenna to the right.

Fig. 4.27 shows another profile section with a clear change in surface elevation. As opposed to Fig. 4.26, the lead in Fig. 4.27 (a) is represented by "green squares" in color-coded surface elevation indicating either a thicker, or a snow-covered refrozen lead. The photograph in Fig. 4.27 (c), taken across-track, confirms a snow-covered lead. The exposure of the photograph is indicated by the vertical bar in (b). The peak in (b) at about 82.7205° N coincides with the "purple crosses" in (a). Additionally, ground elevation derived with a geoid model from 2004 (04) and 2006 (06) is shown together with the lowest levels of 'GPS - laser' and 'extracted scanner'. Obviously, the deviation of the lowest levels is negligible for this section, although a difference of about 0.1 m between the ground elevations is visible and mapped in the surface elevations. However, even if the 'GPS - laser' surface elevation was derived with the geoid model from 2004, the lowest level would be different but the derived surface elevation would still be the same.

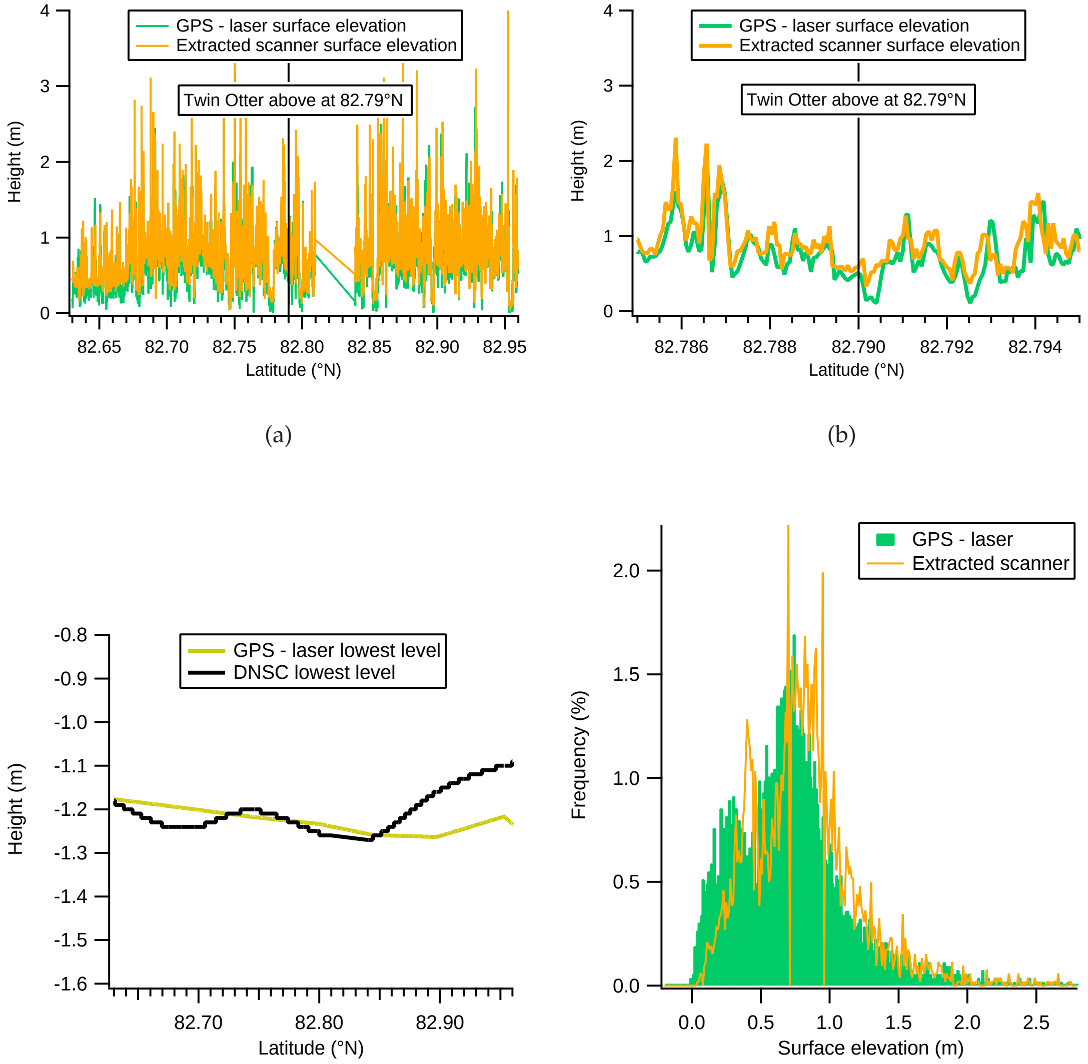

(a) (b)

(c) (d)

Figure 4.25: Profile (a), zoomed-in (b), lowest levels (c), and histograms (d) of surface elevation from the difference 'GPS - laser' and DNSC laser scanner for a 40 km long section before and after the Twin Otter passed the helicopter.

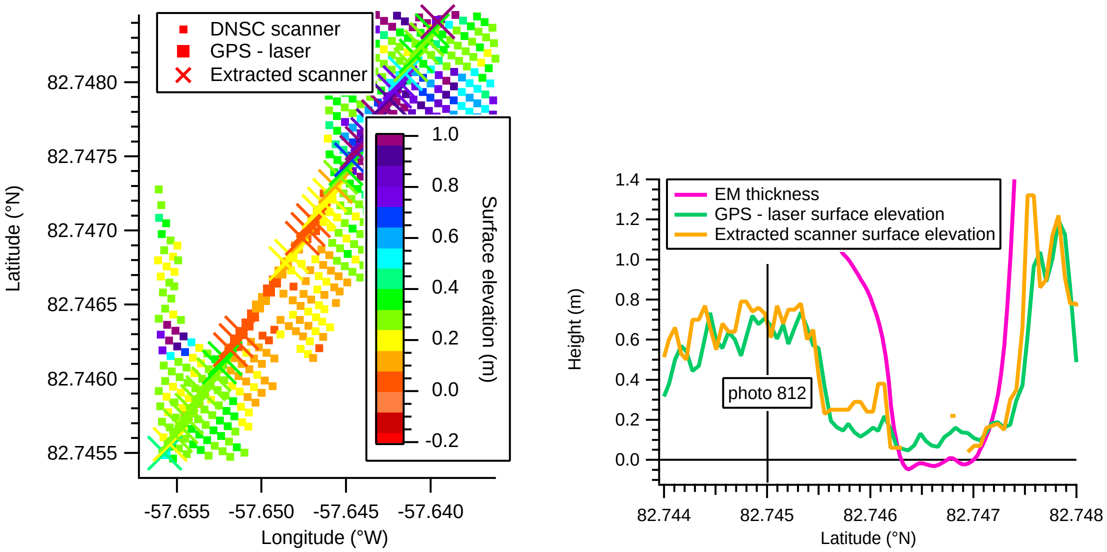

(a) Color-coded surface elevations

(b) Section of photo 812

(c) Photo 812

(d) Twin Otter

Figure 4.26: Color-coded surface elevations from the DNSC laser scanner, GPS/laser, and extracted laser scanner for the EM bird track across an open lead (a), and surface elevation and EM thickness profiles (b) for the section in (a). The photograph (c) shows the lead from (a) and (b), and (d) the Twin Otter passing the helicopter overhead with the helicopter antenna on the right.

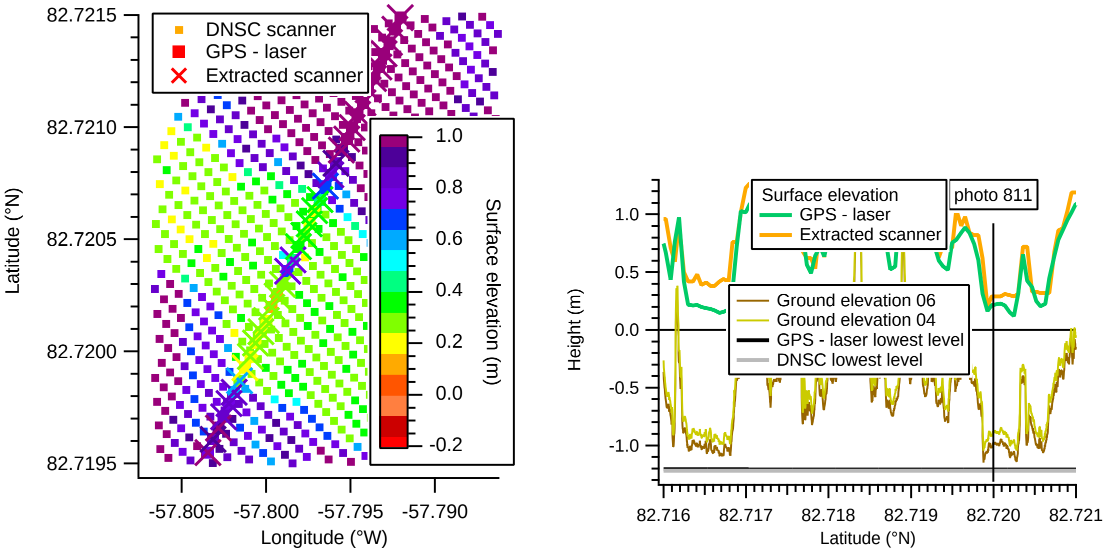

(a) Snow-covered lead

(b)

(c) Photo 811

Figure 4.27: Color-coded surface elevations from the DNSC laser scanner, GPS/laser, and the extracted laser scanner data for the EM bird track across a refrozen lead with a homogeneous snow cover (a) confirmed by the photograph (c), taken across-track. The exposure of the photograph is marked in (b).

4.4.3 Comparison over immobile First-Year Ice

Fig. 4.28 shows a section of first-year ice at the beginning of the profile in the south. Displayed are surface elevations from the ‘extracted scanner’ and ‘GPS - laser’, as well as the corresponding lowest levels (left). Additionally, the EM thickness is shown whose original EM thickness was subtracted by 1.5 m to achieve better visibility in the graph. Similarly, 1.0 m was added to the original lowest levels. Regarding the graph on the left, two prominent pressure ridges are seen in the EM thickness at about 82.057° N and 82.064° N. In surface elevation, these two ridges are also visible confirming immobile ice conditions. Further, a vertical difference of approximately 0.2 m is seen between the lowest levels of the ‘extracted scanner’ and ‘GPS - laser’ (left). Since the behavior of the lowest levels is the same (straight horizontal), differences between the surface elevations are directly related to differences in the laser measurements. Regarding the zoomed-in graph on the right, prominent pressure ridges are seen in the EM thickness at about 82.0613° N, 82.0618° N, 82.0624° N, and 82.0627° N which are mapped in the ‘GPS - laser surface elevation’. Prominent dips in EM thickness are seen at about 82.0615° N and 82.0626° N which are also mapped in the surface elevation of ‘GPS - laser’. However, these pressure ridges and dips are not visible in surface elevation of the ‘extracted scanner’ (except the peak at 82.0618° N). Coincidently mapped features in both surface elevations are seen at about 82.0600° N, 82.0603° N, 82.0609° N, and 82.0618° N. The largest deviation between the two surface elevations is present between 82.0612° N and 82.0615° N. Here, surface elevation of the ‘GPS - laser’ ranges roughly between 0.2 m and 0.45 m whereas the surface elevation of the ‘extracted scanner’ oscillates around 0.22 m. This is also seen in Fig. 4.29 on the left with constant surface elevations around 0.22 m for the ‘DNSC scanner’ and ‘extracted scanner’ respectively, and slightly varying values for the ‘GPS - laser’ surface elevation. Considering the resolution of the ‘extracted scanner’ of about 5 m, it is larger than the footprint of the laser inside the EM bird but still about 1/10 smaller than the EM bird footprint, which in contrast, is capable of resolving smaller pressure ridges and dips in ice thickness.

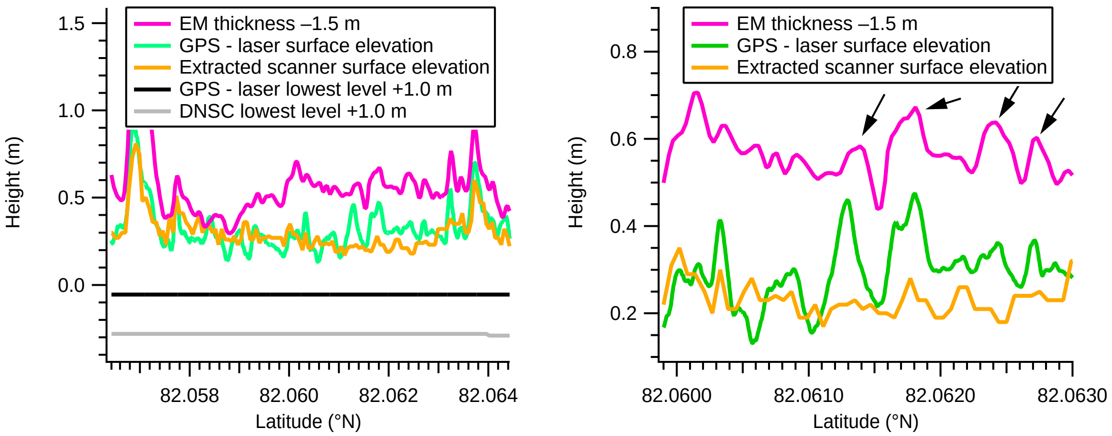

Figure 4.28: Surface elevations of GPS/laser, DNSC laser scanner (‘extracted scanner’), and EM thickness for the coincident flight over first-year ice (left) with a zoomed-in section (right) where arrows indicate prominent pressure ridges. A value of 1.5 m was subtracted from the EM thickness for better visibility. Similarly, the lowest levels were shifted by +1.0 m.

Analyzing the entire profile above first-year ice, a higher mean surface elevation of about 0.22 m with a standard deviation of 0.13 m is detectable for 'GPS-laser' compared to the 'extracted scanner' with a standard deviation of 0.11 m. In Fig. 4.29 (right), the histograms are shown for the surface elevation of 'extracted scanner' and 'GPS-laser'. The peak of the ice mode near 0.28 m is comparable in both histograms and the distributions are in good agreement.

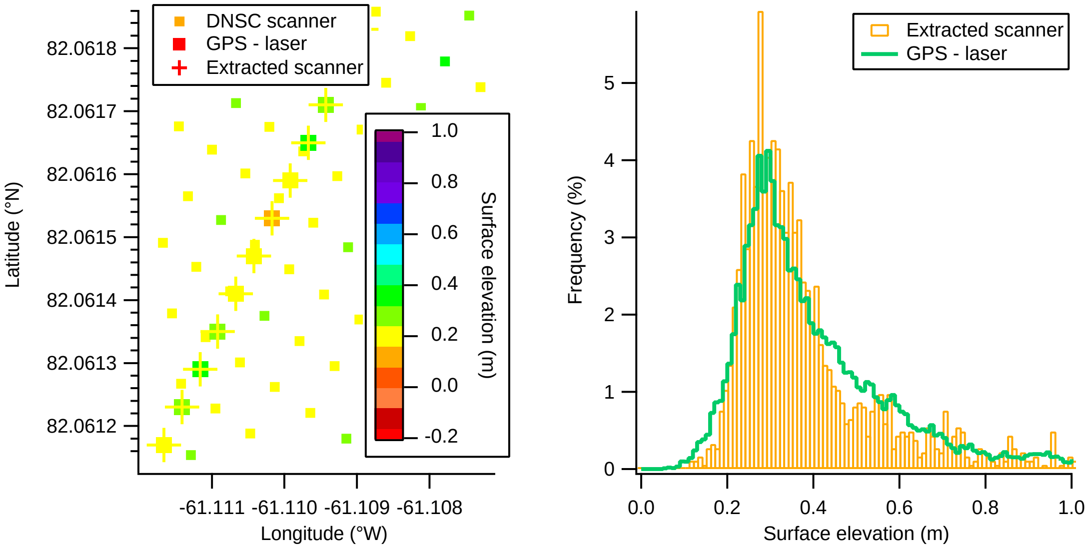

Figure 4.29: Color-coded surface elevations from the DNSC laser scanner, GPS/laser, and extracted laser scanner for the EM bird track (left) and histograms over first-year ice (right).

4.4.4 Summary

- With respect to the coincident profile, 20 km before and 20 km after the Twin Otter passed the helicopter, a slight shift in surface elevation is visible due to slight ice movement. Closer to the "meeting point" this shift is minimized and nearly all surface features are seen in both surface elevation profiles at the same geographical position.

- The range of the minimized ice drift, and hence best correlation between the surface elevation data sets is dependent on the speed of the ice movement. Regarding the execution of future coincident flights, several shorter sections[5] flown coincidently are better than one long section if the ice is moving.

- In the laser scanner data, signals over open water or very thin ice are returned to the sensor with less data loss if they are sent out by the nadir-looking beam. In contrast, the laser signals from the EM bird are always received by the sensor. Consequently, surface elevations below approximately 0.1 m are not included in the extracted laser scanner data if the EM bird track did not coincide with the nadir-looking beam of the laser scanner

- The results of the coincident flight show a good large-scale agreement of surface elevation within the section of best correlation. On the small-scale basis with respect to single surface features such as leads, the extracted laser scanner surface elevations showed on average about 0.1 m larger values than the surface elevation derived from GPS/laser with the EM bird setup.

- Overall, a good agreement is found for the extracted laser scanner surface elevation and GPS/laser over immobile first-year ice. However, not all pressure ridges that are prominent in EM thickness and GPS/laser surface elevation are mapped in the extracted laser scanner surface elevations. Section-wise, the extracted scanner data show almost constant values of surface elevation whereas surface elevation of GPS/laser varies considerably.

- The good agreement between both data sets of surface elevation confirms the quality of the derived GPS/laser surface elevation with the EM bird setup. Although no INS is available to correct for the ground location error, caused by pitch and roll of the EM bird, surface elevation is comparable to the results of a laser scanner on a 5 x 5 m grid that is supported by INS.

---

[5] Sections of up to about 40 km long assuming that the ice drift speed does not exceed that discovered for the analyzed profile.

4.5 Airplane Measurements in the Arctic – NOGRAM

In the following, the results of surface elevation are shown for profiles surveyed during the NOGRAM campaign in 1998, 1999, and 2000. The results have not been transformed to total thickness, because of the problems mentioned in the previous sections and missing ice thickness measurements for comparison. However, the surface elevation data provide important information on their own, and the feasibility of airplane measurements can be shown, as different modes for open water, first-year ice, and multi-year ice must be visible. Moreover, scatterometer[6] data are available for nearly the same months, in which the flights were performed. Thus, it was possible to compare the derived surface elevation with the scatterometer data. From the scatterometer data information can be obtained on the composition of sea ice in terms of thinner or thicker ice as first-year ice shows relatively low backscatter coefficients whereas high backscatter coefficients are attained on less saline multi-year ice. In the scatterometer plots a gradient is visible from thick ice, represented by light colors near the coast of Greenland, to thin ice, represented by dark colors offshore. This gradient is also seen in the surface elevation data derived from laser altimetry.

4.5.1 Estimation of Sea Ice Thickness from Surface Elevation

The chosen flights for this study are shown in Fig. 4.30. They are labeled by a 6-digit number representing the format "yymmdd" (year, month, day). Additionally, scatterometer plots of 25 x 25 km resolution are displayed on May 15, 2000 (left) and May 18, 1998 (right).

May is the beginning of the melting period where the snow melts on the ice floes. The moisture penetration of the upper surface layers causes a general decrease in the backscatter coefficients resulting in similarly low coefficients for first-year ice and multi-year ice. Therefore, the boundary between thinner and thicker ice is seen only as long as the snow has not melted. In both graphs in Fig. 4.30 the boundary between thicker (light colors) and thinner (darker colors) ice is visible. In the left graph, the boundary is closer to the coast of Greenland in the area south of Station Nord whereas in the north at 86° latitude the boundary is recognizable at about the zero meridian. Two years earlier, the boundary in the north was shifted more to the east and in the south more to the west (right graph). Generally, besides the longitudinal shift of the thickness boundary, it is present in every year. White spots indicate data gaps near the land mask.

From Fig. 4.30 it is obvious that the entire profile 000519 lies in an area of homogeneously thin ice. The equivalent histogram for surface elevation in Fig. 4.31 (left) supports this observation as the surface elevation mode derived from airborne laser altimetry shows one mode at about 0.3 m.

Fig. 4.32 shows the typical gradient in ice thickness, and surface elevation respectively, for the coast northeast of Greenland (see Fig. 4.30, left). On the left, the histogram of surface elevation for the entire profile 000515 is shown, whereas

---

[6] Here, data of the Wind Scatterometer (WS) are used that is carried onboard the ERS-2 satellite. The purpose of the Wind Scatterometer is to obtain information on wind speed and direction at the sea surface for incorporation into e. g., climatological data sets. It operates by recording the change in radar reflectivity of the sea due to the perturbation of small ripples by the wind close to the surface. This is possible because the radar backscatter returned to the satellite is modified by wind-driven ripples on the ocean surface and, since the energy in these ripples increases with wind velocity, backscatter increases with wind velocity (http://earth.esa.int/ers/ws/).

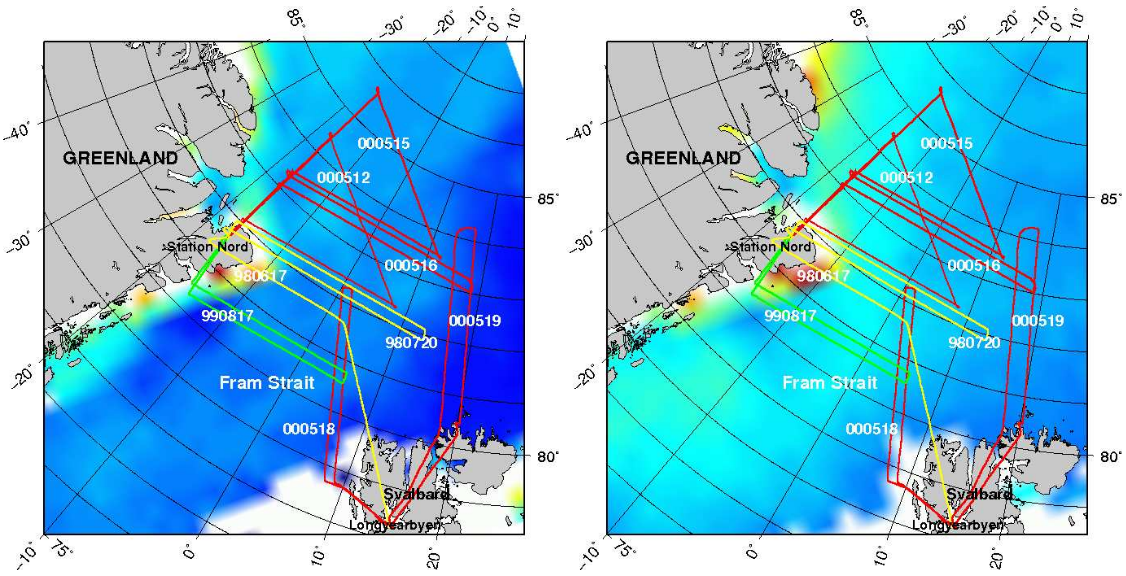

Figure 4.30: Analyzed profiles during the NOGRAM campaign in 1998, 1999, and 2000 underlaid with scatterometer plots on May 15, 2000 (left) and May 18, 1998 (right). Scatterometer plots show boundary between thicker ice (light colors) near the coast of Greenland and thinner ice (darker colors) offshore.

on the right the profile was split in roughly 70 km long sections near the coast, to the north, and to the east. Negative values in the histograms result from the technique of detecting open water as it was described in Section 3.5.3.1. Obviously, the ice condition in the north is similar to that in the east. Both sections show a zero mode, indicating that the ice cover is broken up. Near the coast, two ice modes for thinner and thicker ice are seen together with a long tail, indicating heavy ridging. (All the ice passing northeast of Greenland is pushed against the coast and induces heavy ridging before leaving the Arctic Ocean.)

Profile 000518 lies in a mixed zone of thinner and thicker ice which is shown in the histogram in Fig. 4.31 (right) by the wider ice mode and the additional mode for open water. Considering one leg of profile 000518 (see Fig. 4.30), the opposite is true from what was stated in the beginning of this section. In Fig. 4.33 (left),

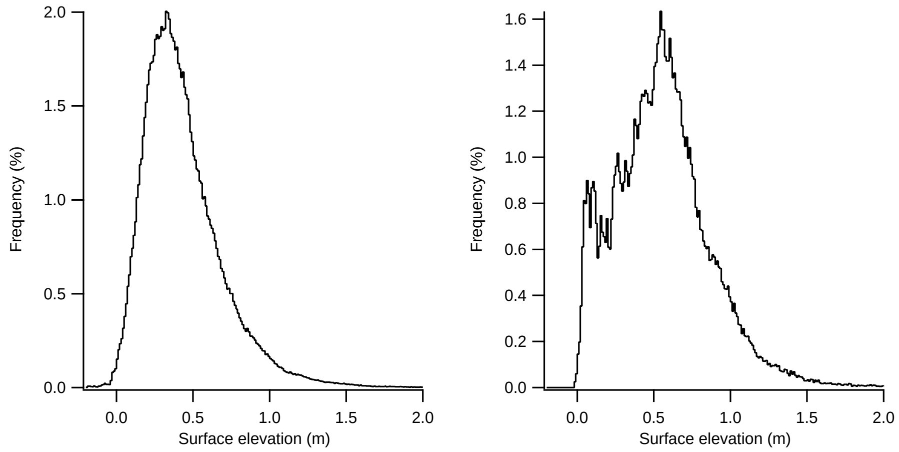

Figure 4.31: Histograms of surface elevation for the profiles 000519 (left) and 000518 (right).

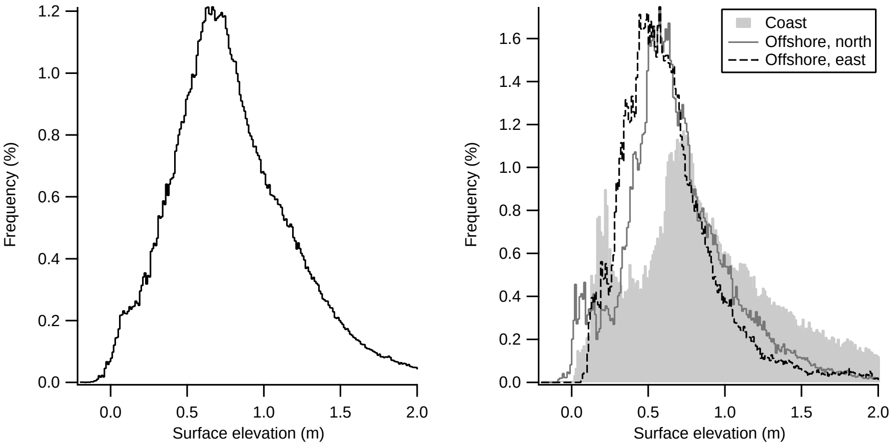

Figure 4.32: Histograms of surface elevation for entire profile 000515 (left) and 70 km long sections near the coast, north, and east (right). See Fig. 4.30.

a clear increase in surface elevation towards the center of the Fram Strait (to the north) is seen. Comparing this result with the entries of the flight protocol that was written during the survey, indeed, very little ice or none at all was present at the coast of Svalbard. The profile section shown in Fig. 4.33 (left) is just north of the ice boundary that was observed at about 79° N. In Fig. 4.33 (right), the equivalent surface elevation distributions are shown for the marked sections in the left graph. The offshore part is comparable to the eastern offshore section in profile 000515 (Fig. 4.32) that comprises about the same area (see Fig. 4.30) and was obtained in the same season in the same year. The modal surface elevation of approximately 0.6 m is similar to the equivalent surface elevation in Fig. 4.32. Further, the offshore mode in Fig. 4.33 shows a tail indicating that the maximum surface elevation reaches values up to 2 m which is also seen in Fig. 4.32.

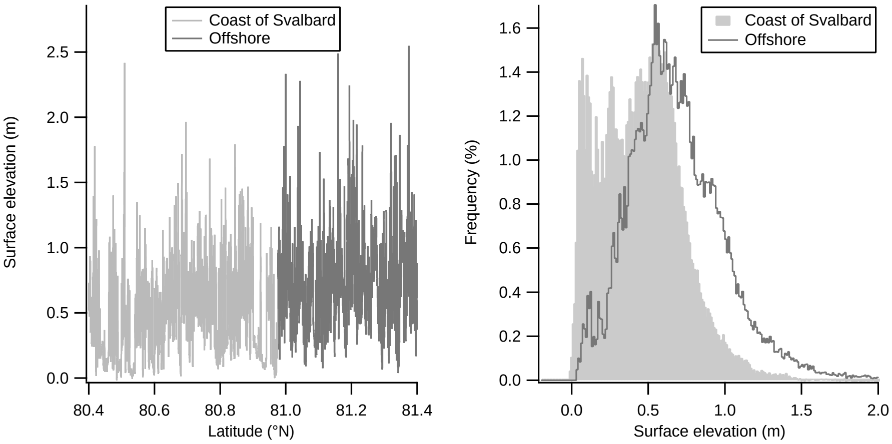

Figure 4.33: Profile 000518 (see Fig. 4.30) with marked sections for thinner (north of the ice boundary) and thicker (offshore) ice (left), and histograms of surface elevation (right) for marked sections in the left graph.

In 1998, the flights were performed in June. Fig. 4.34 shows the result in surface elevation distribution for the entire profile 980617 (left) and for the split version (right). See Fig. 4.30.

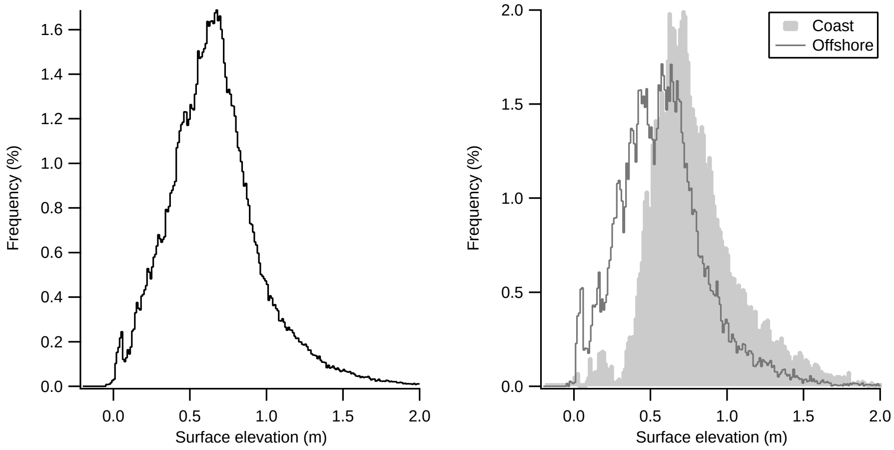

Figure 4.34: Histograms of surface elevation for entire profile 980617 (left) and sections near the coast of Greenland and offshore (right). See Fig. 4.30.

Another sample profile from 1998 that is comparable to the eastern section of profile 000515 in 2000 (Fig. 4.32), is shown in Fig. 4.35. Again, the histogram for the entire profile is shown on the left and the split version on the right. Once more, one clear ice mode and an open water mode are very apparent for the section offshore, whereas two ice modes and, this time, an additional zero mode is visible for the coast. The strong ice modes are clearly below the value of 0.5 m which they exceed in Fig. 4.32. Also, both tails are overall shorter than in Fig. 4.32, indicating a generally thinner ice cover with less ridging. The stronger zero mode may be a sign for the breaking up of the continuous ice cover near the coast of Greenland at the end of July.

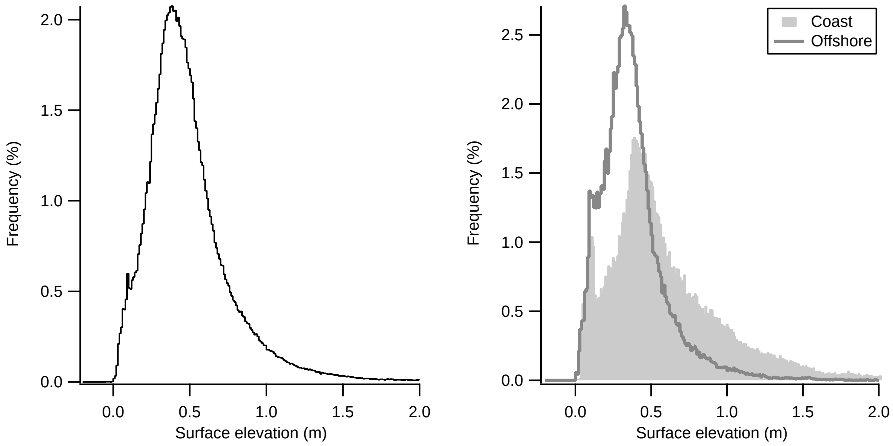

Figure 4.35: Histograms of surface elevation for entire profile 980720 (left) and sections near the coast of Greenland and offshore (right). See Fig. 4.30.

In 1999, the same gradient feature is visible farther south. Fig. 4.36 shows the surface elevation distribution for the entire profile of 990817 (left) and for the split version (near the coast of Greenland and offshore, right). See Fig. 4.30. Here, a zero mode is seen for the section offshore, and a wider ice mode including

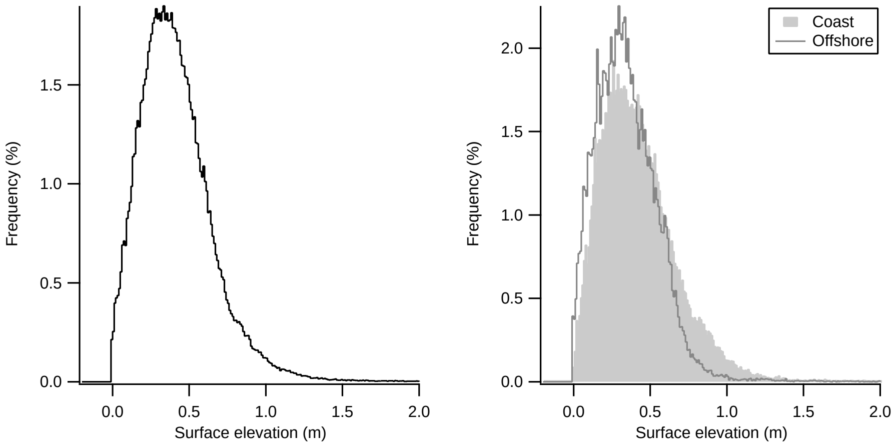

Figure 4.36: Histograms of surface elevation for entire profile 990817 (left) and sections near the coast of Greenland and offshore (right). See Fig. 4.30.

thicker ice and hardly any zero mode is visible for the section near the coast of Greenland. The gradient between both sections (coast and offshore) is not that distinct as in the previous example due to the later season (mid-August) in which the data were collected.

The geographical area of the offshore section of profile 980617 in Fig. 4.34 is comparable to the one of profile 990817 in Fig. 4.36. For the offshore section (Fig. 4.34, right) the ice mode is in fact not as slim as in Fig. 4.36 (right), but it also shows a mode for open water. The histogram of the offshore section of profile 980617 in Fig. 4.34 shows a higher modal surface elevation and has a longer tail than the equivalent distribution of profile 990817 in Fig. 4.36, indicating generally thicker ice with a greater variety of ridged ice. A higher modal surface elevation makes sense, because of the earlier time of the year. That is, the snow has not yet melted completely.

In Fig. 4.37 the histograms of surface elevation are shown for six profile sections (offshore) addressed above. The sections are located between 3° E and 12° E corresponding to a distance of about 140 km at 82° N. Thus, a change in surface elevation can be seen within a certain area. Here, a decrease in the modal surface elevation of about 0.3 m is visible from mid-May (0.6 m) to mid-August (0.3 m) indicating the melting period. With respect to the geographical latitude, there is a gradient in surface elevation from north (000515) to south (990817). However, it is unclear whether the gradient results from regional or seasonal differences. Therefore, the histogram of the southern section for profile 000518 (see Fig. 4.33, 'coast of Svalbard') is shown additionally. Since this section is located geographically in the same area as the 'offshore' section of profile 990817, differences are mainly due to the different seasons as inter-annual changes within one year are considered to be small. Clearly visible is the difference between thicker ice in May 18, 2000 ('000518') and thinner ice in August 17, 1999 ('990817') whereas thin ice is also present for '000518'. Regional differences are visible between '000515' (north) and '000518' (south) as the time of the data recording differs by three days only. Although both histograms show similar modes at about 0.5 m surface elevation, thicker ice is visible along the histogram tail of '000515' whereas an additional mode at about 0.2 m is seen for '000518'. Thus, the north-south gradient in surface elevation is most likely due to regional and seasonal differences.

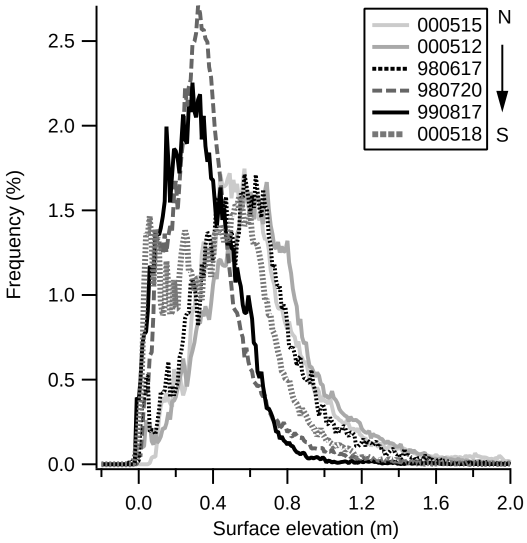

Figure 4.37: Histograms of surface elevation for six profile sections, offshore.

4.5.2 Estimation of the Dynamic Sea Surface Topography (DSST)

As mentioned in Section 3.2 and shown in Section 3.5.4, the local sea level deviates from the geoid. Fig. 4.38 shows the derived local sea level, the geoid, ground elevation and lowest level for the profiles 000512 (a and c) and 000515 (b) (see Fig. 4.30). A similarity is seen in the upper plots, because the triangular flight pattern for 000515 (b) is shifted to the north, compared to 000512 (a), whereas the pattern itself is the same (see Fig. 4.30). The waypoints (WP) 2 mark the northernmost turning points in both profiles. WP 2 in profile 000512 (a) is equivalent to the dip near 2.7e^6 m (WP 2 (a)) in profile 000515 (b). Further, a dip near WP 2 is clearly visible for both profiles indicating a geoid difference of roughly 4 m over a distance of roughly 150 km (see Fig. 4.30). The overall deviation of the local sea level from the geoid varies between 0.3 m and 2.0 m for 000512 (a), and between 0 m and 1.8 m for 000515 (b). Focusing on the overlapping flight leg from WP 1 (southernmost points, see Fig. 4.30) to WP 2 in 000512 (a) and WP 1 to WP 2 (a) in 000515 (b), respectively, a slightly different local sea level is visible. Especially the peak at 2.5e^6 m in (b) (equivalent to 2.6e^6 m in 000512 (a)) looks different for the local sea level. Considering the zoomed profile for the GPS height in Fig. 4.39 (left), a dip of about 1 m is visible at 2.6e^6 m which is equivalent to the dip at 2.6e^6 m in the profile 000512 (a) for the local sea level. Since an equivalent dip of 1 m is visible neither in the zoomed profile for the laser range (Fig. 4.39, right) nor in the pitch (Fig. 4.40, left), this dip is an artifact in the GPS height. Details are found in Section 4.5.3.

Fig. 4.41 shows results for the local sea level and the geoid model for profile 000516 (left) and 980720 (right). WP 3 in profile 980720 marks the easternmost waypoint, which is comparable to WP 3 in profile 000516. The symmetry around WP 3 for each profile is clear, as is the analogy between the two profiles (see Fig. 4.30). A difference of roughly 4 m is seen for WP 3 between the different flights which are approximately 150 km apart.

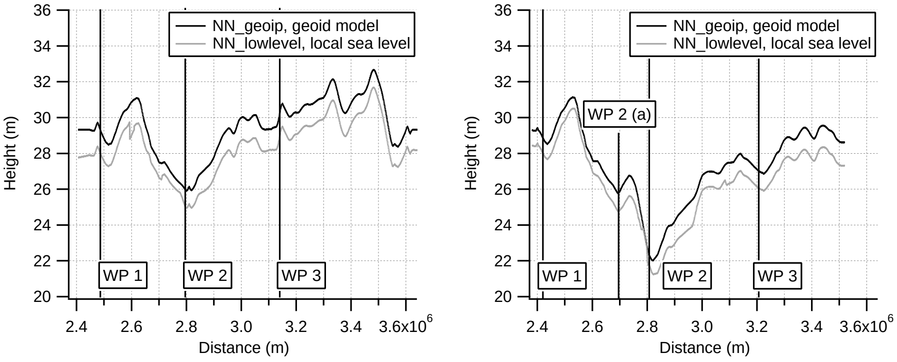

(a) 000512

(b) 000515

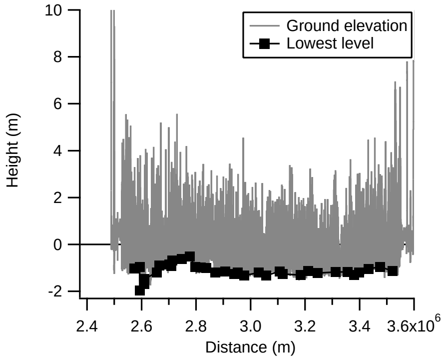

(c) 000512

Figure 4.38: Local sea level versus geoid for profile 000512 (a) and 000515 (b), and ground elevation with lowest level (c). Additionally, the waypoints for the southernmost, northernmost, and easternmost points (WP 1, WP 2, WP 3) of the profile are marked.

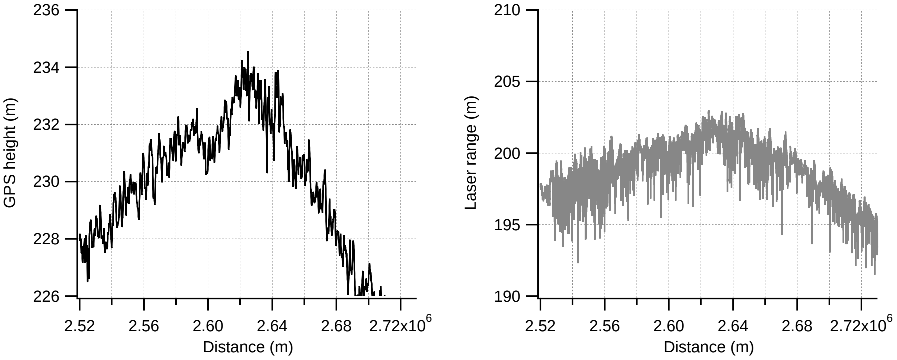

Figure 4.39: Zoomed GPS height (left) and zoomed laser range (right) for profile 000512.

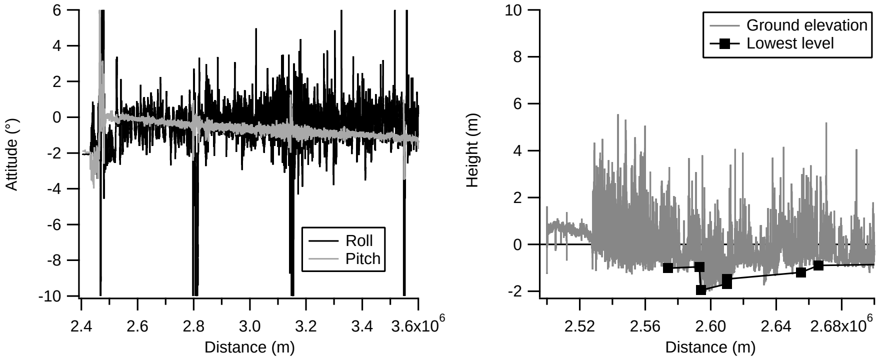

Figure 4.40: Pitch and roll for profile 000512 (left) and zoomed-in section of ground elevation and lowest level (right).

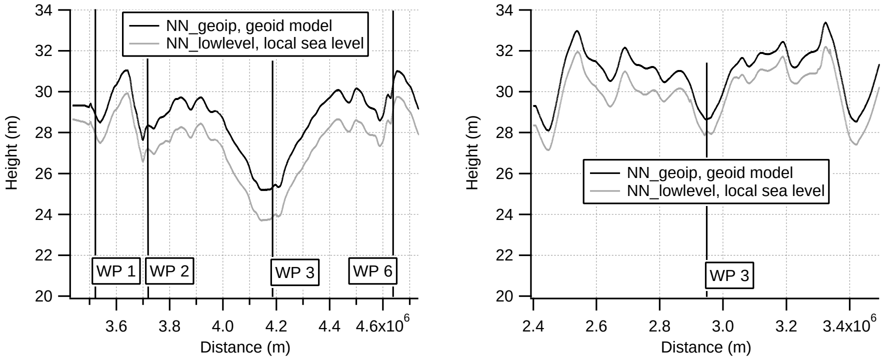

Figure 4.41: Geoid model and local sea level for profile 000516 (left) and 980720 (right).

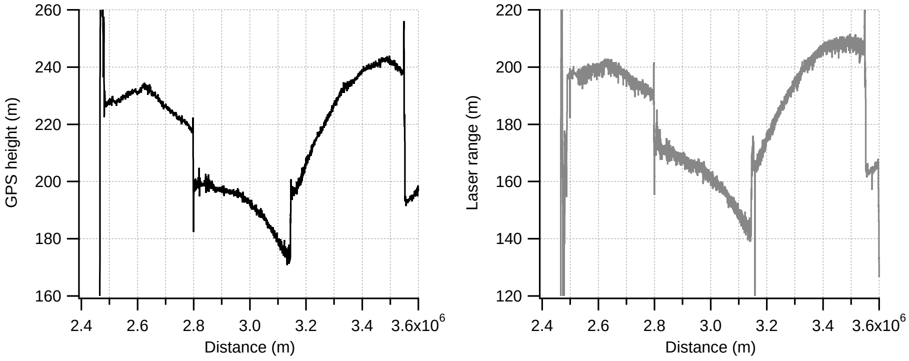

Figure 4.42: GPS height (left) and laser range (right) for profile 000512.

4.5.3 Details

Considering the GPS height and laser height for the entire profile 000512 in Fig. 4.42, three prominent jumps are visible at $2.8e^6$, $3.15e^6$, and $3.55e^6$ m. Since equivalent sudden changes are also obvious in the pitch and roll in Fig. 4.40 (left), they are not artifacts, but real changes in flight altitude. The reason for this is the aircraft maneuver at the northernmost (WP 2) and easternmost (WP 3) waypoints (see Fig. 4.30). This is also seen in the very large negative roll events (Fig. 4.40, left) indicating the right-hand turn. In ground elevation (Fig. 4.40, right), however, these jumps are not visible at this magnitude, meaning that the position of the ground location and thus the ground elevation (see Fig. 4.38 c) and finally the local sea level (see Fig. 4.38 a) is in general determined correctly. In contrast, in Fig. 4.40 (right) the same section of ground elevation is displayed as for the GPS height and laser range in Fig. 4.39. The ground elevation and the lowest level are the same as in Fig. 4.38 (c), but zoomed-in. At about $2.6e^6$ m (Fig. 4.40, right) the same dip of about 1 m is seen in ground elevation that is seen in the GPS height in Fig. 4.39 (left). BOEBEL (2000) also encountered such discontinuities and explained that they were caused by a change in the satellite configuration and incorrectly estimated phase ambiguities. Each time a new satellite is visible above the horizon, or disappears, the set of observed satellites changes and the integer ambiguity in their signals has to be solved for again. Checking the GPS solution again confirmed his explanation. Indeed, for several baseline segments, integer ambiguities could not be solved during the post-processing due to a lack of data. This means, that insufficient satellites were available to the GPS antenna (see Section 2.3.1).

4.5.4 Summary

- A gradient in surface elevation from thick ice near the coast of Greenland to thin ice in the center of the Fram Strait was seen in the analyzed profiles and confirmed by the scatterometer plots.
- The method of deriving surface elevation from airborne laser altimetry confirms once more its suitability for ice thickness studies.
- The estimation of DSST is an additional quantity that results from the determination of surface elevation. It certainly is inadequate for globally precise geoid studies, but it can contribute to local sea level studies in oceanography.

4.6 Calculation of Snow Depth in the Arctic and Antarctic

As mentioned in Section 3.7, it is possible to calculate the snow depth for each profile with the derived surface elevation and R-values from either the histogram modes of surface elevation and EM thickness or the fitting functions. Furthermore, snow depth can also be derived directly from EM thickness and surface elevation (see Eq. (2.2.10)). In any case, the assumed densities for snow, sea water, and especially for sea ice (see Table 2.1), play an important role as introduced in Section 2.2.2.2.

The reason for in-situ snow depth measurements is the representation of typical snow depths on level ice. These measurements were carried out on a 100 m long section with snow depth readings taken about every 5 m. In contrast, snow depth calculations were done for profile sections of about 10 km in length. Thus, it is possible to see to what extent local field observations are representative. Further, and due to external circumstances, the field measurements were made three days earlier than the survey with the EM bird, and hence, snow depths were attained on different ice floes. This may be compensated for by the longer sections for which snow depth was calculated as the chances are higher for including the ice floes on which the in-situ measurements were performed.

4.6.1 Comparisons between EM Bird and in-situ Measurements in the Vicinity of the Profile

Fig. 4.43 shows histograms of the measured (a and b) and calculated (c – f) snow depth for sections north and south of the Lincoln Sea profile in the Arctic (see Fig. 4.44, left). In Fig. 4.43 (c) and (d) histograms of calculated snow depth are shown that was derived with the *R*-values from the histogram modes of surface elevation (see Eq. (2.2.9)), whereas in (e) and (f) the snow depth was derived from the EM thickness and surface elevation (see Eq. (2.2.10)). The density parameters for snow, sea water, and sea ice were used from Table 2.1.

Fig. 4.44 (left) shows calculated snow depths derived with the *R*-values on a geographical grid for the entire profile in the Lincoln Sea on May 14. The equivalent histogram is shown on the right. The in-situ snow depth measurements (and snow depth calculations) were made in the north and south of the right leg near the marked sections in Fig. 4.44 (left). Larger snow depths of up to 0.8 m were found by in-situ measurements with most frequent snow depths ranging between 0.15 m and 0.5 m in the north (Fig. 4.43 a). In the south (Fig. 4.43 b), snow depths of only up to 0.4 m were measured with most frequent snow depths ranging between 0.15 m and 0.2 m. The in-situ observations can be partially reproduced by calculations. At least, the tendency of a thicker snow cover is visible in the north (Fig. 4.43 c) as well as a lower snow cover in the south (Fig. 4.43 d). The mode, of almost 0.5 m in the north (Fig. 4.43 c) does not coincide with the field observations. In the south (Fig. 4.43 d), a better coincidence is visible with the field observations (Fig. 4.43 b) due to immobile ice conditions of almost homogeneous first-year ice (with an almost homogeneous snow cover). The mode at 0.1 m in the south (Fig. 4.43 d) agrees to within 0.1 m with the mode in Fig. 4.43 (b). Comparing the calculated mean snow depth from the north (Fig. 4.43 c) and the south (Fig. 4.43 d), that amounts to 0.4 m, to the mean of the measured snow depth (0.22 m) it agrees to within 0.18 m. However, comparing it to the result of MAYKUT & UNTERSTEINER (1971)[7], based on more comprehensive field experiments in the 1960s, it gives a good agreement. In Fig. 4.43 (e) and (f) histograms of calculated snow depth are shown which was derived from the EM thickness and surface elevation under the assumption of density parameters for snow, sea water, and sea ice (see Table 2.1). A higher mean value of 0.73 m (compared to 0.61 m for the calculated snow depths from the *R*-values in (c)) resulted for the northern section whereas a slightly lower mean value of 0.16 m (compared to 0.19 m for the calculated snow depths from the *R*-values in (d)) was obtained for the southern part.

---

[7] They assumed a linear accumulation of 30 cm between August and October, a further accumulation of 5 cm between November and April, and a final 5 cm in May.

In Fig. 4.45, histograms of snow depth are shown for the profile in the Lincoln Sea on May 11 (a), and the two northern profiles on May 12 (b) and May 13 (c). The mean value of the calculated snow depth (Fig. 4.44 (right), and Fig. 4.45) amounts to 0.50 m, and thus agrees within 0.1 m with the model from MAYKUT & UNTERSTEINER (1971).

Fig. 4.46 shows histograms of measured (left) and calculated (right) snow depth for the Weddell Sea profile 'Dec. 14, leg1 north' in the Antarctic. Here, in-situ measurements were made over a distance of about 1000 m, whereas the snow depth was calculated (with R-values from the modes of surface elevation and EM thickness) along a 10 km long flight profile. Field observations show a clear mode at around 0.8 m snow depth (left). The histogram of the calculated snow depth shows a mode between 0.7 m and 0.8 m (right), which is close to the measurements in the left graph. The mode at around 0.2 m (right) is also close to the lowest surface elevation between 0 m and 0.2 m (left). Overall, a good agreement is visible and is also indicated by the long tail that is similar in both histograms.

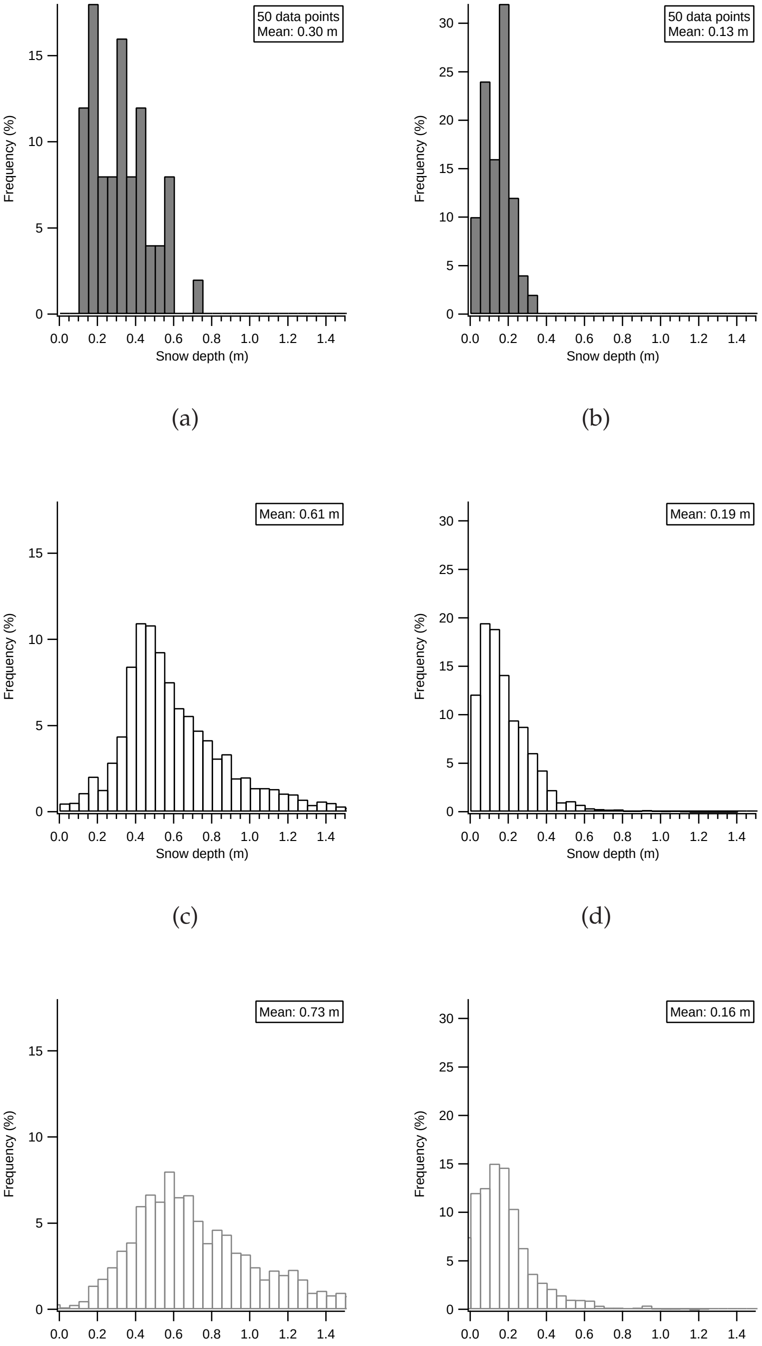

(a) (b)

(c) (d)

(e) (f)

Figure 4.43: Histograms of measured (a and b), calculated snow depths with *R*-values from the modes (c and d) and with EM thickness (e and f) for the section north (a, c, e) and south (b, d, f) in the Lincoln Sea.

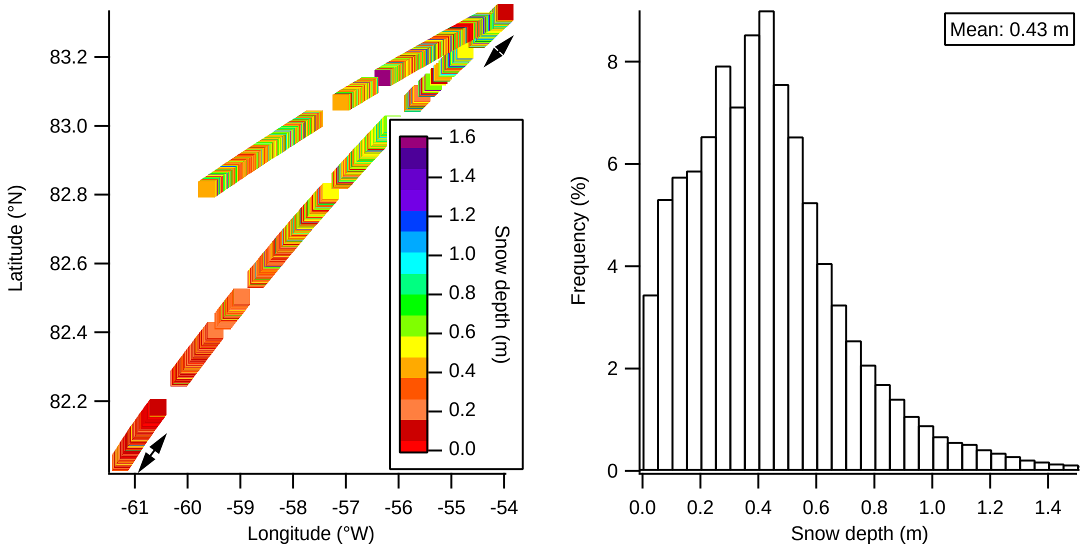

Figure 4.44: Calculated snow depths with R-values on a geographical grid (left) with marked sections of the in-situ snow depth measurements and histogram of snow depth (right) for the entire profile in the Lincoln Sea.

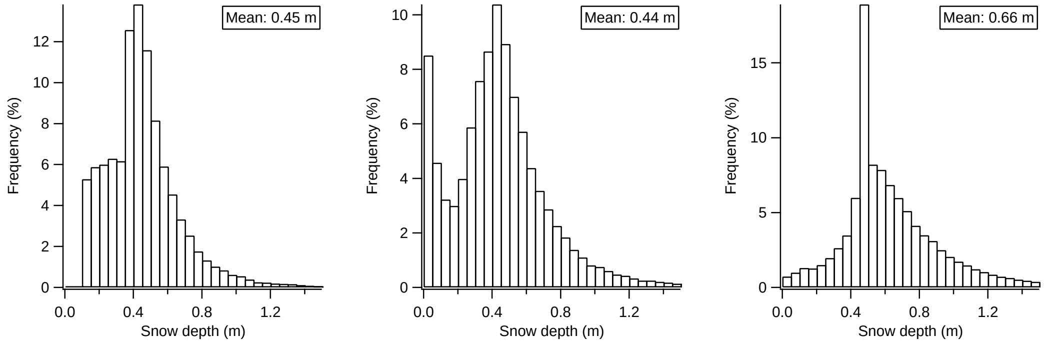

(a) (b) (c)

Figure 4.45: Histograms of calculated snow depths with R-values from the surface elevation modes for the profile in the Lincoln Sea on May 11 (a) and to the north of Ellesmere Island on May 12 (b) and May 13 (c).

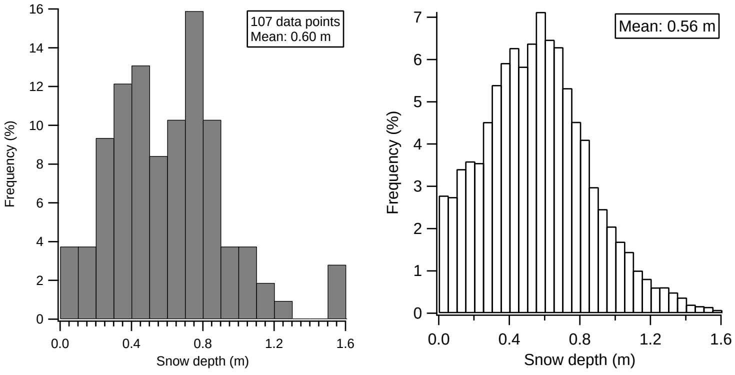

Figure 4.46: Measured (left) and calculated (right) snow depths in the Weddell Sea.

4.6.2 Comparisons between EM Bird and in-situ Measurements along a Validation Line

In contrast to the previous section, here, EM bird and in-situ measurements were made along the same section. The following results refer to the entire northern validation line (not only the section between the corner reflectors) north of Ellesmere Island mentioned in Section 3.1.1 (see Section 5.2). In Fig. 4.47 the EM thickness profile is shown together with total thickness from in-situ measurements (Fig. 4.47 a). Fig. 4.47 (b) displays the surface elevation derived from the difference between the GPS height and laser height ('GPS - laser') with the EM bird setup and the equivalent in-situ results. In Fig. 4.47 (c), the resulting keel depths are shown for both measurement techniques. In the case of the EM bird, the keel depth resulted from the difference between the EM thickness and the 'GPS - laser' surface elevation. In each of the graphs in Fig. 4.47, the validation line was surveyed from south to north, and left to right respectively. Since the validation line did not include any open water spots or very thin ice, and because the validation was established on minimally undeformed first-year ice, a horizontal line was fitted through the lowest value present in ground elevation yielding a rough surface elevation. In the next step, this surface elevation was shifted manually upwards to optimally align, on average, the in-situ surface elevation measurements. Consequently, the mean of the 'GPS - laser' surface elevation matches with the in-situ measurements the best, in the following.

The in-situ measurements were made between May 10 and May 14, whereas the EM bird survey took place on May 15 (see Section 5.2). To account for slight misalignments between both profiles, the drill hole profile was brought manually into line with the EM thickness profile. The pressure ridge to the north was very helpful for this alignment. The shift itself was only about 1 m in the along-track direction.

Misalignments between both data sets result from the fact that neither the team doing the groundwork nor the helicopter track match the imaginary validation line perfectly.

As seen in Fig. 4.47 (a) and (b), the ice is relatively flat, meaning that no large pressure ridges are present, except the one to the northern end (right side). Aside from the pressure ridge, deviations of up to 0.2 m are visible for total ice thickness (a) and up to 0.3 m for surface elevation (b) between 'GPS - laser' and 'in-situ'. The average total thickness of 1.67 m (excluding the pressure ridge) is the same for both data sets (a) with a slightly lower standard deviation of 0.05 m for 'EM thickness' as opposed to 0.07 m for the in-situ measurements. Regarding surface elevation in (b), an average value of 0.33 m is found for 'GPS - laser' and in-situ with a slightly higher standard deviation of 0.05 m for 'GPS - laser' as opposed to 0.03 m for the in-situ measurements. Regarding the comparison between in-situ keel depth measurements and derivations from the EM bird, average values of -1.32 m and -1.34 m are found for the EM bird setup and in-situ respectively, with a slightly lower standard deviation of 0.07 m for the EM bird as opposed to 0.08 m for the in-situ measurements.

Fig. 4.48 shows surface elevations from 'GPS - laser' and in-situ measurements from Fig. 4.47 as well as calculated snow depths from 'GPS - laser' and measured 'in-situ'. Additionally, the resulting freeboard is displayed for 'GPS - laser' with the calculated snow depths being subtracted from surface elevation. In-situ freeboard measurements are shown also. The graph on the right in Fig. 4.48 shows

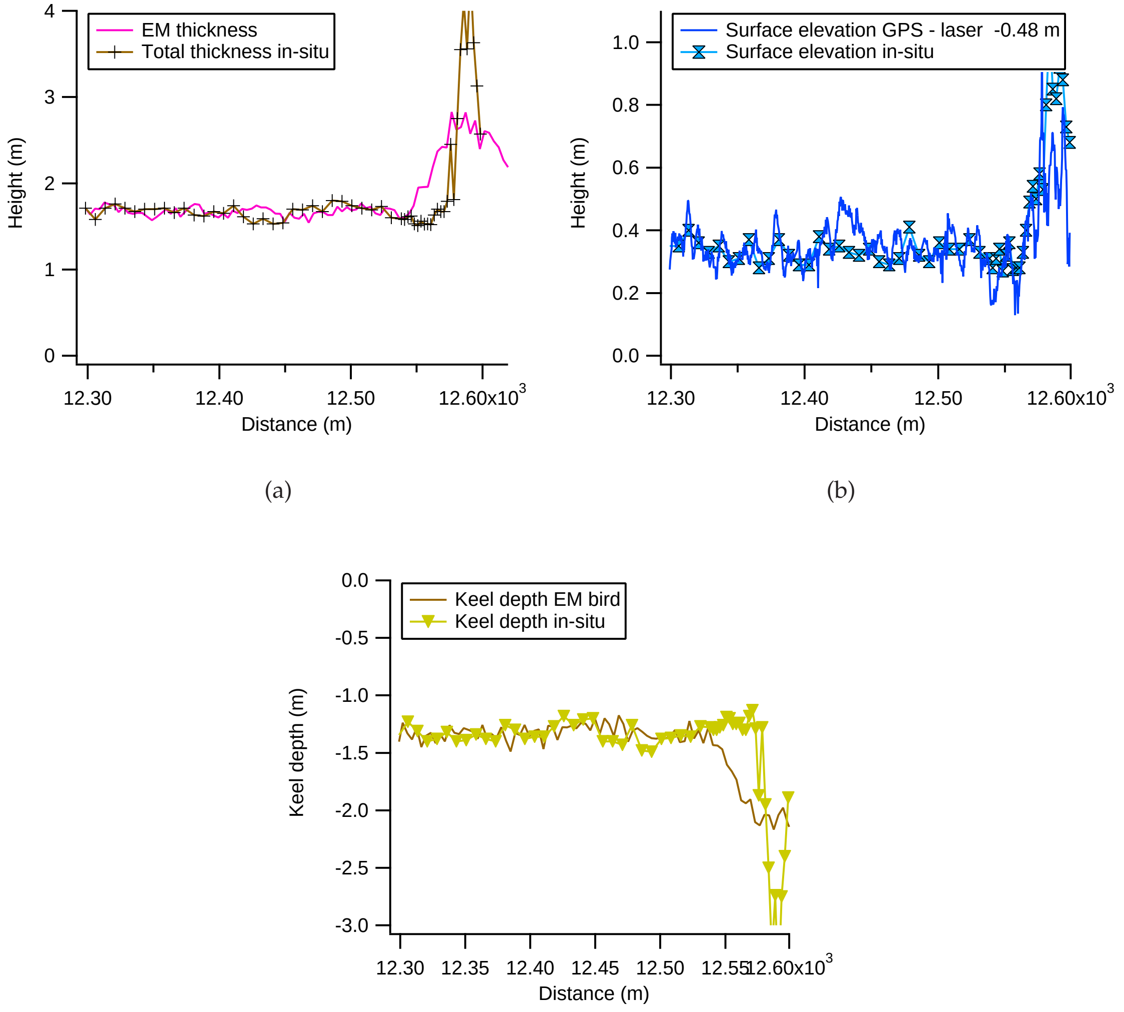

(a) (b)

(c)

Figure 4.47: Total thickness, surface elevation, and keel depth from EM bird and in-situ measurements.

a zoomed-in section of the entire profile on the left. A good agreement of surface elevation and snow depth between 'GPS - laser' and 'in-situ' is visible at the distance between 12475 m and 12485 m. However, the snow depth and surface elevation calculated with 'GPS - laser' is approximately 0.05 m too small compared to the in-situ measurements. A general conformity is seen between the calculated surface elevation and snow depth 'GPS - laser' as well as between the in-situ measurements of surface elevation and snow depth. At the distance of 12490 m, a tiny peak is seen in the 'GPS - laser' surface elevation that is also mapped to the calculated snow depth. In contrast, 5 m before and after the peak, a considerably higher variability is seen in surface elevation at a constant snow depth, meaning that the variation of surface elevation is incompletely mapped to the snow cover, i. e. larger surface elevations do not necessarily mean larger snow depths.

Fig. 4.49 shows the histograms of surface elevation derived from 'GPS - laser' (a) and measured in-situ (c), and histograms of the calculated (b) and measured snow depth (d). A mode is clearly seen at around 0.3 m in all four

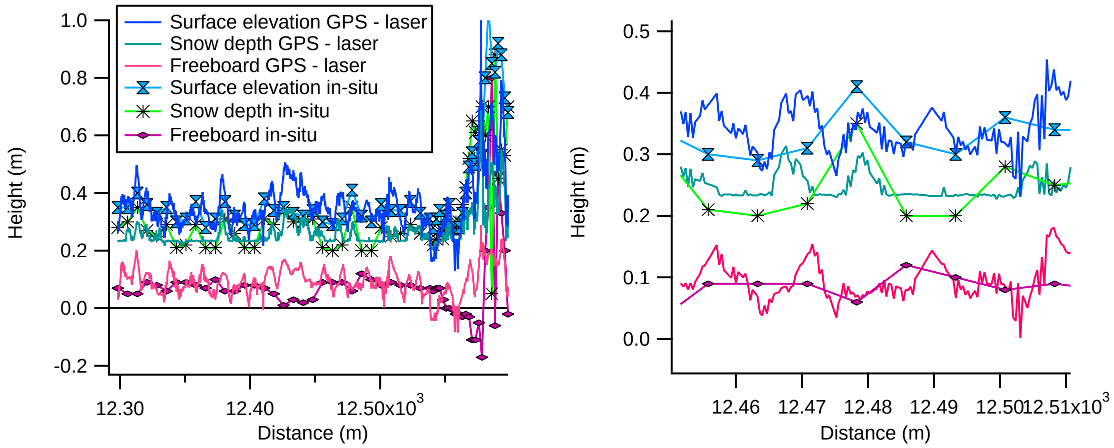

Figure 4.48: Surface elevation, snow depth, and freeboard from 'GPS - laser' and 'in-situ'. Legend from left graph refers also to zoomed-in graph on the right.

histograms and almost no surface elevations and snow depths below the modal value. The clear modes in all histograms and the good fit of the shapes between the histograms (a) and (b) and (c) and (d) confirm a general correlation between calculated surface elevation (a) and calculated snow depth (b) as well as between the in-situ measurements (c) and (d).

4.6.3 Summary

- In-situ snow depth measurements are representative for airborne surveys as long as the same ice (and snow) conditions are present. Then, snow depth measurements derived from 'GPS - laser' with the EM bird setup are in good agreement with the in-situ measurements.
- The calculated mean snow depth for the profiles in the Lincoln Sea and north of Ellesmere Island could be confirmed by data from a climatological model. However, the inter-annual variability was not investigated since snow depth was calculated only for profiles within the same year.
- Since a comparison of measured and calculated snow depths was made over multi-year (north) and first-year ice (south of the Lincoln Sea profile), it can be concluded that the assumed specific density for sea ice is an adequate standard value that suffices for the two main ice regimes.
- A general conformity is seen between surface elevation and snow depth which is more distinct for in-situ measurements above the smooth first-year ice.
- Measurements along a pre-defined validation line allow a better insight into the single measurements at the drill holes, and thus a better comparison with the calculated quantities. That is, each increase in calculated surface elevation does not necessarily mean an increase in calculated snow depth.

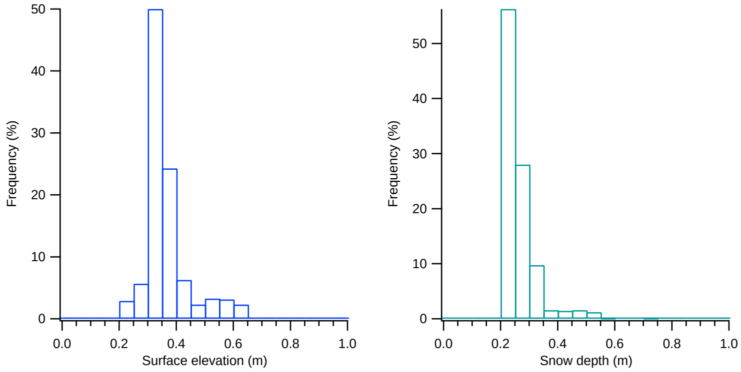

(a) calculated (b) calculated

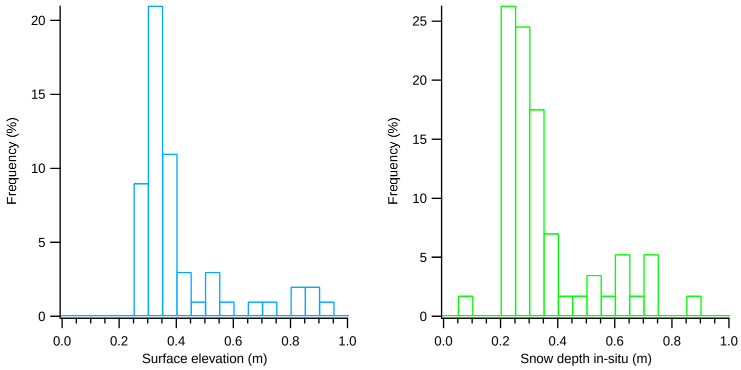

(c) in-situ (d) in-situ

Figure 4.49: Histograms of GPS/laser surface elevation with the EM bird setup (a), measured in-situ (c), and for the calculated (b) and in-situ measured snow depth (d).

5 Results of Radar Altimetry

This chapter presents results of simultaneously obtained radar and laser altimeter data. As mentioned in Section 2.3.5 and Section 3.1.3, a detailed study of the radar altimeter ASIRAS and the single-beam laser altimeter LD 90 was not part of this work. In the following, measurement results of the first two ASIRAS-campaigns over sea ice are shown. The first campaign took place in the Bay of Bothnia where one flight of the ASIRAS airplane was performed simultaneously with the LD 90 and the EM bird. The coincident flights allow comparison of surface elevation from LD 90 with EM thickness. Here, the direct comparison of total thickness was not the main aspect, but rather the behavior of surface elevation from LD 90 in comparison to the EM thickness along a chosen section with a prominent increase in EM thickness. Unfortunately, surface elevation from LD 90 could not be compared with GPS/laser surface elevation derived from from the EM bird setup, because the EM bird was operating during this campaign without DGPS-capability (see Section 2.3.1). Furthermore, direct comparisons between LD 90 and ASIRAS were made on another flight leg for which the difference between both range measurements is displayed as the resulting snow depth (see Section 5.1.2).

The second time, ASIRAS was flown in the Arctic by colleages from DNSC. That time, the LD 90 was replaced by the DNSC laser scanner. The processed laser scanner data were kindly made available by DNSC in Summer 2006. Comparisons among the different data sets including ground and EM bird measurements along a pre-defined validation line were possible and first results are shown in the following sections. Here, the EM bird was equipped with DGPS allowing a comparison between the calculated snow depth derived with the EM bird setup and the snow depth derived from the difference between the laser scanner and ASIRAS measurements.

5.1 Comparisons between Laser- and Radar Altimetry in the Bay of Bothnia

In Fig. 5.1 the flight tracks of the ASIRAS airplane are shown. The two marked legs are highlighted in this chapter. The easterly marked leg was flown coincidently by the airplane and the helicopter. The westerly leg was chosen to compare ASIRAS with the single-beam laser altimeter LD 90. Taking into account the ice drift and the different flight speeds, the helicopter and airplane flew towards each other at their respective flight altitudes. This strategy differed from the GreenICE campaign in the Arctic in 2005 but was necessary due to different operational constraints.

5.1.1 Coincident EM Thickness and LD 90 Surface Elevation

The coincident tracks of the helicopter with the EM bird and the ASIRAS airplane are shown in Fig. 5.2 (a). The maximum across-track distance between the two tracks was found to be smaller than 10 m. In Fig. 5.2 (b), the EM thickness

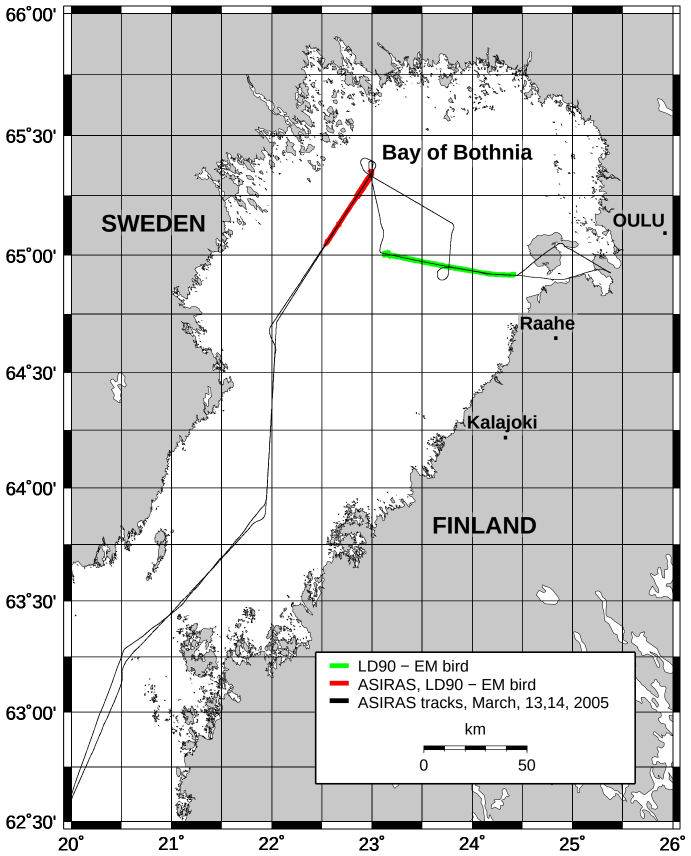

Figure 5.1: ASIRAS flight tracks in the Bay of Bothnia with two marked legs for the coincident flight between the ASIRAS airplane and the helicopter (east), and the comparison between ASIRAS and LD 90 (west).

and LD 90 surface elevation profiles are displayed for a short section showing a prominent height increase in EM thickness, and surface elevation, respectively. The synchronous height increase at the vertical bar indicates the agreement of the recorded data. The photographs in (c) and (d), taken from the helicopter in along-track flight direction, confirm what is visible in the profile, i. e., thicker first-year ice with a compact snow cover (c) to the west (left of vertical bar in (b)) and a thinner ice of dark and light nilas (d) to the east (right of vertical bar in (b)). The histograms of the EM thickness and surface elevation in Fig. 5.3 are divided into two parts, representing thick first-year ice and nilas for the marked sections in the profile in Fig. 5.2 (b). Clearly visible is the difference between both ice types for the EM thickness and LD 90 surface elevation. Regarding the EM thickness of first-year ice, no values below 0.2 m are visible, as confirmed by the photograph in Fig. 5.2 (c), but rather thicknesses of up to 4 m with a modal thickness at 0.9 m (see Fig. 5.3, left). In contrast, the EM thickness of nilas shows a clear mode around 0 m (dark nilas) and ice thicknesses up to about 0.4 m (light nilas). The standard deviations amount to 0.95 m and 0.12 m for EM thickness and LD 90 surface elevation respectively. The surface elevation distribution of LD 90 in Fig. 5.3 (right) corresponds to the EM thickness distribution (Fig. 5.3, left) in a way that a wide range of larger surface elevations is visible for first-year ice and a strong mode for lower values including 0 m for nilas. In Fig. 5.3 (right), a wide zero mode is seen for values up to 0.1 m with a peak at 0.07 m as opposed to a sharp mode

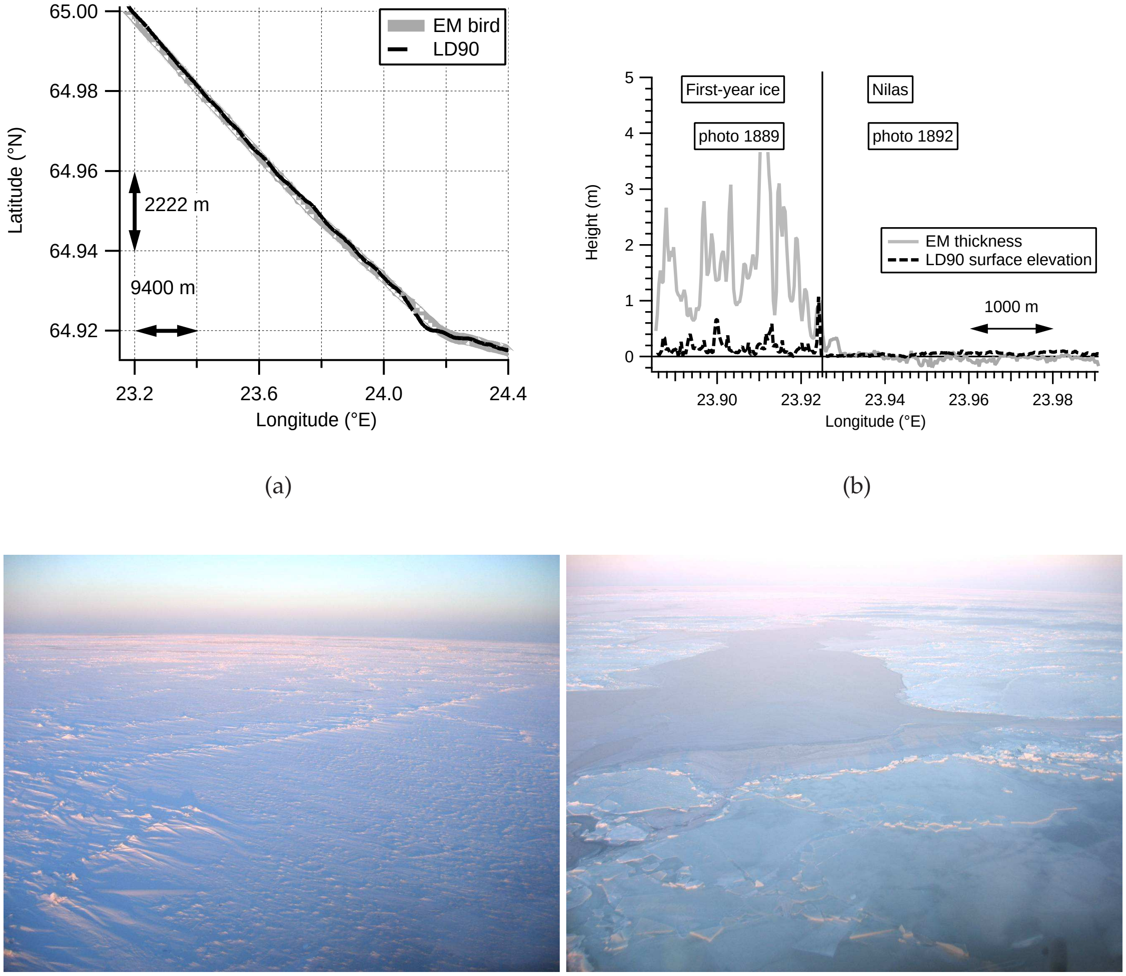

(a) (b)

(c) Photo 1889 (d) Photo 1892

Figure 5.2: Survey area (a), coincident EM thickness and LD 90 profiles (b), and photographs for the sections to the west and to the east of the vertical bar in (b). The photographs confirm what is visible in (b), i. e., thicker first-year ice with a compact snow cover (c) to the west, and thinner ice with dark and light nilas (d) to the east.

around 0 m for the EM thickness (left)[1]. The wide zero mode (right) reflects the uncertainty in surface elevation of ±0.1 m. Thus, both measurements are within their accuracy range. Further, a peak at 0.13 m is recognizable that corresponds to the peak in the EM thickness at 0.4 m (left). This means that the EM bird and the laser altimeter LD 90 are able to distinguish between different thin ice types. Thus, a mixture of very thin ice and slightly thicker ice (dark and light nilas) is seen and is confirmed by the photograph in Fig. 5.2 (d).

Fig. 5.4 shows the EM thickness and LD 90 surface elevation histograms for the entire profile in Fig. 5.2 (a). Here, the same is true as for the short section in Fig. 5.3: a clear zero mode in the EM thickness for very thin ice (1) and a mode at 0.7 m (2) representing thicker ice (Fig. 5.4, left). Regarding the LD 90 surface elevation, two modes at 0.06 m (1) and 0.12 m (2) are visible for the equivalent ice

---

[1] Due to the larger bin-width of 0.1 m in the EM thickness, the zero mode appears to be sharper although it includes the same variety of values as the zero mode for surface elevation.

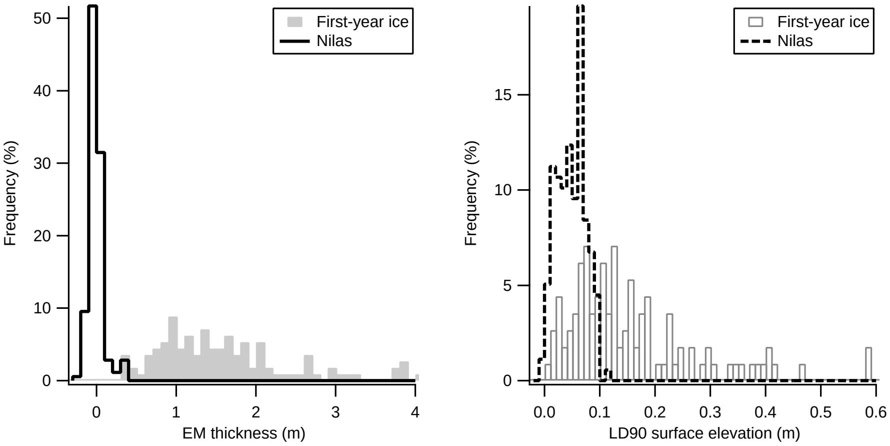

Figure 5.3: Histograms of EM thickness and LD 90 surface elevation for the two marked ice types present in the profile in Fig. 5.2 (b).

types (Fig. 5.4, right). Furthermore, two other modes for thick and very thick ice are recognizable in both histograms. The numbers in both histograms mark the modes which correspond to each other.

This confirms the good agreement between the EM thickness and LD 90 surface elevation and the sensitivity of both systems for generally thinner ice compared to the ice that was found in the high Arctic, see Section 4.6. The standard deviations of 1.03 m and 0.14 m for EM thickness and LD 90 surface elevation are in the range of the equivalent values for the short profile. Thus, the measurements of LD 90 are suitable for further sea ice thickness studies.

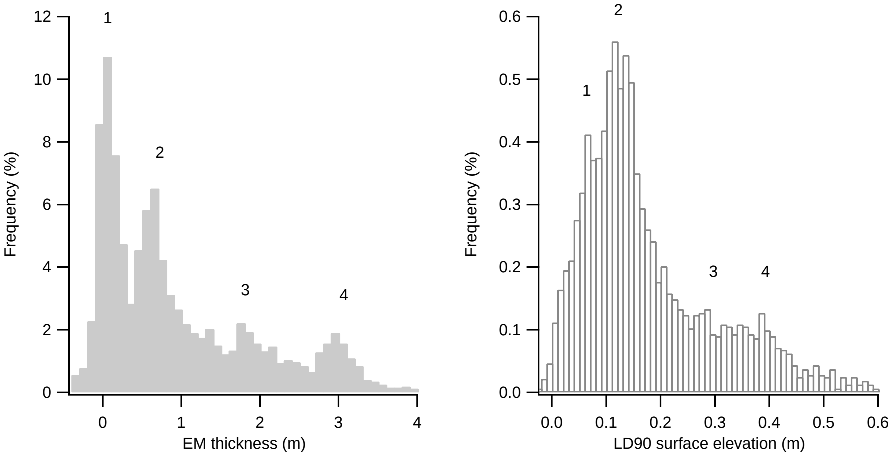

Figure 5.4: Histograms of EM thickness (left) and LD 90 surface elevation (right) for the entire profile shown in Fig. 5.2 (a), and Fig. 5.1 to the east, respectively.

5.1.2 ASIRAS Freeboard and LD 90 Surface Elevation with Snow Depth Estimates

The flight leg chosen for this analysis is shown in Fig. 5.1 in the west. Here, the helicopter flew along this line in the opposite direction to the ASIRAS airplane approximately 30 minutes earlier. In Fig. 5.5, the graph on the left shows a section across an open water lead. Displayed is the ASIRAS freeboard, LD 90 surface elevation, and the resulting snow depth. To trim the ASIRAS data spacing of about 11 m to the LD 90 data spacing of about 25 m, the ASIRAS data were smoothed correspondingly. Between about 22.771° E and 22.778° E very low values for freeboard and surface elevation are visible. Snow depth is oscillating around 0 m for this section. At 22.770° E and about 22.779° E a clear increase in all three quantities is recognized. The vertical bar at 22.778° E indicates the presence of a photograph that is shown on the right. Flight direction was from east to west. In the photograph, taken from the helicopter, an open water lead with very thin ice near the right edge is visible confirming the absence of snow between 22.771° E and 22.778° E in the profile section (left). The equivalent histograms of LD 90 surface elevation, ASIRAS freeboard, and resulting snow depth

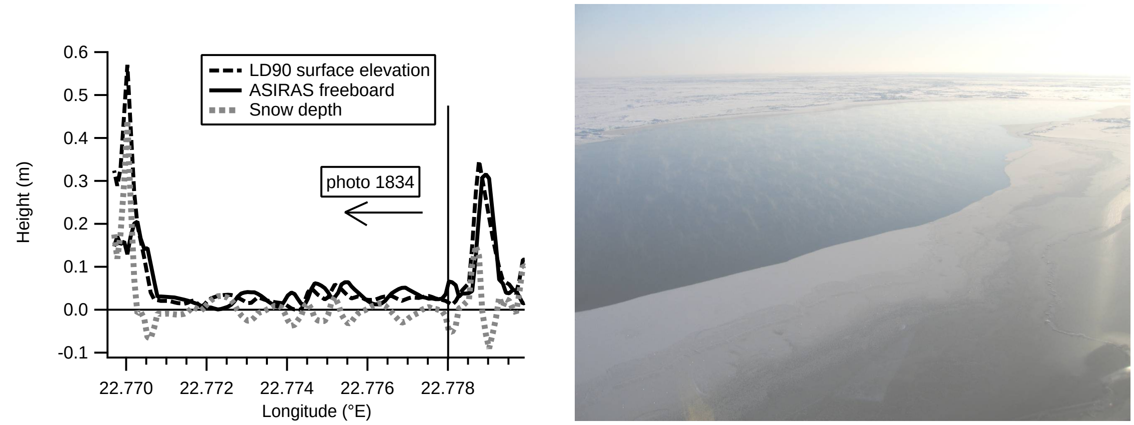

Figure 5.5: ASIRAS freeboard and LD 90 profile with resulting snow depth (left) for an open water lead (right).

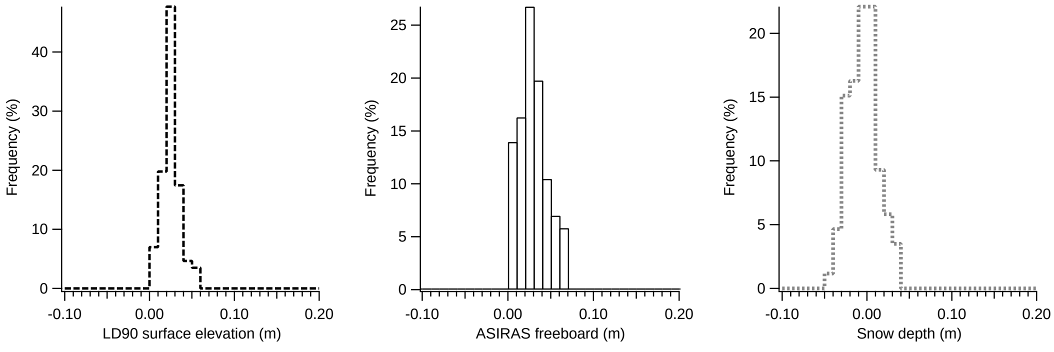

(a) (b) (c)

Figure 5.6: Histograms of LD 90 surface elevation, ASIRAS freeboard, and snow depth for the profile section between 22.771° E and 22.778°E in Fig. 5.5 (left), and the open water lead in Fig. 5.5 (right), respectively.

for the profile section between 22.771° E and 22.778° E (see Fig. 5.5, left) are shown in Fig. 5.6 (a) – (c). In (a) and (b), a modal surface elevation at 0.03 m is visible whereas the mode is sharper for the LD 90 surface elevation in (a). The histogram of snow depth (c) shows a wide mode with a peak at 0 m confirming the absence of snow within this profile section. The average values constitute 0.03 m for surface elevation, 0.03 m for freeboard, and 0.004 m for snow depth at standard deviations of 0.01 m, 0.016 m, and 0.017 m respectively. These numbers confirm a large uncertainty in ASIRAS freeboard and snow depth, that is seen in the wide mode in the distribution in Fig. 5.6 (b) and (c). Therefore, from the similar heights of surface elevation and freeboard around 0 m and the clear increase of snow depth at the ridges in Fig. 5.5 (left) it can not be concluded that the difference between the LD 90 surface elevation and the ASIRAS freeboard yields adequate snow depth estimates. For this reason, another short section was chosen.

The graph on the left in Fig. 5.7 shows a profile section with heavy ridging and a smooth surface (lead) to the right (22.771 °E to 22.772° E). Clearly visible is the height increase in surface elevation and snow depth over the ridges near 22.766° E, 22.767° E, 22.768° E, and 22.770° E while the freeboard does not show these peaks. The photograph on the right shows a closed surface with discrete, identifiable ridges, almost devoid of snow in front but with some snow-covered ridges to the left. Thus, it confirms the presence of ridges and also the lead in the background, but it still does not confirm the snow depth increase over the ridges which indicates uncertainties in the freeboard measurement. Again, the ASIRAS flight direction was from east to west but the photograph was taken in the opposite direction since the helicopter was flying from west to east, in contrast to the previous paragraph.

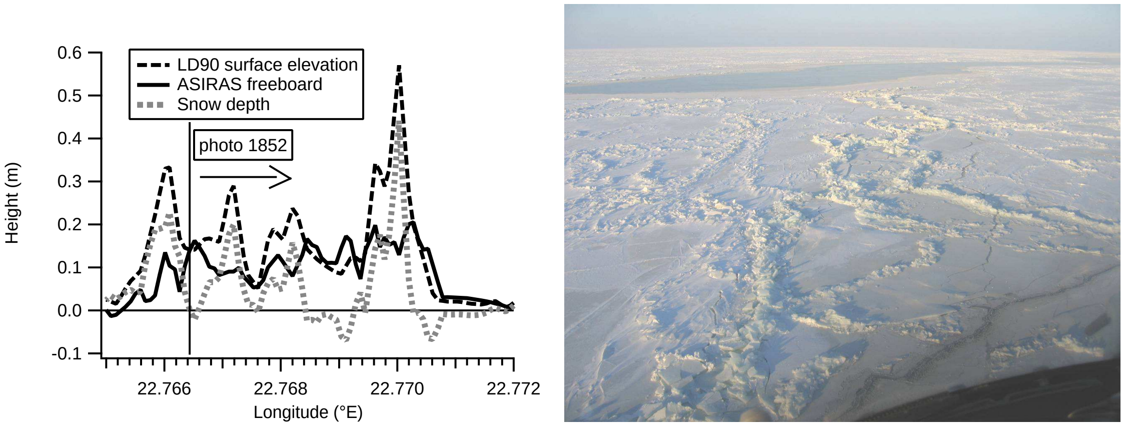

Figure 5.7: Profiles of LD 90 surface elevation and ASIRAS freeboard with resulting snow depth (left) for a section with heavy ridging (right).

In Fig. 5.8, histograms of LD 90 surface elevation (a), ASIRAS freeboard (b), and the resulting snow depth (c) are shown for the entire profile in Fig. 5.1 in the west. The histograms of LD 90 surface elevation (a) and ASIRAS freeboard (b) show a mode at 0.04 m whereas the mode of snow depth (c) is present at 0.03 m. Standard deviations of 0.15 m for LD 90 surface elevation, 0.11 m for ASIRAS freeboard and 0.10 m for snow depth, confirm the general uncertainty of snow depth estimates calculated from the difference between surface elevation and freeboard.

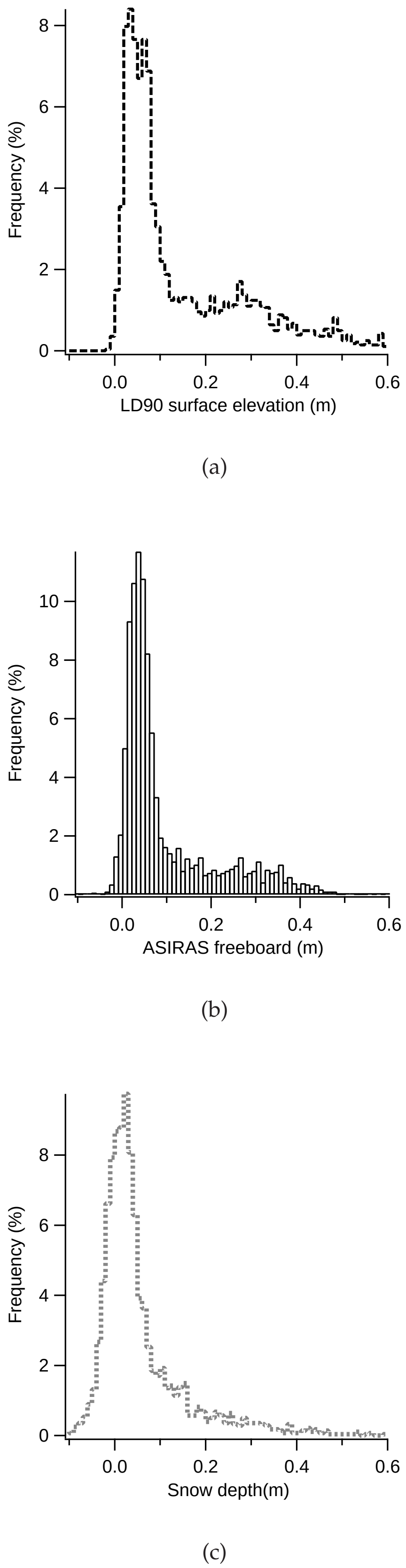

Figure 5.8: Histograms of LD 90 surface elevation, ASIRAS freeboard, and snow depth for the entire profile shown in Fig. 5.1 to the west.

5.2 Comparisons between Laser- and Radar Altimetry in the Arctic

The second campaign in which the ASIRAS radar altimeter was flown over sea ice took place in the Arctic in May 2006. This campaign included ASIRAS flights along two pre-defined validation lines with corner reflectors at either end, about 130 m apart, at which ground measurements had been performed. The ground measurements comprised readings of snow depth, freeboard, surface elevation, and total thickness at drill holes at about 8 m spacing (see Section 3.1.1). The validation experiment was run north of Ellesmere Island (Fig. 3.1, left). One validation line was established on multi-year ice and the other on first-year ice. Here, only the validation line on first-year ice is considered because the results, especially between radar and laser, were expected to agree better for smoother homogeneous first-year ice than for multi-year ice with different ice layers, which influence the radar penetration depth. Thus, deviations between the different data sets were easier to understand and the findings can be used for analyzing data over multi-year ice. Besides ASIRAS, the laser scanner from DNSC was mounted inside the airplane allowing comparisons between the individual measurement quantities as well as between the resulting snow depth and the in-situ observations. Additionally, the EM bird with DGPS-capability (see Section 2.3.1) was operating, and thus another data set is available to which the measurements can be compared. Further, it was the first time that surface elevation, derived from the difference between the GPS height and laser height ('GPS - laser') with the EM bird setup, was validated with ground measurements. The ASIRAS and EM bird flights were conducted on two different days, whereas the ground measurements took place in the mean time. Since the validation line was established on immobile fast ice, the activities were unaffected by ice movements.

In Fig. 5.9 the sections of the other overpasses of ASIRAS on May 10 are shown, as well as the nearest EM bird track on May 15 with respect to the displayed ASIRAS track along with the marked positions of the corner reflectors. The helicopter pilot approached the line and passed the corner reflectors on a visual basis. This was recorded manually as event in the flight log. The positions of the corner reflectors where measured on the ground by a handheld GPS receiver. This measurement was done twice during five days and yielded the same result within 10 m. Regarding the 'ASIRAS_00' track, it is aligned within 7 m to the nearest EM bird track (shown in graph) and the imaginary line connecting the two reflectors.

To align the 'GPS - laser' surface elevations of the EM bird setup as close as possible to the airplane measurements, the EM bird track was extracted from the laser scanner swath to find the corresponding surface elevations (see Section 4.4). Thus, surface elevations of the EM bird setup are comparable to the surface elevations from the laser scanner. For comparisons with surface elevations from ASIRAS, surface elevations were derived from the ASIRAS freeboard with the in-situ measured snow depth being added. Since the ASIRAS freeboard (and ASIRAS surface elevation) refers always to the nadir of the airplane, the EM bird track, and hence the surface elevations of the EM bird are not necessarily aligned to this "track" of nadir measurements[2]. Thus, for snow depth comparisons, the

---

[2] Extraction of the EM bird track from the laser scanner swath allows to find only the corresponding surface elevations in the scanner data which do not necessarily coincide with the surface elevations at the nadir-looking beam of the laser scanner and ASIRAS.

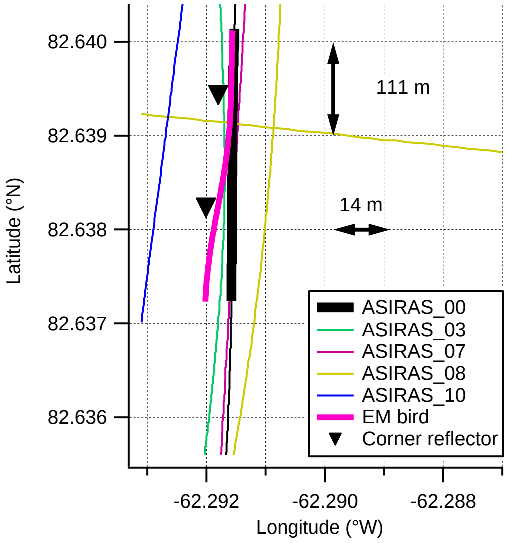

Figure 5.9: ASIRAS and EM bird tracks along the northern validation line on May 10 (ASIRAS) and May 15 with marked positions of the corner reflectors.

ASIRAS track was extracted from the laser scanner swath to detect the corresponding surface elevation for each freeboard measurement (see Section 5.2.2). In Section 4.6.2, the surface elevation was shifted manually to align the in-situ surface elevation measurements on average, because the validation line did not include any open water spots or very thin ice and no other EM bird profiles were available in the vicinity, in which open water or very thin ice could have been detected. Here, the same lowest level could have been used that colleagues from DNSC applied to derive surface elevation from the laser scanner, because some longer laser scanner profiles were available near the validation line that included open water spots. However, this lowest level is insufficient for deriving the ASIRAS freeboard due to a lack of knowledge about cable lengths within the ASIRAS instrument that causes an unknown offset between freeboard and surface elevation measurements. Therefore, the ASIRAS ground elevation was shifted manually until it was visually optimal aligned, with the in-situ freeboard measurements. The variation of the ASIRAS freeboard is still independent of the in-situ observations since the ASIRAS ground elevation was shifted by a constant. However, the absolute snow depth is affected by the shift.

5.2.1 ASIRAS Freeboard, Surface Elevation and in-situ Measurements

In Fig. 5.10 on the left, the laser scanner swath is shown together with the ASIRAS track along the validation line on May 10 with marked positions of the corner reflectors. The positions of the corner reflectors were measured on the ground with a handheld GPS receiver. Additionally, the EM bird track is displayed on May 15. On the right, the EM bird track is shown as extracted track ('extracted scanner') with the equivalent surface elevations from the laser scanner swath ('DNSC scanner'). To match the 5 x 5 m measurement grid of the laser scanner data, the EM bird data were resampled and thus reduced (see Section 4.4). The ASIRAS track is off-center with respect to the scanner swath because of the squint angle of the laser scanner.

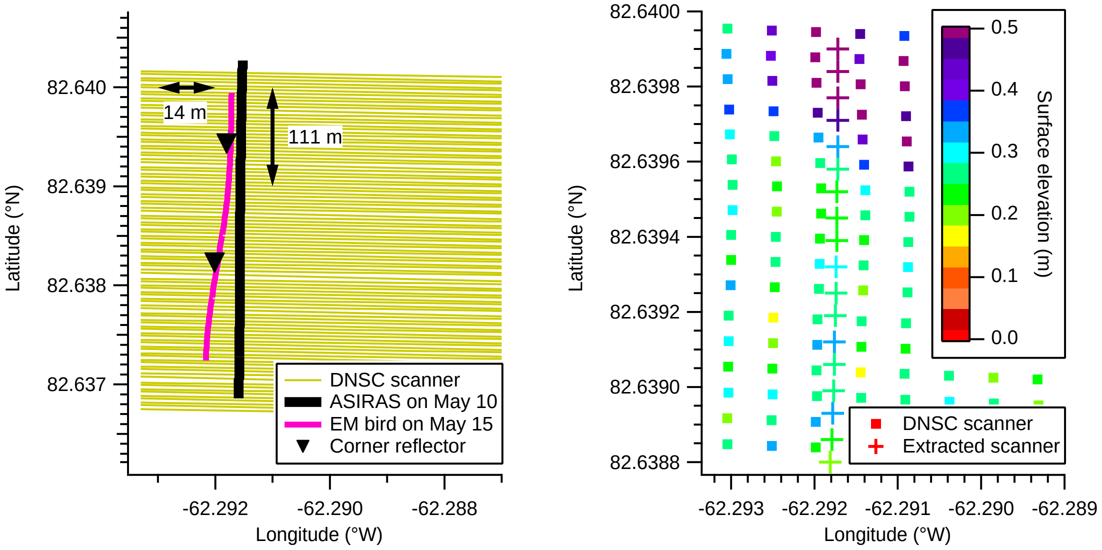

Figure 5.10: DNSC laser scanner, ASIRAS, and EM bird track along the northern validation line with marked positions of the corner reflectors on May 10 (ASIRAS and DNSC laser scanner) and May 15 (EM bird) (left) and color-coded surface elevations of the DNSC laser scanner and extracted for the EM bird track in the left graph (right).

In Fig. 5.11 the ‘GPS - laser’ surface elevation is shown that was derived with the lowest level from DNSC. Additionally displayed are the reduced data for which surface elevation was extracted from the laser scanner. Fig. 5.12, left shows the reduced surface elevation data (‘GPS - laser reduced’) and the equivalent extracted surface elevation from the laser scanner (‘extracted scanner’). Also shown is the surface elevation from ASIRAS[3] and the in-situ measured surface elevation. In Fig. 5.12 (right), freeboard from ASIRAS and in-situ readings for freeboard and snow depth are shown. The four vertical lines in ASIRAS freeboard (Fig. 5.12, right), and ASIRAS surface elevation (Fig. 5.12, left) respectively, indicate the corner reflectors at either end of the validation line. A vertical offset between the ‘GPS - laser’ surface elevation shown in Fig. 5.11 and the ‘extracted scanner’ surface elevation shown in Fig. 5.12 (left) is partially due to a different geoid when ground elevation was derived. Usually, the derived surface elevation is unaffected by different geoid models, as long as the lowest level refers to that ground elevation, in which it was detected. Here, ground elevation for ‘GPS - laser’ was derived with a geoid model from 2006 whereas the ground elevation for the ‘extracted scanner’ surface elevation in Fig. 5.11 was derived with a geoid model from 2004. The lowest level, however, that was applied to derive surface elevation for ‘GPS - laser’ referred to the ground elevation of the ‘extracted scanner’ and hence a different geoid. However, even if the offset between both geoid models of about 0.08 m is accounted for, the ‘GPS - laser’ surface elevation would be still too large compared to the different surface elevations in Fig. 5.12 (left). Therefore, the reduced EM bird surface elevation in Fig. 5.11 was shifted vertically by -0.48 m to match approximately the prominent peak near 82.6388° N in-situ surface elevation yielding ‘GPS - laser reduced’ (Fig. 5.12, left).

Regarding the ‘extracted scanner’ surface elevation, a mean vertical difference of about 0.1 m is visible compared to the equivalent in-situ observations (Fig. 5.12, left). However, a vertical agreement within 0.05 m with the in-situ snow

---

[3] ASIRAS freeboard plus in-situ measured snow depth.

depth measurements is seen indicating that the surface elevation from the laser scanner is too low. That is, the lowest level that served for deriving the surface elevation from the laser scanner does not match the local sea level perfectly. Inspecting the reduced 'GPS - laser' surface elevation in Fig. 5.12 (left), peaks are seen in the data which correspond to the pattern of height variation but not to the absolute values of the peaks seen in the 'extracted scanner' surface elevation at about 82.6386° N, 82.6389° N, and 82.6391° N. That these peaks are not aligned is due to the coarse grid spacing of the laser scanner data and the reduced 'GPS - laser' data as the measurement grid spacing slightly disagrees. Regarding the in-situ measurements, equivalent peaks are recognized at nearly the same locations, confirming a general agreement in surface elevation.

Freeboard derived from ASIRAS is shown by itself (Fig. 5.12, right) and together with the added in-situ measured snow depth to yield ASIRAS surface elevation (Fig. 5.12, left). This allows a comparison with surface elevations described before. Equivalent peaks are also seen in the ASIRAS surface elevation near 82.6386° N, 82.6389° N, and 82.6391° N. The ASIRAS surface elevation matches the 'GPS - laser' surface elevation better than it does the laser scanner, due to the manual alignment of freeboard and 'GPS - laser' surface elevation with the in-situ measurements by a constant. Comparing the ASIRAS freeboard (Fig. 5.12, right) to the readings at the drill holes, a higher variability is seen. The prominent dip in ASIRAS freeboard at 82.6389° N seems to be too low compared to the ground measurements resulting in a corresponding dip in ASIRAS surface elevation (Fig. 5.12, left). The mean values for 'GPS - laser', 'extracted scanner', ASIRAS surface elevation, and in-situ surface elevation are 0.36 m, 0.26 m, 0.38 m, and 0.33 m with standard deviations of 0.05 m, 0.04 m, 0.05 m, and 0.02 m respectively. Considering the in-situ surface elevation as the most accurate measurement, the 'extracted scanner' surface elevation shows the largest deviation of the mean values. Since the ASIRAS surface elevation was derived from the ASIRAS freeboard and the in-situ snow depth, these mean values and standard deviations need also to be considered. The mean values amount to 0.12 m and 0.26 m for the ASIRAS freeboard and the in-situ snow depth respectively (see Section 5.2.2) The standard deviations are 0.04 m each, indicating a good quality of the ASIRAS data for this short section of relatively smooth first-year ice.

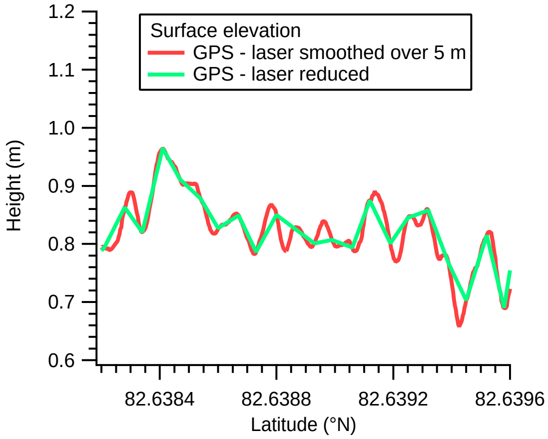

Figure 5.11:
'GPS - laser' surface elevation, derived with the EM bird setup, smoothed over 5 m and reduced to match the measurement grid of the laser scanner data.

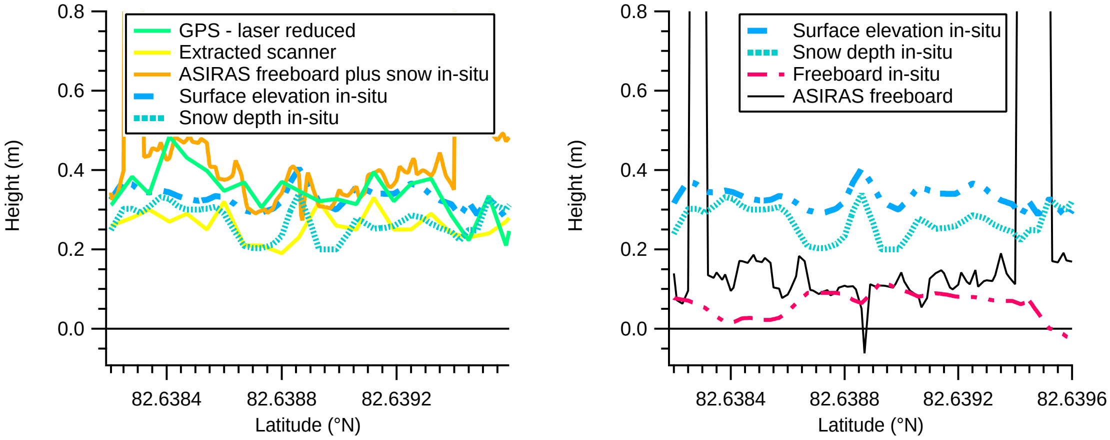

Figure 5.12: 'GPS - laser' surface elevation, extracted surface elevation from laser scanner, and in-situ measurements (left) and ASIRAS freeboard and in-situ measurements (right).

5.2.2 Comparison of Snow Depth – extended

In order to derive snow depth from the difference between surface elevation measured by the laser scanner and freeboard measured by ASIRAS, the ASIRAS track was extracted from the laser scanner swath, to account for the squint angle of the laser scanner, in the same way as the EM bird track was extracted in the previous section and in Section 4.4 to find the corresponding surface elevation. Fig. 5.13 (left) shows the reduced[4] ASIRAS freeboard for which the corresponding surface elevation was extracted from the laser scanner and the ASISRAS freeboard in its full resolution. In Fig. 5.13 (right) the resulting snow depth is shown for the ASIRAS flight on May 10. Additionally, the calculated snow depths from the EM bird setup (from coincident EM thickness and surface elevation data) and measured in-situ (see Section 4.6.2) are displayed.

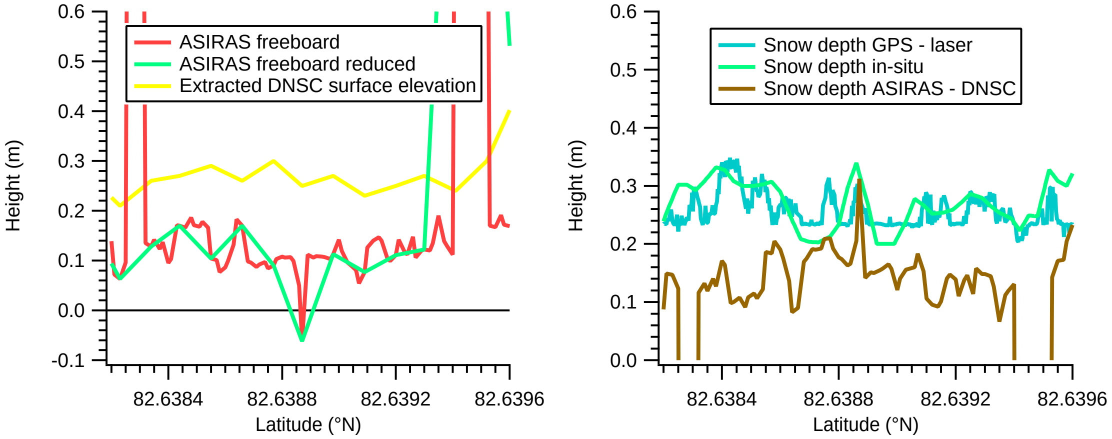

Figure 5.13: Surface elevation measured by the laser scanner and freeboard measured by ASIRAS (left). Snow depths from EM bird, in-situ, and from the difference between surface elevation measured by the laser scanner and freeboard measured by ASIRAS (right).

Obviously, the snow depth derived from the difference between surface elevation by the laser scanner and freeboard by ASIRAS is lower than the calculated snow depth from the EM bird and the measured snow depth on the ground. The mean values of 0.15 m for 'Snow depth ASIRAS - DNSC', 0.26 m for the snow depth from the EM bird, and 0.30 m for the in-situ measurement, confirm this observation. Correspondingly, standard deviations range between 0.04 m, 0.06 m, and 0.11 m. At about 82.6389° N, however, it agrees with the calculated snow depth from the EM bird. The histograms for the snow depths in Fig. 5.13 (right) are shown in Fig. 5.14. Compared to the histogram modes of the calculated and in-situ measured snow depths (a) and (b), which lie between 0.2 m and 0.3 m, the mode of the snow depth from the difference of the laser scanner and ASIRAS is at 0.12 m, and thus reflects approximately the difference between both data sets. The high variation of the ASIRAS - DNSC snow depth (Fig. 5.13 (right) and Fig. 5.14 c) as well as the penetration depth of the radar, need to be further investigated on the basis of several longer profiles along different ice regimes which induce a varying snow cover in terms of depth and composition.

---

[4] Reduced means that ASIRAS data were removed to match the grid spacing of the laser scanner data, similarly to 'GPS - laser reduced' in Fig. 5.11 in Section 5.2.1.

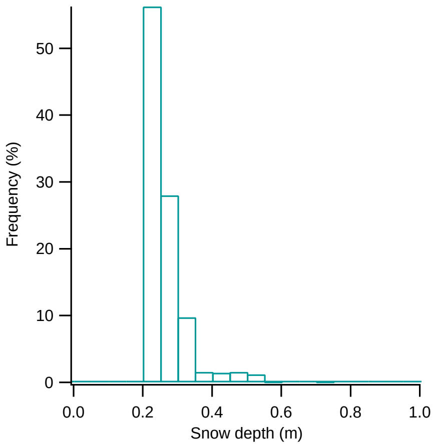

(a) EM bird

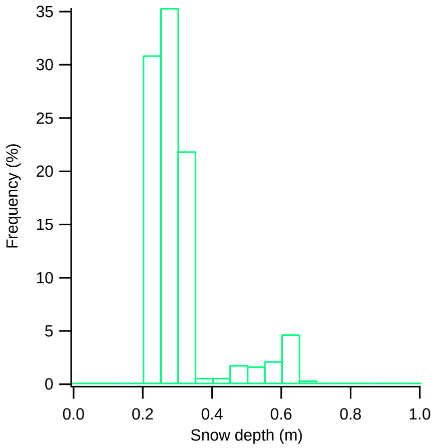

(b) in-situ

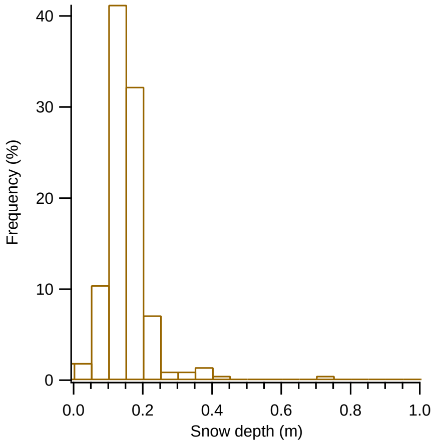

(c) ASIRAS - DNSC

Figure 5.14: Histograms of snow depth calculated with the EM bird setup (a), measured in-situ (b), and from the difference between surface elevation measured by the laser scanner (DNSC) and freeboard measured by ASIRAS on May 10 (c).

5.3 Summary

- The first comparison between EM thickness and surface elevation from the LD 90 laser altimeter showed a good agreement in the Bay of Bothnia and suggests that the results of LD 90 are suitable for further sea ice thickness studies.

- The first comparison between freeboard derived from the ASIRAS radar altimeter and surface elevation from the LD 90 laser altimeter in the Bay of Bothnia yielded nearly the same height for both measurement quantities along a short section across an open water lead. This indicated that both systems were well calibrated. However, from this cannot be concluded that snow depth can be derived sufficiently from the difference of the two measurements. Another short section showed uncertainties with respect to predictions of snow depth where ridging was present.

- The absence of open water spots along the validation line in the Arctic required taking the lowest level from profiles in the vicinity of the validation line. Since no other EM bird profiles were available on the same day on which the overflights were carried out, the lowest level from the DNSC laser scanner profile was used. Despite accounting for the different geoids used in deriving ground elevation, the ‘GPS - laser’ surface elevation was too large compared to the surface elevation measured in-situ. After a manual shift of the data, the topography of the ‘GPS - laser’ surface elevation agreed well with the extracted laser scanner surface elevation, i. e., three prominent peaks could be found in both profiles at almost the same position. The same three peaks were found in ASIRAS surface elevation and could be confirmed by in-situ measurements even if the peaks were not that distinct. Although an absolute comparison between the different surface elevations was not possible due to the uncertainty in the individual lowest levels (for surface elevation and freeboard), prominent surface features could be confirmed by the different measurement techniques.

- Snow depth resulting from the difference between the laser scanner and ASIRAS is consistently lower than snow depth from the EM bird and in-situ. This indicates that either the ASIRAS freeboard measurements are too large, which was partially confirmed by the in-situ freeboard readings, or the extracted surface elevation from the laser scanner is too low, which was also seen in the ground measurements. Further, a greater variation is seen as a consequence of the greater variable freeboard. Longer coincident profiles, including different ice regimes with different types of snow but also open water, to derive freeboard without shifting it to the in-situ measurements, are necessary to investigate the penetration depth of ASIRAS in detail.

- In contrast to the heavily ridged surface in the Bay of Bothnia, the validation line in the Arctic was ideal regarding the estimation of snow depth, apart from missing open water spots to derive freeboard. However, for this study ASIRAS test files have only been available from the first day that ASIRAS was used in the Arctic. More promising findings are expected as soon as more profiles from different days are available to increase the relevance of the results.

6 Discussion and Conclusions

After post-processing the GPS data, applying a geoid model, and synchronizing the GPS data and laser data, the ground elevation above the applied geoid was derived from the difference between the GPS height and the laser range. Due to deviations of the geoid model from the local sea level and under the assumption that each ground elevation profile includes very low values which represent open water or very thin ice, and hence the local sea level, a method of detecting these lowest values was introduced. Linear interpolation resulted in the lowest level that was subsequently subtracted from the ground elevation profile yielding surface elevation.

The accuracy of the ground elevation is dependent on the accuracy of the GPS and laser measurements, the geoid and the dynamic sea surface topography (DSST). If these quantities were perfectly known, ground elevation would be equal to surface elevation. Since this is not the case, the reference for surface elevation (the local sea level) is derived from detecting open water leads or very thin ice in the ground elevation profile. Therefore, the presence of clearly identifiable open water leads or thin ice throughout the profile is a necessary requirement in the determination of surface elevation. Ideally, leads of a certain width should be spaced continuously, not exceeding a spatial distance of approximately 15 km. Regarding the length of the segments[1] obtained with the EM bird setup the leads should be distributed in a way that at least two are present in each segment. Otherwise, temporal and spatial sea level variations cannot be resolved. In the profile segments obtained in the Arctic and Antarctic, approximately three to six leads, and hence an equal number of detected lowest values yielded a spatial distance of about 5 – 15 km. The required width of the leads is generally dependent on the measurement point spacing of surface elevation. With respect to the EM bird setup, a minimum width of 1 m is adequate (regarding the measurement point spacing of 0.4 m for the laser).

Furthermore, the accuracy of the derived surface elevation is dependent on the attitude of the EM bird. Since no INS is mounted inside the EM bird, the slant range of the laser is used instead of the true vertical height above ground. The slant range variation is mainly affected by roll events of the EM bird. Analyzing profile sections above a homogeneously frozen polynya with a very thin ice cover yielded surface elevations of $0\,\mathrm{m} \pm 0.1\,\mathrm{m}$. This number is considered to be an estimate of the measurement accuracy of surface elevation. The uncertainty of $\pm 0.1\,\mathrm{m}$ is equivalent to a roll angle of about 4° in the case of the EM bird. Occasionally, however, larger roll angles were estimated by visual observation causing an increased uncertainty in surface elevation.

Another major issue in this study was the transformation of surface elevation to total thickness and the validation by simultaneous thickness measurements with the EM bird. In order to validate the total thickness derived from surface

---

[1] In the Arctic, the entire flight profile, composed of separate segments, was analyzed in concert whereas in the Antarctic the profile was split into these segments which were analyzed separately. The segments result from necessary calibrations of the EM bird, which are performed roughly every 15 km.

elevation with the EM thickness, the footprint and measurement point spacing of the EM bird has to be taken into account. Ideally, the surface elevation is smoothed over the same area that is covered by the footprint and resampled to match the measurement grid of the EM bird. Then, the histograms and both thickness profiles agree very well. However, the agreement between the surface elevation and EM thickness is misleading, because, in reality surface elevation does not necessarily correspond to the ice draft, and hence total thickness. Therefore, the surface elevation profiles were transformed to total thickness neglecting the footprint size and the grid spacing. A smoothing of the surface elevation over 12 m was found to be adequate in order to reduce the small-scale surface roughness while preserving all topographic features such as ridges.

Errors in the retrieved total thickness result from uncertainties in the R-values which were used to transform surface elevation. Due to the large variability and sensitivity of R, it is impossible to find a standard rule for transforming surface elevation to total thickness. Therefore, the R-value was derived from the histogram modes of the simultaneous measurements of surface elevation and total thickness with the EM bird yielding EM thickness. Thus, an agreement within the accuracy of the EM thickness (± 0.1 m) was possible for level ice. To approximate the error of total thickness, first, the error of R in dependence on surface elevation had to be determined. Here, the error approximation was based on total thickness as it was derived from the histogram modes of surface elevation and EM thickness. The errors of the modes were estimated with 0.01 m for surface elevation and 0.1 m for the EM thickness. After applying the Gaussian error propagation for all profiles in the Arctic, an exponential fitting function was used to approximate the error of R. Subsequently, the error of total thickness was calculated with this error function. Apart from a strong increase and decrease in the total thickness error for surface elevations below 0.2 m, a linear increase was found for surface elevations larger than 0.2 m.

The generation of a set of fitting functions for open water, first-year ice and multi-year ice, and their application to surface elevation profiles different from that for which they were created, is seen as an alternative and first approach to derive the total thickness if coincident thickness measurements are not available. However, this approach has deficiencies if the surface elevation differences are considerable between profiles. In the area of the Lincoln Sea and north of Ellesmere Island one fitting function was sufficient, with one exception, and even worked well for a profile from another year. In contrast, in the Weddell Sea more than one set of fitting functions was necessary to account for the larger variability of surface elevation.

Regarding the validation of satellite missions, such as ICESat, this study showed a high relevance of the measurements performed with the EM bird setup. The large measurement point spacing of ICESat makes it especially difficult to detect leads of open water. The GPS/laser measurements of the EM bird setup clearly support the determination of surface elevation, and hence total thickness.

Calculating total thickness on the basis of hydrostatic equilibrium and assuming parameters for the specific densities of sea water, sea ice, and snow as well as snow depth, is unreliable because slightly inaccurate snow depth estimates have unacceptably large and undesirable effects on the total thickness. On the other hand, snow depth can be calculated from the simultaneous measurements of surface elevation and total thickness. The retrieval of snow depth is seen as a valuable "by-product" in the determination of surface elevation with respect to the simultaneous EM thickness measurements. Averaging the calculated snow depth over profile sections of different lengths resulted in a good agreement with data from a climatological model. Furthermore, the calculated snow depth was within ±5 cm in good agreement with the in-situ measured snow depth.

The results for snow depth can thus be used as estimates in areas for which climatological data are missing and/or sparsely available (e. g., shelf seas of Antarctica), or to complete the existing data set. In any case, the calculated snow depth estimates are suitable to support future satellite missions in terms of transforming surface elevation, and freeboard respectively, to total thickness.

Another topic addressed in this study comprised the comparison between laser and radar altimetry. However, a detailed investigation of the radar altimeter ASIRAS was not the main aspect, but rather an illustration of first measurement results for chosen profile sections. The radar altimeter ASIRAS was flown in the Bay of Bothnia in March 2006 for the first time over sea ice. Here, a single-beam laser altimeter LD 90 was additionally installed in the airplane. The data processing yielded freeboard from ASIRAS, and surface elevation from LD 90. Two different profile sections were analyzed with respect to the difference between both measurement results that is mainly due to the different penetration depth of radar and laser beams. Since laser beams are always reflected by the uppermost surface layer and radar signals are expected to return from the snow/ice interface, the resulting height difference yields the snow depth. As a consequence, a snow depth of 0 m should result from measurements above open water and bare ice. Upon analyzing an open water lead with a snow-free frozen edge, the measurements indicated the absence of snow. Moreover, they showed almost equal results for freeboard and surface elevation confirming that this ice section was impermeable to radar signals. An increase of freeboard, surface elevation and snow depth was visible at the transition from the lead to thicker snow-covered ice, indicating promising results in terms of determining the snow depth.

However, a detailed investigation over different ice types with a varying snow cover (in depth and composition) is necessary to fully understand the penetration behavior of radar beams. In contrast to the snow depth calculation with the EM bird setup, mentioned before, here, large scale measurements of snow depth are possible due to the larger range of the airplane compared to the helicopter. Nevertheless, the snow depth calculations based on the EM bird setup show a valuable, independent approach and support the coincident laser/radar measurements with respect to deriving snow depth.

In conclusion, this study demonstrated the potential of deriving surface elevation and total thickness with helicopter-borne laser altimetry, but it also pointed out the difficulties and uncertainties of transforming the former to the latter. Especially, if coincident total thickness measurements are not available, large errors are induced in total thickness very easily. Therefore, promising techniques were introduced with respect to this issue. Specifically, the influence of the unknown snow depth, and hence the sensitivity on the R-values, makes it impractical to find an explicit relation that accounts for its large variability.

Regarding the conducted measurements, this work provides a comprehensive set of *R*-values for the Lincoln Sea area in the Arctic, and for the first time, a similar set for the Weddell Sea in the Antarctic. The techniques discussed in this study of estimating snow depth are highly relevant, e. g., for the upcoming CryoSat-2 mission where accurate snow depth estimates are required. With respect to airborne and spaceborne laser altimetry, this investigation showed the feasibility of deriving and validating surface elevation and illuminates the need for a more cautious evaluation of the derived total sea ice thickness results.

7 Outlook

Assuming that it was possible to establish a standard rule regarding the usage of the correct *R*-values, the simultaneous measurements of surface elevation and total thickness with the EM bird setup would still allow for a better understanding of the relationship between both quantities than that afforded by measurements from airborne or spaceborne missions which need to be validated by independent observations.

In general, the intra-annual variability in total thickness can be investigated and the error from inaccurate *R*-values minimized, if such measurements were done more often throughout the year to account for seasonal changes in snow depth. Problems may arise in winter when no open water leads are present at all. The derived *R*-values and snow depths could be summarized in a look-up table, separated in seasons, and repeat measurements in the following years would allow a better understanding of the inter-annual variability and reveal a trend from which predictions with respect to *R* may be derived. Ideally, the measurements should be conducted in characteristic areas such as the Lincoln Sea and the seas in the West Siberian Arctic where the sea ice floes from the entire Arctic Ocean are pushed together and form very thick ice. Equivalently, the Beaufort Sea should be surveyed to get an overview of the changes on the opposite side of the Arctic where the retreat of ice extent is considerable. The Fram Strait represents an interesting area with respect to the ice quantity leaving the Arctic Ocean, and thus is highly relevant for sea ice thickness studies and as such, should be monitored. In the Antarctic, similar measurements in the Eastern and Western Weddell Sea as well as in the other seas are conceivable.

Regarding airborne and spaceborne satellite missions, the improved *R*-values and snow depths, compared to single mean values, would improve the conversion of surface elevation, and freeboard respectively, and hence the total sea ice thickness results. A combination of laser and radar altimetry would improve the results even further as surface elevation and freeboard can be transformed to total thickness with a higher accuracy if the snow depth is known. As soon as snow depth can be derived sufficiently from the difference between surface elevation and freeboard, improved results of total thickness are expected.

Bibliography

ALTAMIMI, Z., BOUCHER, C. & DUHEM, L. (1993): The worldwide centimetric terrestrial reference frame and its associated velocity field. *Advances in Space Research*, 13, 151–160.

ALTAMIMI, Z., SILLARD, P. & BOUCHER, C. (2001): Review and Progress of the ITRF Datum Definition: New Results From ITRF2000. *AGU Fall Meeting Abstracts*, A2+.

BADER, H. (1962): The Physics and Mechanics of Snow as a Material. Technical Report II–B, p.1, Cold Regions Research and Engineering Laboratory, Hanover, NH.

BEUTLER, G., ROTHACHER, M., SCHAER, S., SPRINGER, T. A., KOUBA, J. & NEILAN, R. E. (1999): The international GPS service (IGS): an interdisciplinary service in support of earth sciences. *Advances in Space Research*, 23, 631–653.

BOEBEL, T. (2000): Airborne topography and gravimetry: System and application to Fram Strait, Svalbard and Northeast Greenland. Technical Report Reports on Polar Research, 366, Alfred Wegener Institute for Polar and Marine Research, Bremerhaven, Germany.

BRANDON, M. A., BRIERLEY, A. S., FERNANDES, P. G., BANKS, C. J., JENKINS, A., HAYES, D. & AUTOSUB ENGINEERING TEAM, . (2003): The sea ice Thickness Distribution and Iceberg Size Distribution From AUV Measurements in the Northern Weddell and Eastern Amundsen Seas. *AGU Fall Meeting Abstracts*, A8+.

CAMPBELL, K. J. & ORANGE, A. S. (1974): A continuous profile of sea ice and freshwater ice thickness by impulse radar. *Polar Records*, 17, 31–41.

CANNON, M. E., SCHWARZ, K.-P. & WONG, R. V. C. (1986): Kinematic positioning with GPS – an analysis of road tests. In *Proceedings of the Fourth International Geodetic Symposium on Satellite Positioning, Austin, Texas*, volume 2, 1251–1268.

CHAMBERS, D. P., MEHLHAFF, C. A., URBAN, T. J., FUJII, D. & NEREM, R. S. (2002): Low-frequency variations in global mean sea level: 1950-2000. *Journal of Geophysical Research (Oceans)*, 107, 1–1.

COMISO, J. C. (2003): Larg–scale Characteristics and Variability of the Global Sea Ice Cover. In THOMAS, D. N. & DIECKMANN, G. S., eds., *SEA ICE An Introduction to its Physics, Chemistry, Biology and Geology*, 112–142, Blackwell Science Ltd.

COMISO, J. C., WADHAMS, P., KRABILL, W. B., SWIFT, R. N., CRAWFORD, J. P. & TUCKER, W. B. (1991): Top/bottom multisensor remote sensing of Arctic sea ice. *Journal of Geophysical Research*, 96(C2), 2693–2709.

COX, G. F. N., RICHTER-MENGE, J. A., WEEKS, W. F. & MELLOR, M. (1984): Mechanical properties of multiyear sea ice – Phase 1 test results. Technical Report 84–9, U.S. Army Corps of Engineers, Cold Regions Research and Engineering Laboratory, Hannover, NH.

CURRY, J. A., SCHRAMM, J. L. & EBERT, E. E. (1995): Sea Ice–Albedo Climate Feedback Mechanism. *Journal of Climate*, 8, 240–247.

DICK, W. R. & RICHTER, B. (2004): *The International Earth Rotation and Reference Systems Service (IERS)*, 159–+. ASSL Vol. 310: Organizations and Strategies in Astronomy, Vol. 5.

DRINKWATER, M. R., RATIER, R. F. G. & WINGHAM, D. J. (2004): The European Space Agency's Earth Explorer Mission CryoSat: measuring variability in the cryosphere. *Annals of Glaciology*, 39, 313–320.

EICKEN, H. (2003): From the Microscopic, to the Macroscopic, to the Regional Scale: Growth, Microstructure and Properties of Sea Ice. In THOMAS, D. N. & DIECKMANN, G. S., eds., *SEA ICE An Introduction to its Physics, Chemistry, Biology and Geology*, 22–81, Blackwell Science Ltd.

EICKEN, H., LENSU, M., LEPPÄRANTA, M., TUCKER, W. B., GOW, A. J. & SALMELA, O. (1995): Thickness, structure, and properties of level summer multiyear ice in the Eurasian sector of the Arctic Ocean. *Journal of Geophysical Research*, 100, 22697–22710.

EVANS, S. (1965): Dielectric properties of ice and snow – A review. *Journal of Glaciology*, 5(42), 773–792.

FORSBERG, R. & KENYON, S. (2003): Gravity Field of the Arctic Region – Filling One of the Polar Gaps For the New Satellite Missions. *EGS – AGU – EUG Joint Assembly, abstract #7884*, 7884–+.

FORSBERG, R. & SKOURUP, H. (2005): Arctic Ocean gravity, geoid and sea–ice freeboard heights from ICESat and GRACE. *Geophysical Research Letters*, 32, 21502–+.

FORSBERG, R., OLESEN, A., BASTOS, L., GIDSKEHAUG, A., MEYER, U. & TIMMEN, L. (2000): Airborne geoid determination. *Earth, Planets, and Space*, 52, 863–866.

FORSBERG, R., KELLER, K. & JACOBSEN, S. M. (2001): Laser monitoring of ice elevations and sea–ice thickness in Greenland. *Int. Arch. Photogramm. Remote Sens. Spatial Inf. Syst.*, 163–169.

GARRITY, C. (1991): *Passive microwave remote sensing of snow covered floating ice during spring conditions in the Arctic and Antarctic*. Ph.d. dissertation, York University, CRESS Dept., North York, Canada.

HAAS, C. (1998): Evaluation of ship-based electromagnetic-inductive thickness measurements of summer sea–ice in the Bellingshausen and Amundsen Sea. *Cold Regions Science and Technology*, 27, 1–16.

HAAS, C. (2003): Dynamics versus Thermodynamics: The Sea Ice Thickness Distribution. In THOMAS, D. N. & DIECKMANN, G. S., eds., *SEA ICE An Introduction to its Physics, Chemistry, Biology and Geology*, 82–111, Blackwell Science Ltd.

HAAS, C., GERLAND, S., EICKEN, H. & MILLER, H. (1997): Comparison of sea–ice thickness measurements under summer and winter conditions in the Arctic using a small electromagnetic induction device. *Geophysics*, 62(3), 749–757.

HAAS, C., RUPP, K.-H. & UUSKALLIO, A. (1999): Comparison of along track EM ice thickness profiles with ship performance data. In TUHKURI, J. & RISKA, K., eds., *15th International Conference on Port and Ocean Engineering under Arctic Conditions (POAC 99)*, volume 1, 23–27, Espoo, Finland.

HAAS, C., GOEBELL, S., HENDRICKS, S., MARTIN, T., PFAFFLING, A. & VON SALDERN, C. (2006a): Airborne electromagnetic measurements of sea ice thickness: methods and applications. In WADHAMS, P. & AMANATIDIS, G., eds., *Arctic Sea Ice Thickness: Past, Present and Future*, Climate Change and Natural Hazards Series, Bruxelles.

HAAS, C., HENDRICKS, S. & DOBLE, M. (2006b): Comparison of the sea ice thickness distribution in the Lincoln Sea and adjacent Arctic Ocean in 2004 and 2005. *Annals of glaciology*, 44.

HALL, D. K. & MARTINEC, J. (1985): *Remote Sensing of Ice and Snow*. Chapman and Hall Ltd., London.

HARMS, S., FAHRBACH, E. & STRASS, V. H. (2001): Sea ice transports in the Weddell Sea. *Journal of Geophysical Research*, 106, 9057–9073.

HAWLEY, R. L., MORRIS, E. M., CULLEN, R., SHEPHERD, A. P. & WINGHAM, D. (2006): ASIRAS airborne radar resolves internal annual layers in the dry–snow zone of Greenland. *Geophysical Research Letters*, 33.

HEISKANEN, W. A. & MORITZ, H. (1993): *Physical Geodesy*, Reprint. Institute of Physical Geodesy, Technical University Graz.

HELLMER, H. H., DIECKMANN, G. S., HAAS, C. & SCHRÖDER, M. (2006): Sea ice feedbacks observed in western Weddell Sea. *EOS, Transactions, American Geophysical Union*, 87(18), 173–179.

HELM, V., HENDRICKS, S., GOEBELL, S., RACK, W., HAAS, C., NIXDORF, U. & BOEBEL, T. (2006): CryoVex 2004 an 2005 (BoB) data acquisition and final report. Technical report, ESA.

HIBLER, W. D. I. (1972): Removal of aircraft altitude variation from laser profiles of the Arctic ice pack. *Journal of Geophysical Research*, 77(36), 7190–7195.

HOFMANN-WELLENHOF, B. & LICHTENEGGER, H. (1992): *GPS Theory and Practice*. Springer–Verlag Wien New York.

HOLLADAY, J. S. (1993): Operational electromagnetic ice thickness sensor trial. Technical Report TP1160, Canadian Coast Guard Report.

HUDSON, R. (1990): Annual measurement of sea–ice thickness using an upward–looking sonar. *Nature*, 344, 135—-137.

HVIDEGAARD, S. M. & FORSBERG, R. (2002): Sea–ice thickness from airborne laser altimetry over the Arctic Ocean north of Greenland. *Geophysical Research Letters*, 29(20), doi:10.1029/2001GL014474, 1952.

ISHIZU, M., MIZUTANI, K. & T., I. (1999): Airborne freeboard measurements of sea ice and lake ice at the Sea of Okhotsk coast in 1993–95 by a laser altimeter. *International Journal of Remote Sensing*, 20(12), 2461–2476.

KARCHER, M. J., GERDES, R., KAUKER, F. & KÖBERLE, C. (2003): Arctic warming: Evolution and spreading of the 1990s warm event in the Nordic seas and the Arctic Ocean. *Journal of Geophysical Research (Oceans)*, 108, 16–1.

KENYON, S. (2000): Arctic Gravity Project. In *IAG proceedings volume of Gravity, Geoid and Geodynamics conference*, Banff, Springer Verlag.

KENYON, S. & FORSBERG, R. (2001): Arctic Gravity Project – A Status. In SIDERIS, M. G., ed., *Gravity, Geoid and Geodynamic 2000, International Association of Geodesy Symposia*, Springer, New York.

KETCHUM, R. D. (1971): Airborne laser profiling of the Arctic pack ice. *Remote Sensing of Environment*, 2, 41–52.

KING, A. D. (1998): Inertial navigation – forty years of evolution. *GEC Review*, 13(3), 140–149.

KÖNIG, R., SCHWINTZER, P., BODE, A. & REIGBER, C. (1996): GFZ–1: a small laser satellite mission for gravity field model improvement. *Geophysical Research Letters*, 23, 3143–3146.

KÖNIG, R., SCHWINTZER, P., BODE, A. & REIGBER, C. (1999): Improvement in Global Gravity Field Recovery Using GFZ–1 Satellite Laser Tracking Data. *Journal of Geodesy*, 73, 398–406.

KOVACS, A. (1978): A radar profile of multiyear pressure ridge fragment. *Arctic*, 31, 59–62.

KOVACS, A. & HOLLADAY, J. S. (1990): Sea ice measurement using a small airborne electromagnetic sounding system. *Geophysics*, 55, 1327–1337.

KOVACS, A., HOLLADAY, J. S. & BERGERON, C. J., J. (1993): Footprint Size of a Helicopter–Borne Electromagnetic Induction Sounding System Versus Antenna Altitude. Technical Report CRREL Report 93–12, U.S. Army Corps of Engineers, Cold Regions Research and Engineering Laboratory.

KOWALIK, Z. & PROSHUTINSKY, A. Y. (1993): Diurnal Tides in the Arctic Ocean. *Journal of Geophysical Research*, 98(C9), 16449–16468.

KRABILL, W. B., SWIFT, R. N. & TUCKER, W. B., I. (1990): Characterization of the surface roughness and floe geometry of the sea ice over the continental shelves of the Beaufort and Chukchi Seas. In ACKLEY, S. F. & WEEKS, W. F., eds., *Sea Ice Properties and Processes, Monogr.*, 132–136, U.S. Army Cold Regions Research and Engineering Laboratory, Hanover, N. H.

KRISTOFFERSON, Y. (2004): Dynamics versus Thermodynamics: The Sea Ice Thickness Distribution. In KRISTOFFERSON, Y. & MIKKELSEN, N., eds., *Scientific Drilling in the Arctic Ocean and the site survey challenge: Tectonic, paleoceanographic and climate evolution of the Polar Basin*, Geological Survey of Denmark and Greenland, Special publication, JEODI Workshop, Copenhagen, 2003.

KUMAI, M. & ITAGAKI, K. (1988): Cinematographic study of ice crystal formation in water. Technical Report Ser. II, 4, Faculty of Science, Hokkaido Universtiy, Hokkaido, Japan.

KWOK, R. & CUNNINGHAM, G. F. (2002): Seasonal ice area and volume production of the Arctic Ocean: November 1996 through April 1997. *Journal of Geophysical Research (Oceans)*, 107(C10), 12–1.

KWOK, R., ZWALLY, H. J. & YI, D. (2004): ICESat observations of Arctic sea ice: A first look. *Geophysical Research Letters*, 31, 16401–+.

KWOK, R., CUNNINGHAM, G. F., ZWALLY, H. J. & YI, D. (2006): ICESat over Arctic sea ice: Interpretation of altimetric and reflectivity profiles. *Journal of Geophysical Research (Oceans)*, 111(C10), 6006–+.

LACHAPELLE, G., CANNON, M. E., ERICKSON, C. & FALKENBER, W. (1992): High precision C/A code technology for rapid static DGPS surveys. In *Proceedings of the Sixth International Geodetic Symposium on Satellite Positioning, Columbus, Ohio*, volume 1, 165–173.

LAXON, S. & PEACOCK, N. SMITH, D. (2003): High interannual variability of sea ice thickness in the Arctic region. *Nature*, 425, 947–950.

LEMOINE, F. G., KENYON, S. C., FACTOR, J. K., TRIMMER, R. G., PAVLIS, N. K., CHINN, D. S., COX, C. M., KLOSKO, S. M., LUTHCKE, S. B., TORRENCE, M. H., WANG, Y. M., WILLIAMSON, R. G., PAVLIS, E. C., RAPP, R. H. & OLSON, T. R. (1998): The Development of the Joint NASA GSFC and NIMA Geopotential Model EGM96. Technical Report NASA/TP–1998–206861, NASA Goddard Space Flight Center, Greenbelt, Maryland, 20771 USA.

LEWIS, E. O., LIVINGSTONE, C. E., GARRITY, C. & ROSSITER, J. R. (1994): Properties of Snow and Ice. In HAYKIN, S., LEWIS, E. O., RANEY, R. K. & ROSSITER, J. R., eds., *Remote Sensing of Sea Ice and Icebergs*, 21–96, John Wiley and Sons, New York.

LINDENBERGER, J. (1993): Laser–Profilmessung zur topographischen Geländeaufnahme. Technical Report C(400), Deutsche Geodätische Kommision, München.

LOHMAR, F. J. (1988): World geodetic system 1984 – geodetic reference system of GPS orbits. *Lecture Notes in Earth Sciences, Berlin Springer Verlag*, 19, 476–486.

MARSH, J. G., KOBLINSKY, C. J., LERCH, F., KLOSKO, S. M., ROBBINS, J. W., WILLIAMSON, R. G. & PATEL, G. B. (1990): Dynamic sea surface topography, gravity, and improved orbit accuracies from the direct evaluation of Seasat altimeter data. *Journal of Geophysical Research*, 95, 13129–13150.

MARTIN, S. (2004): *An Introduction to Ocean Remote Sensing*. Cambridge University Press, Cambridge, U.K.

MASSOM, R. A., EICKEN, H., HAAS, C., JEFFRIES, M. O., DRINKWATER, M. R., STURM, M., WORBY, A. P., WU, X., LYTLE, V. I., USHIO, S., MORRIS, K., REID, P. A., WARREN, S. G. & ALLISON, I. (2001): Snow on Antarctic sea ice. *Reviews of Geophysics*, 39, 413–445.

MAYKUT, G. A. & UNTERSTEINER, N. (1971): Some results from a time–dependent thermodynamic model of Arctic sea ice. *Journal of Geophysical Research*, 76(6), 1550–1575.

MELLING, H. & RIEDEL, D. A. (1995): Comparison of sea–ice thickness measurements under summer and winter conditions in the Arctic using a small electromagnetic induction device. *Journal of Geophysical Research*, 100, 13641–13653.

MELLING, H., RIEDEL, D. A. & GEDALOF, Z. (2005): Trends in the draft and extent of seasonal pack ice, Canadian Beaufort Sea. *Geophysical Research Letters*, 32, 24501–+.

NAGURNY, A. P., KOROSTOLEV, V. G. & ABAZA, V. P. (1994): A method for determination of effective sea ice thickness in the Arctic basin for climate monitoring. *Bull. Russian Acad. Sci., Phys. Suppl.*, 58.

NIELL, A. E. (1996): Global mapping functions for the atmosphere delay at radio wavelengths. *Journal of Geophysical Research*, 101, 3227–3246.

OSWALD, J., MITCHELL, J. & WHITING, L. (1986): Simple differential techniques using the Trimble 4000A GPS locator. In *Proceedings of the Fourth International Geodetic Symposium on Satellite Positioning, Austin, Texas*, volume 1, 503–511.

OTTO, D. (2004): *Validierung von Bodenradar–Messungen der Eis– und Schneedicke auf ein–und mehrjährigem Meereis in Arktis und Antarktis*. Masterthesis, Technical University Clausthal, Germany.

PEROVICH, D. K. (1985): Dynamics versus Thermodynamics: The Sea Ice Thickness Distribution. In LEPPÄRANTA, M., ed., *Physics of Ice–covered Seas*, Vol. 1,195–230, University of Helsinki Press, Helsinki, Finland.

PILKINGTON, G. R. & WRIGHT, B. D. (1991): Beaufort Sea ice thickness measurements from an acoustic, under ice, upward looking ice keel profiler. In *Proceedings of the 1st International Offshore and Polar Engineering Conference, Edinburgh*.

PRINSENBERG, S. J., HOLLADAY, J. S., ROSSITER, J. R. & LALUMIERE, L. A. (1992): Beaufort Sea EM/Radar ice and snow sounding project. Technical Report 139, Canadian Technical Report of Hydrology and Ocean Science.

RANEY, R. K. (1998): The Delay–Doppler Radar Altimeter. *IEEE Transactions on Geoscience and Remote Sensing*, 36(5).

REID, J. E. & VRBANCICH, J. (2004): A comparison of the inductive–limit footprints of airborne electromagnetic configurations. *Geophysics*, 69(5), 1229–1239.

REIGBER, C., JOCHMANN, H., WÜNSCH, J., PETROVIC, S., SCHWINTZER, P., BARTHELMES, F., NEUMAYER, K.-H., KÖNIG, R., FÖRSTE, C., BALMINO, G., BIANCALE, R., LEMOINE, J.-M., LOYER, S. & PEROSANZ, F. (2005): Earth gravity field and seasonal variability from CHAMP. In REIGBER, C., LÜHR, H., SCHWINTZER, P. & WICKERT, J., eds., *Earth Observation with CHAMP: Results from Three Years in Orbit*, 25–30, Springer–Verlag, Berlin, Germany.

REIGBER, C., SCHMIDT, R., FLECHTNER, F., KONIG, R., MEYER, U., NEUMAYER, K. H., SCHWINTZER, P. & ZHU, S. Y. (2005): An Earth gravity field model complete to degree and order 150 from GRACE: EIGEN–GRACE02S. *Journal of Geodynamics*, 39, 1–10.

ROSSITER, J. R. (1980): Review of impulse radar sounding of sea ice. In ROSSITER, J. R. & BAZELEY, D. P., eds., *International Workshop on the Remote Estimation of Sea Ice Thickness*, volume 80–5, 77–107.

ROSSITER, J. R. & LALUMIERE, L. A. (1988): Evaluation of sea ice thickness sensors. Technical Report TP9169E, Transportation Development Centre.

ROSSITER, J. R., LANGHORNE, P., RIDINGS, T. & J., A. A. (1977): Study of sea ice using impulse radar. In *Fourth International Conference on Port and Ocean Engineering under Arctic Conditions*, 556–567.

ROTHROCK, D. A., YU, Y. & MAYKUT, G. A. (1999): Thinning of the Arctic sea–ice cover. *Geophysical Research Letters*, 26, 3469–3472.

SCHEINERT, M. (2005): The Antarctic Geoid Project: Status Report and Next Activities. In JEKELI, C., BASTOS, L. & FERNANDES, J., eds., *Gravity, Geoid and Space Missions, IAG Symposia*, 137–142, Springer Berlin Heidelberg New York.

SCHUTZ, B. E., ZWALLY, H. J., SHUMAN, C. A., HANCOCK, D. & DIMARZIO, J. P. (2005): Overview of the ICESat Mission. *GRL*, 32, 21–+.

SCHWARTZ, J. & WEEKS, W. F. (1977): Engineering properties of sea ice. *Journal of Glaciology*, 19(81), 499–530.

SCHWINTZER, P., REIGBER, C., BODE, A., KANG, Z., ZHU, S. Y., MASSMAN F.-H. AD RAIMONDO, J. C., BIANCALE, R., BALMINO, G., LEMOINE, J. M., MOYNOT, B., MARTY, J. C., BARLIER, F. & BOUDON, Y. (1997): Long–wavelength global gravity field models: GRIM4–S4, GRIM4–C4. *Journal of Geodesy*, 71, 949–7714.

STRANGE, W. E. (1985): High–precision, three–dimensional differential positioning using GPS. In *Proceedings of the First International Symposium on Precise Positioning with the Global Positioning System, Rockville, Maryland*, volume 2, 543–548.

TAPLEY, B., RIES, J., BETTADPUR, S., CHAMBERS, D., CHEN, M., CONDI, F., GUNTER, B., KANG, Z., NAGEL, P., PASTOR, R., PEKKER, T., POOLE, S. & WANG, F. (2005): GGM02 – An improved Earth gravity field model from GRACE. *Journal of Geodesy*, 79, 1394–1432.

TAPLEY, B. D., BETTADPUR, S., WATKINS, M. & REIGBER, C. (2004): The gravity recovery and climate experiment: Mission overview and early results. *GRL*, 31, 9607–+.

THORNDIKE, A. S., ROTHROCK, D. A., MAYKUT, G. A. & COLONY, R. (2005): The Thickness Distribution of Sea Ice. *Journal of Geophysical Research*, 80(33), 4501–4513.

TSCHERNING, C. C., FORSBERG, R. & KNUDSEN, P. (1992): The GRAVSOFT package for geoid determination. In *Continental Workshop on the Geoid in Europe*, 327–334.

TUCKER, W. B., WEEKS, W. F. & FRANK, M. (1979): Sea ice ridging over the Alaskan continental shelf. *Journal of Geophysical Research*, 84, 4885–4897.

VINJE, T., NORDLUND, N. & KVAMBEKK, A. (1997): Monitoring ice thickness in Fram Strait. *Journal of Geophysical Research*, 103, 10437–10450.

WADHAMS, P. (1976): Sea ice topography in the Beaufort Sea and its effect on oil containment. *AIDJEX Bulletin*, 33, 11–52, Div. of Mar. Resour., Univ. of Washinngton, Seattle.

WADHAMS, P. (1988): The underside of Arctic sea ice imaged by sidescan sonar. *Annals of Glaciology*, 12, 217–217.

WADHAMS, P. (1990): Evidence for thinning of the Arctic ice cover north of Greenland. *Nature*, 345, 795–797.

WADHAMS, P. (1991): Concurrent remote sensing of Arctic sea ice from submarine and aircraft. *International Journal of Remote Sensing*, 12(9), 1829–1840.

WADHAMS, P. (2000): *Ice in the Ocean*. Gordon and Breach Science Publishers, Amsterdam.

WADHAMS, P. & HORNE, R. J. (1980): An analysis of ice profiles obtained by submarine sonar in the Beaufort Sea. *Journal of Glaciology*, 25, 401–424.

WADHAMS, P., TUCKER, W. B., KRABILL, W. B., SWIFT, R. N., COMISO, J. C. & DAVIS, N. R. (1992): Relationship between sea ice freeboard and draft in the Arctic Basin, and implications for ice thickness monitoring. *Journal of Geophysical Research*, 97(C12), 20325–20334.

WADHAMS, P., WILKINSON, J. P. & MCPHAIL, S. D. (2006): A new view of the underside of Arctic sea ice. *Geophysical Research Letters*, 33, 4501–+.

WARREN, S. G., RIGOR, I. G. & UNTERSTEINER, N. (1999): Snow depth on Arctic sea ice. *Journal of Climate*, 12(6), 1814–1829.

WEEKS, W. F. & LEE, O. S. (1958): Observations on the physical properties of sea ice at Hopedale, Labrador. *Arctic*, 11, 135–155.

WEEKS, W. F., TUCKER, W. B., I., FRANK, M. & FUNGCHAROEN, S. (1980): Characterization of the surface roughness and floe geometry of the sea ice over the continental shelves of the Beaufort and Chukchi Seas. In PRITCHARD, R. S., ed., *Sea Ice Processes and Models*, 300–312, University of Washington Press, Seattle.

WENZEL, M. & SCHRÖTER, J. (2006): The Global Ocean Mass Budget in 1993 – 2003 estimated from Sea Level Change. *Journal of physical oceanography*, 37(2), 203–213.

WILLIAMS, E., SWITHINBANK, C. & ROBIN, G. D. Q. (1975): A submarine sonar study of Arctic pack ice. *Journal of Glaciology*, 15, 349–362.

WINGHAM, D. (1999): The First of the European Space Agency's Opportunity Missions: CryoSat. Technical Report Earth Observation Quarterly, 63, ESA.

WINGHAM, D. (2003): CRYOSAT: A Mission to Determine Fluctuations in the Earth's Ice Fields. *EGS – AGU – EUG Joint Assembly, Abstracts from the meeting held in Nice, France, 6 – 11 April 2003, abstract #14579*, 14579–+.

WINGHAM, D. J., FRANCIS, C. R., BAKER, S., BOUZINAC, C., BROCKLEY, D., CULLEN, R., DE CHATEAU–THIERRY, P., LAXON, S. W., MALLOW, U., MAVROCORDATOS, C., PHALIPPOU, L., RATIER, G., REY, L., ROSTAN, F., VIAU, P. & WALLIS, D. W. (2006): CryoSat: A mission to determine the fluctuations in Earth's land and marine ice fields. *Advances in Space Research*, 37, 841–871.

WMO (1989): WMO Sea Ice Nomenclature, supplement no. 5, 1989, World Meteorological Organization, Geneva.

WORBY, A. P., BUSH, G. M. & ALLISON, I. (2001): Seasonal development of sea–ice thickness distribution in East Antarctica: measurements from upward–looking sonar data. *Annals of Glaciology, vol.33, pp.177–180*, 33, 177–180.

ZWALLY, H. J., SCHUTZ, B., ABDALATI, W., ABSHIRE, J., BENTLEY, C., BRENNER, A., BUFTON, J., DEZIO, J., HANCOCK, D., HARDING, D., HERRING, T., MINSTER, B., QUINN, K., PALM, S., SPINHIRNE, J. & THOMAS, R. (2002): ICESat's laser measurements of polar ice, atmosphere, ocean, and land. *Journal of Geodynamics*, 34, 405–445.

A Index of important Symbols

A.1 Index of Latin Symbols

$a_0 - a_4$	Coefficients for fitting functions – Arctic
$b_0 - b_5$	Coefficients for fitting functions – Antarctic
d	Draft
D	Distance
dx	Vector along plumb line
f	Freeboard
$gelev_{geoid}$	Ground elevation above geoid
$gelev_{WGS84}$	Ground elevation above WGS 84
g	Gravity vector
h_i	Ice thickness
h_s	Snow depth
H	Orthometric height
$L1$	Primary carrier frequency
$L2$	Secondary carrier frequency
N	Geoidal height
R	Total thickness/surface elevation ratio
$s_0 - s_3$	Coefficients for snow fitting function
$selev$	Surface elevation
t	Total thickness
V	Gravitational potential
W	Gravity potential
y_0, a, τ	Coefficients for R error function
Z	Ellipsoidal WGS height

A.2 Index of Greek Symbols

Δ	Laplace operator
φ	Geographical latitude
κ	Newton's gravitational constant
λ	Geographical longitude
ρ_s	Density of snow
ρ_i	Density of sea ice
ρ_w	Density of sea water
ρ	Density of unit mass
ω	Angular velocity of the Earth's rotation

Acknowledgments

First of all, I would like to thank Prof. H. Miller for the opportunity to conduct and complete my doctoral thesis at the Alfred-Wegener-Institute for Polar and Marine Research (AWI) in Bremerhaven and for supervising this study on behalf of the University of Bremen.

Further, I am grateful to Christian Haas, who did a great job as an advisor in terms of being available for short questions and long discussions, as well as providing assistance and advice at any time. I also appreciate the accurate reading of this thesis and the comments.

I express my gratitude to my colleague Stefan Hendricks for his great help, ideas, and support with respect to generating certain graphs and special IDL-routines, as well as for suggesting improvements in form and content regarding this study. His patience and faithful dedication in explaining and discussing special issues and his general calm and quiet nature contributed to a very pleasant working atmosphere.

This work was substantially improved linguistically, following the careful review by Mark Hinga at Sandia National Laboratories, NM, USA, to whom special thanks is due. Without his great efforts the text would not be in the present form.

Special thanks go to René Forsberg, Sine Hvidegaard, and Henriette Skourup, for the good cooperation during the measurement campaigns and regarding the data exchange.

Furthermore, I thank Daniel Steinhage from the glacialogy section at AWI for providing support and access to the NOGRAM data,
Tobias Boebel and Jutta Vernaleken at Optimare for their initial help regarding the GPS post-processing
Malte Thoma for helpful suggestions regarding LaTex and GMT, and providing assistance at any time
Richard Crawford for pre-correcting the text linguistically, and Wolfgang Cohrs for administrating and maintaining the SUN computing environment.

Last but not least, I would like to thank the sea ice physics working group, the entire research division, climate sciences, and others who contributed to the success of this study.

I also gratefully acknowledge support for this work from the European Union (EU) under grant EVK2-CT-2002-00156 – GreenICE.

Bremerhaven, February, 2007

„Berichte zur Polarforschung“

Eine Titelübersicht der Hefte 1 bis 376 (1981 - 2000) erschien zuletzt im Heft 413 der nachfolgenden Reihe „Berichte zur Polar- und Meeresforschung“. Ein Verzeichnis aller Hefte beider Reihen sowie eine Zusammenstellung der Abstracts in englischer Sprache finden Sie im Internet unter der Adresse: http://www.awi-bremerhaven.de/Resources/publications.html

Ab dem Heft-Nr. 377 erscheint die Reihe unter dem Namen: „Berichte zur Polar- und Meeresforschung“

Heft-Nr. 377/2000 – „Rekrutierungsmuster ausgewählter Wattfauna nach unterschiedlich strengen Wintern“ von Matthias Strasser

Heft-Nr. 378/2001 – „Der Transport von Wärme, Wasser und Salz in den Arktischen Ozean“, von Boris Cisewski

Heft-Nr. 379/2001 – „Analyse hydrographischer Schnitte mit Satellitenaltimetrie“, von Martin Losch

Heft-Nr. 380/2001 – „Die Expeditionen ANTARKTIS XI/1-2 des Forschungsschiffes POLARSTERN 1998/1999“, herausgegeben von Eberhard Fahrbach und Saad El Naggar.

Heft-Nr. 381/2001 – „UV-Schutz- und Reparaturmechanismen bei antarktischen Diatomeen und Phaeocystis antarctica“, von Lieselotte Riegger.

Heft-Nr. 382/2001 – „Age determination in polar Crustacea using the autofluorescent pigment lipofuscin“, by Bodil Bluhm.

Heft-Nr. 383/2001 – „Zeitliche und räumliche Verteilung, Habitatspräferenzen und Populationsdynamik benthischer Copepoda Harpacticoida in der Potter Cove (King George Island, Antarktis)“, von Gritta Veit-Köhler.

Heft-Nr. 384/2001 – „Beiträge aus geophysikalischen Messungen in Dronning Maud Land, Antarktis, zur Auffindung eines optimalen Bohrpunktes für eine Eiskerntiefbohrung“, von Daniel Steinhage.

Heft-Nr. 385/2001 – „Actinium-227 als Tracer für Advektion und Mischung in der Tiefsee“, von Walter Geibert.

Heft-Nr. 386/2001 – „Messung von optischen Eigenschaften troposphärischer Aerosole in der Arktis“ von Rolf Schumacher.

Heft-Nr. 387/2001 – „Bestimmung des Ozonabbaus in der arktischen und subarktischen Stratosphäre“, von Astrid Schulz.

Heft-Nr. 388/2001 – „Russian-German Cooperation SYSTEM LAPTEV SEA 2000: The Expedition LENA 2000“, edited by Volker Rachold and Mikhail N. Grigoriev.

Heft-Nr. 389/2001 – „The Expeditions ARKTIS XVI/1 and ARKTIS XVI/2 of the Research Vessel ‘Polarstern’ in 2000“, edited by Gunther Krause and Ursula Schauer.

Heft-Nr. 390/2001 – „Late Quaternary climate variations recorded in North Atlantic deep-sea ostracodes“, by Claudia Didié.

Heft-Nr. 391/2001 – „The polar and subpolar North Atlantic during the last five glacial-interglacial cycles“, by Jan. P. Helmke.

Heft-Nr. 392/2000 – „Geochemische Untersuchungen an hydrothermal beeinflußten Sedimenten der Bransfield Straße (Antarktis)“, von Anke Dählmann.

Heft-Nr. 393/2001 – „The German-Russian Project on Siberian River Run-off (SIRRO): Scientific Cruise Report of the Kara-Sea Expedition ‘SIRRO 2000’ of RV ‘Boris Petrov’ and first results“, edited by Ruediger Stein and Oleg Stepanets.

Heft-Nr. 394/2001 – „Untersuchung der Photooxidantien Wasserstoffperoxid, Methylhydroperoxid und Formaldehyd in der Troposphäre der Antarktis“, von Katja Riedel.

Heft-Nr. 395/2001 – „Role of benthic cnidarians in the energy transfer processes in the Southern Ocean marine ecosystem (Antarctica)“, by Covadonga Orejas Saco del Valle.

Heft-Nr. 396/2001 – „Biogeochemistry of Dissolved Carbohydrates in the Arctic“, by Ralph Engbrodt.

Heft-Nr. 397/2001 – „Seasonality of marine algae and grazers of an Antarctic rocky intertidal, with emphasis on the role of the limpet Nacilla concinna Strebel (Gastropoda: Patellidae)“, by Dohong Kim.

Heft-Nr. 398/2001 – „Polare Stratosphärenwolken und mesoskalige Dynamik am Polarwirbelrand“, von Marion Müller.

Heft-Nr. 399/2001 – „North Atlantic Deep Water and Antarctic Bottom Water: Their Interaction and Influence on Modes of the Global Ocean Circulation“, by Holger Brix.

Heft-Nr. 400/2001 – „The Expeditions ANTARKTIS XVIII/1-2 of the Research Vessel ‘Polarstern’ in 2000“ edited by Victor Smetacek, Ulrich Bathmann, Saad El Naggar.

Heft-Nr. 401/2001 – „Variabilität von CH_2O (Formaldehyd) - untersucht mit Hilfe der solaren Absorptionsspektroskopie und Modellen“ von Torsten Albrecht.

Heft-Nr. 402/2001 – „The Expedition ANTARKTIS XVII/3 (EASIZ III) of RV ‘Polarstern’ in 2000“, edited by Wolf E. Arntz and Thomas Brey.

Heft-Nr. 403/2001 – „Mikrohabitatansprüche benthischer Foraminiferen in Sedimenten des Südatlantiks“, von Stefanie Schumacher.

Heft-Nr. 404/2002 – „Die Expedition ANTARKTIS XVII/2 des Forschungsschiffes ‘Polarstern’ 2000“, herausgegeben von Jörn Thiede und Hans Oerter.

Heft-Nr. 405/2002 – „Feeding Ecology of the Arctic Ice-Amphipod Gammarus wilkitzkii. Physiological, Morphological and Ecological Studies“, by Carolin E. Arndt.

Heft-Nr. 406/2002 – „Radiolarienfauna im Ochotskischen Meer - eine aktuopaläontologische Charakterisierung der Biozönose und Taphozönose“, von Anja Nimmergut.

Heft-Nr. 407/2002 – „The Expedition ANTARKTIS XVIII/5b of the Research Vessel ‘Polarstern’ in 2001, edited by Ulrich Bathmann.

Heft-Nr. 408/2002 – „Siedlungsmuster und Wechselbeziehungen von Seepocken (Cirripedia) auf Muschelbänken (Mytilus edulis L.) im Wattenmeer“, von Christian Buschbaum.

Heft-Nr. 409/2002 – „Zur Ökologie von Schmelzwassertümpeln auf arktischem Meereis - Charakteristika, saisonale Dynamik und Vergleich mit anderen aquatischen Lebensräumen polarer Regionen“, von Marina Carstens.

Heft-Nr. 410/2002 – „Impuls- und Wärmeaustausch zwischen der Atmosphäre und dem eisbedeckten Ozean“, von Thomas Garbrecht.

Heft-Nr. 411/2002 – „Messung und Charakterisierung laminarer Ozonstrukturen in der polaren Stratosphäre“, von Petra Wahl.

Heft-Nr. 412/2002 – „Open Ocean Aquaculture und Offshore Windparks. Eine Machbarkeitsstudie über die multifunktionale Nutzung von Offshore-Windparks und Offshore-Marikultur im Raum Nordsee“, von Bela Hieronymus Buck.

Heft-Nr. 413/2002 – „Arctic Coastal Dynamics. Report of an International Workshop. Potsdam (Germany) 26-30 November 2001“, edited by Volker Rachold, Jerry Brown and Steve Solomon.

Heft-Nr. 414/2002 – „Entwicklung und Anwendung eines Laserablations-ICP-MS-Verfahrens zur Multielementanalyse von atmosphärischen Einträgen in Eisbohrkernen“, von Heiko Reinhardt.

Heft-Nr. 415/2002 – „Gefrier- und Tauprozesse im sibirischen Permafrost – Untersuchungsmethoden und ökologische Bedeutung“, von Wiebke Müller-Lupp.

Heft-Nr. 416/2002 – „Natürliche Klimavariationen der Arktis in einem regionalen hochauflösenden Atmosphärenmodell“, von Wolfgang Dorn.

Heft-Nr. 417/2002 – „Ecological comparison of two sandy shores with different wave energy and morphodynamics in the North Sea“, by Iris Menn.

Heft-Nr. 418/2002 – „Numerische Modellierung turbulenter Umströmungen von gebäuden“, von Simón Domingo López.

Heft-Nr. 419/2002 – „Scientific Cruise Report of the Kara-Sea Expedition 2001 of RV „Academic Petrov“: The German-Russian Project on Siberian River Run-off (SIRRO) and the Project „ESTABLISH“, edited by Ruediger Stein and Oleg Stepanets.

Heft-Nr. 420/2002 – „Vulkanologie und Geochemie pliozäner bis rezenter Vulkanite beiderseits der Bransfield-Straße / West-Antarktis“, von Andreas Veit.

Heft-Nr. 421/2002 – „POLARSTERN ARKTIS XVII/2 Cruise Report: AMORE 2001 (Arctic Mid-Ocean Ridge Expedition)“, by J. Thiede et al.

Heft-Nr. 422/2002 – „The Expedition „AWI of RV „L’Atalante“ in 2001“, edited by Michael Klages, Benoit Mesnil, Thomas Soltwedel and Alain Christophe with contributions of the participants.

Heft-Nr. 423/2002 – „Über die Tiefenwasserausbreitung im Weddellmeer und in der Scotia-Sea: Numerische Untersuchungen der Transport- und Austauschprozesse in der Weddell-Scotia-Konfluenz-Zone“, von Michael Schodlok.

Heft-Nr. 424/2002 – „Short- and Long-Term Environmental Changes in the Laptev Sea (Siberian Arctic) During the Holocene“, von Thomas Müller-Lupp.

Heft-Nr. 425/2002 – „Characterisation of glacio-chemical and glacio-meteorological parameters of Amundsenisen, Dronning Maud Land, Antarctica“, by Fidan Göktas.

Heft-Nr. 426/2002 – „Russian-German Cooperation SYSTEM LAPTEV SEA 2000: The Expedition LENA 2001“, edited by Eva-Maria Pfeiffer and Mikhail N. Grigoriev.

Heft-Nr. 427/2002 – „From the Inner Shelf to the Deep Sea: Depositional Environments on the West Antarctic Peninsula Margin – A Sedimentological and Seismostratigraphic Study (ODP Leg 178)“, by Tobias Mörz.

Heft-Nr. 428/2002 – „Concentration and Size Distribution of Microparticles in the NGRIP Ice Core (Central Greenland) during the Last Glazial Period“, by Urs Ruth.

Heft-Nr. 429/2002 – „Interpretation von FCKW-Daten im Weddellmeer“, von Olaf Klatt.

Heft-Nr. 430/2002 – „Thermal History of the Middle and Late Miocene Southern Ocean - Diatom Evidence“, by Bernd M. Censarek.

Heft-Nr. 431/2002 – „Radium-226 and Radium-228 in the Atlantic Sector of the Southern Ocean“, by Claudia Hanfland.

Heft-Nr. 432/2002 – „Population dynamics and ecology of the surf clam Donax serra (Bivalvia, Donacidae) inhabiting beaches of the Benguela upwelling system“, by Jürgen Laudien.

Heft-Nr. 433/2002 – „Die Expedition ARKTIS XVII/1 des Forschungsschiffes POLARSTERN 2001“, herausgegeben von Eberhard Fahrbach.

Heft-Nr. 434/2002 – „The Rôle of Sponges in High-Antarctic Carbon and Silicon Cycling – a Modelling Approach“, by Susanne Gatti.

Heft-Nr. 435/2003 – „Sedimente des Changeable-Sees, Oktoberrevolutions-Insel (Severnaja Zemlja), als Archive der Paläoumwelt Mittelsibiriens seit dem Frühweichsel“, von Alexandra Raab.

Heft-Nr. 436/2003 – „The charnockite-anorthosite suite of rocks exposed in central Dronning Maud Land, East Antarctica: a study on fluid-rock interactions, and post-entrapment change of metamorphic fluid inclusions“, by Bärbel Kleinefeld.

Heft-Nr. 437/2003 – „Variable C:N Ratios of Particulate Organic Matter and Their Influence on the Marine Carbon Cycle“, by Birgit Schneider.

Heft-Nr. 438/2003 – „Population ecology and genetics of the polychaete Scoloplos armiger (Orbiniidae)“, by Inken Kruse.

Heft-Nr. 439/2003 – „Architecture and geodynamic evolution of the Svalbard Archipelago, the Yermak Plateau and the Fram Strait oceanic Province from deep seismic experiments“, by Oliver Ritzmann.

Heft-Nr. 440/2003 – „Occurrence, induction and physiological importance of UV-absorbing substances in polar macroalgae“, by Kirsten Hoyer.

Heft-Nr. 441/2003 – „Sea ice conditions in the Transpolar Drift in August/September 2001. Observations during POLARSTERN cruise ARKTIS XVII/2“, compiled by Christian Haas and Jan J. Lieser.

Heft-Nr. 442/2003 – Süßwassereintrag und Festeis in der ostsibirischen Arktis - Ergebnisse aus Boden- und Satellitenbeobachtungen sowie Sensitivitätsstudien mit einem thermodynamischen Festeismodell“, von Jörg Bareiss.

Heft-Nr. 443/2003 – „Arctic Coastal Dynamics. Report of the 3rd International Workshop. University of Oslo (Norway) 2-5 December 2002“, edited by Volker Rachold, Jerry Brown, Steven Solomon and Johan Ludvig Sollid.

Heft-Nr. 444/2003 – „Ventilation der Grönlandsee – Variabilität und ihre Ursachen 1994-2001“, von Stephanie Ronski.

Heft-Nr. 445/2003 – „Die Expedition ANTARKTIS XVIII/3-4 des Forschungsschiffes POLARSTERN 2000/2001 sowie die Aktivitäten an Land und bei der Neumayer-Station“, herausgegeben von Eberhard Fahrbach, Dieter Fütterer, Saad El Naggar und Hans Oerter.

Heft-Nr. 446/2003 – „The Expedition ARKTIS XVIII/1 a, b of the Research Vessel „Polarstern“ in 2002“, edited by Peter Lemke

Heft-Nr. 447/2003 – „Investigation of the Greenland Atmospheric Boundary Layer over Summit 2002 (IGLOS). Field Phase Report“, by Clemens Drüe and Günther Heinemann.

Heft-Nr. 448/2003 – „Die Expedition ANTARKTIS XIX mit FS „Polarstern“ 2001/2002. Bericht von den Fahrtabschnitten 1 und 2“, herausgegeben von Wilfried Jokat und Gunther Krause.

Heft-Nr. 449/2003 – „The Expedition ARKTIS XVIII/2 of RV „Polarstern“ in 2002. Contributions of the Participants“, edited by Wilfried Jokat.

Heft-Nr. 450/2003 – „Scientific Cruise Report of the joint Russian-German Kara Sea Expedition in 2002 with RV „Akademik Boris Petrov“, edited by Frank Schoster and Michael Levitan.

Heft-Nr. 451/2003 – „Die Krustenstruktur der Fjordregion Ostgrönlands zwischen dem präkambrischen Schild und den rezenten mittelozeanischen Rücken: Ergebnisse seismischer und gravimetrischer Modellierungen“, von Mechita Schmidt-Aursch.

Heft-Nr. 452/2003 – „Untersuchungen zur Biodiversität antarktischer benthischer Amphipoda (Malacostraca, Crustacea)“, von Anne-Nina Lörz.

Heft-Nr. 453/2003 – „The Antarctic Circumpolar Current: Dynamics of a circumpolar channel with blocked geostrophic contours“, by Daniel Borowski.

Heft-Nr. 454/2003 – „The effects of climate induced temperature changes on Cod (Gadus morhua L.): Linking ecological and physiological investigations“, by Torsten Fischer.

Heft-Nr. 455/2003 – „Sediment Transport on Arctic Shelves – Seasonal Variations in Suspended Particulate Matter Dynamics on the Laptev Sea Shelf (Siberian Arctic)“, by Carolyn Wegner.

Heft-Nr. 456/2003 – „Dynamics of the Ocean Surface in the Polar and Subpolar North Atlantic over the last 500 000 Years“, by Evguenia S. Kandiano

Heft-Nr. 457/2003 – „Structure and dynamics of a submarine continent: Tectonic-magmatic evolution of the Campbell Plateau (New Zealand). report of the RV „SONNE“ cruise SO-169, Project CAMP, 17 January to 24 February 2003“, edited by Karsten Gohl

Heft-Nr. 458/2003 – „Antioxidative properties of marine macroalgae from the Arctic“ by Angelika Dummermuth.

Heft-Nr. 459/2003 – „Analysing benthic communities in the Weddell Sea (Antarctica): a landscape approach“, by Núria Teixidó Ullod

Heft-Nr. 460/2003 – „The Expeditions Amery Oasis, East Antarctica, in 2001/02 and Taylor Valley, Southern Victoria Land, in 2002“, by Bernd Wagner.

Heft-Nr. 461/2003 – „Late Quaternary climate history of Northern Siberia – evidence from ground ice“, by Hanno Meyer.

Heft-Nr. 462/2003 – „The Expedition ANTARKTIS XIX/5 (LAMPOS) of RV ‘Polarstern’ in 2002“, edited by Wolf E. Arntz and Thomas Brey.

Heft-Nr. 463/2003 – „Distribution, composition, flux and variability of organic carbon in Fram Strait/Yermak Plateau (Arctic Ocean) and (palaeo) environmental significance“, by Daniel Birgel.

Heft-Nr. 464/2003 – „The influence of aerosols on the oceanic sedimentation and environmental conditions in the Arctic“, by Vladimir Shevchenko.

Heft-Nr. 465/2003 – „Chemical ecology and palatability of marine invertebrates in the sub-Arctic Kongsfjord (Spitsbergen), by Heike Lippert.

Heft-Nr. 466/2003 – „Russian-German Cooperation SYSTEM LAPTEV SEA. The Expedition LENA 2002“, edited by Mikhail N. Grigoriev, Volker Rachold, Dmitry Yu. Bolshianov, Eva-Maria Pfeiffer, Lutz Schirrmeister, Dirk Wagner and Hans-Wolfgang Hubberten.

Heft-Nr. 467/2003 – „Effekte von UV-Strahlung auf die antarktische Rotalge Palmaria decipiens“, von Frank Poppe.

Heft-Nr. 468/2003 – „Einfluss arktischer Süßwasserquellen auf die Zirkulation im Nordmeer und im Nordatlantik in einem prognostischen Ozean-Meereis-Modell“, von Matthias Prange.

Heft-Nr. 469/2003 – „Acclimation of the photosynthetic apparatus of the endemic Antarctic red marcroalga Palmaria decipiens to seasonally changing light conditions“, by Ulrike H. Lüder.

Heft-Nr. 470/2003 – „The Expeditions ANTARKTIS-XIX/3-4 of the Research Vessel POLARSTERN in 2002 (ANDEEP I and II: Antarctic benthic deep-sea biodiversity – colonization, history and recent community patterns)“, edited by Dieter K. Fütterer, Angelika Brandt and Gary C. B. Poore.

Heft-Nr. 471/2004 – „Late Quaternary Sedimentation History of the Lena Delta“, by Georg Johannes Schwamborn

Heft-Nr. 472/2004 – „Late Jurassic to Early Cretaceous black shale formation and paleoenvironment in high northern latitudes“, by Uwe Langrock.

Heft-Nr. 473/2004 – „Melatoningehalt in marinen Makroalgen. Entwicklung und Validierung quantitativer Bestimmungen mittels HPLC und Enzym-gekoppeltem Immunoassay“, von Carsten Pape.

Heft-Nr. 474/2004 – „On the nature, interpretation, and application of electromagnetic reflections in cold ice“, by Olaf Eisen.

Heft-Nr. 475/2004 – „The Expedition ARKTIS XIX/4 of the Research Vessel POLARSTERN in 2003. Reports of Legs 4a and 4b“, edited by Wilfried Jokat.

Heft-Nr. 476/2004 – „Variabilität chemischer und physikalischer Parameter des Aerosols in der antarktischen Troposphäre“, von Claudia Piel.

Heft-Nr. 477/2004 – „Die Entwicklung der deutschen Wattforschung: Ein wissenschaftshistorischer Beitrag zur Bedeutung der Pionierarbeiten“, von Hauke Bietz.

Heft-Nr. 478/2004 – „Multidecadal and NAO related variability in a numerical model of the North Atlantic circulation“, by Jennifer P. Brauch

Heft-Nr. 479/2004 – „Scientific Cruise Report of the Kara Sea Expedition with RV „Akademik Boris Petrov“ in 2003 within the frames of the Russian-German project „SIRRO“ and the Russian-Norwegian project „MAREAS“, edited by Frank Schoster and Michael Levitan.

Heft-Nr. 480/2004 – „Environment, adaptation and evolution: Scallop ecology across the latitudinal gradient“, by Olaf Heilmayer.

Heft-Nr. 481/2004 – „The Expedition ARKTIS XIX/1 a, b and XIX/2 of the Research Vessel „POLARSTERN“ in 2003“, edited by Ursula Schauer and Gerhard Kattner.

Heft-Nr. 482/2004 – „Arctic Coastal Dynamics. Report of the 4th International Workshop. VNIIOkeangeologia, St. Petersburg (Russia), 10-13 November 2003“, edited by Volker Rachold, and Georgy Cherkashov.

Heft-Nr. 483/2003 – „Reproductive trade-offs in benthic decapod crustaceans of high southern latitudes: tolerance of cold and food limitation“, by Sven Thatje.

Heft-Nr. 484/2004 – „Wavelength dependent induction and biosynthesis of UV-absorbing mycosporine-like amino acids in marine macroalgae“, by Gudrun Kräbs.

Heft-Nr. 485/2004 – „A Numerical Model for Short-term Sea Ice Forecasting in the Arctic“, by Jan Leonhard Lieser.

Heft-Nr. 486/2004 – „Zum Einfluß troposphärischer Aerosole auf das Klima der Arktis“, von Martin Fortmann.

Heft-Nr. 487/2004 – „Parallel Filter Algorithms for Data Assimilation in Oceanography“, by Lars Nerger.

Heft-Nr. 488/2004 – „The Expedition ARKTIS XIX/3 of the Research Vessel POLARSTERN in 2003. Reports of Legs 3a, 3b and 3c“, edited by Michael Klages, Jörn Thiede and Jean-Paul Foucher.

Heft-Nr. 489/2003 – „Expeditions in Siberia in 2003“, edited by Lutz Schirrmeister.

Heft-Nr. 490/2004 – „Modern Sedimentation Processes in the Kara Sea (Siberia)“, by Andrea Catalina Gebhardt.

Heft-Nr. 491/2004 – „Bentho-pelagische Kopplungsprozesse im arktischen Mellemfjord (Westgrönland) unter besonderer Berücksichtigung benthischer Peracarida (Malacostraca, Crustacea)“, von Jörg Nickel.

Heft-Nr. 492/2004 – „The coastal ecosystem of Kongsfjorden, Svalbard. Synopsis of biological research performed at the Koldewey Station in the years 1991-2003“, edited by Christian Wiencke.

Heft-Nr. 493/2004 – „Ontogeny of osmoregulatory functions and structures of three decapod crustaceans from the North Sea“, by Ude Cieluch.

Heft-Nr. 494/2005 – „Community dynamics and development of soft bottom macrozoobenthos in the German Bight (North Sea) 1969-2000“, by Alexander Schroeder.

Heft-Nr. 495/2005 – „The Expedition ANTARKTIS-XX of RV ‘Polarstern’ in 2002/2003. Reports of Legs 1 and 2“, edited by Dieter K. Fütterer and Gerhard Kattner.

Heft-Nr. 496/2005 – „Reproduction strategies and distribution of larvae and juveniles of benthic soft-bottom invertebrates in the Kara Sea (Russian Arctic)“, by Ingo Fetzer.

Heft-Nr. 497/2005 – „Großräumige Zirkulationsstrukturen in einem nichtlinearen adaptiven Atmosphärenmodell“, von Matthias Läuter.

Heft-Nr. 498/2005 – „Terrigener Sedimenteintrag und Paläoumwelt im spätquartären Arktischen Ozean: Rekonstruktionen nach Haupt- und Spurenelementverteilungen“, von Frank Schoster.

Heft-Nr. 499/2005 – „Der Einfluss der Großen Meteorbank auf die Ernährungsbiologie und Verteilung dominanter Calanoida (Crustacea, Copepoda)“, von Lutz Fischer.

Heft-Nr. 500/2005 – „The Expeditions ANTARKTIS XXI/3-4-5 of the Research Vessel „Polarstern“ in 2004“, edited by Victor Smetacek, Ulrich Bathmann, Elisabeth Helmke.

Heft-Nr. 501/2005 – „Pechora Sea Environments: Past, Present, and Future“, edited by H. A. Bauch, Yu. A. Pavlidis, Ye. I. Polyakova, G. G. Matishov, N. Koç.

Heft-Nr. 502/2005 – „Distribution and Mobility of Juvenile Polychaeta in a Sedimentary Tidal Environment“, by Norma Angélica Hernández-Guevara.

Heft-Nr. 503/2005 – „The Expedition ANTARKTIS XXI/2 (BENDEX) of RV ‘Polarstern’ in 2003/2004“, edited by Wolf E. Arntz and Thomas Brey.

Heft-Nr. 504/2005 – „Sea ice conditions in the northern North Atlantic in 2003 and 2004. Observations during RV POLARSTERN cruises ARKTIS XIX/1a and b and ARKTIS XX/2“, compiled by Jan L. Lieser.

Heft-Nr. 505/2005 – „Biodiversity, zoogeography and ecology of polychaetes from the Magellan region and adjacent areas“, by Américo Montiel San Martín.

Heft-Nr. 506/2005 – „Arctic Coastal Dynamics. Report of the 5th International Workshop. McGill University, Montreal (Canada), 13-16 October 2004“, edited by Volker Rachold, Hugues Lantuit, Nicole Couture and Wayne Pollard.

Heft-Nr. 507/2005 – „Evolution of Antarctic Fauna. Extended Abstracts of the IBMANT/ANDEEP International Symposium and Workshop in 2003“, edited by Sven Thatje, Javier A. Calcagno and Wolf E. Arntz.

Heft-Nr. 508/2005 – „Calanoid copepod resting eggs – a safeguard against adverse environmental conditions in the German Bight and the Kara Sea?“, by Marcus Engel.

Heft-Nr. 509/2005 – „The Expedition El'gygytgyn Lake 2003 (Siberian Arctic)", edited by Martin Melles, Pavel Minyuk, Julie Brigham-Grette and Olaf Juschus.

Heft-Nr. 510/2005 – „Stability of the Climate System and Extreme Climates in Model Experiments", by Vanya Romanova.

Heft-Nr. 511/2005 – „Untersuchungen zu gezeitenbedingten Höhenänderungen des subglazialen Lake Vostok, Antarktika, von Anja Wendt.

Heft-Nr. 512/2005 – „Demography, Reproductive Biology and Trophic Ecology of Red Coral (Corallium rubrum L.) at the Costa Brava (NW Mediterranean)", by Georgios Tsounis.

Heft-Nr. 513/2005 – „Rekonstruktion tausendjähriger aerosolchemischer Eiskernzeitreihen aus Nordostgrönland: Quantifizierung zeitlicher Veränderungen in Atmosphärenzirkulation, Emission und Deposition", von Birgit Mieding.

Heft-Nr. 514/2005 – „Radiation conditions in an Antarctic environment", by Sigrid Wuttke.

Heft-Nr. 515/2005 – „Südöstlicher Atlantik und südwestlicher Indik. Rekonstruktion der sedimentären und tektonischen Entwicklung seit der Kreide. AISTEK-I: Agulhas Transect. Report of the RV „Sonne" cruise SO-182, Project AISTEK-I. 4 April to 18 May 2005", edited by Gabriele Uenzelmann-Neben.

Heft-Nr. 516/2005 – „Kontinental-Verschiebungen", Originalnotizen und Literaturauszüge von Alfred Wegener, herausgegeben von Reinhard Krause und Jörn Thiede.

Heft-Nr. 517/2005 – „Scientific Cruise Report of the Arctic Expedition ARK-XX/3 of RV „Polarstern" in 2004: Fram Strait, Yermak Plateau and East Greenland Continental Margin", edited by Ruediger Stein.

Heft-Nr. 518/2005 – „Exploring the neogene sedimentation of the eastern South Atlantic with reflection seismic data", by Etienne Wildeboer Schut.

Heft-Nr. 519/2006 – „The Influence of an Improved Soil Scheme on the Arctic Climate in a Regional Climate Model (RCM)", by Subodh Kumar Saha.

Heft-Nr. 520/2006 – „Global Implications of Arctic Climate Processes and Feedbacks. Report of the Arctic Climate Workshop. Alfred Wegener Institute for Polar and Marine Research, Potsdam (Germany), 5-7 September 2005", edited by Annette Rinke and Klaus Dethloff.

Heft-Nr. 521/2006 – „Südöstlicher Atlantik und südwestlicher Indik: Rekonstruktion der sedimentären und tektonischen Entwicklung seit der Kreide. AISTEK-II: Mosambik Rücken und Mosambik Becken. Report of the RV „Sonne" cruise SO-183, Projekt AISTEK-II. 20 May to 7 July 2005", edited by Wilfried Jokat.

Heft-Nr. 522/2006 – „Benthische Foraminiferenvergesellschaftungen als Anzeiger für spätquartäre Positionsänderungen der Fronten des Antarktischen Zirkumpolarstroms im Südatlantik", von Miriam Rudolph.

Heft-Nr. 523/2006 – „Late Weichselian to Holocene Sedimentation in the Inner Kara Sea: Qualification and Quantification of Processes", by Klaus Hauke Dittmers.

Heft-Nr. 524/2006 – „Nichtlineare Dynamik atmosphärischer Zirkulationsregime in einem idealisierten Modell", von Mario Sempf.

Heft-Nr. 525/2006 – „Processing of shipborne magnetometer data und revision of the timing and geometry of the Mesozoic break-up of Gondwana", by Matthias König.

Heft-Nr. 526/2006 – „Effects of ultraviolet radiation on early life stages of cold temperate and Arctic macroalgae: implications for recruitment and vertical depth distribution", by Michael Y. Roleda.

Heft-Nr. 527/2006 – „Kleinskalige Heterogenität in der arktischen Tiefsee: Einfluss kleiner Kaltwasser-Schwämme auf die Diversität benthischer Nematoden-Gemeinschaften", von Christiane Hasemann.

Heft-Nr. 528/2006 – „Makrozoobenthos-Gemeinschaften arktischer Weichböden: Struktur und Bedeutung als Nahrungsgrundlage demersaler Fische", von Marko Herrmann.

Heft-Nr. 529/2006 – „Strategies of cellular ageing in polar and temperate marine Invertebrates", by Eva Philipp.

Heft-Nr. 530/2006 – „Schiffstagebuch der Steam-Bark GROENLAND geführt auf einer Fangreise in die Antarktis im Jahre 1873/1874 unter der Leitung von Capitain Ed. Dallmann", herausgegeben und kommentiert von Reinhard A. Krause und Ursula Rack.

Heft-Nr. 531/2006 – „Aggregations of Arctic deep-sea scavenging amphipods at large food falls", by Katrin Premke.

Heft-Nr. 532/2006 – „Ecological Preferences of Benthic Foraminifera in the Eastern South Atlantic: Distribution Patterns, Stable Carbon Isotopic Composition, and Paleoceanographic Implications", by Laetitia Licari.

Heft-Nr. 533/2006 – „The Expedition ANTARKTIS-XXII/3 of the Research Vessel 'Polarstern' in 2005, edited by Eberhard Fahrbach.

Heft-Nr. 534/2006 – „Sensitivitätsstudien und Analyse von Atmosphäre-Meereis-Wechselwirkungen mit dem regionalen Atmosphärenmodell HIRHAM4 auf Basis eines neu entwickelten beobachtungsgestützten unteren Modellantriebs während ausgewählter Sommer über der Arktis / Laptewsee", von Klaus Görgen.

Heft-Nr. 535/2006 – „Beobachtung und Modellierung der Schneeschmelze und Aufeisbildung auf arktischem und antarktischem Meereis", von Marcel Nicolaus.
[Notice for corrections: The name of the author Nicolaus was regrettably misprinted on the title pages of that volume]

Heft-Nr. 536/2006 – „Tunicaten (Ascidiacea) der Nordsee: Chemische Ökologie und pharmakologisches Potential", von Jana Stefanie Barenbrock.

Heft-Nr. 537/2006 – „The Expeditions ANTARKTIS-XXII/4 and 5 of the Research Vessel 'Polarstern' in 2005", edited by Hans-Werner Schenke and Walter Zenk.

Heft-Nr. 538/2006 – „Radition Measurements and Synoptic Observations at Ny-Ålesund, Svalbard", by Heike Kupfer, Andreas Herber and Gert König-Langlo. – Notice: The report including the large appendix ist published at: http://epic.awi.de/Publications/Kup2006a.pdf

Heft-Nr. 539/2006 – „The Expedition LENA 2004 in Siberia and the Expedition LIVINGSTON 2005 in Antarctica", edited by Dirk Wagner.

Heft-Nr. 540/2006 – „Seafloor analysis based on multibeam bathymetry and backscatter data“, by Andreas Beyer.

Heft-Nr. 541/2006 – „The Exchange of Energy, Water and Carbon Dioxide between Wet Arctic Tundra and the Atmosphere at the Lena River Delta, Northern Siberia“, by Lars Kutzbach.

Heft-Nr. 542/2007 – „Identification of seafloor provinces - specific applications at the deep-sea Håkon Mosby Mud Volcano and the North Sea“, by Kerstin Jerosch.

Heft-Nr. 543/2007 – „Farming in a High Energy Environment: Potentials and Constraints of Sustainable Offshore Aquaculture in the German Bight (North Sea)“, by Bela Hieronymus Buck.

Heft-Nr. 544/2007 – „The Expeditions ARKTIS XX/1 and XX/2 of the Research Vessel ‘Polarstern’ in 2004“, edited by Gereon Budéus and Peter Lemke.

Heft-Nr. 545/2007 – „Lakustrine Sedimente als Archive des spätquartären Umweltwandels in der Amery-Oase, Ostantarktis“, von Nadja Hultzsch.

Heft-Nr. 546/2007 – „Detaillierte Biomarkeruntersuchungen an Sedimentkernen von ODP-Leg 177“, von Petra Weller.

Heft-Nr. 547/2007 – „Development of a novel balloon-borne optical sonde for the measurement of ozone and other stratospheric trace gases“, von Mareile Wolff.

Heft-Nr. 548/2007 – „Holocene and Last Glacial Maximum (paleo-)productivity off Morocco. Evidence from benthic foraminifera and stable carbon isotopes“, by Astrid Eberwein.

Heft-Nr. 549/2007 – „11th International Conference on the Physics and Chemistry of Ice (PCI-2006). Bremerhaven, Germany, 23-28 July 2006. Abstracts“, edited by Frank Wilhelms and Werner F. Kuhs.

Heft-Nr. 550/2007 – „Expeditions in Siberia in 2005“, edited by Lutz Schirrmeister.

Heft-Nr. 551/2007 – „The Expeditions ANTARKTIS-XXII/1 and XXII/2 of the Research Vessel ‘Polarstern’ in 2004/2005“, edited by Saad El Naggar, Gerhard Dieckmann, Christian Haas, Michael Schröder and Michael Spindler.

Heft-Nr. 552/2007 – „Spatial distribution of snow accumulation and snowpack properties in Dronning Maud Land, Antarctica: Observational techniques and methods for surface mass-balance assessments of polar ice sheets“, by Gerit Rotschky.

Heft-Nr. 553/2007 – „Helicopter Electromagnetic sea ice thickness estimation: An induction method in the centimetre scale“, by Andreas Pfaffling.

Heft-Nr. 554/2007 – „Late Quaternary environment of Central Yakutia (NE Siberia): Signals in frozen ground and terrestrial sediments“, by Steffen Popp.

Heft-Nr. 555/2007 – „Bestimmung verschiedener Eisklassen durch statistische Analyse der Rauigkeit von Meereis“, von Carola von Saldern.

Heft-Nr. 556/2007 – „The Expedition ANTARKTIS-XXIII/1 of the Research Vessel „Polarstern“ in 2005“, edited by Michiel Rutgers van der Loeff.

Heft-Nr. 557/2007 – „The Expedition ANTARKTIS-XXIII/4 of the Research Vessel „Polarstern“ in 2006“, edited by Karsten Gohl.

Heft-Nr. 558/2007 – „The Expedition ANTARKTIS-XXIII/3 of the Research Vessel „Polarstern“ in 2006“, edited by Christine Provost.

Heft-Nr. 559/2007 – „Determination of Sea Ice Surface Elevation with Laser and Radar Altimetry and Comparison with Ice Thickness Data Sets in the Arctic and Antarctic“, by Sibylle Göbell.

* vergriffen/out of print.

** nur noch beim Autor/only from the author.